Department of Civil, Environmental and Geomatic Engineering
University College London

Multiscale Characterisation of Microstructure and Mechanical Properties of Alkali-Activated Fly Ash-Slag Concrete

Guohao Fang

Supervisors:
Dr Mingzhong Zhang
Dr Zhifu Mi

A thesis submitted for the degree of
Doctor of Philosophy in Civil Engineering
October 2020

Statement of Originality

I, Guohao Fang, confirm that the work presented in this thesis is my own. Where information has been derived from other sources, I confirm that this has been indicated in the thesis.

Signed:

Date:

Abstract

Alkali-activated fly ash-slag (AAFS) concrete manufactured through the reaction of alkaline activator with industrial aluminosilicate by-products (fly ash and slag) is considered as a promising alternative to Portland cement (PC) concrete because of its environmental benefits (e.g. low CO_2 emission and low consumption of natural resources) and superior engineering properties under ambient curing condition. There is about 55% less CO_2 emissions in the production of AAFS comparing with the production of PC concrete. In addition, AAFS concrete can achieve a good synergy between fresh properties, mechanical properties and durability under ambient curing which cannot be achieved by the sole alkali-activated concrete, e.g., alkali-activated fly ash (AAF) and alkali-activated slag (AAS). AAF needs to be cured under an elevated temperature (60 ~ 85 °C) to gain early-age strength, whereas AAS concrete has some drawbacks including poor workability and quick setting.

The mechanical properties of AAFS concrete are highly dependent on its heterogeneous microstructure with multiscale (nano- to macro-scale) and multiphase (pore, reaction products, unreacted fly ash and slag particles, and aggregate). Although the microstructure and mechanical properties of AAFS concrete have been studied for decades, a systematic understanding of the microstructure and micromechanical properties of individual phases within AAFS concrete and their corresponding relationships with the macroscopic mechanical properties is still lacking to date. More specifically, the following aspects for AAFS concrete have not been fully understood: (i) reaction mechanism of fly ash and slag particles in AAFS system; (ii) microstructure evolution of interfacial transition zone (ITZ) in AAFS concrete; (iii) multiscale micromechanical properties of AAFS concrete; (iv) multiscale microstructure-mechanical properties relationship in AAFS concrete.

To fill these research gaps, this thesis aims to systematically characterise the microstructure and mechanical properties of AAFS concrete cured at ambient temperature at multiscale from nano- to macro-scale and to investigate the microstructure-mechanical properties relationship in AAFS concrete in depth. The multiscale features of AAFS concrete are identified based on four length levels: Level 0 (solid gel particle: 1 nm ~ 10 nm), Level I (gel matrix: 10 nm ~ 1 μm), Level II (paste: 1 μm ~ 100 μm), and Level III (concrete: 1 mm ~ 10 cm).

Regarding the multiscale characterisation of microstructure, the nanostructure of solid gel particle at Level 0 is characterised using nuclear magnetic resonance (NMR), while the chemical composition of gel matrix at Level I is evaluated by means of X-ray

diffraction (XRD) and Fourier transform infrared spectroscopy (FTIR). The in-situ monitoring of microstructure evolution of fly ash and slag particles in AAFS paste at Level II is achieved using X-ray microcomputed tomography (XCT), providing new insights into their reaction mechanism. The microstructure evolution of ITZ in AAFS concrete at Level III is characterised using backscattered scanning electron microscopy (BSEM) and energy dispersive spectrometry (EDS), which delivers needed insight into the mechanism of ITZ evolution. The results of microstructural characterisation provide a systematic understanding of the microstructure of individual phases in AAFS concrete and their inherent relationships at different length scales.

With respect to the multiscale characterisation of micromechanical properties, nanoindentation is used to evaluate the micromechanical properties (elastic modulus and hardness) of individual phases at Level I. It is the smallest material length scale that can be measured through experimental tests. The effective mechanical properties of AAFS paste at Level II are estimated using the self-consistent continuum micromechanics model by assuming that each nanoindentation test serves for a single phase in the material. Afterwards, the micromechanical properties of ITZ in AAFS concrete at Level III are evaluated through a series of statistical analysis. The multiscale micromechanical analysis offers the first-hand information of micromechanical properties of different phases in AAFS concrete and their contributions to the macroscopic mechanical properties of AAFS concrete. Lastly, the relationships between chemistry, microstructure, and mechanical properties of AAFS concrete from Level 0 to Level III are established based on the experimental results obtained above, which enable us to better understand the development of overall mechanical properties of this new type of concrete.

The experimental and simulated results indicate that the dissolutions of fly ash and slag particles in AAFS system are not uniform due to their inherently heterogeneous characteristics, which would consequently lead to the formation of non-uniform reaction products, mostly accumulating within the boundary of the original particles. The polymerisation degree and cross-linking of reaction products are improved over curing age, potentially through the initial formation of C-A-S-H gels followed by the gradual development of N-A-S-H and N-C-A-S-H gels with a higher cross-linking degree. Within these three types of reaction products, the N-A-S-H gels have a relatively low elastic modulus due to their high level of structural disorder and gel porosity. In addition, it is found that the elasticity of reaction products and their relative volumetric proportions mainly determine the macroscopic elasticity of AAFS paste, while the porosity and pore size distribution primarily condition its macroscopic strength. Furthermore, it is also

observed that ITZ formed in AAFS concrete has a comparable microstructure and micromechanical properties to the paste matrix, which indicates that ITZ might be not the weakest region within this new type of concrete. The ITZ with compact microstructure and high micromechanical properties would help to improve its macroscopic mechanical strength, especially for the fracture properties.

Impact statement

Alkali-activated fly ash-slag (AAFS) concrete, as a promising alternative binder to Portland cement (PC) concrete, is manufactured through the chemical reaction between alkaline activators and industry by-products (fly ash and slag), which leads to the microstructure evolution and the development of mechanical properties. Nevertheless, the relationships between chemistry, microstructure and mechanical properties of this new type of concrete remain unclear, due to a lack of systematic characterisation of its microstructure and mechanical properties at multiple length scales from nano- to macro-scale. Thus, the main objective of this research is to systematically explore the microstructure and mechanical properties of AAFS concrete at multiscale, which would enable us to build a link between microstructure and mechanical properties, bringing new insights into the influence of different phases on the overall mechanical properties of AAFS concrete.

From the academic perspective, this study fills some critical research gaps existing in this field. In terms of microstructure characterisation, it provides the first-ever 3D in-situ monitoring of microstructure evolution of fly ash and slag particles in AAFS paste, which would help us to better understand their reaction mechanism. Additionally, a systematic analysis of the microstructure evolution of interfacial transition zone (ITZ) in AAFS concrete addresses the limitation of simple analysis of local ITZ morphology in previous research, providing essential insight into the mechanism of ITZ evolution. Regarding the characterisation of micromechanical properties, this study offers the first-hand information of micromechanical properties of different phases in AAFS concrete and their contributions to the macroscopic mechanical properties, which have not been explored elsewhere. Lastly, the experimental results obtained in this study can serve as the database for numerical simulations in the future that are important and required for predicting and optimising the overall performance of AAFS concrete for engineering applications. Based on these studies, four high-quality papers have been published in prestigious journals in the field of construction and building technology.

From the industrial perspective, this research can benefit the development and application of sustainable concrete in the future. It is known that the current applications of other alkali-activated concrete such as alkali-activated fly ash (AAF) concrete and alkali-activated slag (AAS) concrete are generally limited to pre-cast concrete due to the requirement of high-temperate curing and the limitation of quick setting. Since the reactivity of fly ash under ambient curing condition is relatively low, adding fly ash into AAS concrete to form the blended concrete (i.e., AAFS concrete) would help to reduce

the overall reactivity of concrete and increase its setting time. To this end, the developed AAFS concrete under ambient curing conditions in this research with desired engineering properties such as workability, setting time and strength would promote its practical application, especially for the cast in situ. More specifically, AAFS concrete is appropriate for the non-structural application (e.g., road) based on this research. However, it is unknown whether this new type of concrete is suitable for the structural application (e.g., reinforced concrete structure) due to uncertain corrosion resistance of steel in this concrete.

Acknowledgements

Undertaking this PhD at UCL has been an invaluable and life-changing journey for me. I am really appreciated for the help, support, and guidance that I received from my supervisors, colleagues, friends, and family during the past four years in London.

First, I would like to say a huge thank you to my supervisor Dr Mingzhong Zhang, for providing guidance and support throughout this project. He had patiently taught me how to do academic research and guided me to carry out my research. He has always given me the freedom and encouragement to develop new ideas and skills in the research. In the meantime, he would also provide some opportunities for me to enhance my other skills, such as presentation and teaching skills. Furthermore, he has given me some helpful feedback for the writing and publication of journal papers. I would like to sincerely thank Dr Zhang for his strong supports and wise advice during my PhD study. I would also like to thank my secondary supervisor, Dr Zhifu Mi, for his kind guidance and valuable suggestions to my research and career development.

I am very thankful to Prof Xiangming Zhou and Dr Cise Unluer for serving as my PhD Viva examiners. The online Viva was conducted due to the COVID-19 pandemic. I am appreciated for their time and work during this special and hard period, and for their brilliant and valuable comments, which help me to improve this thesis.

Special appreciation goes to my colleagues and friends at UCL. The long list starts with, but is not limited to, Wenlin Tu, Cheng Liu, Trabacchin Giulia, Yi Wang, Hui Zhong, Guosheng Zhang, Tangwei Mi, Siyu Yang, Shuqiong Luo, Danqian Wang, Ucak Kaan, Mengke Ni, Mengjia Li, Zhengkui Wang and Linghui Zhou. I am really grateful for their help and encouragement during this four-year study in London. I would also like to thank Warren Gaynor, Dr Shi Shi, and Dr Judith Zhou from UCL Laboratory for their help with experiments. I would further thank Prof Biqin Dong from Shenzhen University, Prof Fazhou Wang, Prof Xiaochun Fan and Dr Tao Sun from Wuhan University of Technology for their supports with experimental tests.

The financial support provided by the China Scholarship Council (201608440242) and UCL Dean's Prize to me is gratefully acknowledged. It is also grateful for financial support from the Engineering and Physical Sciences Research Council (EP/RO41501/1) and the Royal Society (IE150587) to this research project.

Lastly, I would like to say a heartfelt appreciation to my Mum and Dad, my sister and my brother, for supporting and helping me without any conditions throughout these four years of my pursuit for a PhD. Thank you for raising me with all your love.

Table of Contents

List of Figures

List of Tables

List of Abbreviations

AAC: Alkali-activated concrete

AAF: Alkali-activated fly ash

AAFS: Alkali-activated fly ash-slag

AAS: Alkali-activated slag

AL: Alkaline activator

C-A-S-H: Calcium-alumina-silicate-hydrate

CH: Calcium hydroxide ($Ca(OH)_2$)

HD: High-density

IP: Inner products

ITZ: Interfacial transition zone

LD: Low-density

N-A-S-H: Alkali-aluminosilicate-hydrate

OP: Outer products

P: Precursor

PC: Portland cement

SH: Sodium hydroxide

SP: Superplasticizer

SS: Sodium silicate

BSEM: Backscattered scanning electron microscopy

EDS: Energy dispersive spectrometry

FTIR: Fourier transform infrared spectroscopy

MIP: Mercury intrusion porosimetry

NMR: Nuclear magnetic resonance

QXRD: Rietveld-based quantitative X-ray diffraction

SEM: Scanning electron microscopy

SHPB: Split Hopkinson pressure bar

TEM: Transmission electron microscopy

XRD: X-ray diffraction

XCT: X-ray microcomputed tomography

Chapter 1 Introduction

1.1 Research background

Portland cement (PC) concrete is the most widely used construction material attributing to its high performance in terms of workability and strength as well as the low cost (Aïtcin, 2000). Every year, about 25 billion tonnes of PC concrete are produced around the world (CSI Progress Report, 2009). The growing demand of PC concrete poses great challenges to concrete industry because of its large carbon emissions, accounting for approximately 8% of global CO_2 emissions (Scrivener and Kirkpatrick, 2008; Provis and Bernal, 2014), which motivates researchers for seeking suitable alternatives to PC concrete. In recent years, alkali-activated concrete (AAC) is regarded as a potential alternative by utilising industry by-products such as fly ash and slag (Shi et al., 2006; Pacheco-Torgal et al., 2014; Provis, 2018). There are about 55% less CO_2 emissions in the production of AAC comparing with the production of PC concrete (Yang et al., 2013).

It has been demonstrated that AAC can achieve comparable engineering properties (e.g. mechanical properties and durability) to PC concrete (Shi et al., 2011; Provis, 2018). However, some critical issues have also emerged in the commonly used AAC, e.g. alkali-activated fly ash (AAF) concrete and alkali-activated slag (AAS) concrete. For instance, AAF concrete requires rigorous curing conditions with elevated temperature (60 ~ 85 °C) to gain early-age strength, whereas AAS concrete has some drawbacks including poor workability and quick setting (Fan et al., 1999; Puertas et al., 2000; Somna et al., 2011). To conquer these limitations, recent development in the field of AAC has led to an increasing interest in the blended AAC, called alkali-activated fly ash-slag (AAFS) concrete, which can achieve desired fresh properties, mechanical properties and durability under ambient curing conditions (Puertas et al., 2000; Lee and Lee, 2015; Shang et al., 2018). Nevertheless, the practical applications of AAFS concrete remain low due to its uncertain reaction mechanism and the unclear relationship between microstructure and macroscopic properties.

AAFS concrete is a complex heterogeneous material composed of aggregates (fine and coarse aggregates), AAFS paste and interfacial transition zone (ITZ) between them. AAFS paste is produced by the chemical reaction between alkaline activators and aluminosilicate source materials, i.e. fly ash and slag, which leads to the microstructure evolution and motivates the development of macroscopic properties (Ismail et al., 2014; Marjanović et al., 2015; Lee and Lee, 2015). The reaction of fly ash and slag would result in the generation of tetracoordinate Al charge-balanced by Na and reaction products in the Na_2O-CaO-Al_2O_3-SiO_2 system, containing N-A-S-H gels, C-A-S-H gels and N-C-A-

S-H gels (Ismail et al., 2014). The reaction process of fly ash and slag is not independent, but the interaction occurs between them (Lloyd et al., 2009c; Lee and Lee, 2015; Ye and Radlińska, 2016). Accordingly, the relative content of fly ash and slag would consequently affect the development of microstructure and properties of AAFS concrete (Nath and Sarker, 2014; Marcin et al., 2016). The AAFS mixture with a high slag content shows a high reaction rate and a dense microstructure due to the soluble Ca from slag, which would promote the generation of C-A-S-H gels and result in a quicker setting as well as a higher strength than the mixture with a low slag content (Puligilla and Mondal, 2013). Nevertheless, more cross-linked binders with durable solid microstructure can be obtained in the mixture with a high fly ash content, attributing to the formation of N-A-S-H gels (Ismail et al., 2014).

Although the reaction process of fly ash and slag particles in AAFS system has been extensively investigated, the reaction mechanism of these particles has not been fully understood to date due to a lack of in-situ characterisation of their microstructure evolution. The existing results obtained using destructive testing method such as scanning electron microscopy (SEM) and energy dispersive spectrometry (EDS) can provide valuable 2D information for evaluating the microstructure evolution of fly ash and slag particles (Durdziński et al., 2015; Gebregziabiher et al., 2015). However, the preparation of samples for these tests requires pre-treatment such as cutting, grinding and polishing that may cause destruction of the samples and the in-situ monitoring of 3D microstructure development cannot be achieved using these techniques. To better understand the reaction process of fly ash and slag particles in AAFS, it is vital to find a test method that can non-destructively track the evolution of location, morphology and density of the reacted particles. X-ray microcomputed tomography (XCT) provides a great opportunity for the in-situ characterisation of microstructure evolution of fly ash and slag particles in AAFS, owing to the penetration ability of X-ray to pass through the thick and opaque objects (Landis and Keane, 2010; Brisard et al., 2020). Through image reconstruction technique, the internal 3D structure of AAFS can be qualitatively and quantitatively characterised without destructing the testing samples.

Regarding the ITZ between aggregate and paste matrix, it is usually considered as one of the most important features affecting the overall performance of concrete (Ollivier et al., 1995; Bentur et al., 2000; Scrivener et al., 2004). The ITZ with less compact microstructure and low strength would negatively affect the macroscopic strength of concrete, but this effect tends to become weak with the increase of compactness and strength of ITZ (Yu et al., 2018). Although the investigation on ITZ in PC concrete has

been undertaken by previous research (Xie et al., 1991; Elsharief et al., 2003; Wu et al., 2016), the existing knowledge about ITZ in AAFS concrete is limited to the simple analysis of local morphology, which cannot provide the needed information to understand the mechanism of ITZ evolution (Singh et al., 2016). Therefore, it is vital to conduct more comprehensive studies for a better understanding of the microstructure and properties of ITZ in AAFS concrete, particularly the microstructure formation and development of ITZ that have not been explored. The lack of consent related to the microstructure of ITZ in AAFS concrete would lead to open issues regarding its engineering applications, as it might bring with a positive or negative influence on the mechanical and transport properties of AAFS concrete.

The chemical reaction and microstructure evolution at multiple length scales from nano- to macro-scale are strongly associated with the development of mechanical properties of AAFS concrete (Puertas et al., 2000). The characteristics of microstructure at each scale would determine the properties (e.g. micromechanical properties) at the corresponding scale (Němeček et al., 2011; Lee et al., 2016; Ma et al., 2017). In the meantime, the properties of each component in microstructure at a lower scale would control the properties of a microstructure at a higher scale, and consequently govern the macroscopic properties of concrete (Šmilauer et al., 2011; Das et al., 2015). Up to now, the multiscale micromechanical properties of PC concrete and sole AAC (AAF and AAS concrete) have been extensively investigated, providing valuable information to understand the development of overall performance of these types of concrete (Constantinides et al., 2003; Němecek et al., 2010; Thomas et al., 2018). However, a systematic understanding of the micromechanical properties of individual phases within AAFS concrete and the corresponding relationship with its macroscopic mechanical properties is still lacking. In summary, the following aspects regarding the microstructure and mechanical properties of AAFS concrete are still inadequate:

- Fundamental insights and understanding of the reaction mechanism of fly ash and slag particles in AAFS system.
- Systematic investigation of the microstructure evolution of ITZ in AAFS concrete.
- Multiscale micromechanical analysis of AAFS concrete.
- Estimation of multiscale microstructure-mechanical properties relationship in AAFS concrete.

According to the current state of the understanding of microstructure and mechanical properties of AAFS concrete, the aim, objectives, and strategy of this research are given below.

1.2 Aim, objectives and scope

This research aims to systematically characterise the microstructure and mechanical properties of AAFS concrete cured at ambient temperature at multiscale from nano- to macro-scale and estimate the multiscale microstructure-mechanical properties relationship in AAFS concrete. The results of this study provide new insights into the reaction mechanism of AAFS binder and offer a thorough understanding of the microstructure and micromechanical properties of individual phases in AAFS concrete, as well as their corresponding relationship with the macroscopic mechanical properties of AAFS concrete. The main objectives of this study are:

(i) To explore the engineering properties of AAFS concrete considering the effects of main influencing factors including fly ash/slag ratio, alkaline activator/precursor (AL/P) ratio, molarity of sodium hydroxide (SH) and sodium silicate/sodium hydroxide (SS/SH) ratio and to obtain the optimal mixture of AAFS concrete based on the performance criteria of workability, setting time and compressive strength.

(ii) To in-situ monitor the microstructure evolution of fly ash and slag particles in AAFS paste from the early age (1 d) to the later age (28 d), indicating the morphology changes on the surface and interior of particles and the spatial distribution of reaction products, which has not been achieved in the existing research.

(iii) To characterise the microstructure evolution of ITZ in AAFS concrete from the very early age (3 h) to the later age (28 d) and provide the needed insights into the mechanism of ITZ evolution, which has not been obtained from the existing research.

(iv) To investigate the micromechanical properties of AAFS concrete at multiple length scales from nano- to macro-scale, providing the first-hand micromechanical information of individual phases (unreacted particles and reaction products) and composites (paste matrix and ITZ) in this new type of concrete.

(v) To build the multiscale relationships between chemistry, microstructure, and mechanical properties in AAFS concrete, which have not been extensively addressed and would enable us to better understand the development of overall mechanical properties of AAFS concrete.

1.3 Research strategy

The used strategy of this research is shown in Figure 1-1, where the macroscopic properties of AAFS concrete are evaluated firstly, followed by the detailed characterisation of its microscopic properties.

(i) At macro-scale, the engineering properties of AAFS concrete including workability, setting time, compressive strength, splitting tensile strength, elastic modulus and fracture properties are measured according to the existing standards, focusing on the effects of fly ash/slag ratio, AL/P ratio, SH molarity and SS/SH ratio.

(ii) Based on the experimental results obtained above, the optimal mixtures of AAFS concrete are evaluated to achieve the desired performance in terms of acceptable workability, suitable setting time and high compressive strength. The AAFS concrete with an optimal mixture is then used to characterise the microscopic properties in the following research.

(iii) At micro-scale, the microstructure evolution of AAFS concrete is characterised based on four length levels: Level 0 (solid gel particle), Level I (gel matrix), Level II (paste) and Level III (concrete). The nanostructure of solid gel particle at Level 0 is characterised using nuclear magnetic resonance (NMR), while the chemical composition of gel matrix at Level I is tested by means of X-ray diffraction (XRD) and Fourier transform infrared spectroscopy (FTIR). The microstructure of paste at Level II is evaluated through X-ray microcomputed tomography (XCT), backscattered scanning electron microscopy (BSEM), energy dispersive spectrometry (EDS) and mercury intrusion porosimetry (MIP) tests. Lastly, BSEM and EDS tests are conducted to characterise the microstructure evolution of ITZ at Level III.

(iv) The multiscale micromechanical properties of AAFS concrete are characterised according to the microstructural features identified above. The micromechanical properties (i.e. elastic modulus and hardness) of gel matrix at Level I are measured using nanoindentation, while the effective mechanical properties of AAFS paste at Level II are determined based on the self-consistent continuum micromechanics model. The micromechanical properties of ITZ in AAFS concrete at Level III are evaluated through a series of statistical analysis.

(v) Lastly, the multiscale microstructure-mechanical properties relationship in AAFS concrete from Level 0 to Level III is discussed in detail based on the results of chemistry, microstructure and mechanical properties at micro- and macro-scale obtained above.

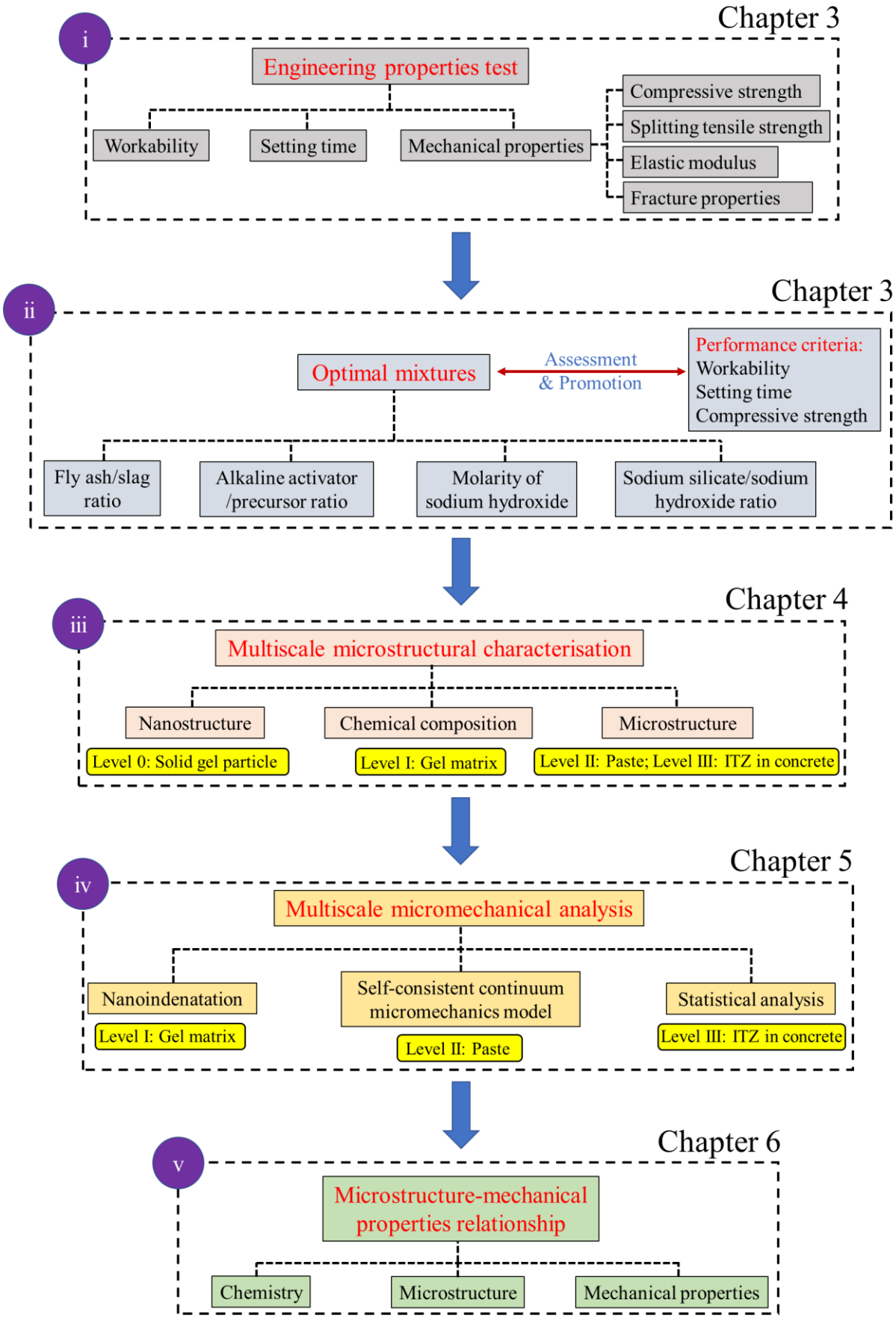

Figure 1-1 Schematic illustration of the research strategy

1.4 Thesis outline

This thesis consists of the following seven chapters.

Chapter 1 provides a brief introduction of this study, in which the research background, the aim and objectives as well as the research strategy are presented.

Chapter 2 displays a critical review on multiscale microstructure and mechanical properties of AAFS concrete, where the main challenges and limitations in this field are identified and discussed.

Chapter 3 presents an experimental study of the engineering properties of AAFS concrete cured at ambient temperature with an emphasis on the effects of some main influencing factors (e.g. fly ash/slag ratio and AL/P ratio), based on which the optimal mixtures of AAFS concrete are obtained considering the performance criteria of workability, setting time and compressive strength.

Chapter 4 demonstrates a multiscale characterisation of the microstructure evolution of AAFS concrete from nano- to macro-scale, using the optimal mixtures obtained in Chapter 3. Herein, different test methods including NMR, XRD, FTIR, XCT, BSEM, EDS and MIP are used to characterise the microstructure development of AAFS concrete at four multiple length levels: Level 0 (solid gel particle), Level I (gel matrix), Level II (paste) and Level III (concrete).

Chapter 5 illustrates a multiscale micromechanical analysis of AAFS concrete using nanoindentation test, self-consistent continuum micromechanics modelling and statistical analysis, according to the microstructure features identified in Chapter 4.

Chapter 6 establishes the multiscale relationship between microstructure and mechanical properties of AAFS concrete based on the results obtained and presented in Chapters 3 to 5.

Chapter 7 is dedicated to summarising the main contributions made in this research and drawing main conclusions of this study. In addition, the limitations of this research are critically mentioned and some recommendations for the future research are given accordingly.

Chapter 2 Literature review

2.1 Introduction

This chapter presents a critical review on multiscale microstructure and mechanical properties of AAFS concrete. The review starts with a brief description of the motivation for the development of AAFS concrete, which offers a basic understanding of the practical significance of this new class of concrete. After that, a summary of the mix design of AAFS concrete including the identification of influencing factors and the selection of mix design method is given, followed by a general illustration of reaction mechanism of AAFS concrete. Lastly, the emphasis is placed on the in-depth review of microstructure and mechanical properties of AAFS concrete at multiple length scales from nano- to macro-scale, to identify the research gaps and limitations in this field of research.

2.2 Motivation for the development of AAFS concrete

PC concrete is the most widely used construction material around the world owing to its numerous advantages, such as wide material availability, desired workability and mechanical properties, easy maintenance and low cost (Ding et al., 2016). Roughly 25 billion tonnes of PC concrete are produced worldwide each year (CSI Progress Report, 2009). Given the extensive use of PC concrete in civil construction, it consumes a huge amount of natural resources (e.g. limestone) and energy to produce PC, which introduces significant environmental issues, contributing to around 8% of global man-made CO_2 emissions (Scrivener and Kirkpatrick, 2008). Therefore, it is an urgent need for the development of sustainable concrete which enables to fulfil the requirement of housing and infrastructure of billions of people without further aggravating the burden of the earth's atmospheric CO_2 levels (Provis and Bernal, 2014).

AAC, including those classified as geopolymer concrete, has been regarded as a potential alternative to PC concrete because of the low CO_2 emissions and low consumption of natural resources (Shi et al., 2011; Zhuang et al., 2016; Provis, 2018). There are about 55% less CO_2 emissions in the production of AAC in comparison with the production of PC concrete, due to the avoidance of high-temperature processing of PC components in a fossil fuel-fired kiln (Yang et al., 2013; Provis and Bernal, 2014). AAC is manufactured through the chemical reaction between alkaline activator and aluminosilicate precursors (e.g. fly ash and slag), leading to a hard matrix that binds the aggregates together into a durable concrete (Provis and van Deventer, 2014). Based on

the chemical compositions of precursors, AAC can be divided into two sole systems, including high calcium system (e.g. AAS concrete) and low calcium system (e.g. AAF concrete) (Pacheco-Torgal et al., 2014). Although these two sole systems would achieve comparable engineering properties to PC system, they possess some critical drawbacks during their applications. AAF concrete needs to be cured under an elevated temperature of 60 ~ 85 ℃ due to the low reactivity of fly ash (Fan et al., 1999; Puertas et al., 2000; Somna et al., 2011), whereas AAS concrete has issues related to fresh properties such as rapid setting time and low workability (Palacios et al., 2008; Arbi et al., 2015). These limitations would hinder the practical application of AAC, especially for the cast-in-situ concrete. Thus, there is an increasing drive to develop a new AAC system that can achieve superior engineering properties under ambient curing conditions.

In recent years, AAFS concrete as a blended AAC has attracted increasing attention because of its potential to provide a good synergy between mechanical properties and durability under ambient curing conditions, which cannot be achieved by the sole AAC, e.g. AAF and AAS concrete (Puertas et al., 2000; Provis and van Deventer, 2014; Lee and Lee, 2015). Given that AAF has a low strength under ambient curing condition due to the relatively low reactivity of fly ash, whereas AAS can achieve a high strength due to the high reactivity of slag but has issue of quick setting, mixing these two raw materials together can help to achieve a balance between setting time and strength. Nevertheless, the practical applications of AAFS concrete are still low mainly due to lack of a comprehensive understanding of its reaction mechanism, microstructure evolution and performance development. Thus, the systematic investigations on these aspects of this new class of concrete are highly demanded, devoting to the development of AAFS concrete and its engineering applications.

2.3 Mix design of AAFS concrete

The concept of mix design of AAFS concrete is similar to that of PC concrete, which mainly consists of two steps: (1) the identification of influencing factors and (2) the selection of appropriate mix design method. Thus, the mix design of AAFS concrete will be reviewed based on these two steps below.

2.3.1 Influencing factors

As shown in Figure 2-1, AAFS concrete consists of AAFS binder and aggregates, similar to PC concrete that is composed of PC binder and aggregates. It should be noted that the aggregates play the same role in AAFS concrete and PC concrete and can be dealt

well with the established procedures of mix design for PC concrete. Thus, the influencing factors in terms of AAFS binder are mainly discussed in this section. Figure 2-1 highlights the two main components of the AAFS binder, i.e., aluminosilicate precursor (P) and alkaline activator (AL)， where the AL/P ratio is a key parameter affecting the properties of AAFS mixtures. The AL/P ratio refers to the mass ratio of alkaline activator to precursor, in which the mass of precursor is the mass of fly ash and slag. Besides, extra water and superplasticizer (SP) are commonly added to improve the workability of AAFS mixtures. Fly ash and ground granulated blast-furnace slag are commonly used as precursors in AAFS concrete, for which the key factors are the natural characteristics of these raw materials and the relative amount of fly ash and slag. Up to now, there are four types of AL (i.e., alkali hydroxides, alkali silicates, alkali carbonates and alkali sulfates) have been used in AAFS concrete to activate the raw materials. Alkali hydroxides (e.g., sodium hydroxide solution (SH)) and alkali silicate (e.g., sodium silicate solution (SS)) are most used as AL in AAFS concrete, where the mixing ratio of SS to SH is considered as a key parameter. The key parameters related to SS and SH are molarity and modulus ($[SiO_2]/[NaO]$ ratio), respectively. Furthermore, the properties of aggregates including particle size, chemical composition and surface properties would also significantly affect the overall performance of AAFS concrete. Nevertheless, the effects of aggregate's properties on the performance of AAFS concrete are outside the scope of this research.

According to the literature, the effects of these factors on the microstructure and engineering properties of AAFS concrete are summarised in Table 2-1 and discussed in detail below. This information can be taken as a reference for the mix design of AAFS concrete.

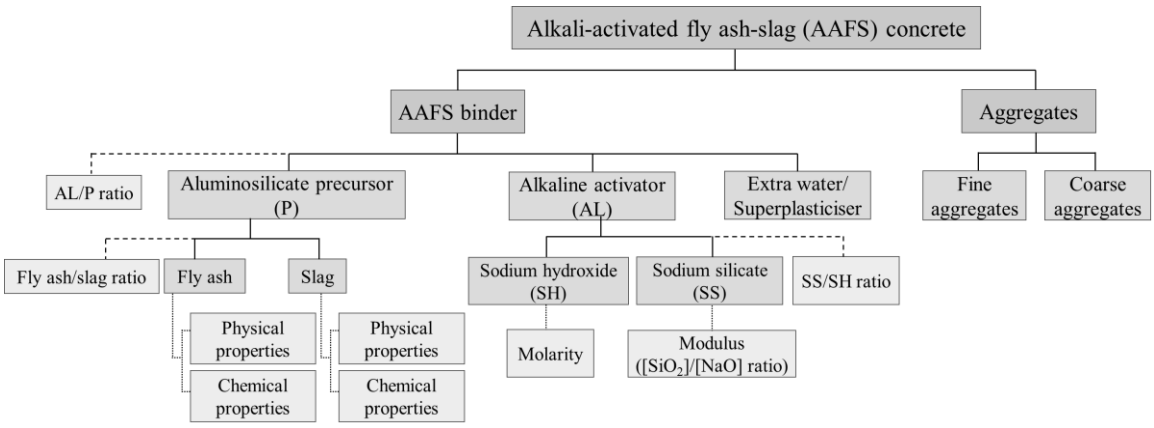

Figure 2-1 Components and influencing factors for AAFS concrete

Table 2-1 Effects of different factors on microstructure and engineering properties of AAFS concrete

References	Chemical composition of precursors (P)		Alkaline activator (AL)	Fly ash/slag	SS/SH ratio	AL/P ratio	Water/P ratio	Curing condition	Main findings	Optimal mixtures
	Fly ash	slag								
Ye and Radlinska (2016)	SiO_2 (48.67%) Al_2O_3 (25.13%)	CaO (43.83%) SiO_2 (30.04%)	Molarity of SH (2 ~ 6 M) $[SiO_2]/[Na_2O]$ ratio of SS (1.6)	100:0; 80:20; 50:50;	0 ~ 2	0.75	-	Ambient condition (23 ± 0.5 °C)	Microstructure: 1. The microstructure of AAFS is affected by fly ash/slag ratio, type and dosage of activator. 2. Increasing the slag proportion and the $[SiO_2]$ content in activator can both densify the microstructure. 3. The chemical structure of SS-activated mixtures is more amorphous than that of SH-activated mixtures, as a result of the suppressed formation of crystalline phases.	-
Ismail et al. (2014)	SiO_2 (62.93%) Al_2O_3 (24.91%)	CaO (42.56%) SiO_2 (33.80%)	- $[SiO_2]/[Na_2O]$ ratio of SS (0.96)	100:0; 75:25; 50:50; 25:75; 0:100	-	0.08; 0.12	0.4	Elevated condition (30 °C)	Microstructure: 1. The microstructure of AAFS is strongly dependent on the fly ash/slag ratio, as the differences in chemistry and mineralogy of these precursors promote the formation of different binder products. 2. With a high content of slag (>50% of P), the reaction products are dominated by C-A-S-H gel, indicating the strong influence of calcium on the gel chemistry, particular concerning the bound water within the gel. 3. With the increase of fly ash, the reaction products seem to be mainly composed of a hybrid binding phase (N-C-A-S-H type gel).	-
Marjanovic (2015)	SiO_2 (55.23%) Al_2O_3 (21.43%)	CaO (38.48%) SiO_2 (37.50%)	- $[SiO_2]/[Na_2O]$ ratio of SS (0.5 ~ 1.5)	100:0; 75:25; 50:50; 25:75; 0:100	-	Na_2O concentration of P (4% ~ 10%)	-	Elevated condition for early 24 h (95 °C); Ambient condition for long-term curing (20 °C)	Microstructure: 1. The reaction products of AAFS chemically and physically depend on the fly ash to slag ratio. 2. With the increase of slag content in the precursor up to 50%, the reaction products are dominated by N-A-S-H type of gel. 3. The reaction products of the precursor with 75% of slag are composed of morphologically undifferentiated C-A-S-H and N-A-S-H gel phases, as well as the hydrotalcite gel phase. 4. The dominant presence of N-A-S-H gel in the reaction products positively affects flexural strength, while the dominant presence of C-A-S-H gel positively affects compressive strength.	-
Lee et al. (2015)	SiO_2 (67.26%) Al_2O_3 (14.76%)	CaO (42.47%) SiO_2 (35.17%)	Molarity of SH (4 M) $[SiO_2]/[Na_2O]$ ratio of SS (0.94)	90:10; 70:30; 50:50	-	-	0.4	Ambient condition (20 °C)	Microstructure: 1. The amount of slag primarily affects the amount of reaction product and its silicate structure. 2. With the increase of slag, the amount of C-A-S-H gels increases, whereas the amount of aluminosilicate gel decreases.	-
Garcia et al. (2006)	SiO_2 (55.6%) Al_2O_3 (25.6%)	CaO (38.05%) SiO_2 (3.18%)	- $[SiO_2]/[Na_2O]$ ratio of SS (0 ~ 2.0)	100:0; 75:25; 50:50; 25:75; 0:100	-	Na_2O concentration of P (4% ~ 8%)	-	Elevated condition for early 24 h (75 °C); Ambient condition for long-term curing (20 °C)	Engineering properties: 1. The SS modulus have strong effects on the compressive strength development of AAFS. 2. The modulus of SS is generally set in the range of 1.0 ~ 1.5 for the sake of compressive strength.	-
Puligilla and Mondal (2013)	SiO_2 (60.17%) Al_2O_3 (21.91%)	CaO (39.4%) SiO_2 (35.7%)	- $[SiO_2]/[K_2O]$ ratio of potassium silicate (0.94)	100:0; 99:1; 95:5; 90:10; 85:15	-	-	0.32	Ambient condition (21 ± 2 °C)	Microstructure: 1. The calcium dissolving from slag is important for both early and long-term age properties. Slow reaction rate and low strength development have been confirmed in the AAFS mixtures with low slag content. 2. The hardening process is initiated by the precipitation of C-A-S-H and continues due to the accelerated polymerization. 3. The presence of calcium enhances the rate and the extent of fly ash dissolution as well as the extent of product formation.	-

Table 2-1 (Continued)

References	Chemical composition of precursors (P)		Alkaline activator (AL)	Fly ash/ slag	SS/SH ratio	AL/P ratio	Water/P ratio	Curing condition	Main findings	Optimal mixtures
	Fly ash	Slag								
Gao et al. (2015)	SiO_2 (54.6%) Al_2O_3 (24.36%)	CaO (38.6%) SiO_2 (35.5%)	- $[SiO_2]/[Na_2O]$ ratio of SS (1.0 ~ 1.8)	10:90; 20:80; 30:70; 40:60; 50:50	-	Na_2O concentration of P (5.6%)	0.35	Ambient condition (20°C)	Microstructure: 1. Increasing slag content and lowering the activator modulus would significantly increase the reaction intensity and shorten the main reaction processes, in which the activator modulus has a more significant influence than slag content. 2. Changing the activator modulus and slag content (>50%) shows very limits influence on the main gel structure. Engineering properties: 1. The compressive strength increases with the addition of slag content and activator modulus, but too high or too low modulus (1.8 or 1.0 in this case) will lead to relatively low strength.	-
Garcia et al. (2006)	SiO_2 (55.6%) Al_2O_3 (25.6%)	CaO (38.05%) SiO_2 (34.18%)	Molarity of SH (14 M) $[SiO_2]/[Na_2O]$ ratio of SS (0.75 ~ 2.0)	100:0; 75:25; 50:50; 25:75; 0:100	-	Na_2O concentration of P (4% ~ 8%)	-	Elevated condition for early 24 h (75 °C); Ambient condition for long-term curing (20 °C)	Engineering properties: 1. The Na_2O concentration and SS modulus have strong effects on the compressive strength of AAFS. 2. Strongly alkaline solutions are required for fly ash to react, whereas for the slag to produce hydration products, relatively moderate alkalinity is needed.	-
Nath and Sarker (2014)	SiO_2 (50%) Al_2O_3 (28.25%)	CaO (43.1%) SiO_2 (32.46%)	Molarity of SH (14 M) $[SiO_2]/[NaO]$ ratio of SS (2.69)	100:0; 90:10; 80:20; 70:30	1.5 ~ 2.5	0.35 ~ 0.45	-	Ambient condition (20 ~ 23°C)	Engineering properties: 1. The increase of slag content in AAFS would reduce its workability and setting time but increase its compressive strength. 2. The workability and setting time increases with the increase of AL/P ratio. 3. Variation of SS/SH ratio from 1.5 to 2.5 would decrease the workability, setting time and compressive strength.	Fly ash/slag (90/10); SS/SH ratio (1.5 ~ 2.5); AL/P ratio (0.4)
Deb et al. (2014)	SiO_2 (53.71%) Al_2O_3 (27.20%)	CaO (45.45%) SiO_2 (29.96%)	Molarity of SH (14 M) $[SiO_2]/[NaO]$ ratio of SS (2.61)	100:0; 90:10; 80:20;	1.5 ~ 2.5	0.35 ~ 0.40	-	Ambient condition (20 ± 2 °C)	Engineering properties: 1. The workability and setting time of AAFS decrease with the increase of slag. 2. The Workability of AAFS also decreases with the reduction of AL/B ratio from 0.4 to 0.35. 3. The compressive strength of AAFS increases with the increase of the slag content.	Fly ash/slag (80/20); SS/SH ratio (1.5); AL/P ratio (0.4)
Lee et al. (2013)	SiO_2 (46%) Al_2O_3 (33%)	CaO (56.10%) SiO_2 (21%)	Molarity of SH (4 ~ 8 M) $[SiO_2]/[NaO]$ ratio of SS (2.9)	90:10; 85:15; 80:20; 75:25; 70:30	0.5 ~ 1.5	0.38	(0.27~0.30)	Ambient condition (20 °C)	Engineering properties: 1. The workability and setting time of AAFS decrease with the increase of slag. 2. The 28-d compressive strength of AAFS increased with the amount of slag, except when the amount of slag is 25% and 30%.	Fly ash/slag (80/20; 85/15);
Singh et al. (2016)	SiO_2 (54.76%) Al_2O_3 (26.41%)	CaO (33.23%) SiO_2 (32.26%)	Molarity of SH (10 ~ 16 M) $[SiO_2]/[NaO]$ ratio of SS (3.375)	67:33	2.5	0.35 ~ 0.40	(0.19~0.21)	Ambient condition	Engineering properties: 1. Activator concentration is a significant factor in controlling the reaction products formation, microstructure and strength of the hardened concrete.	-
Wang et al. (2015)	SiO_2 (61.83%) Al_2O_3 (20.39%)	CaO (40.54%) SiO_2 (33.32%)	Molarity of SH (5 M)	60:40; 40:60; 20:80; 0:100	-	0.5	-	Ambient condition	Engineering properties: 1. The workability of AAFS increases with the increase of fly ash content.	-

References	Chemical composition of precursors (P)		Alkaline activator (AL)	Fly ash/ slag	SS/SH ratio	AL/P ratio	Water/P ratio	Curing condition	Main findings	Optimal mixtures
	Fly ash	Slag								
Ishwarya et al. (2019)	SiO_2 (56.95%) Al_2O_3 (31.17%)	CaO (40.73%) SiO_2 (31.90%)	Na_2CO_3/Na_2SiO_3 = 1.5/1.0	80:20; 75:25; 67:33;	-	0.18	(0.2¬0.29)	Ambient condition (27 ± 2 °C); Elevated condition (80 ± 2 °C);	Engineering properties: 1. The compressive strength of AAFS paste increases with increasing slag content and decreases with the increase of water/P ratio. 2. The AAFS sample cured at 27 °C for 28 days gains higher compressive strength than the sample cured at 80 °C, due to the formation of pores or cavities after prolonged curing at elevated temperature.	-
Keulen et al. (2018)	SiO_2 (59.7%) Al_2O_3 (24.6%)	CaO (41.8%) SiO_2 (34.3%)	Molarity of SH (3 M)	75:25	-	0.33	-	Ambient condition (20°C)	Engineering properties: 1. The addition of admixture content would significantly improve the workability and strength of AAFS concrete. Microstructure: 1. The addition of admixture content would also reduce the total and effective capillary porosity.	-
Saha and Rajasekaran (2017)	SiO_2 (58.90%) Al_2O_3 (32.24%)	CaO (34.07%) SiO_2 (32.57%)	$[SiO_2]/[NaO]$ ratio of SS (3.29)	90:10; 80:20; 70:30; 60:40; 50:50;	1.0	0.4	-	Ambient condition (20°C)	Engineering properties: 1. The initial and final setting time of AAFS paste both are reduced significantly with the increase of slag content. 2. Compressive strength of AAFS paste is increased with the increase of slag content.	-

Note: SH (sodium hydroxide); SS (sodium silicate)

2.3.1.1 Natural characteristic of aluminosilicate precursor

Although the nature of precursor cannot be specified due to the different manufacturing process of industry which varies from country to country, the basic requirements should be defined in order to produce good binding material. It was found that the physical properties of each raw material especially its fineness and particle size distribution, play a crucial role in the rheological and mechanical properties of the resultant matrix (Chindaprasirt et al., 2005; Xu et al., 2014). Generally, the binder with finer particle has a relatively higher reactivity and thus contributes to producing the matrix with a denser microstructure, higher compressive strength and enhanced fresh properties (Kumar et al., 2007; Temuujin et al., 2009b; Komljenović et al., 2010). In this regard, it was suggested that fly ash should have 80% ~ 90% particles with a size of under 45 μm (Fernández-Jiménez and Palomo, 2003), whereas the size of slag should be ground to smaller than 40 μm at least (Wang et al., 2005). Secondly, the mineralogical characteristics of raw materials also have a significant effect on alkaline activation process of AAFS. The amorphous phase of raw materials mainly contributes to alkaline activation, while the crystalline phase can be considered practically inert. Thus, the vitreous phase of fly ash and slag is required to be over 50% and 90%, respectively (Swamy and Ammar, 1990; Mostafa et al., 2001; Li et al., 2002; Fernández-Jiménez and Palomo, 2003). Thirdly, the chemical composition of raw materials should also be considered since it will condition the formation of main reaction products and consequently affect the setting and strength development of AAFS. The $[SiO_2]/[Al_2O_3]$ ratio of fly ash and the $[CaO]/[SiO_2]$ ratio of slag are recognised as key parameters governing the properties of AAFS (Talling and Brandstetr, 1989; Thakur and Ghosh, 2009; Ghosh and Ghosh, 2012; Timakul et al., 2015). The $[SiO_2]/[Al_2O_3]$ ratio of fly ash and the $[CaO]/[SiO_2]$ ratio of slag should be greater than 1.5 and 1.0 respectively to fulfil the requirements for alkaline reaction (Fernández-Jiménez and Palomo, 2003; Winnefeld et al., 2015).

2.3.1.2 Characteristic of alkaline activator

It is necessary to introduce the characteristics of the AL used in AAFS because they are the second essential component in this system. Up to now, SH and SS solutions are commonly used as AL to activate the aluminosilicate precursors within AAFS. The presence of OH^- ions from SH solution helps to catalyse the hydrolytic reactions and raise the pH to the values required for precursor dissolution and the subsequent condensation during alkaline activation (Garcia-Lodeiro et al., 2015). The soluble silica from SS would

promote the properties development of AAFS mixtures such as workability, setting time and mechanical properties via modifying gel composition and the microstructure of reaction products (Garcia-Lodeiro et al., 2015). It should be noted that the producing of AL (e.g., SS and SH) would introduce some energy consumption and CO_2 emission. However, the CO_2 emissions per tonne of AAFS is still much lower than CO_2 emissions associated with the production of PC due to the solid of AL usually account for < 10% by mass of an AAFS binder (Provis and Bernal, 2014).

2.3.1.3 Alkaline activator/precursor ratio

The AL/P ratio has a significant effect on the engineering properties of AAFS concrete, which is similar to the effect of water/cement ratio on the properties of PC concrete. Increasing the AL/P ratio would improve the workability, delay the setting time and reduce the compressive strength of AAFS concrete (Nath and Sarker, 2014; Deb et al., 2014). The slump value of AAFS concrete is increased significantly from 100 mm to 235 mm as the AL/P ratio increases from 0.35 to 0.45 (Nath and Sarker, 2014). With the increase of AL/P ratio from 0.35 to 0.45, the initial setting time of AAFS pastes increases from 220 min to 388 min, with about 33% increase for every 5% increment of AL content (Nath and Sarker, 2014). In the meantime, the compressive strength of AAFS concrete at 28 d is decreased from 45 MPa to 30 MPa (Nath and Sarker, 2014). It was suggested that the AL/P ratio of 0.40 can be considered as the optimal dosage to ensure the balance between fresh and hardened properties (Nath and Sarker, 2014; Deb et al., 2014).

2.3.1.4 Fly ash/slag ratio

The fresh and hardened properties of AAFS also depend on the fly ash/slag ratio since these precursors have different chemistry and mineralogy, which would affect the formation of binding products (Parthiban et al., 2013; Ismail et al., 2014; Winnefeld et al., 2015; Marcin et al., 2016). The early-age compressive strength of AAFS concrete without slag increases dramatically with the addition of slag (Lee and Lee, 2013; Nath and Sarker, 2014; Marcin et al., 2016), attributing to the formation of C-A-S-H gel from the activation of slag, which is a more space-filling product in comparison with the N-A-S-H gel formed in the fly ash-containing systems (Provis et al., 2012; Ye and Radlińska, 2016). It is consistent with the identification that the addition of slag would significantly modify the microstructure of AAFS by reducing coarse pores and homogenizing morphology (Ye and Radlińska, 2016). More specifically, the 28-d compressive strength of AAFS concrete is increased from 26 MPa to 55 MPa with the increase of slag

replacement level from 0% to 30%, where the strength increases by about 10 MPa for every 10% increment of slag replacement (Nath and Sarker, 2014). The workability and setting time obtained in AAFS mixtures with less than 20% slag replacement are considered suitable for casting different concrete structural members (Lee and Lee, 2013; Deb et al., 2014). Thus, the appropriate replacement ratio of fly ash with slag can be considered as 15% ~ 20% (Lee and Lee, 2013; Deb et al., 2014; Nath and Sarker, 2014).

2.3.1.5 Molarity of sodium hydroxide solution

Generally, a strongly alkaline medium is required to activate the raw materials and achieve the desired properties of AAFS mixtures. However, the over-high molarity would have negative effects on the strength development and increase the leaching of Si and Al (Part et al., 2015). The presence of OH^- ions from SH would lead to the hydrolysis of Si-O-Si and Si-O-Al bonds and catalyse the dissolution of Si^{4+} and Al^{3+} cations. Additionally, it would increase the pH value to fulfil the precursor dissolution and the subsequent condensation reactions (Pacheco-Torgal et al., 2014). It was reported that AAFS mixtures with 14 M SH achieve the highest compressive strength due to the fully condensed gel products (Singh et al., 2016). The formation of gels cannot be fully poly-condensed at the lower molarity (12 M), leading to a lower strength. The compressive strength of samples with 16 M SH is lower than that of a matrix made of 14 M SH due to the accelerated dissolution of SiO_2, which would result in the formation of silicic acid (Escalante-García et al., 2003). Meanwhile, several cracks and unreacted particles can be found at such high molarity level, which would result in the reduction of compressive strength (Singh et al., 2016). In addition, it should be also noted that the high SH molarity would also cause a rapid setting and poor workability (Nath and Sarker, 2014; Deb et al., 2015; Singh et al., 2016). Therefore, the SH solution ranging from 8 to 14 M is usually used for AAFS (Puertas et al., 2000; Lee and Lee, 2013). Up to now, there is no consensus about the optimal molarity of SH considering the balance of setting time, workability, and mechanical properties.

2.3.1.6 Modulus of sodium silicate solution

The modulus, i.e. the molar ratio of $[SiO_2]/[Na_2O]$, is the most important characteristic of SS because it would affect the gel composition and the microstructure of formed products, and consequently influence the development of engineering properties of AAFS concrete (Pacheco-Torgal et al., 2014). It was identified that the SS modulus has a strong effect on the compressive strength of AAFS paste (Escalante-García et al.,

2006). With the increase of SS modulus from 0 to 1, the compressive strength of AAFS paste is increased significantly, followed by a slight increase between the modulus of 1.0 and 1.5 and a slight decrease between the modulus of 1.5 and 2.0. The increase of SS modulus would enhance the polymerisation of the silicate unit, but the over high concentration of silica would decrease the pH level and increase the solution viscosity, and thereby reducing the reaction degree. Thus, the silica modulus is normally kept preferably at around 1.0 ~ 2.0 to ensure a sufficient high pH while avoiding rapid polymerisation of the sodium silicate (Bernal et al., 2011b; Escalante-García et al., 2006; Talha Junaid et al., 2015). Otherwise, the AAFS matrices would densify before the attendance of sufficient reaction products, which would interfere with further reactions (Escalante-García et al., 2006; Pacheco-Torgal et al., 2014).

2.3.1.7 Sodium silicate/sodium hydroxide ratio

The relative amount of SS and SH would also significantly influence the engineering properties of AAFS mixtures due to the difference of chemical and physical properties between these two activators, which would condition the reaction process and the formation of binding products. If the compositions of SS and SH are kept constant, the workability of AAFS mixture tends to decrease with increasing SS/SH ratio since SS is the most viscous component among these two solutions (Nath and Sarker, 2014; Deb et al., 2014). It was observed that the AAFS mixture with SS/SH ratio of 1.5 has the highest slump value (245 mm) and the slump value decreases to 240 mm and 230 mm respectively along with the increase of SS/SH ratio from 1.5 to 2.0 and 2.5 (Nath and Sarker, 2014). Moreover, the change of SS/SH ratio would strongly influence the setting of AAFS mixtures (Nath and Sarker, 2014; Deb et al., 2015). The mixtures with a lower SS/SH ratio were found to take a longer time to set compared to those with higher SS/SH ratios (Nath and Sarker, 2014). When the SS/SH ratio is increased from 1.5 to 2.5, the initial setting time of the mixture decreases from 445 min to 300 min (Nath and Sarker, 2014). The reason is that the high SS/SH ratio increases the amount of soluble silica, which would modify the rate of crystallization and reaction kinetics by enhancing condensation process and thus decline the setting time (Criado et al., 2007). Finally, the SS/SH ratio would also affect the mechanical properties of AAFS mixtures (Nath and Sarker, 2014; Deb et al., 2015). The AAFS mixtures activated by the activator with a lower SS/SH ratio can achieve higher compressive strength. For instance, the 28-d compressive strength of mixtures with SS/SH ratio of 1.5 is approximately 15% higher than that of mixtures with SS/SH ratio of 2.5 (Deb et al., 2014). Based on the previous research, the optimal range

of SS/SH ratio is suggested to be 1.5 to 2.5, considering workability, setting time and mechanical properties (Deb et al., 2014; Nath and Sarker, 2014; Deb et al., 2015).

2.3.1.8 Extra water content

Since the main role of water has been considered in the design of alkaline activator, the extra water is merely used as a kind of admixture to improve the workability of AAFS (Rattanasak et al., 2011). Normally, the dosage of additional water is set at 1% by mass of precursor in the mixture design (Ferdous et al., 2015). If too much water is added into the mixture the other properties of AAFS would be strongly affected, such as setting time and mechanical properties (Zhang et al., 2009; Xie and Kayali, 2014). The increase in water content would retard the setting time and reduce the compressive strength (Al-majidi et al., 2016).

2.3.1.9 Superplasticizer content

SP, known as a high range water reducer, has been widely used to improve the workability of PC concrete by keeping constant water with no significant change in mechanical properties and durability (Gołaszewski and Szwabowski, 2004; Antoni et al., 2017; Qian et al., 2018). Recently, two types of SP including the polycarboxylate-based and naphthalene-based SP are used in AAFS mixtures (Jang et al., 2014; Keulen et al., 2018). It was found that the polycarboxylate-based SP would improve the workability of AAFS pastes more effectively than the naphthalene-based SP (Jang et al., 2014). With the addition of 1 wt% polycarboxylate-based SP of precursor, the workability of AAFS paste can be improved by about 30% (Jang et al., 2014). Besides, the addition of polycarboxylate-based SP was found to be able to control the workability of AAFS concrete over time, leading to a slowly declining slump between 6 min and 120 min after mixing (Keulen et al., 2018). The retention of the slump value between 6 min and 120 min suggests a longer setting time of AAFS mixture (Keulen et al., 2018).

Furthermore, recent research also indicated that the compressive strength of AAFS concrete would be affected by the addition of SP. Jang et al. (2014) stated that there is a negligible effect on the compressive strength of AAFS concrete when the amount of SP is controlled under 1 wt% of precursor. When the amount of polycarboxylate-based SP is higher than 2 wt% of precursor the development of compressive strength would be positively affected before 7 d, whereas the adverse effects can be found after this point (Jang et al., 2014). However, Keulen et al. (2018) claimed a different conclusion that the compressive strength of AAFS concrete is improved significantly over time with the

addition of higher SP content (> 2 wt %), especially at later ages (> 7 d). The improvement of compressive strength has a strong relation with the refinement of pore structure. A significant reduction of the total and effective capillary porosity can be found in the AAFS mixture with a high SP content (Keulen et al., 2018). Although there is a controversy about the effect of high SP content (> 2 wt%) on the compressive strength of AAFS concrete between these two studies, it was agreed that the low amount of SP (≤ 1 wt%) has no negative effect on the strength of AAFS concrete, regardless of early or later ages.

2.3.2 Mix design method

According to the influencing factors identified above, the mix design method of AAFS concrete was investigated in recent years. In 2017, Rafeet et al. (2017) proposed some guidelines for the mix design of AAFS concrete, where a step-by-step mix design procedure starting from the requirements of consistency, setting time and compressive strength is used to determine the mix proportions of AAFS concrete. Initially, the target consistency slump class, initial setting time and compressive strength are set as a starting point for the design process. And then, the fly ash/slag ratio and water/solid ratio are determined according to the target setting time and strength. Here, the water/solid ratio stands for the mass ratio of the water in the system including the water in activator and extra water to the solid including precursors and alkali solids. Next, the paste volume is determined to achieve the required consistency. Subsequently, the paste content and the relevant content of precursors, activator and water are determined. Finally, the aggregate quantities are determined from the relative proportion.

Although some valuable guidelines for the mix design of AAFS concrete were provided based on this method, the effects of type and content of alkaline activators were not considered. To conquer these limitations, Reddy et al. (2018) suggested a new mix design method considering the effects of two main types of alkaline activators (SH and SS), where the molarity of SH and SS/SH ratio were regarded as the key parameters for the mix design of AAFS concrete. However, only one specified content of SH molarity and SS/SH ratio was adopted in this research, which did not fully consider the influencing factors in the mix design of AAFS concrete. Therefore, more investigations regarding the mix design method for the AAFS concrete should be conducted in the future.

2.4 Reaction mechanism and reaction products of AAFS concrete

Simply stated, the alkaline activation of AAFS can be described as a mixed activation of AAF (low-calcium system) and AAS (high-calcium system). As shown in Figure 2-2, previous research has revealed that AAF and AAS follow the so-called sol-gel reaction process: (1) dissolution, (2) rearrangement, (3) gel nucleation, and (4) solidification, but exhibit distinct hydration products when separately activated (Li et al., 2010; Provis and Bernal, 2014). In the sol-gel process, a colloidal solution of fine particles (the sol) is generated under the activation of alkaline activator, which would then be combined into a continuous solid gel phase (the gel). This process begins with the dissolution of fly ash and slag upon the activation of AL via rupture Si-O-Si and Al-O-Al bonds in fly ash and Ca-O and Si-O-Si bonds in slag. Consequently, a great variety of dissolved species are generated, including silica monomers ($Si(OH)_4$), alumina monomers ($Al(OH)_4^-$), sodium monomers (Na^+) and calcium monomers (Ca^{2+}). With the increase of monomer species, the monomers would react with each other to form dimers, such as silica dimers and silica-alumina dimers. Afterwards, two main reaction products with cross-linked and disorder structure start to form and precipitate. The alkali-aluminosilicate-hydrate (N-A-S-H) gels are formed in AAF, while the calcium-alumina-silicate-hydrate (C-A-S-H) gels are formed in AAS, along with the formation of secondary products such as crystalline zeolites and layered double-hydroxides (Ismail et al., 2014; Sun and Vollpracht, 2018).

Nevertheless, recent studies have revealed that there may exist chemical interactions between fly ash and slag during alkaline activation and report that N-A-S-H and C-A-S-H gels do not develop separately, but they undergo structural and compositional changes in the reaction process (Garcia-Lodeiro et al., 2011; Lee and Lee, 2015). Ismail et al. (2014) reported that the interaction process between fly ash and slag continues well beyond the normal 28-d period of laboratory studies, with a significant change in gel and crystalline phase formation up to 180 d. During the interaction, part of Ca^{2+} released by slag dissolution can incorporate into the N-A-S-H gel to form N-C-A-S-H gel during the interaction process (Ismail et al., 2014). Lee et al. (2015) observed that the chemical composition of N-C-A-S-H gel and C-A-S-H gel is nearly the same, but the silicate structures between them are different. Ye et al. (2016) proposed a more comprehensive description of the interaction mechanism between fly ash and slag, which can be divided into three main aspects: (a) modified nanostructure and chemical composition of precipitates, (b) depressing or triggering the formation of some crystalline phases and (c) spatial heterogeneity of composition in the microstructure. It was also pointed out that there may exist local phase transformation among N-A-S-H, N-C-A-S-H and C-A-S-H

gel due to the interaction between fly ash and slag that occurs locally rather than uniformly (Ye and Radlińska, 2016).

Up to now, however, there is a lack of general model to comprehensively describe the reaction mechanism of AAFS systems. It is crucial to do a further in-depth investigation on reaction and interaction mechanism within Na_2O-CaO-Al_2O_3-SiO_2-H_2O system, to provide more detailed insight into the parameters that control the gel formation kinetics, and equilibrium composition, chemical and dimensional stability, and mechanical properties.

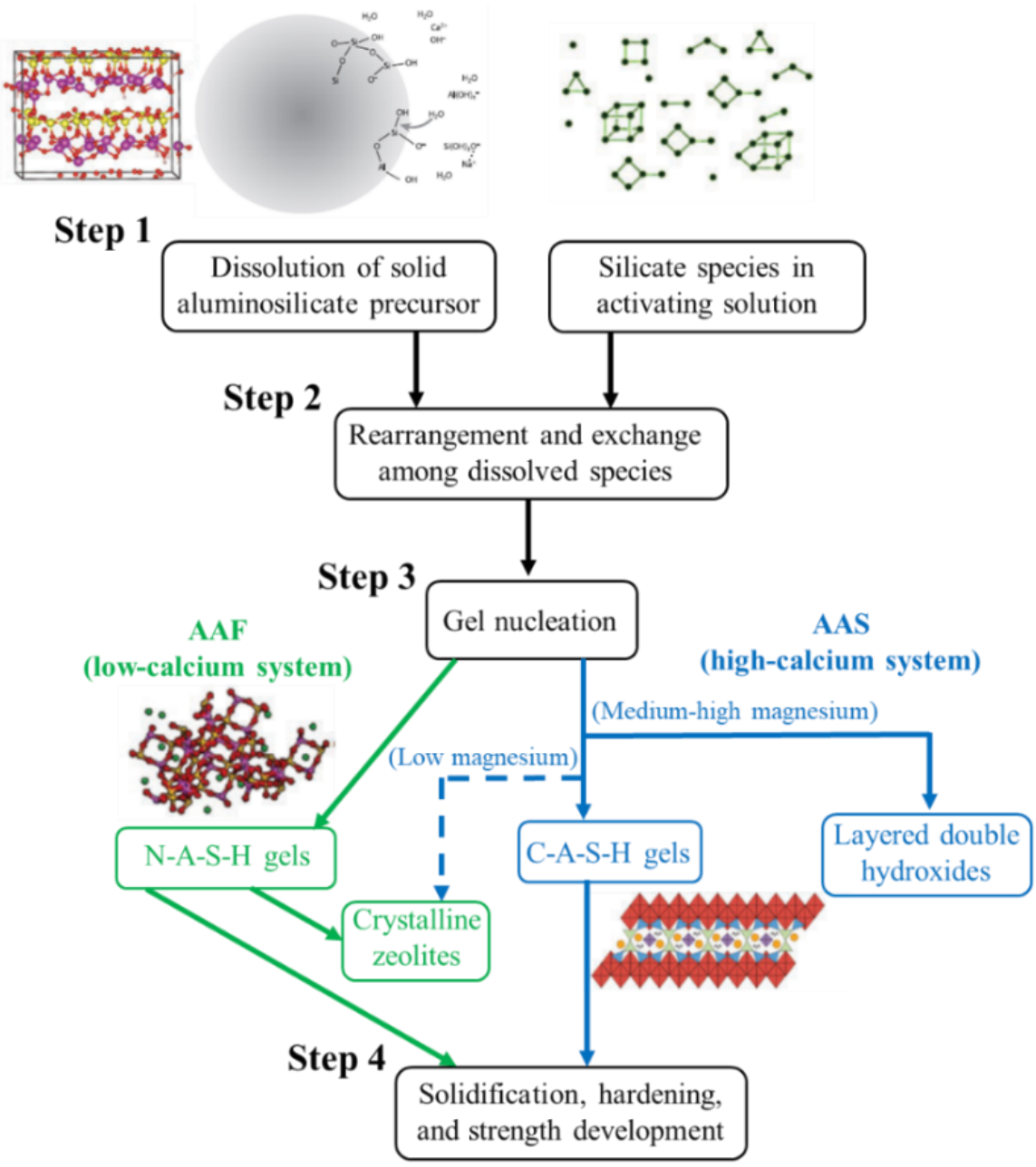

Figure 2-2 Conceptual scheme for the alkaline activation of a solid aluminosilicate precursor including low-calcium precursor (fly ash) and high-calcium precursor (slag) (Provis and Bernal, 2014)

2.5 Multiscale microstructure of AAFS concrete

AAFS concrete is a complex heterogeneous composite consisting of multiphase including aggregates (fine and coarse aggregates), AAFS paste and ITZ between them, with a random microstructure at multiple length scales from nano- to macro-scale. To make a comprehensive characterisation, it is essential to identify different microstructural features based on the length scales and evaluate the relevant morphological and chemical characteristics at each scale. As shown in Figure 2-3, the microstructure of AAFS concrete can be divided into four-multiple length scales: Level 0 (solid gel particle), Level I (gel matrix), Level II (paste), and Level III (mortar and concrete).

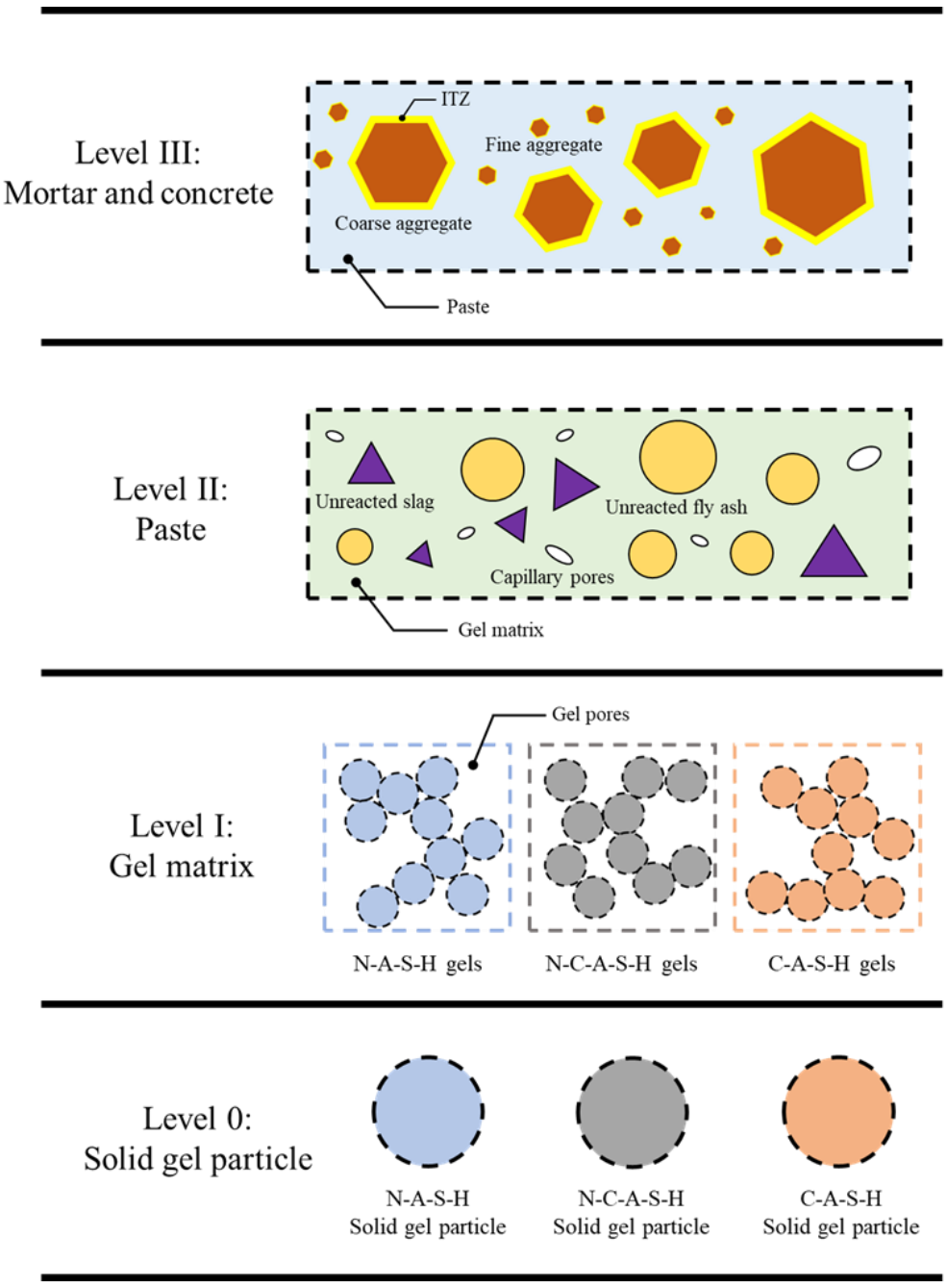

Figure 2-3 Schematic illustration of multiscale microstructure of AAFS concrete

2.5.1 Level 0: Solid gel particle

Level 0 defines the length scale referred to the solid gel particle at nanoscale that is the elementary component of the crystal or amorphous structure of the phases (Constantinides, 2006). As described in Section 2.4, N-A-S-H gel, C-A-S-H gel and N-C-A-S-H gel are the main reaction products of AAFS concrete, while the crystalline zeolite and the layered double-hydroxide are the secondary products. Zeolite is crystalline hydrated aluminosilicate, consisting of SiO_4 and AlO_4 tetrahedra linked through O atom (Nikolov et al., 2017), while the hydrotalcite phase exhibits a layered double hydroxide structure, where the interlayer region contains CO_3^{2-} ions and water molecules (Wang and Scrivener, 1995). The content of crystalline zeolite and hydrotalcite phase is extremely low in AAFS (normally ≤ 5% by mass of binder) (Yang et al., 2012; Ye and Radlińska, 2016).

In comparison, the main reaction products (i.e. N-A-S-H gel, N-C-A-S-H gel and C-A-S-H gel) dominate the AAFS matrix (normally over 90% by mass of binder) (Ye and Radlińska, 2016). The formation of binding products (e.g. N-A-S-H gel and C-A-S-H gel) is normally regarded as the main cause contributing to the development of microstructure (Ye and Radlińska, 2016). The formation of C-A-S-H gel would improve the reaction kinetics of AAFS, and thereby accelerating the evolution of microstructure (Temuujin et al., 2009a; Puligilla and Mondal, 2013). It was identified that C-A-S-H gel formed by activation of slag is more space-filling than N-A-S-H gel formed during the activation of fly ash (Provis et al., 2012). Thus, the formation of C-A-S-H gel would help to modify the microstructure of AAFS by reducing coarse pores and homogenising morphology (Ye and Radlińska, 2016). With the extension of curing time, the more cross-linked binding products (N-A-S-H gel) would be formed, which also help to dense the microstructure of AAFS (Ismail et al., 2014). Furthermore, it is also found that the formation of hybrid binding gel (N-C-A-S-H gel) would modify the nanostructure and chemical composition of precipitates, as well as improve the spatial heterogeneity of composition in microstructure (Ye and Radlińska, 2016). Therefore, the microstructural characteristics of these main reaction products are mainly discussed in the following subsections.

2.5.1.1 N-A-S-H solid gel particle

As seen in Figure 2-4, the N-A-S-H gel with a highly cross-linked disordered structure is generated from the reaction of fly ash, which has a three-dimensional framework of SiO_4 and AlO_4 tetrahedra linked through shared O atoms (Palomo et al., 1999; Pacheco-Torgal et al., 2014; Provis, 2014). The crosslinking of chains offers adequate cavities to

contain alkali cations (Na^{+}), thereby compensating the charge deficit due to the replacement of silica (Si^{4+}) by aluminium (Al^{3+}). Besides, the terminal hydroxyl groups also exist on the surface of N-A-S-H gel, but their presence is not noticeable in the gel structure. The N-A-S-H gel has considerable content of Q^4(mAl) sites (a silicon tetrahedron linking with other three tetrahedrons to form a three-dimensional network), where the distribution of m values depends on the Si/Al ratio of the reactive component of fly ash and the content of Si supplied from the activator (Provis and Bernal, 2014). The structure of N-A-S-H gel would change from Al-rich gel (Gel 1: Si/Al ratio ≈ 1) to Si-rich gel (Gel 2: Si/Al ratio ≈ 2) with the increase of curing ages (Fernández-Jiménez et al., 2006; Criado et al., 2010). Initially, the N-A-S-H gel is established by an Al-rich phase, in which Si tetrahedra are encircled by four Al tetrahedra towards to form Q^4(4Al) sites, because the crosslinking of Al atoms is preferred over the linking of Si atoms at this stage. Later, the N-A-S-H gel with Si-rich phase is generated via the condensation reactions between Si-OH groups, leading to a more stable structure with high cross-linking of Q^4(3Al) and Q^4(2Al) sites.

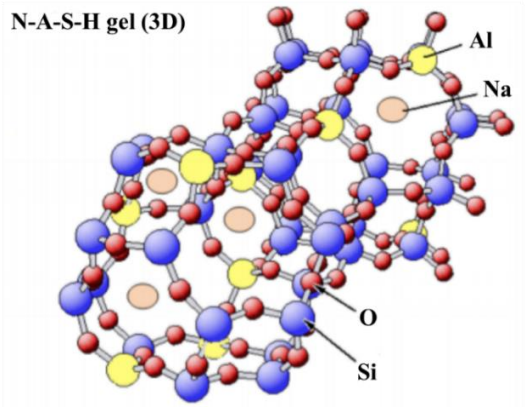

Figure 2-4 Three-dimensional structure of N-A-S-H gel (Pacheco-Torgal et al., 2014)

2.5.1.2 C-A-S-H solid gel particle

The main reaction product resulted from the reaction of slag is C-A-S-H gel that has a disorder tobermorite-like structure, consisting of silicate chains held together by CaO layers (Richardson, 2008). It can be seen from Figure 2-5 that the C-A-S-H gel structure follows a so-called dreierketten arrangement with SiO_4 tetrahedra chains, like C-S-H gel in PC, in which SiO_4 tetrahedra repeat themselves at intervals of three units with each chain containing (3n-1) tetrahedra for an integer value of n (Provis and Bernal, 2014). The interlayer region encloses alkali cations (Ca^{2+} and Na^{+}) and H_2O that is chemically

bonded with the gel structure, where alkali cations would contribute to balance the net negative charge deduced by the replacement of Si^{4+} by Al^{3+} in the tetrahedral chain sites. The incorporation of Al^{3+} in the bridge SiO_4 tetrahedra modifies the Si-Al skeleton and interlayer H_2O in C-A-S-H gel, which improves its crystalline order and cross-linking degree via transforming the layered C-S-H structure to cross-linked C-A-S-H structure (Yang et al., 2018). It was found that the structure of C-A-S-H gel is determined by the nature of alkaline activator (Puertas et al., 2011). Under the activation of SH, the C-A-S-H structure is represented as the co-existence of tobermorite 1.4 nm with a chain length of 5 tetrahedra and tobermorite 1.1 nm with a chain length of 14 tetrahedra. Regarding the activation of SS, the structure of C-A-S-H gel is characterised as the tobermorite 1.4 nm with a chain length of 11 tetrahedra and tobermorite 1.1 nm with a chain length of 14 tetrahedra.

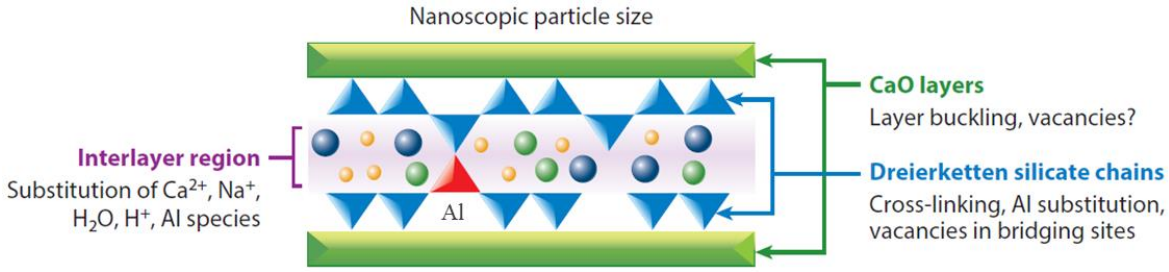

Figure 2-5 Tobermorite-like C-A-S-H structure (Provis and Bernal, 2014)

2.5.1.3 N-C-A-S-H solid gel particle

Since the dissolution and reaction mechanism of fly ash and slag are different from each other, the interaction between them exists during the alkaline activation of AAFS (Ye and Radlińska, 2016). As shown in Figure 2-6, part of Na^+ in N-A-S-H gel would be replaced by free Ca^{2+} during the reaction process leading to the formation of N-C-A-S-H gel, due to the strong polarising power of the aqueous Ca^{2+} relative to Na^+ (Garcia-Lodeiro et al., 2011; Ismail et al., 2014). After this reorganisation, the N-C-A-S-H gel may have a mineral feature between N-A-S-H gel and C-A-S-H gel, which retains the original 3D aluminosilicate framework structure but tends to have a similar composition with C-A-S-H gel (Garcia-Lodeiro et al., 2011). It also suggested that the N-C-A-S-H gel might be formed through the incorporation of Na^+ in C-A-S-H gel (Ismail et al., 2014). However, this transition seems difficult to happen due to the strong binding of Ca within C-A-S-H gels, which is difficult to be distorted by the presence of Na^+ because the polarising power of Na^+ is weaker than that of Ca^{2+}.

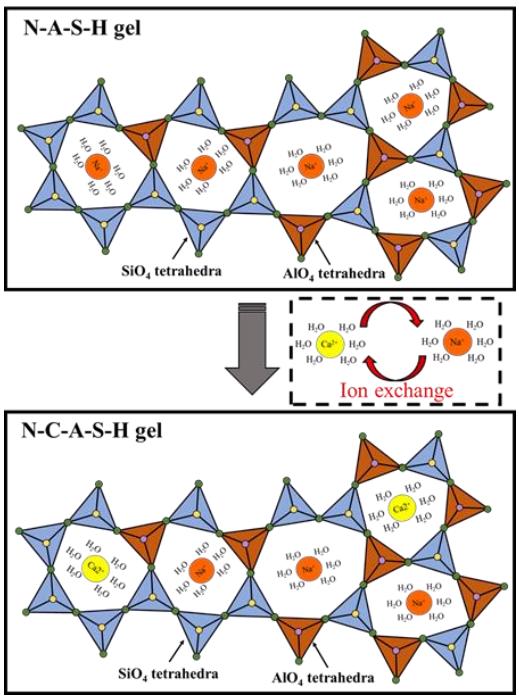

Figure 2-6 Nanostructure of N-C-A-S-H gel (García-Lodeiro et al., 2013)

2.5.2 Level I: Gel matrix

Level I represents the length scale corresponding to the generation of gel matrix which is agglomerated by the solid gel particles along with the presence of gel pores. The agglomeration process of solid gel particles (e.g. N-A-S-H and C-A-S-H gel particles) is commonly described referring to the colloidal model which is the simplified model used to represent the agglomeration of C-S-H gel particles (Jennings, 2000; Duxson et al., 2005; Kapeluszna et al., 2017). As shown in Figure 2-7, the tobermorite-like or jennite-like solid phases are assumed as the fundamental units, i.e. the basic building blocks, to pack together into the structure called globules and then the globules cluster together to form gel matrix. Accordingly, the microstructural characteristics of gel matrix are logically determined by the inherent properties of 'globules' and their parking density reflected by gel porosity.

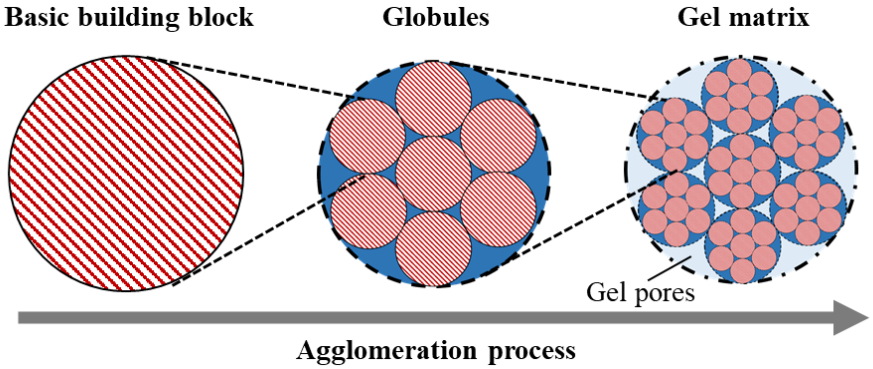

Figure 2-7 The agglomeration process of solid gel particles (Jennings, 2000)

2.5.2.1 N-A-S-H gel matrix

The N-A-S-H gel matrix formed by the sol-gel process is made of primary globular polymeric entities with 0.8-2.0 nm in diameter, which is densely packed based on hydrolysis-polycondensation process (Duxson et al., 2005). The fundamental mechanism of hydrolysis-polycondensation is associated with the formation of Si-O-Si or Al-O-Al bonds accompanied by the expulsion of water into larger pores, for agglomerating monomeric species into polymeric clusters that evolve into particles and consequently gels. In the sol-gel system, the structure of N-A-S-H gels depends on the degree of reversibility during the polycondensation process (Ma and Ye, 2015). If the polycondensation process is nearly irreversible, a space-filling gel would form and eventually link together into a continuous gel (Scherer, 1999). If the polycondensation rate is slightly higher than the bond breaking, the products would grow with the addition of new monomers (Thomas and Jennings, 2006). In this case, the N-A-S-H gels would restructure and reorganize themselves into a more stable and denser state. In AAFS, the N-A-S-H gels generally occur under the intermediate condition between the reversible and irreversible cases, where the highly cross-linked gel products grow in size until they are large enough to precipitate out of the suspension (Bernal et al., 2013; Ismail et al., 2014).

2.5.2.2 C-A-S-H gel matrix

The particle packing of C-A-S-H gels is similar to that of C-S-H gels, in which the agglomeration of colloidal particles ('globules') has two distinct packing arrangements, generating two characteristic forms with different packing densities: low-density (LD) and high-density (HD) (Jennings, 2000; Vandamme and Ulm, 2009; Puertas et al., 2011). The LD packing is similar to the so-called random close packing, while the HD packing is close to the packing known as the face-centred cubic lattice (Constantinides, 2006). The LD and HD C-A-S-H gels are characterised as a packing density of ϕ_{LD} = 0.63 ~ 0.71 and ϕ_{HD} = 0.68 ~ 0.79, respectively (Puertas et al., 2011). Accordingly, the corresponding gel porosities of LD and HD C-A-S-H gels are characterised as P_{LD} = 1- ϕ_{LD} =29% ~ 37% and P_{HD} = 1- ϕ_{HD} =21% ~ 32%, respectively. It can be seen that C-A-S-H gels cover a wide range of packing density between 0.63 and 0.29 and gel porosity between 21% and 37%, which is affected by the available space for the packing of C-A-S-H gels, with tighter packing close to source particles (e.g. slag), and looser packing far from them (Puertas et al., 2011). In addition, it was reported that the structure of C-A-S-H gel matrix depends on the nature of activator. The SH-activated C-A-S-H gels have a relatively high

gel porosity of 21% ~ 37%, while the SS-activated C-A-S-H gels have a relatively low gel porosity of 21% ~ 29% (Puertas et al., 2011).

2.5.2.3 N-C-A-S-H gel matrix

Since the N-C-A-S-H gel is formed through the incorporation of Ca^{2+} into N-A-S-H gel, the agglomeration of this type of gel particles logically follows the packing process of N-A-S-H, according to the hydrolysis-polycondensation process (Duxson et al., 2005; Garcia-Lodeiro et al., 2011; Ismail et al., 2014). Although the original 3D aluminosilicate framework structure is retained in N-C-A-S-H gels, the polarising effect of Ca^{2+} would rearrange the aluminosilicate structure via distorting the Si-O-Al bonds to form Si-O-Ca bonds, leading to less polymerised structures (García-Lodeiro et al., 2013). With the continuous combination of Ca^{2+} into N-C-A-S-H gels, the crosslinking degree of this gel matrix is continuously decreased and eventually bring a comparable structure with C-A-S-H gels, correlating strongly with the chemical composition (Garcia-Lodeiro et al., 2011).

2.5.3 Level II: Paste

Level II denotes the length scale at paste level, which correlates to AAFS paste consisting of gel matrix (i.e. reaction products) from Level I, unreacted fly ash and slag particles and capillary pores. The microstructure at paste level can be directly visualised by microscopy imaging techniques, due to the relatively large characteristic length scale of the phases presented at this scale (Constantinides, 2006). For example, as shown in Figure 2-8, the unreacted fly ash and slag particles, reaction products and pores can be identified.

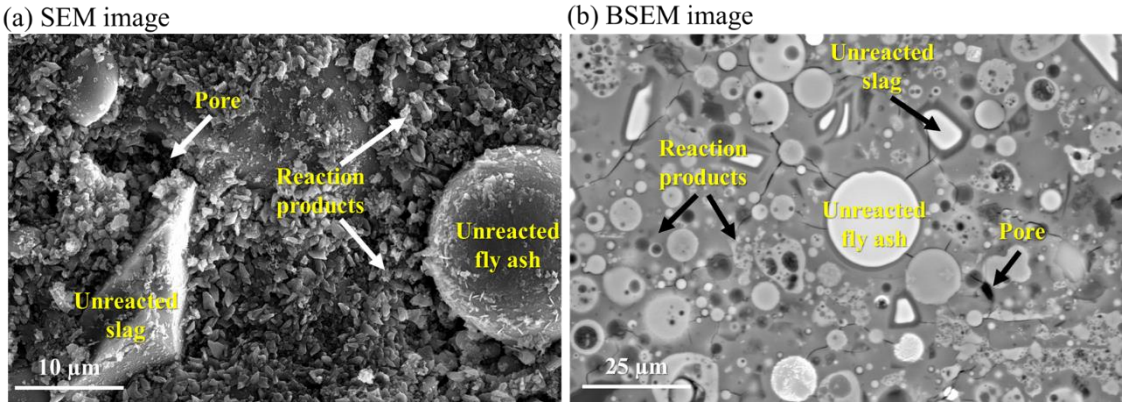

Figure 2-8 Microscopy image of AAFS paste

2.5.3.1 Unreacted particles

It is known that the dissolution of fly ash and slag particles and the subsequent formation of binding gels are crucial features controlling the development of microscopic and macroscopic performance of AAFS system (Ismail et al., 2014; Marjanović et al., 2015; Lee and Lee, 2015). According to the dissolution and reactivity tests, it was reported that the dissolution behaviour of fly ash and slag particles depends on the relationship between forward and backward reactions leading to equilibrium (Antonić et al., 1993). The forward reaction is about the breaking of surface bonds (e.g. Si-O-Si and Al-O-Al bonds in fly ash; Ca-O and Si-O-Si bonds in slag) and the dissolution of soluble species (e.g. Si and Al species) under the activation of alkaline activators, while the backward reaction is related to the reaction between soluble species and the formation of binding gels (Antonić et al., 1993). A balance between the forward dissolution rate and the backward reaction rate of a particle would promote the formation of desirable phases, resulting in good matrix integrity and durability (Hajimohammadi and van Deventer, 2016). The forward and backward reactions would control the release of different species and accordingly affect the synthesis and structure development of binding gels. The rapid release of Al species would hinder the dissolution of Si species and result in the formation of high crystalline zeolite products, while more amorphous products prefer to form with the slower releasing rate of Al species (Hajimohammadi et al., 2010).

Although some theoretical information about the dissolution of fly ash and slag particles has been acquired through the dissolution and reactivity tests, the actual dissolutions of these particles in the paste matrix are still not clear, as these tests presented above are carried out outside of paste. Therefore, the characterisation of the microstructure evolution of fly ash and slag particles in a paste matrix is required to better understand the dissolution and reaction mechanism of these particles. Up to now, the combination of SEM and EDS tests is commonly used to characterise the microstructural development of fly ash and slag particles in AAFS mixes (Puligilla and Mondal, 2013; Ye and Radlińska, 2016), which can provide valuable morphological and chemical information for evaluating the microstructure evolution of particles (Durdziński et al., 2015; Gebregziabiher et al., 2015). Based on these testing methods, it was demonstrated that the microstructure evolution of fly ash and slag particles in the paste matrix is not uniform but varies locally from one region to another, depending on the particle sizes and local chemistry (e.g. pH value) (Fernández-Jiménez et al., 2005; Bae et al., 2014; Nguyen et al., 2018). The fly ash/slag ratio and the type and concentration of activator would also affect the microstructure evolution of source particles (Puligilla and Mondal, 2013;

Pacheco-Torgal et al., 2014). The Ca species released from the dissolution of slag particle would enhance the dissolution of fly ash particle and the formation of geopolymer gels (Puligilla and Mondal, 2013). However, SEM and EDS belong to the destructive testing method, which cannot be used to in-situ monitor the actual microstructure evolution of fly ash and slag particles in AAFS. Therefore, a non-destructive testing method is extremely needed to provide an in-depth understanding of the reaction process of these particles in this new class of binder.

XCT has been regarded as a promising non-destructive method to characterise the internal microstructure of cementitious materials, which provides a potential opportunity to in-situ monitor the microstructure evolution of fly ash and slag particles in AAFS paste (Landis and Keane, 2010; Brisard et al., 2020). Based on the image reconstruction technique, the internal 3D structure of a testing sample can be qualitatively and quantitatively characterised. In the past decades, XCT has been successfully used to non-destructively explore the hydration and microstructure of cementitious materials, such as the time-dependent reaction process, dissolution of cement particles, subsequent formation and development of reaction products, and pore structure features (Gallucci et al., 2007; Gastaldi et al., 2012; Zhang et al., 2012a; Bossa et al., 2015; Hu et al., 2016; Adrien et al., 2016; Zhang, 2017). Wang et al. (Wang et al., 2014) applied XCT to investigate the cement hydration and 3D microstructure development of cement mixes at different curing ages. Gastaldi et al. (2012) utilized XCT to measure the grey level histograms during cement hydration and characterise the evolution of hydration products. More recently, Hu et al. (2016) used this technique to monitor the 3D microstructure evolution of C_3S particle before and after reaction (2.5 h of hydration), which provides direct insight into the morphological change of the particle (both surface and interior) and surrounding hydration products.

In recent years, several attempts have been made to characterise the microstructure evolution of alkali-activated materials with a particular focus on pore structure development using XCT (Provis et al., 2012; Rivera et al., 2016; Borges et al., 2016). Provis et al. (2012) provided the first-ever systematic 3D analysis of pore network geometry in AAFS paste in terms of porosity, pore size distribution, the tortuosity and connectivity of pores using XCT. Zhu et al. (2018) used the same method to measure the pore connectivity in alkali-activated slag paste, which agrees well with the results obtained from electrical response measurements. However, the research on the use of XCT to trace the changes in the microstructure of fly ash or slag particles and the surrounding reaction products is extremely limited. To date, only one study (Provis et al.,

2011) presented the XCT characterisation of the binding between geopolymer gel and unreacted fly ash particle and the 3D pore structure of the aluminosilicate geopolymer gel in AAF paste. The XCT technique proves very effective to gain a 3D view of nanoporous inorganic materials, which help to better understand the reaction process and microstructure development of AAF and optimise its mix proportions. Nevertheless, the existing studies are limited to the qualitative analysis of particle structure, while the relevant quantitative characterisation, as well as the time-dependent development of particle structure, have not been addressed. Furthermore, the effects of size and structure on the microstructure development of fly ash and slag particles in AAFS remain unknown. It is vital to investigate the 3D microstructure evolution of fly ash and slag particles in AAFS paste, which would provide a comprehensive understanding of their reaction mechanism.

2.5.3.2 Reaction products

The microstructure of reaction products consisting of main reaction products (N-A-S-H, C-A-S-H and N-C-A-S-H gels) and secondary products (crystalline zeolites and the layered double-hydroxides) is commonly characterised using SEM, EDS and transmission electron microscopy (TEM) based on their different morphology and chemical compositions. As shown in Figure 2-9, the chemical compositions of reaction products are discussed using the ternary CaO-Al_2O_3-SiO_2 diagram. The Ca substituted N-A-S-H gels (N-C-A-S-H gels) with a globular-like morphology can be identified, which have a limited Ca content with CaO/SiO_2 ratios of 0 ~ 0.3. The C-A-S-H gels with a negligible Na content have a foil-like morphology (García-Lodeiro et al., 2013).

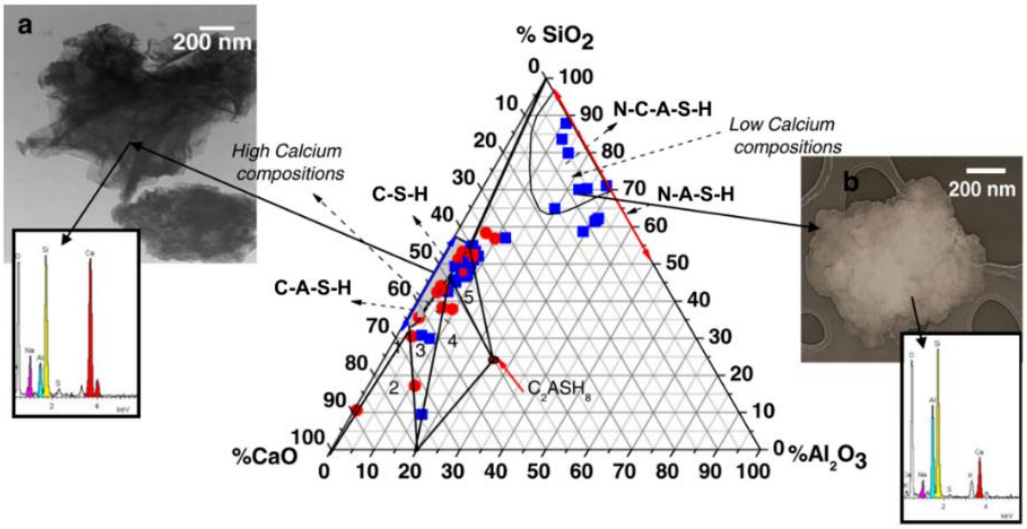

Figure 2-9 TEM/EDS analyses of N-A-S-H, N-C-A-S-H and C-A-S-H gels ((a) foil-like morphology in a type C-A-S-H gel and (b) globular-like morphology in an N-C-A-S-H type gel) (García-Lodeiro et al., 2013)

In addition, the reaction products can be also divided into inner products and outer products in the microstructural characterisation, based on the difference in density and their locations relative to the original boundary of original particle (Gebregziabiher et al., 2015; Nguyen et al., 2018). As seen in Figure 2-10, two distinguishable reaction products generated from the activation of fly ash and slag particles are clearly identified: inner products (IP) and outer products (OP), in which the former are denser than the latter (Nguyen et al., 2018). The formation of a thin layer of products around the surface of source particles (i.e. the formation of IP) is a spontaneous process when the alkaline activator interacts with the source particles (Gebregziabiher et al., 2015). Afterwards, the initial formed IP would act as a natural physical barrier, preventing the transport of ions between unreacted particles and the surrounding region and thus inhibiting the formation of OP (Gebregziabiher et al., 2015). However, the boundary between IP and OP would be changed along with the continuous reaction of source particles (Nguyen et al., 2018). In the beginning, the boundary between IP and OP can be easily distinguished in the partially reacted particles due to the different reaction process. When the particles are fully reacted, the IP-OP boundary turns to be invisible due to the equilibrium of reaction. Although the existences of IP and OP have been identified by previous research, the formation and transition mechanisms remain unknown due to a lack of in-situ characterisation of the microstructure evolution of IP and OP. Hence, it is vital to in-situ monitor the microstructure development of IP and OP, which would provide a comprehensive understanding of the reaction mechanism of fly ash and slag particles and microstructure evolution of AAFS concrete.

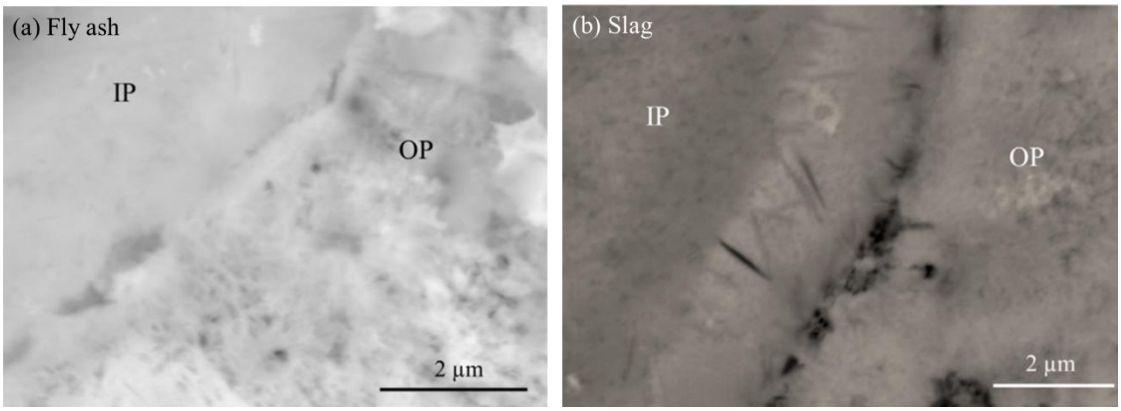

Figure 2-10 Morphologies of inner products (IP) and outer products (OP) in AAF and AAS pastes (Nguyen et al., 2018)

2.5.3.3 Pores

The pore structure is comprehensively investigated through four experimental techniques, including nitrogen adsorption, mercury intrusion porosimetry (MIP), BSEM

and XCT (Promentilla et al., 2009; Ma et al., 2018). MIP can be used to determine almost the whole range of pore sizes in materials (from 6 nm to 350 μm), while nitrogen adsorption can be adapted to accurately detect the small pores with size ranging from 0.3 to 300 nm. BSEM allows the characterization of pore structure in a real 2D image of the material with a limit pore size of > 100 nm, whereas XCT can reconstruct the pore structure in 3D with a limit pore size of > 1 μm. Additionally, XCT belongs to the non-destructive method, which allows for in-situ tracing of pore structure evolution.

Based on these testing methods, it was observed that the pores in AAFS concrete cover multiple length scales from nano- to micro-scale, which can be divided into two types of pore: gel pore (0.5 ~ 10 nm) and capillary pore (10 nm ~ 10 μm) (Keulen et al., 2018). The gel pores are formed in the interstices between solid gel particles, while the capillary pores remain in the originally liquid-filled spaces. The key properties of pore structure include the porosity, tortuosity and extent of percolation of the pore network (Lloyd et al., 2009a; Promentilla et al., 2009; Bossa et al., 2015). The porosity of AAFS paste is correlated with the tortuosity and affected by the slag content and the curing age (Provis et al., 2012). The increase of slag content reduces porosity and increase tortuosity (notably at a high slag content of 50% or higher), whereas the extended curing provides lower porosity and higher tortuosity. This indicates that the AAFS samples with high slag content are dominated by the space-filling C-A-S-H gels, where the samples with low slag content are instead controlled by the N-A-S-H gels that do not chemically bind water and therefore some level of pore network obstruction cannot be given.

2.5.4 Level III: Mortar and concrete

Level III represents the length scale at mortar and concrete level, which is composed of three phases: paste matrix from Level II, aggregate and ITZ between them. Since the microstructure of paste matrix has been described above, this section will mainly focus on the other two phases, i.e. aggregate and ITZ.

2.5.4.1 Aggregate

Aggregate is a broad category of fine-coarse-grained particulate material used in concrete, including natural sand, gravel, crushed stone and geosynthetic aggregate. The aggregates are generally composed of fine and coarse aggregates. The natural sand or crushed stone with a size smaller than 5 mm are regarded as fine aggregates, while the coarse aggregates consist of gravel or crushed stone with size larger than 5 mm (Kosmatka et al., 2002). Aggregate is considered as the major constituent of concrete and

usually occupies 60% ~ 80% of concrete volume (Thomas and Folliard, 2007). Given the high content of aggregates in concrete, it is easy to understand that aggregate is the main factor affecting the fresh, hardened and long-term performance of concrete, regardless of PC or AAFS concrete. The chemical and physical characteristics of aggregates can directly influence the concrete performance such as workability and mechanical properties and the long-term durability such as alkali-aggregate reactivity and frost susceptibility (Thomas and Folliard, 2007; Shi et al., 2015).

2.5.4.2 Interfacial transition zone (ITZ)

ITZ between aggregate and paste matrix is typically regarded as one of the most important features affecting the overall performance of concrete (Ollivier et al., 1995; Scrivener et al., 2004; Bentur et al., 2000). It has long been a key area of research in PC concrete (Barnes et al., 1979; Xie et al., 1991; Elsharief et al., 2003; Wu et al., 2016). It is generally agreed that the ITZ lies on the so-called "wall effect", where the packing of cement grains would be disrupted through the surface of aggregates (Ollivier et al., 1995; Scrivener et al., 2004). In addition, the formation of ITZ would also be affected by the internal bleeding water which would tend to accumulate near the elongated, flat and large pieces of aggregates (Mehta and Monterio, 2013). These phenomena represent the response for the key features of ITZ, which are primarily related to the deficit of large cement grains and a higher local water-to-cement (w/c) ratio in the ITZ than that in the paste matrix (Scrivener et al., 2004). As seen in Figure 2-11, it would accordingly result in the difference in chemical and physical properties between the ITZ and paste matrix, where a higher proportion of pores, calcium hydroxide (CH) crystals and ettringite can be found in the ITZ (Larbi and Bijen, 1990; Pope and Jennings, 1992; Mehta and Monterio, 2013). Therefore, the ITZ is often regarded as the "weak link" in concrete due to its nature. The relatively high porosity presented in the ITZ would provide an easier pathway for the aggressive ions to penetrate concrete (Scrivener and Nemati, 1996), and the higher content of CH crystals in the ITZ would lower the resistance of concrete to ionic penetration and facilitate the leaching of CH (Cwirzen and Penttala, 2005). Additionally, the relationships between ITZ's features and transport properties of concrete have been investigated by several researchers (Winslow et al., 1994; Wong et al., 2009; Zheng et al., 2009). Winslow et al. (1994) applied a hard core/soft shell computer model to simulate the percolation of ITZ in mortar and concrete specimens and reported that the probability of ITZ percolation can be decreased by reducing the ITZ thickness or the porosity in the ITZ. Wong et al. (2009) estimated the effects of ITZ and

microcracking on the transport properties of cement-based materials after drying. It was found that the net effect of ITZ on overall transport properties is less significant, whereas the effects of total porosity, tortuosity and microcracks on transport properties are much more significant, especially permeability. Furthermore, the effects of different factors on the ITZ's features and transport properties of cement-based materials have also been extensively investigated (Scrivener et al., 1988; Leemann et al., 2006; Leemann et al., 2010). Scrivener et al. (1988) observed that the particle size distribution of cement would determine the ITZ width, while the presence of aggregate may affect the gradients of microstructure in the ITZ. Leemann et al. (2006) found that compaction has notable effects on the porosity and width of ITZ, where the ITZ in conventionally vibrated concrete has a higher porosity and width than self-compacting concrete, leading to a higher oxygen permeability and water conductivity. Different types of cement have minor effects on the porosity and width of ITZ in self-compacting concrete, while the cement types have a strong influence on its permeability (Leemann et al., 2010). Zhang et al. (1990) proved that the lightweight aggregates with a porous outer layer would contribute to the formation of a dense ITZ microstructure, as opposed to the porous ITZ formed around the normal-weight aggregates. Based on this finding, Bentz (2009), used lightweight aggregates as internal curing agents for mortar, the results of which indicated that the internal curing using lightweight aggregates can help reduce the ITZ percolation and enhance the resistance to the penetration of chloride ions.

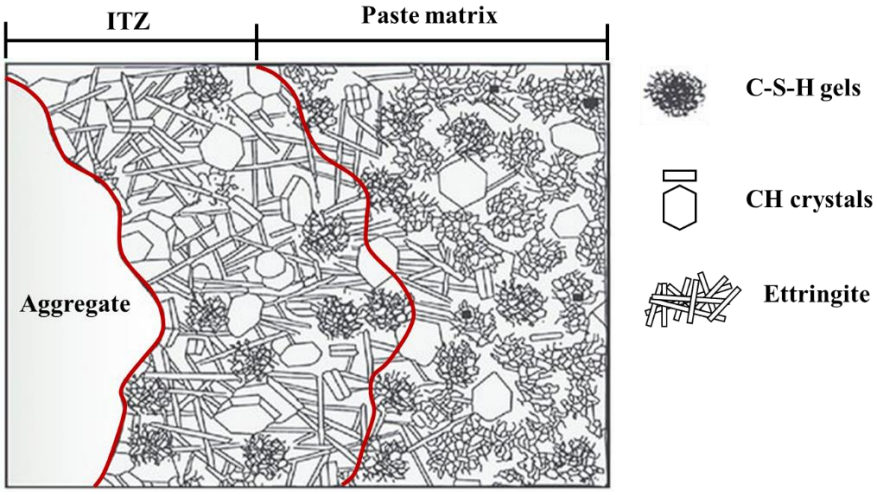

Figure 2-11 Schematic diagram of ITZ in PC concrete (Mehta and Monterio, 2013)

However, the ITZ formed in AAC has different features compared to that in PC concrete (Brough and Atkinson, 2000; Ji et al., 2017). A few studies have discussed the microstructure and properties of ITZ in AAF and AAS concrete (Brough and Atkinson,

2000; Lee and van Deventer, 2004; Nicolas and Provis, 2015). It was found that there is no apparent weak ITZ near the aggregates in AAF concrete due to the formation of N-A-S-H gels rather than the CH crystals in this region (Lee and van Deventer, 2004). The N-A-S-H gels are the major binding phases in AAF concrete, which would promote the interparticle bonding and the macroscopic strength in the ITZ. Additionally, the existence of soluble silicates in the initial alkaline solution would also effectively improve the interfacial bonding between aggregates and pastes in AAF concrete (Lee and van Deventer, 2004). In AAS concrete, it was observed that the ITZ between aggregates and paste matrix is condensed and uniform, which can be attributed to the refinement of pore structure as a result of the filling of reaction products (Brough and Atkinson, 2000; San Nicolas et al., 2014). This is because this zone is mainly composed of N-C-A-S-H or C-A-S-H gels with lower Ca/Si ratio rather than the expansive (Al-free) gels (Nicolas and Provis, 2015).

Although the investigations on ITZ in the sole AAC have been made, the existing knowledge of ITZ in AAFS concrete is limited to the simple analysis of local morphology (Singh et al., 2016). Therefore, it is vital to conduct more comprehensive studies for a better understanding of the microstructure and properties of ITZ in AAFS concrete, particularly the microstructure formation and development of ITZ that have not been explored. It is known that the microstructure of ITZ can be changed over curing time due to the ongoing chemical reaction, which may affect the performance development of AAFS concrete. Hence, it is necessary to monitor the evolution of ITZ's microstructure over time, starting from a very early age. Furthermore, the mechanism behind its microstructure evolution is still unknown. Thus, the lack of consent related to the microstructure of ITZ in AAFS concrete would lead to open issues regarding its engineering applications, as it might provide with a positive or negative influence on the mechanical and transport properties of concrete.

2.5.5 Summary

In this section, the existing studies on the microstructure of AAFS concrete are critically reviewed according to multiple length scales from nano- to macro-scale. The multiscale microstructure of AAFS concrete has been studied for decades, providing valuable information to understand the reaction mechanism and the corresponding relationship with the macroscale performance of concrete. However, a systematic study of the microstructure of individual phases within AAFS concrete is still lacking to date. The limitations of recent research on the microstructure of AAFS concrete can be

highlighted as two points. First, there is a lack of in-situ microstructure characterisation of fly ash and slag particles and reaction products during the reaction process, which would inhibit a deep understanding of the reaction mechanism. Second, the studies of the ITZ microstructure are limited to the simple analysis of local morphology, which cannot provide full insight into the mechanism of ITZ evolution.

2.6 Multiscale micromechanical properties of AAFS concrete

AAFS concrete is a highly heterogeneous composite, which has various phases with different micromechanical properties at multiscale from nano- to macro-scale, as described in Section 2.5. The multiscale micromechanical analysis based on experimental and theoretical methods provides a framework to evaluate the mechanical properties of individual phases at microscale and the corresponding contribution to the macroscopic mechanical properties (Ulm et al., 2004). The experimental analysis is based on the micromechanical test, i.e. nanoindentation (Fischer-Cripps, 2004), while the theoretical analysis is conducted based on the continuum micromechanics which can be used to split a heterogeneous material into phases with average continuous material properties (Aboudi et al., 2013). The analysis of continuum micromechanics generally includes the following three steps (Constantinides, 2006):

Representation deals with the identification of the different phases in a Representative Element Volume (REV) of the composite structure (Constantinides, 2006). The REV contains a sufficient number of phase volumes which can statistically represent the composite. The length scale l of REV should greatly smaller than the characteristic length L of the whole structure (i.e. $l << L$), to fulfil the basic principle of continuum mechanics, i.e. the assumption of continuum hypothesis, where the material is composed of continuum mass. In addition, l should be large enough as compared to the length d of the individual phases within the REV (i.e. $d << l$). These two conditions are also regarded as the principle of scale separation. The separation of the multiscale microstructure of AAFS concrete presented in Figure 2-3 is complied with this principle, referring to the multiscale micromechanical analysis of AAC and PC concrete (Constantinides and Ulm, 2004; Ulm et al., 2005; Šmilauer et al., 2011; Tatar et al., 2019).

Localization builds the link between the macroscopic stress (or strain) at the boundary of the REV and the microscopic stress (or strain) in the individual phases within the REV (Constantinides, 2006). The classical theory called Eshelby's solution is commonly used to define this link, which considers the phases as the ellipsoidal inclusions embedded in the matrix (the REV) (Eshelby, 1957). Nevertheless, it did not provide an analytical

solution for the materials with non-linear behaviour. To overcome this limitation, the Mori-Tanaka and self-consistent schemes were developed and widely used based on different situations (Mori and Tanaka, 1973; Zaoui, 2002). The Mori-Tanaka scheme is proper for matrix-inclusion morphology by choosing the prevailing phase as the matrix (Mori and Tanaka, 1973), while the self-consistent scheme is suitable for the perfect disorder morphology by using the homogenized medium as the matrix (Zaoui, 2002).

Homogenization drives the macroscopic mechanical properties of the REV as a function of microscopic properties of the individual phases including their mechanical properties, volume fractions and specific morphologies (Constantinides, 2006). Following the continuum micromechanics, the average stress ($\bar{\sigma}$) and strain ($\bar{\varepsilon}$) of the REV can be defined as (Gao et al., 2017a):

$$\bar{\sigma} = \frac{1}{V}\int_V \sigma \, dV = \sum_{i=1}^{N} f_i \bar{\sigma}_i \qquad (2-1)$$

$$\bar{\varepsilon} = \frac{1}{V}\int_V \varepsilon \, dV = \sum_{i=1}^{N} f_i \bar{\varepsilon}_i \qquad (2-2)$$

where f_i is the fraction of the i^{th} inclusion, σ is the stress tensor of the i^{th} inclusion, $\bar{\sigma}_i$ is the average stress of the i^{th} inclusion, ε is the strain tensor of the i^{th} inclusion and the $\bar{\varepsilon}_i$ is the average strain of the i^{th} inclusion.

As defined in Figure 2-3, the microstructure of AAFS concrete can be divided as a four-level structure, separated by one or several order of length magnitude, in which each level can be theoretically considered as a REV, consisted of homogeneous phases with constant material properties (Ulm et al., 2004). The detailed micromechanical analysis of AAFS concrete is presented below.

2.6.1 Level 0: Solid gel particle

Level 0 is the lowest level of a mechanical representation in the AAFS microstructure, which refers to the solid gel particles (e.g. N-A-S-H and C-A-S-H gel) and is solely determined by the physical chemistry of the formation process of material, referring to the PC microstructure (Ulm et al., 2004). Nevertheless, the mechanical properties of the solid gel particles at nanoscale are unable to be directly characterised so far due to the limitation of the testing technique (Constantinides, 2006). Therefore, the understanding of the mechanical properties of solid gel particles is merely limited to the simulation to date.

It was found from nanoscale modelling that the chemical composition and internal structure of solid gel particle have strong relations with its mechanical properties, e.g. elastic modulus and hardness (Lolli et al., 2018; Yang et al., 2018). The elastic modulus

and hardness of a solid gel with crystalline structure (order structure) are generally higher than those of a solid gel with amorphous structure (disorder structure) (Lolli et al., 2018). The crystalline structure can sustain the highest tensile load, but its failure is brittle, whereas the amorphous structure is expected to have better ductile behaviour (Lolli et al., 2018). The implication is that the level of structural disorder has a strong impact on the mechanical behaviour of solid gel.

In addition, the enhance of cross-linking degree of solid gel is also suggested to improve its mechanical properties, due to the ability to form a covalent bond between the gel layers (Yang et al., 2018). The increase of Al/Si ratio in C-A-S-H solid gel would improve its crystalline order and crosslinking degree, and thereby enhancing its mechanical properties. The incorporation of Al branch structures would resist the tensile loading and strengthen the soft interlayer zone in C-A-S-H solid gel and consequently enhance the interlayer cohesive strength and stiffness (Yang et al., 2018).

Based on these simulation results, the distinctions of chemical composition and nanostructure between N-A-S-H gel, C-A-S-H gel and N-C-A-S-H gel would logically induce the different mechanical properties among them. However, this assumption has not been verified to date.

2.6.2 Level I: Gel matrix

The gel matrix at Level I is formed by the agglomeration of solid gel particles from Level 0 with the presence of gel pores, leading to three types of gel matrix (N-A-S-H, C-A-S-H, N-C-A-S-H gels) in AAFS concrete. Level I is the smallest material length scale which can be characterised directly through the micromechanical tests, e.g. nanoindentation (Constantinides et al., 2003). Nanoindentation is regarded as a powerful tool to detect the local elastic modulus and hardness of the material at nano- and micro-scale (Randall et al., 2011; Hu and Li, 2015b; Brown et al., 2018). The elastic modulus is related to stiffness, while the hardness is associated with mechanical strength (Hu and Li, 2015b).

The micromechanical properties of gel matrix in PC system have been extensively explored using nanoindentation (Hughes and Trtik, 2004; Constantinides and Ulm, 2004; Randall et al., 2011). Two distinct types of C-S-H gels, i.e. HD C-S-H gels with elastic modulus of 29.4 ± 2.4 GPa and LD C-S-H gels with elastic modulus of 21.7 ± 2.2 GPa, were demonstrated from a micromechanical point of view (Constantinides et al., 2003). Such difference can be attributed to the different packing process of C-S-H solid gel particles, leading to the formations of HD C-S-H gels with gel porosity of 24% and an

LD C-S-H gels with gel porosity of 37% (Constantinides, 2006). In addition, it was reported that the micromechanical properties of C-S-H gels as intrinsic material properties would not be affected by the mix proportions of PC. The volume fractions of these two C-S-H gels dominates the macroscopic mechanical properties of PC mixtures (Constantinides and Ulm, 2004).

Recently, several attempts have been also made to investigate the micromechanical properties of gel matrix in sole AAC system (i.e. AAF and AAS system), as summarized in Table 2-2. Regarding the AAF system, it was reported that the main reaction products (N-A-S-H gels) cover a wide range of elastic modulus between 4.44 and 20 GPa (Němeček et al., 2011; Lee et al., 2016; Ma et al., 2017). The elastic modulus of N-A-S-H gels is expected to be affected by the nature of alkaline activator, curing condition and curing age due to the change of reaction process and consequently the chemical and physical properties (Ma et al., 2017; Luo et al., 2020). Luo et al. (2020) reported that the elastic modulus of the N-A-S-H gels formed in the heat-cured AAF sample (14.30 GPa) is higher than that formed in the ambient-cured sample (11.05 GPa), due to the accelerated polymerisation process of AAF occurred under heat-cured conditions. Nevertheless, this finding contradicts with the result found by Němeček et al. (2011), where the elastic modulus of N-A-S-H gels is constant between 17 GPa and 18 GPa, irrespective of curing conditions. Regarding the effects of alkaline activator, it was found that the AAF sample activated by SS solution has a higher elastic modulus than that activated by SH (Luo et al., 2020). The addition of silica may improve the fully condensed degree of tetrahedral aluminosilicate network structures, which would consequently enhance the elastic modulus of N-A-S-H gels due to the relatively high strength of Si-O-Si bonds comparing with Si-O-Al bonds (Duxson et al., 2005). It was also stated that the elastic modulus of N-A-S-H gels varies with the curing ages, which is mainly affected by the evolution of pores at nano- and micro-scale (Ma et al., 2017). With the increase of curing ages, the threshold pore diameter is decreased while the elastic modulus of N-A-S-H gels is increased.

With respect to the AAS system, the elastic modulus and hardness of its main reaction products (C-A-S-H gels) are affected by the selection of alkaline activator (Puertas et al., 2011; Thomas et al., 2018). The hardness and elastic modulus of C-A-S-H gels in SS-activated slag are in the range of 0.84 ~ 2.5 GPa and 28 ~ 47 GPa, respectively, which are higher than those in SH-activated slag with a hardness of 0.30 ~ 1.32 GPa and elastic modulus of 12 ~ 25 GPa (Puertas et al., 2011; Thomas et al., 2018). It was also reported that the micromechanical properties of reaction products in SH-activated slag depend on

the activator molarity, while those in SS-activated slag are slightly improved with the increase of silica modulus (Thomas et al., 2018).

Although these studies have provided some valuable information on the micromechanical properties of gel matrix in the sole AAC system, the existing research on the gel matrix of blended system (i.e. AAFS system) is limited to the analysis of carbonation effects on its elastic modulus (Nedeljković et al., 2018). The elastic modulus of gel matrix in the uncarbonated AAFS paste is between 21 GPa and 45 GPa, which is significantly higher than that in the carbonated AAFS paste (4 ~ 21 GPa). Nevertheless, the distinction of micromechanical properties between different types of gels (i.e. N-A-S-H, C-A-S-H and N-C-A-S-H gels) are not considered in this research. Moreover, the existing knowledge is often limited to a micromechanics viewpoint and the relationships between microstructure and micromechanical properties have been rarely addressed in previous studies. Up to now, the micromechanical properties of different reaction products within AAFS and the relationship with microstructure are still unknown.

Table 2-2 Summary of the micromechanical properties of individual phases in AAC system

Types	Precursors	Alkaline activator	Curing condition	Elastic modulus (E) and hardness (H) (GPa)					Pores	Paste	References
				Unreacted particles		Reaction products					
				Fly ash	Slag	N-A-S-H	C-A-S-H	N-C-A-S-H			
AAF	Fly ash	SH and SS	Ambient curing (20 ℃) and Heat curing (80 ℃)	E = 79.65 ± 16.99 (ambient-cured) E = 79.15 ± 14.34 (heat-cured)	-	E = 17.72 ± 3.75 (ambient-cured) E = 17.03 ± 3.48 (heat-cured)	-	-	-	E: 28.28	(Němeček et al., 2011; Šmilauer et al., 2011)
	Fly ash	SH	Heat curing (60 ℃)	E = 72.0 ± 6.8	-	E = 16.3 ± 4.1	-	-	-	E: 17.5	(Das et al., 2015)
	Fly ash	SH and SS	Ambient curing (23 ℃)	-	-	E = 4.44 ~ 16.78 H = 0.11 ~ 0.75	-	-	-	-	(Lee et al., 2016)
	Fly ash	SH and SS	Heat curing (40 ℃)	E of Fe-rich fly ash = 71.0 ~ 137.7 E of Ca-rich fly ash = 75.7 ~ 91.2 E of Si-rich fly ash = 82.9 E of Al-rich fly ash = 33.3 ~ 65.4	-	E = 7 ~ 25	-	-	-	-	(Ma et al., 2017)
	Fly ash	SH and SS	Ambient curing (22 ℃) and Heat curing (70 ℃)	-	-	E = 11.05; H = 0.40 (SS-activated; Ambient-cured) E = 10.05; H = 0.41 (SH-activated; Heat-cured) E = 12.21 ~ 14.30 H = 0.45 ~ 0.57 (SS-activated; Heat-cured)	- - -	-	-	-	(Luo et al., 2020)
AAS	Slag	SH and SS	Ambient curing (22 ± 2 ℃)	-	-	-	E = 28 ~ 47 H = 0.84 ~ 1.53 (SS-activated) E = 12 ~ 20 H = 0.30 ~ 1.32 (SH-activated)	-	-	-	(Puertas et al., 2011)
	Slag	SH and SS	Ambient curing (22 ± 2 ℃)	-	E = 70 H = 6	-	E = 30; H = 2.5 (SS-activated) E = 25; H = 1 (SH-activated)	-	H < 0.5	-	(Thomas et al., 2018)
AAFS	Fly ash and slag	SH and SS	Ambient curing (20 ℃)	E > 46	E > 46	E = 21 ~ 45 (gel matrix)			E < 4	-	(Nedeljković et al., 2018)

Note: SH (sodium hydroxide solution); SS (sodium silicate solution)

2.6.3 Level II: Paste

The AAFS paste at level II is composed of unreacted particles (fly ash and slag particles), reaction products (N-A-S-H, C-A-S-H and N-C-A-S-H gels) and pores. For the micromechanical analysis, it is first to experimentally characterise the micromechanical properties (elastic modulus and hardness) of these phases and the corresponding volumetric fractions based on the nanoindentation test. Afterwards, the continuum micromechanics models (e.g. Mori-Tanaka and self-consistent models) would be upscale the micromechanical properties from level I (individual phases) to level II (composite) and estimate the effective mechanical properties of the composite, i.e. AAFS paste.

This combined experimental-theoretical micromechanical method has been successfully used to evaluate the micromechanical properties of PC paste. Based on the testing results of nanoindentation, five different phases including anhydrous clinker, calcium hydroxide, HD C-S-H gels, LD C-S-H gels and pores can be identified from the micromechanical point of view. The anhydrous clinker has the highest elastic modulus of > 65 GPa and hardness of > 3 GPa, due to its compacted structure with nearly no pores (Ulm et al., 2010; Wilson et al., 2018). It is followed by the calcium hydroxide with elastic modulus of around 40 GPa and hardness of 1.35 ~ 2.26 GPa, attributing to its crystalline structure with low disorder degree (Davydov et al., 2011; Hu and Li, 2015b; Wilson et al., 2018). Following these two phases, two types of C-S-H gels (HD C-S-H with elastic modulus of around 32 GPa and hardness of around 1.1 GPa; LD C-S-H with elastic modulus of around 22 GPa and hardness of around 0.7 GPa) are identified, resulting from their different gel porosity or packing density (Constantinides et al., 2003; Zhu et al., 2007; Vandamme and Ulm, 2013). Lastly, the lowest elastic modulus with lower than 1 GPa is assigned to the existence of capillary pores, in which the non-zero modulus of pores might be attributed to the contact of indenter with solid/pores interface during the nanoindentation test (Ma et al., 2017). Most researchers would prefer to adjust the elastic modulus of pores to be zero during the statistical analysis of nanoindentation results (da Silva et al., 2013; Hu and Li, 2015b; Wilson et al., 2018). After the nanoindentation test, the Mori-Tanaka and self-consistent model are commonly used to predict the effective elastic modulus of paste (e.g. effective bulk modulus and shear modulus) (Bernard et al., 2003; Gao et al., 2017a; Brown et al., 2018). The predicted effective elastic modulus has been demonstrated to agree well with the macroscopic elastic modulus obtained from experiments, e.g. ultrasonic pulse velocity and resonant frequency tests (Pichler et al., 2008; Pichler and Hellmich, 2011).

Over the past decade, the micromechanical properties of individual phases within AAC system at paste level have also been investigated. In terms of AAF paste, it was reported that the unreacted fly ash particles have the highest elastic modulus with a wide range of 33.3 ~ 137.7 GPa, while the elastic modules of N-A-S-H gels is relatively low, ranging from 4.44 to 20 GPa (Němeček et al., 2011; Lee et al., 2016; Ma et al., 2017). The elastic modulus of fly ash particles is affected by mineral features (Ma et al., 2017). The Fe-rich fly ash has the highest elastic modulus of 71.0 ~ 137.7 GPa, followed by the Ca-rich fly ash with an elastic modulus of 75.7 ~ 91.2 GPa. The Si-rich and Al-rich fly ashes have relatively low elastic modulus with 51.7 ~ 82.9 GPa and 33.3 ~ 65.4 GPa, respectively (Hu and Li, 2015a; Ma et al., 2017). The elastic modulus of N-A-S-H gels is determined by the selection of activator and curing condition, as explained in Section 2.6.2. Lastly, the AAFS paste with the effective elastic modulus of 17.5 ~ 28.28 GPa has also been predicted using Mori-Tanaka model and self-consistent model, which agrees well with the results obtained from macro-scale experimental tests (Šmilauer et al., 2011; Das et al., 2015). In terms of AAS paste, the unreacted slag with the highest elastic modulus of around 70 GPa and hardness of around 6 GPa is identified (Thomas et al., 2018). The C-A-S-H gels have a wide range of elastic modulus between 12 and 47 GPa and hardness between 0.30 and 2.5 GPa, depending on the nature of alkaline activator, as introduced in Section 2.6.2 (Puertas et al., 2011; Thomas et al., 2018).

Although the combined experimental-theoretical micromechanical method has been extensively used in the PC system and sole AAC system (i.e. AAF and AAS), the relevant research in the blend AAFS system is still rare to date. The existing research on the micromechanical properties of AAFS system is limited to the simple analysis of overall elastic modulus of different phases, in which the unreacted fly ash and slag particles with an elastic modulus of > 65 GPa are identified, followed by the reaction products (21 ~ 45 GPa) and pores (< 4 GPa) (Nedeljković et al., 2018). However, the detailed information about the micromechanical properties of different types of reaction products (N-A-S-H, N-C-A-S-H and C-A-S-H gels) is not provided in the existing research. In addition, the evolution of micromechanical properties of individual phases in AAFS as a function of curing age is still unknown. Lastly, the micromechanical relationship between individual phases and AAFS paste is not fully understood.

2.6.4 Level III: Mortar and concrete

The mortar and concrete at level III are considered as a three-phase composite consisting of paste matrix from level II, aggregates (fine aggregates in the case of mortar

and additional coarse aggregates in the case of concrete) and the ITZ between aggregate and paste matrix. The micromechanical properties of these phases would directly determine the macroscopic mechanical properties of mortar and concrete. Since the micromechanical properties of paste matrix have been discussed in Section 2.6.3, this section will mainly review the micromechanical properties of aggregate and ITZ.

Aggregate, as the main component in concrete, has stable mechanical properties which are difficult to be changed during the reaction process, regardless of PC or AAC system (da Silva et al., 2013). The elastic modulus of aggregate depends on its types, in which the crushed quartzite has the highest elastic modulus with around 110 GPa, followed by the crushed granite, marble coarse aggregate and limestone with 75, 64 and 60 GPa, respectively (Wu et al., 2001). Due to the inherent stiffness and high volume of aggregates existed in concrete, aggregates would strongly affect the overall elastic modulus of concrete (Kim and Abu Al-Rub, 2011). It was found that the PC concrete with crushed quartzite (the aggregate with highest elastic modulus) has a higher elastic modulus than that with other aggregates (Wu et al., 2001). Since the aggregates have a stable chemical, physical and mechanical properties during the reaction process, it is generally agreed that the aggregates play the same role in PC concrete and AAC (Talha Junaid et al., 2015).

The ITZ between aggregate and paste matrix is normally considered as a key microstructural feature that significantly influences the macroscopic mechanical properties of concrete, because it acts a bridge transferring forces between aggregates and the binding matrix (paste) (Bentur et al., 2000; Akçaoğlu et al., 2005; Khedmati et al., 2018). It was reported that macroscopic mechanical properties of concrete are merely determined by the strength of paste matrix but strongly affected by the thickness and strength of ITZ (Kim and Abu Al-Rub, 2011; Yu et al., 2018; Zhang et al., 2018). The low ITZ strength would negatively affect the macroscopic strength of concrete, but this effect tends to become weak with the increase of ITZ strength (Yu et al., 2018). When the ITZ strength is over 0.5 times the strength of the surrounding matrix, this effect is almost disappeared. In addition, the ITZ strength would affect the fracture behaviour of concrete (Yu et al., 2018). When the ITZ strength is relatively low, the fracture process of concrete is dominated by the ITZ, in which the cracks would prone to occur and propagate in the ITZ, and finally coalesce through the surrounding matrix. When the ITZ strength is high enough to reach the strength of the surrounding matrix, the heterogeneous mechanical properties of ITZ and matrix determine the fracture process of concrete

together, in which the cracks would firstly generate and propagate in ITZ and matrix, leading to the macroscopic fractures.

In PC concrete, ITZ is normally considered as the weakest link with low strength and stiffness between aggregate and paste, due to its relatively high porosity comparing with the surrounding paste (Ollivier et al., 1995; Scrivener et al., 2004; Mondal et al., 2009). The elastic modulus of ITZ was found to be about 15% to 30% lower than that of paste matrix (Trtik and Bartos, 2000; Mondal et al., 2009). In return, the ITZ with low strength and stiffness is prone to cracking as a result of shrinkage or mechanical loading, which would consequently affect the overall mechanical properties of concrete (Akçaoğlu et al., 2005; Zhang et al., 2018). The micromechanical properties of ITZ are strongly related to the w/c ratio. Reducing the w/c ratio tends to decrease the porosity of ITZ, leading to a comparable microstructure to paste matrix (Elsharief et al., 2003) and would change the influence of ITZ on the overall elastic properties of concrete from negative into positive (Simeonov and Ahmad, 1995). Besides, the mechanical properties of ITZ are also affected by the size, shape and surface roughness of aggregates (Ulrik Nilsen and Monteiro, 1993; Akçaoğlu et al., 2004). The ITZ strength is decreased with the increase of aggregate size and the decrease of surface roughness of aggregate (Akçaoğlu et al., 2004).

However, the ITZ in AAC seems to play an entirely different role in governing the macroscopic properties of AAC (Lee and van Deventer, 2004; Sarker et al., 2013; Nicolas and Provis, 2015; Ji et al., 2017). The ITZ in AAF concrete has comparable mechanical properties to paste matrix, attributing to the dense microstructure formed in this region (Khedmati et al., 2018). This is mainly because of the formation of N-A-S-H gels instead of the CH crystals formed in PC concrete, which would help to produce a strong bond between aggregate and paste (Lee and van Deventer, 2004) and contribute to the improvement of mechanical properties of AAF concrete (Sarker et al., 2013). Additionally, AAS concrete activated by SS also exhibits superior interfacial properties, in which ITZ has low porosity and high strength, leading to high mechanical strength of AAS concrete (Brough and Atkinson, 2002; Bernal et al., 2011a; Ji et al., 2017). This can be attributed to the excess SiO_2 supplied by the activator, which would promote the formation of C-A-S-H gels with low Ca/Si ratio and refine the porosity in ITZ (Shi and Xie, 1998; Brough and Atkinson, 2002). Moreover, the ITZ in AAS concrete might have no negative effects on the long-term durability as it would not provide a preferred pathway for the penetration of aggressive species (Nicolas and Provis, 2015).

The micromechanical properties of ITZ in AAF and AAS concrete have been increasingly investigated, whereas the relevant studies on AAFS concrete are extremely

rare. Since the macroscopic mechanical properties of concrete are highly related to the microstructure and micromechanical properties of ITZ, as demonstrated for PC concrete (Wu et al., 2016; Scrivener et al., 2004), and AAF and AAS concrete (Lee and van Deventer, 2004; Nicolas and Provis, 2015), a good understanding of these microscopic properties would advance our insights into the effects of ITZ on the macroscopic performance of AAFS concrete. In addition, the homogenization of AAFS concrete is also a big challenge due to the uncertainty of ITZ, in which its strength and thickness might vary from one aggregate to another.

2.6.5 Summary

In this section, the existing investigations on the multiscale micromechanical properties of AAFS concrete are critically reviewed. Characterising the micromechanical properties at multiscale from nano-scale to micro-scale would enable us to build a link between chemistry and properties, bringing new insights into the development of mechanical properties of concrete. However, the relevant research in AAFS concrete is extremely rare, where the micromechanical properties of individual phases (unreacted particles and reaction products) and their contributions to the composites (paste matrix and ITZ) in AAFS concrete are still unknown to date. Therefore, it is crucial to make a systematic micromechanical analysis of AAFS concrete at multiple length scales from Level 0 (solid gel particle) to Level III (concrete).

2.7 Macroscopic mechanical properties of AAFS concrete

Macroscopic mechanical properties are important engineering properties of concrete, which mainly includes compressive strength, tensile strength, elastic modulus, fracture properties and dynamic mechanical properties. A critical review of the macroscopic mechanical properties of AAF concrete is given in this section.

2.7.1 Compressive strength

Compressive strength is one of the most important mechanical properties of concrete, which is commonly used as the index for its design. According to the BS EN 206:2013+A1:2016 (2016), the 28-d compressive strength of concrete needs to achieve at least 15 MPa for the engineering application of concrete without the risk of corrosion or attack. For the corrosion protection of reinforcement in concrete, the minimum compressive strength of concrete is decided based on different corrosion environments as follows: carbonation-induced corrosion (≥ 25 MPa), chloride-induced corrosion (≥ 37

MPa), freeze/thaw attack (≥ 37 MPa) and aggressive chemical environments (≥ 37 MPa). It should be noted that the minimum compressive strength mentioned here is based on the characteristic cube strength.

Based on these criteria, it has been demonstrated that the AAFS concrete can fulfil the requirement of engineering applications when the appropriate mixtures are chosen (Deb et al., 2014; Nath and Sarker, 2014). As discussed in Section 2.3.1, the compressive strength of AAFS concrete is mainly affected by the fly ash/slag ratio (slag content), AL/P ratio, SH molarity, SS modulus and SS/SH ratio. Accordingly, the relationships between compressive strength and these influencing factors are presented in Figure 2-12 based on the literature review (Lee and Lee, 2013; Nath and Sarker, 2014; Deb et al., 2014; Alanazi et al., 2019). As seen in Figure 2-12a, the AAFS mixtures with relatively low slag content (10% ~ 20%) and SH molarity (4 ~ 10 M) can achieve the compressive strength in the range of 20 to 30 MPa, while other parameters can be kept in a relatively wide range (SS/SH ratio from 0.5 to 2.0; AL/P ratio from 0.4 to 0.56; SS modulus from 2.0 to 2.9). As shown in Figure 2-12b, for achieving a higher compressive strength between 30 and 40 MPa, the SH molarity and the SS/SH ratio can be enhanced up to 14 MPa and 2.5, respectively. Moreover, the slag content is increased up to 25 % whereas the maximum AL/P ratio is decreased to 0.45 to obtain a higher compressive strength of 40 ~ 50 MPa (Figure 2-12c). Lastly, it can be seen from Figure 2-12d that the relatively high slag content (20 ~ 30 %) and SH molarity (10 ~ 14 M) are required to achieve the high compressive strength between 50 and 60 MPa. At the same time, the AL/P ratio should be limited under 0.4 for achieving such high compressive strength.

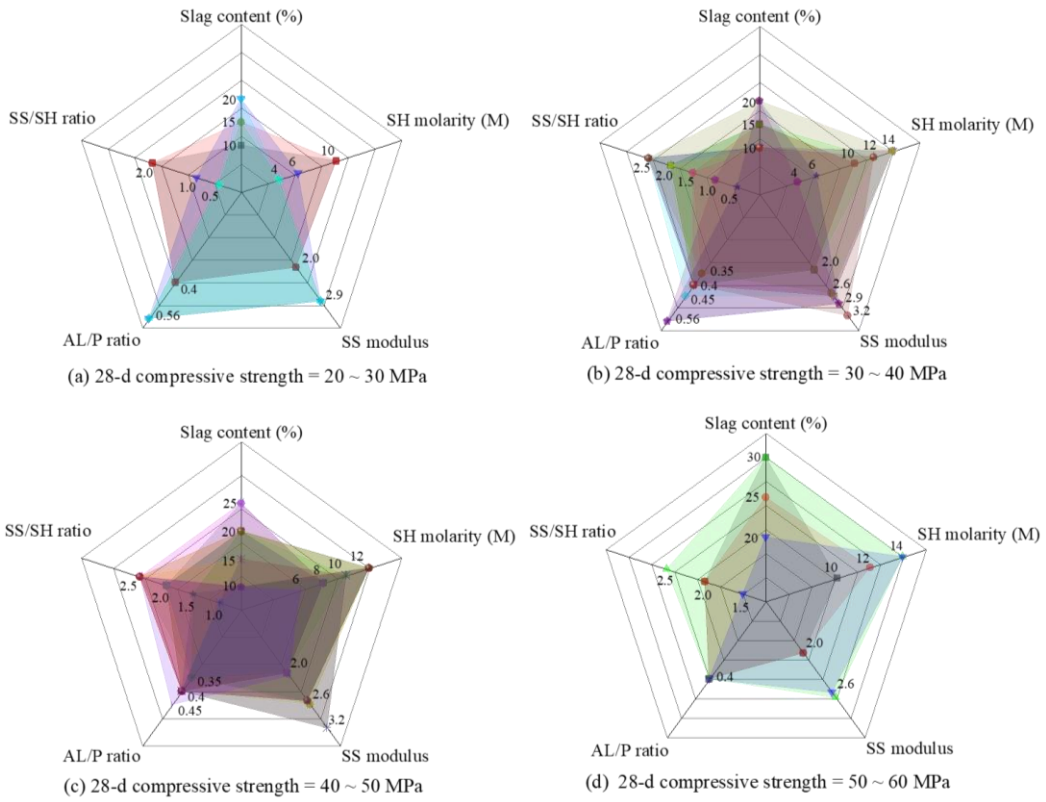

Figure 2-12 Radar diagrams showing the 28-d compressive strength of AAFS concrete against different parameters (Lee and Lee, 2013; Nath and Sarker, 2014; Deb et al., 2014; Alanazi et al., 2019)

The change of parameters would directly affect the development of compressive strength. The increase of compressive strength seems more sensitive to the change of slag content compared to other parameters, which implies that the slag content in the AAFS concrete might give a good estimate of the compressive strength of AAFS concrete. Thus, the slag content is generally adopted as the indicative parameter to determine the compressive strength in the mix design of AAFS concrete (Rafeet et al., 2017). Furthermore, since the compressive strength of concrete in the engineering application is commonly in the range of 30 ~ 50 MPa, the scope of parameters is previously selected based on the compressive strength within this range. Herein, the slag content is selected from 15% to 25% of precursor, while the AL/P ratio is set in the range of 0.35 to 0.4. The SS/SH ratio is set from 1.5 to 2.0 with different SH molarity (10 ~ 12 M) and SS modulus (2.0). However, it should be noted that the range of compressive strength in code cannot be directly used to compare with the actually measured strength. This is because the strength in code refers to the characteristic strength, which is difference comparing with the mean strength obtained in the actually measure strength.

2.7.2 Splitting tensile strength

Generally, the tensile strength of PC concrete or AAC is conveniently evaluated by the splitting tensile strength or estimated based on the compressive strength (Ding et al., 2016). The experimental results of AAFS concrete indicated that its splitting tensile strength is affected by fly ash/slag ratio and the type and content of AL (Deb et al., 2014). The splitting tensile strength of AAFS concrete is increased significantly with the increase of slag and the decrease of SS/SH ratio (Deb et al., 2014). The 28-d splitting tensile strength of AAFS concrete with 10% and 20% slag is approximately 25% and 45% respectively higher than that without slag, while that of AAFS concrete is increased from 3.09 MPa to 4.81 MPa with the decrease of SS/SH ratio from 2.5 to 1.5.

For the estimation of splitting tensile strength based on the compressive strength, ACI M318-08 (2008) and Eurocode 2 (2004) are commonly used for PC concrete, as described below.

$$f_{ct} = 0.56\sqrt{f_c'} \qquad (2-3)$$

$$f_{ct} = \left(\frac{1}{3}\right)(f_c)^{2/3} \quad for\ f_c < 50\ \text{MPa} \qquad (2-4)$$

where f_{ct} is the splitting tensile strength at 28 d (MPa), f_c' is the specified compressive strength at 28 d (MPa) and f_c is the average compressive strength at 28 d (MPa).

As shown in Figure 2-13, the measured splitting tensile strength of AAFS concrete is lower than that predicted by the ACI M318 and Eurocode 2 used for PC concrete. It indicates that the splitting tensile strength of AAFS concrete is lower than that of PC concrete, given the same compressive strength. Lee and Lee (2013) mentioned that the splitting tensile strength of AAFS concrete has a linear relationship with the square root of the compressive strength with a constant of 0.45 ($f_{ct} = 0.45\sqrt{f_c}$). Similarly, Sofi et al. (2007) found the linear relationship between splitting tensile strength and the square root of compressive with the constant of 0.48 ($f_{ct} = 0.48\sqrt{f_c}$), which was slightly higher than the fitting outcomes obtained by Lee and Lee (2013). The slight difference between these two fitting results can be attributed to the difference in chemistry and physical properties of raw materials used in these two tests.

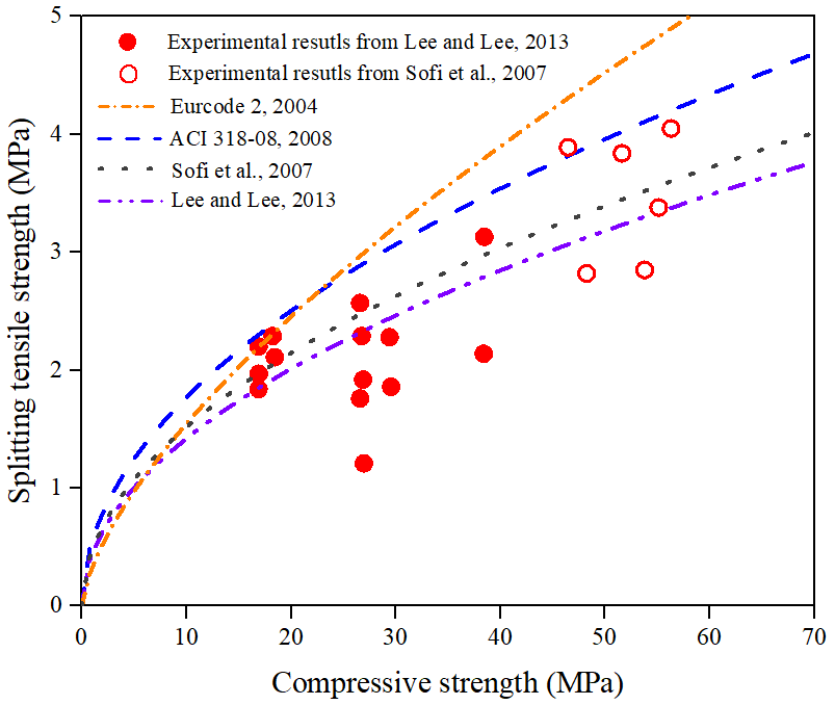

Figure 2-13 Comparison of experimental and predicted splitting tensile strength of AAFS concrete (Eurocode 2, 2004; Sofi et al., 2007; ACI M318-08, 2008; Lee and Lee, 2013)

2.7.3 Elastic modulus

The elastic modulus of concrete is generally determined by the type and content of coarse aggregate and the elastic modulus of paste matrix (Ding et al., 2016). The elastic modulus of AAFS concrete is highly dependent on the fly ash/slag ratio. As seen in Figure 2-14, the elastic modulus of AAFS concrete obtained by Sofi et al. (2007) is higher than that obtained by Lee and Lee (2013). This is mainly because that the fly ash/slag ratio in the former case (around 0.45) is much lower than that in the latter case (3 ~ 9), leading to the difference in the formation of reaction products. The main reaction products of AAFS mixtures with high slag content are the C-A-S-H gels with an elastic modulus of 12 ~ 47 GPa (Puertas et al., 2011; Thomas et al., 2018), which is higher than that of N-A-S-H gels (4.44 ~ 20 GPa) formed in the mixtures with a high content of fly ash (Němeček et al., 2011; Lee et al., 2016; Ma et al., 2017). However, the effects of other factors such as the type and content of AL on the elastic modulus of AAFS are still not fully understood.

In addition, it can be found from Figure 2-14 that the measured elastic modulus of AAFS concrete is lower than that predicted using the commonly used CEM-FIP model code (1995) and ACI M318-08 building code (2008). The elastic modulus (E_C) of PC concrete can be predicted from the compressive strength according to the CEB-FIP model code (Eq. (2-5)) and ACI M318-08 code (Eq. (2-6)), as follows:

$$E_C = 18275 \times (f_c/10)^{1/3} \quad (2-5)$$

$$E_C = 5055 \times \sqrt{f_c'} \quad (2-6)$$

Furthermore, the predicted elastic modulus of AAFS concrete is also presented by Lee and Lee (2013) ($E_C = 5300 \times (f_c)^{1/3}$), indicating that the elastic modulus of AAFS concrete is 20% ~ 40% lower than the predictions by the two codes. A similar trend was observed by Ding et al. (2018b) that the elastic modulus of AAFS concrete is overestimated for about 20% ~ 30% by CEB-FIP model. Nevertheless, it should be highlighted that a general relationship between elastic modulus and compressive strength of AAFS concrete is still unclear due to the limited available data and variability of mixture composition in this type of concrete.

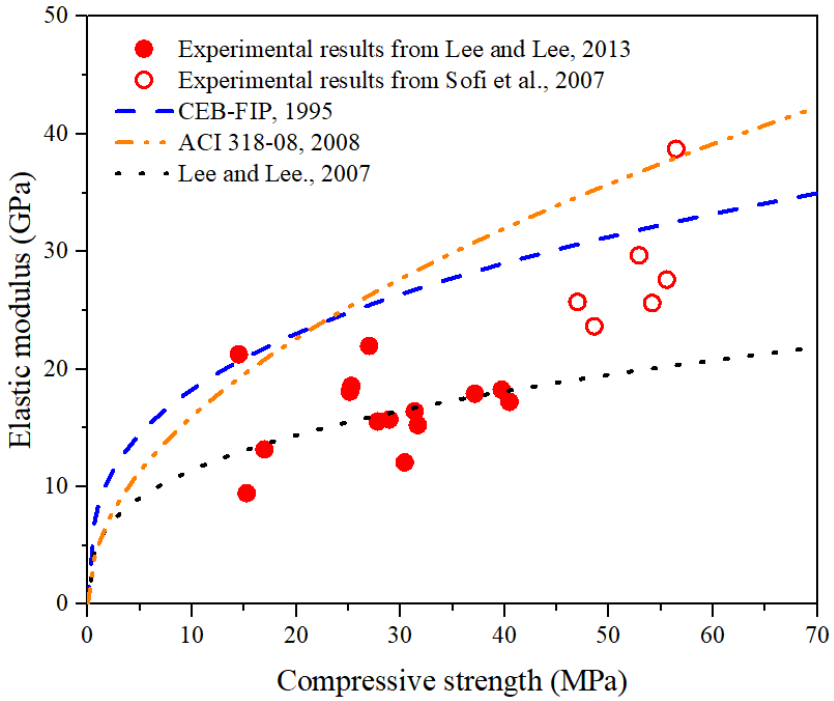

Figure 2-14 Comparison of experimental and predicted elastic modulus of AAFS concrete (CEB-FIP Model Code, 1995; Sofi et al., 2007; ACI M318-08, 2008; Lee and Lee, 2013)

2.7.4 Fracture properties

The fracture properties are the key index used to describe the cracking process of concrete and reflect its brittleness under tension (Ding et al., 2016), which are generally quantified through the load-displacement curve, fracture toughness and fracture energy. The fracture properties of AAFS concrete have been investigated using three-point bending tests of notched beam specimens, according to RILEM TC 50-FMC (RILEM TC 50-FMC, 1985; Nath and Sarker, 2016; Ding et al., 2018b). It was found that the fracture

properties of AAFS concrete are mainly affected by four factors including the fly ash/slag ratio, AL concentration (Na_2O by mass of precursor), AL/P ratio and modulus of AL (Nath and Sarker, 2016; Ding et al., 2018b). The fracture energy of AAFS concrete was improved with the addition of AL concentration and the increase of AL modulus and the slag replacement level, but decreased with the increase of AL/P ratio. The fracture energy was increased by 16.3% with the increase of AL concentration from 3% to 5%, while a 22.4% increase of fracture energy can be observed when the modulus of AL increased from 1.0 to 2.0. Similarly, the improvement of fracture energy was 14.1% and 26.4% with the increase of slag replacement proportion from 50% to 100% and the decrease of AL/P ratio from 0.5 to 0.4, respectively.

In addition, it was found that AAFS concrete achieves higher fracture energy as compared to PC concrete, given a similar compressive strength (Nath and Sarker, 2016). The deflection before failure of AAFS concrete is slightly larger than that of PC concrete, suggesting that AAFS concrete exhibits a higher ductility than PC concrete (Nath and Sarker, 2016). Furthermore, the measured fracture energy of AAFS concrete was compared with the that predicted using the CEB-FIP model and the Bazant and Becq-Giraduon model used for PC concrete (CEB-FIP Model Code, 1995; Bažant and Becq-Giraudon, 2002) presented in Eqs. (2-7) and (2-8), respectively. As shown in Figure 2-15, the measured fracture energy of AAFS concrete is underestimated by the CEB-FIP model, while it is close to the predictions by the Bazant and Becq-Giraduon model.

$$G_F = (0.0469 \times D_{max}^2 - 0.5D_{max} + 26) \times (\frac{f_c}{10})^{0.7} \quad (2-7)$$

$$G_F = 2.5\alpha_0(\frac{f_c}{0.051})^{0.46}(1 + \frac{D_{max}}{11.27})^{0.22}(\frac{w}{c})^{-0.30} \quad (2-8)$$

where G_F is the fracture energy (N/m), f_c is the compressive strength at 28 d (MPa), D_{max} is the maximum size of aggregate (mm), α_0 is the aggregate shape factor (α_0 = 1 for rounded aggregates, α_0 = 1.44 for angular aggregates), and w/c is the water/cement ratio. Herein, D_{max} = 10 mm and α_0 = 1.44 are used in literature.

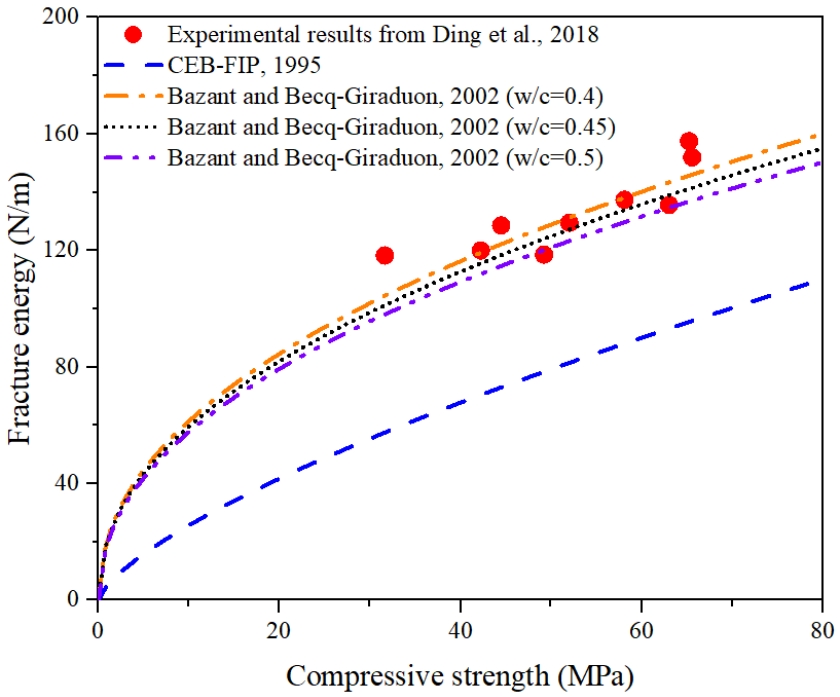

Figure 2-15 Comparison of measured and predicted fracture energy of AAFS concrete (CEB-FIP Model Code, 1995; Bažant and Becq-Giraudon, 2002; Ding et al., 2018b)

2.7.5 Dynamic mechanical properties

The dynamic mechanical properties are used to describe the response of concrete to dynamic loading, which is a prerequisite for the design of concrete structure considering the potential threat of tornadoes, earthquakes or ocean waves (Chen et al., 2013). The dynamic mechanical properties are mainly related to the strain rate effect under the high-amplitude-short-duration load, which can be evaluated using the dynamic increase factor (DIF) (Yon et al., 1992; Li and Huang, 1998; Beppu et al., 2008). The DIF is defined as the ratio of dynamic strength to static strength, reflecting the increase of strength under impact loading.

The dynamic mechanical properties of AAFS concrete have been investigated by Luo et al. (2013) through split Hopkinson pressure bar (SHPB) test that are commonly used to measure the dynamic behaviour of concrete at high strain rates (Wu et al., 2017; Chen et al., 2019). It was demonstrated that AAFS concrete is a strain-rate sensitive material, where DIF increases linearly with the logarithm of the average strain rate, and the threshold of strain rate sensitivity is 28.89 s^{-1}. Under the low strain rate loading, the propagation of cracks mainly accumulates along the ITZ between aggregates and matrix, while the cracks occur in both aggregate and ITZ when the loading is kept at a high strain rate. These phenomena are consistent with that observed for PC concrete (Chen et al., 2013), while the AAFS concrete has a higher strain-rate sensitivity than PC concrete. This

can be attributed to the reaction products formed in AAFS concrete, which possess a unique polycondensed 3D oxide network structure, leading to a tight internal structure of concrete and help to efficiently transfer the stress from the loading part to the inner position of specimen (Luo et al., 2013).

In addition, it was reported that the dynamic mechanical properties of AAFS concrete are strongly affected by the types of AL (Luo et al., 2014). The AAFS mixtures activated by SS and SH solution can achieve better deformation properties under dynamic compression than that activated by SH and Na_2CO_3 solution. Thus, it was suggested that the SS and SH solution should be considered as a priority for AAFS concrete when earthquake is considered in the structural design (Luo et al., 2014). The addition of slag would also increase the dynamic compressive strength of AAFS concrete under a specific strain rate (see Figure 2-16a) (Tang et al., 2020). Taking the strain rate of 100 s^{-1} as an example, the dynamic compressive strength of AAFS concrete is increased significantly from 17 MPa to 94 MPa with the increase of slag replacement ratio from 0% to 30%. This can be ascribed to the condensation of microstructure with the addition of slag, leading to high compatibility between coarse aggregate and the surrounding mortar (Tang et al., 2020). It can be also observed from Figure 2-16b that the AAFS concrete with a higher content of slag has higher DIF at a relatively low strain rate, while a more noticeable improvement of DIF can be found in the AAFS concrete with lower content of slag at a high strain rate (Tang et al., 2020). However, the mechanism about the effect of slag content on the strain rate sensitivity of AAFS concrete is still unknown, and thus further research is required.

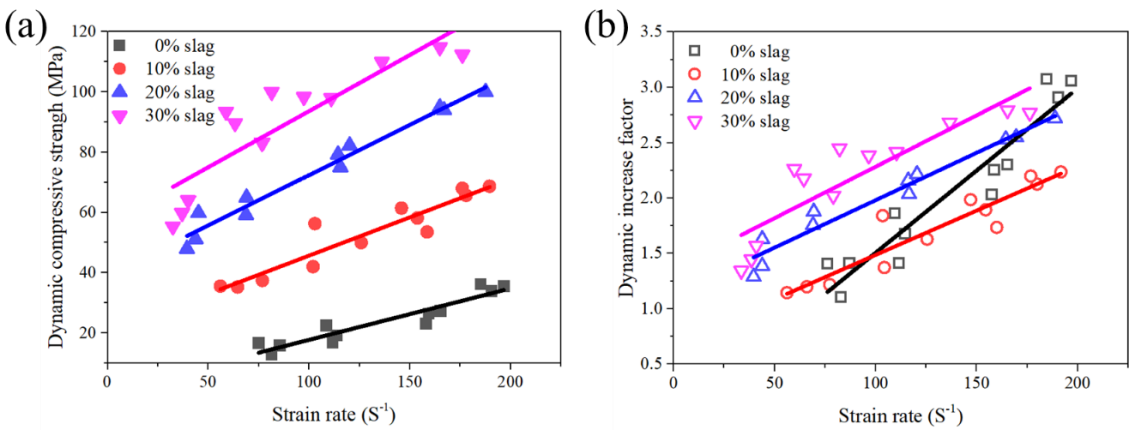

Figure 2-16 Relationship between dynamic compressive strength and strain rate (a) and relationship between dynamic increase factor and strain rate (b) of AAFS concrete (Tang et al., 2020)

2.7.6 Summary

In this section, the macroscopic mechanical properties of AAFS concrete have been critically reviewed. It has been demonstrated that the AAFS concrete with appropriate mixtures can achieve desired mechanical properties comparable to PC concrete. However, the effects of some factors such as the type and content of activators on the mechanical properties are still not fully understood, especially for the elastic modulus and dynamic mechanical properties. Therefore, it is of importance to systematically investigate the effects of different factors on the mechanical properties of AAFS concrete.

2.8 Concluding remarks

In this chapter, the multiscale microstructure and mechanical properties of AAFS concrete are critically reviewed according to different length scales from Level 0 (solid gel particle) to Level III (mortar and concrete). Up to now, the microstructure and mechanical properties of AAFS concrete have been extensively studied. Nevertheless, the chemical reaction, microstructure evolution and performance development of AAFS concrete have not been fully understood, due to a lack of systematic characterisation of microstructure and mechanical properties at multiscale, from nano- to macro-scale. The main challenges and limitations are summarised as follows:

(i) The existing studies of the microstructure evolution of fly ash and slag particles in AAFS paste mainly depend on the destructive testing methods, such as SEM and EDS, which cannot reveal their actual dissolution and reaction process, leaving an open question about the reaction mechanism of these particles in AAFS paste. To this end, XCT provides a potential opportunity to non-destructively characterise the microstructure evolution of these particles in AAFS paste, but the relevant research is still lacking to date.

(ii) The existing knowledge about the ITZ in AAFS concrete is limited to the simple analysis of local morphology, which cannot provide needed information to understand the mechanism of ITZ evolution.

(iii) The characterisation of multiscale micromechanical properties of AAFS concrete would enable us to build a link between chemistry, microstructure, and mechanical properties, bringing an in-depth insight into the development of mechanical properties of this new type of concrete. However, the existing research of micromechanical properties of AAFS concrete is limited to the analysis of carbonation effects on its elastic modulus. Up to now, a systematic understanding of the micromechanical properties of individual phases within AAFS concrete and the corresponding relationship with the macroscopic mechanical properties is still lacking.

(iv) The multiscale microstructure-mechanical properties relationship in AAFS concrete has not been addressed, which would cause some issues regarding its engineering application in the future, as the macroscopic performance cannot be accurately evaluated and predicted without such information.

Chapter 3 Engineering properties of AAFS concrete

3.1 Introduction

Workability, setting time and mechanical properties are the basic engineering properties of AAFS concrete, which are commonly utilised as the key indexes for its mix design and engineering application in practice. These engineering properties of AAFS concrete are affected by several factors such as fly ash/slag ratio, and type and content of activator. According to the literature review in Chapter 2, the influences of these factors on the engineering properties of AAFS concrete are still not fully understood. Hence, the main purpose of this chapter is to present a systematic experimental study and provide a thorough understanding of workability, setting time and mechanical properties (e.g. compressive strength, splitting tensile strength, elastic modulus and fracture properties) of AAFS concrete, considering the effects of different factors including fly ash/slag ratio, AL/P ratio, SH molarity and SS/SH ratio. Based on the experimental results, the optimal mixtures of AAFS concrete are obtained according to the standard criteria for the engineering applications.

As shown in Figure 3-1, the basic engineering properties of AAFS concrete were tested in this research in accordance with the relevant standards. The flow value of paste and slump value of AAFS concrete were measured to investigate its workability. The setting time of AAFS paste was evaluated based on Vicat setting time test. A series of tests were conducted to estimate mechanical properties of AAFS concrete, including compressive strength, splitting tensile strength, elastic modulus and fracture properties.

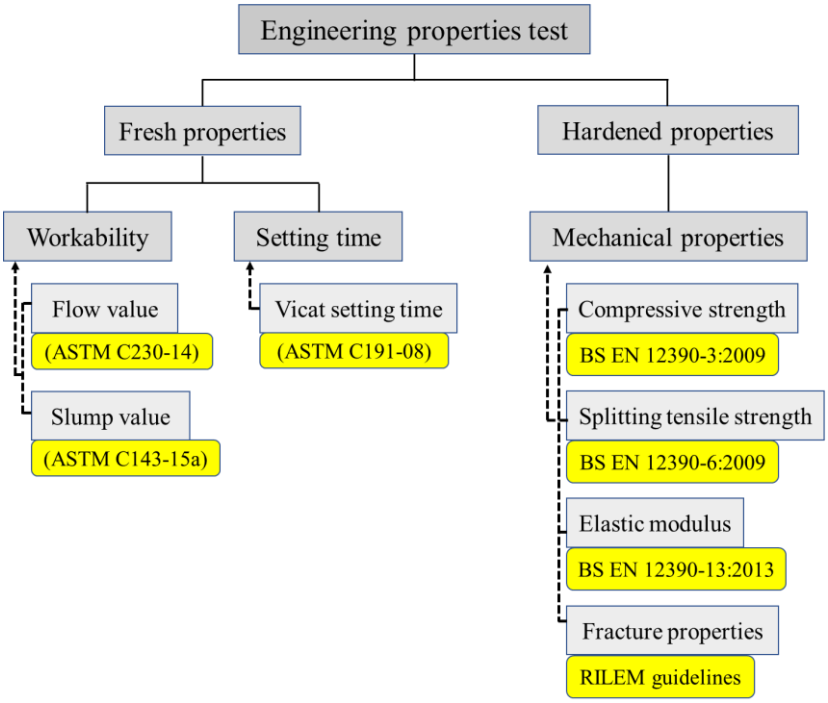

Figure 3-1 Engineering properties test of AAFS concrete

3.2 Experimental program

3.2.1 Materials

The low calcium fly ash (Huadian Industrial Co. Ltd, China) and ground granulated blast-furnace slag (Wuxin New Building Materials Co. Ltd, China) were used as precursors in the study. The apparent morphologies of fly ash and slag are presented in Figure 3-2. Fly ash is represented as a spherical shape with smooth surface, while slag has an angular shape with a rough surface. The chemical compositions of fly ash and slag are presented in Table 3-1, where the $[SiO_2]/[Al_2O_3]$ ratio of fly ash and the $[CaO]/[SiO_2]$ ratio of slag are 1.85 and 1.25, respectively. Figure 3-3 shows the particle size distribution of fly ash and slag, where 95% fly ash and 92% slag are smaller than 45 μm and 40 μm, respectively. The particle size distributions of fly ash and slag used here close to that of Type I PC as presented by previous researcher (Sua-iam et al., 2016). The surface areas of fly ash and slag are 1.46 m^2/g and 0.31 m^2/g, respectively. These characteristics can meet the performance criteria for the usage of fly ash and slag in AAFS concrete (Mostafa et al., 2001; Li et al., 2002; Fernández-Jiménez and Palomo, 2003; Wang et al., 2005).

Table 3-1 Chemical composition (wt%) of fly ash and slag

Oxide	SiO_2	Al_2O_3	Fe_2O_3	CaO	K_2O	MgO	TiO_2	Na_2O	SO_3	P_2O_5	LOI
Fly ash	55.76	30.22	3.56	2.33	0.91	0.46	1.72	0.40	0.79	0.27	1.96
Slag	33.22	13.49	0.40	41.57	0.64	7.04	0.50	0.34	2.14	-	1.9

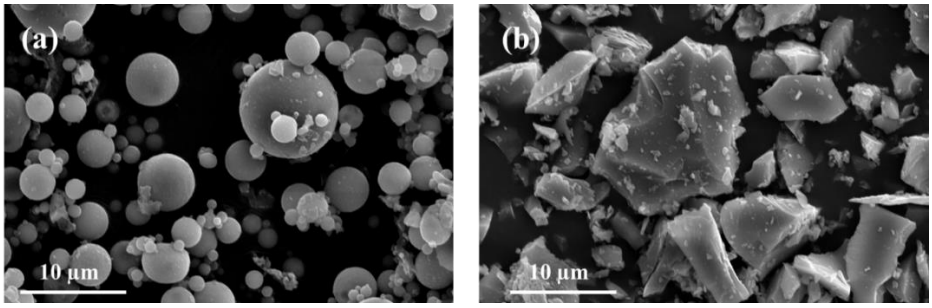

Figure 3-2 SEM image of (a) fly ash and (b) slag

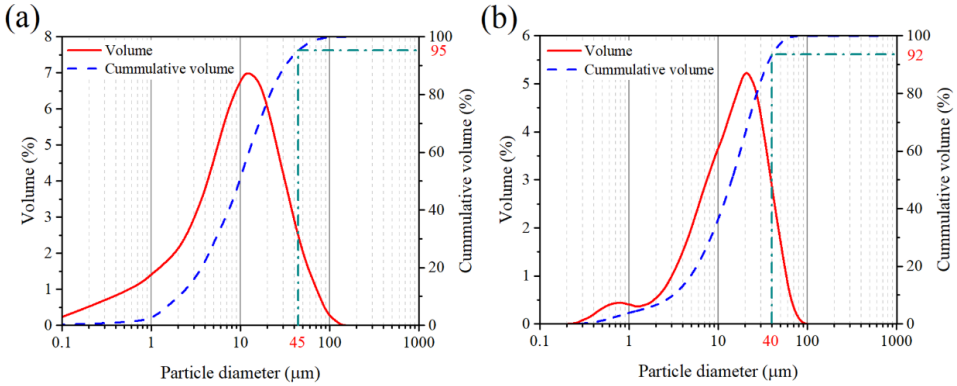

Figure 3-3 Particle size distribution of (a) fly ash and (b) slag

The commonly used alkaline solutions including sodium silicate (SS) solution (Hubei Xinrunde Chemical Co. Ltd, China) and sodium hydroxide (SH) solution were used as alkaline activators (AL). The SS with modulus (molar ratio of $[SiO_2]/[Na_2O]$) of 2.0 is composed of 30.71 wt% SiO_2, 15.36 wt% Na_2O and 53.93 wt% H_2O, which has been commonly used in AAFS concrete (Escalante-García et al., 2006; Pacheco-Torgal et al., 2014). The SH solution was prepared by mixing SH solid powder (> 98% purity) with tap water. The SH solid powder was provided by the company of Aladdin Biochemical Technology, China. Taking SH solution with 10 M as an example, 400 g SH solid powder was dissolved into tap water to prepare 1 litre SH solution. It is worth mentioning that the SH solution should be prepared 24 h before specimen preparation to ensure that it is cooled down to room temperature. To adjust the workability of AAFS paste, the modified polycarboxylate-based superplasticizer (SP) (Sika®ViscoFlow®2000, Sika, UK) was applied as the admixture, which can help to effectively increase the workability of AAFS paste by around 30% with the addition of 1 wt% SP of precursor (Jang et al., 2014). In addition, the low amount of SP (≤ 1 wt%) has no negative effect on the compressive strength of AAFS concrete (Jang et al., 2014; Keulen et al., 2018). The chemical and physical properties of SP are presented in Table 3-2.

Table 3-2 Physical and chemical properties of superplasticizer

Specific gravity (25°C)	pH (25°C)	Content of chloride ion (%)	Content of alkaline (%)
1.08	4-5	≤ 0.1	≤ 0.4

The standard river sands were used as fine aggregates, while the limestone aggregates were chosen as coarse aggregates. Figure 3-4 shows the particle size distributions of fine and coarse aggregates. The specific gravity of each ingredient in AAFS concrete is listed in Table 3-3.

Table 3-3 Specific gravity of different ingredients in AAFS concrete

	Fly ash	Slag	SS	SH	SP	Fine aggregate	Coarse aggregate
Specific gravity	2.25	2.90	1.21	1.38	1.08	2.57	2.62

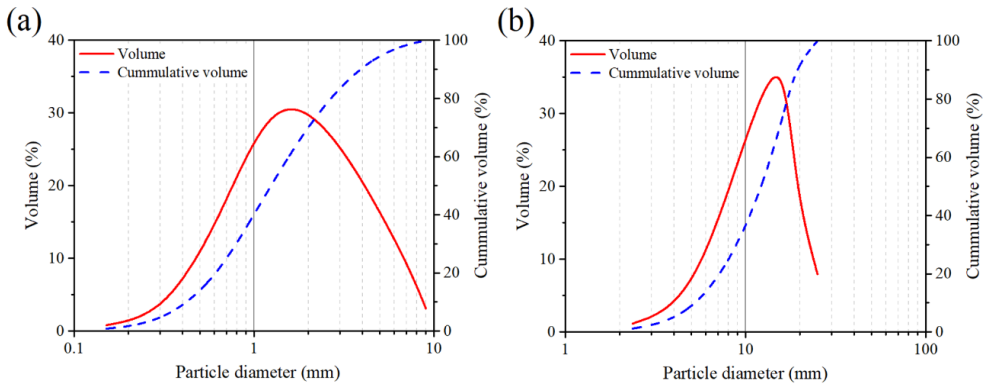

Figure 3-4 Particle size distribution of (a) fine aggregate and (b) coarse aggregate

3.2.2 Mix proportions

AAFS concretes with different fly ash/slag ratio, AL/P ratio, SH molarity and SS/SH ratio were designed in this research. The scope of mixture proportions was selected according to the literature review (Puertas et al., 2000; Lee and Lee, 2013; Nath and Sarker, 2014; Deb et al., 2014; Jang et al., 2014). The mixture proportions of AAFS concrete are listed in Table 3-4 and labelled with specific codes. The labels 'A', 'B', 'C', and 'D' represents different specimen series. In series A, mixture 1 (A00) to mixture 6 (A30) were designed with slag as 0%, 10%, 15%, 20%, 25% and 30% of precursor by weight, respectively. The AL/P ratio in these mixtures was constant at 0.45 with a molarity of SH and SS/SH ratio of 10 M and 2.0, respectively. The slag replacement ratio for fly ash was kept as 25% for series B to series D. In series B including mixture 7 (B0.40) and mixture 8 (B0.50), the AL/P ratio was changed to 0.4 and 0.5, while the molarity of SH and SS/SH ratio were kept as 10 M and 2.0, respectively. In series C including mixture 9 (C8) and mixture 10 (C12), the molarity of SH was changed to 8 M and 12 M, while the AL/P ratio and SS/SH ratio were kept as 0.45 and 2.0, respectively. In series D, the SS/SH ratio was varied as 1.5 and 2.5 in mixture 11 (D15) and mixture 12 (D25). The SP content was kept constant at 1% of precursor by weight for all mixtures.

Here, the effect of slag content on the engineering properties of AAFS concrete was studied using series A with different slag content from 0% to 30% of precursor by weight. The effect of AL/P ratio was investigated using the control mixture A25 (B0.45) and series B, with various AL/P ratio from 0.4 to 0.5. A25 (C10) and series C were designed to investigate the effect of SH molarity, with different molarity from 8 M to 12 M. Furthermore, A25 (D2.0) and series D were conducted to evaluate the effect of SS/SH ratio, with SS/SH ratio changing from 1.5 to 2.5. Since two types of AL were used in this research, the interaction between SS and SH should also be considered, which would directly change the alkali modulus of total AL from about 1.0 to 2.0.

Regarding the calculation of aggregates, the total volume of aggregates was the residual volume except for the volume of binding materials, which can be calculated based on the mass of binding materials and their specific density (see Table 3-3). Here, the fine and coarse aggregates were set as 35% and 65% by the volume of total aggregates, respectively, to achieve an adequate consolidation of concrete (Kosmatka et al., 2002). The mass of fine and coarse aggregates was then obtained using their specific density. The mixture of AAFS concrete was determined accordingly, as shown in Table 3-4.

Table 3-4 Mix proportions and quantities of AAFS concrete

Mix no.		Labels	Mixture proportions						Concrete mixture quantity (kg/m^3)						
			Fly ash/ slag	AL/P ratio	SH molarity (M)	SS/SH ratio	SP/P ratio	Alkaline modulus of AL	Fly ash	slag	SS	SH	SP	Fine aggregate	Coarse aggregate
A	1	A00	100/0	0.45	10	2	0.01	1.13	400	0	120	60	4	613	1161
	2	A10	90/10	0.45	10	2	0.01	1.13	360	40	120	60	4	617	1168
	3	A15	85/15	0.45	10	2	0.01	1.13	340	60	120	60	4	619	1172
	4	A20	80/20	0.45	10	2	0.01	1.13	320	80	120	60	4	621	1175
	5	A25 (B0.45/C10/D2.0)	75/25	0.45	10	2	0.01	1.13	300	100	120	60	4	622	1178
	6	A30	70/30	0.45	10	2	0.01	1.13	280	120	120	60	4	624	1182
B	7	B0.40	75/25	0.40	10	2	0.01	1.13	300	100	107	53	4	636	1204
	8	B0.50	75/25	0.50	10	2	0.01	1.13	300	100	133	67	4	609	1152
C	9	C8	75/25	0.45	8	2	0.01	1.25	300	100	120	60	4	622	1178
	10	C12	75/25	0.45	12	2	0.01	1.04	300	100	120	60	4	622	1178
D	11	D1.5	75/25	0.45	10	1.5	0.01	0.99	300	100	108	72	4	621	1176
	12	D2.5	75/25	0.45	10	2.5	0.01	1.9	300	100	129	51	4	623	1180

Note: AL (alkaline activator); P (precursor); SH (sodium hydroxide); SS (sodium silicate); SP (superplasticiser)

3.2.3 Sample preparation

The mixing process of AAFS concrete consists of two steps. Fly ash, slag and aggregates (fine aggregates and coarse aggregates) were firstly dry-mixed for 3 min to ensure homogeneity of the mixture. Then, SS, SH and SP were added separately into the solid mixture and mixed for another 3 min. After that, the fresh concrete is immediately cast into three different moulds (see Table 3-5). The cube specimens with a size of 100 × 100 × 100 mm were prepared for the compressive strength and splitting tensile strength tests, while the prism specimens with a size of 100 × 100 × 300 mm were used for the elastic modulus test. The prism specimens (100 × 100 × 400 mm) with a notch (100 × 40 × 3 mm) in the middle were applied for the three-point bending test, to obtain the fracture properties. Three specimens were prepared for each mixture at each testing age. The moulds were put on the vibrating table for 2 min to remove the air bubbles and then sealed by the plastic sheet for first 24-h curing in room temperature (20 ± 2 °C). Afterwards, the samples were demoulded and placed in the curing room (20 ± 2 °C, 95% RH) until the age of testing (see Figure 3-5). The curing ages of different samples can be found in Table 3-5.

Table 3-5 Specimen preparations for mechanical property tests

Sample	Shape	Size	Test performed	Curing age (d)
Cube		100×100×100 mm	Compressive strength test Splitting tensile strength test	1, 3, 7, 28, 56 7, 28
Prism	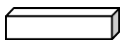	100×100×300 mm	Elastic modulus test	7, 28
Prism with notch	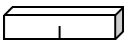	100×100×400 mm (Notch in the middle-(100×40×3 mm))	Fracture properties test	28

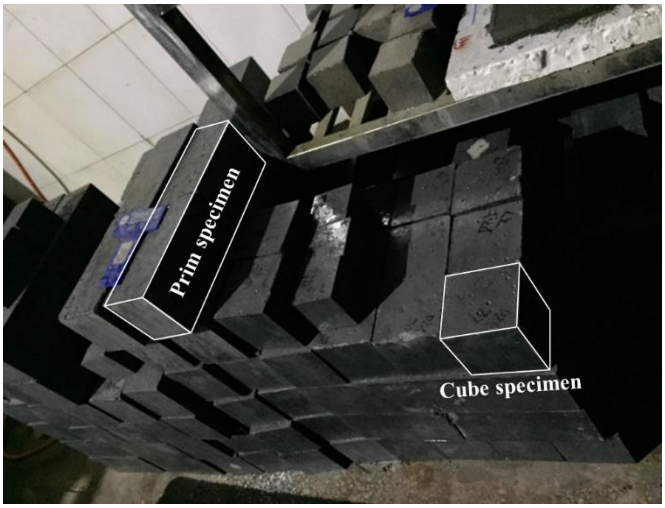

Figure 3-5 AAFS concrete specimens in the curing room

3.2.4 Test methods

As shown in Figure 3-1, the workability of AAFS paste was investigated using flow table test according to ASTM C230-14 (2014). The diameters of the paste spread in two directions at right angles were measured to calculate the flow value. Slump test as described in ASTM C143-15a (2015) was conducted to determine the workability of AAFS concrete. The vertical difference between the top of the mould and the displaced original centre of the top surface of the specimen was measured as the slump value.

The initial and final setting time of AAFS pastes was determined by the Vicat setting test according to ASTM C191-08 (2008). Periodic penetration tests were performed by allowing a 1-mm Vicat needle to settle into the fresh paste. The Vicat initial setting time was the time elapsed between the initial contact of raw materials and activator and the time when penetration was measured to be 25 mm. The Vicat final setting time was the time elapsed between initial contact of raw materials and activator and the time when the needle did not leave a complete circular impression in the paste surface.

According to BS EN 12390-3:2009 (2009), a universal testing machine was used to measure the compressive strength of AAFS concrete at 1, 3, 7, 28 and 56 d, where the constant rate of loading was set as 0.6 MPa/s. The splitting tensile strength was tested at 7 and 28 d according to BS EN 12390-6:2009 (2009), with a loading rate of 1.4 MPa/min. The elastic modulus was tested according to BS EN 12390-13:2013 (2013), in which the loading and unloading rate was set as 0.6 MPa/s in each loading cycle and the linear variable differential transformers were used to measure the vertical deformation of sample. The three-point bending test was conducted to evaluate the fracture properties of concrete specimens according to the RILEM guidelines (Guinea et al., 1992; Planas et al., 1992; Elices et al., 1992). The loading rate was set as 0.01 mm/s to induce a vertical mid-section deflection of concrete specimen. The load and vertical deflection data were recorded by an automatic data acquisition system with the accuracy of load and deflection data of 0.01 kN and 0.01 mm, respectively.

3.3 Results and discussion

3.3.1 Workability

Generally, the workability of AAC is lower than that of PC concrete because the presence of silicate in AAC would bring a sticky characteristic. Nevertheless, AAC can compact well on a vibrating table even for relatively low slump value. Therefore, the workability of AAC is classified based on the condition of compaction as shown below (Talha Junaid et al., 2015). When AAC achieves a slump value of 90 mm and over, it is regarded as a

highly workable concrete. AAC with a slump value in the range of 89 and 50 mm is classified as medium workability, while AAC with a slump value below 50 mm is considered as low workability due to the significant vibration of compaction (Talha Junaid et al., 2015). Thus, in this study, this criterion was applied to identify the optimal mixture of AAFS concrete in terms of workability.

Figure 3-6 shows the flow value of AAFS pastes and slump value of AAFS concrete, in which four series of mixtures were designed to study the effects of differencing factors. Series A was used to investigate the effect of fly ash/slag ratio, i.e. the replacement ratio of slag in precursor. A25 was chosen as the control mixture for investigating the effect of AL/P ratio (see series B), SH molarity (see series C) and SS/SH ratio (see series D), where A25 can be equivalent to B0.45, C10 and D2.0, respectively.

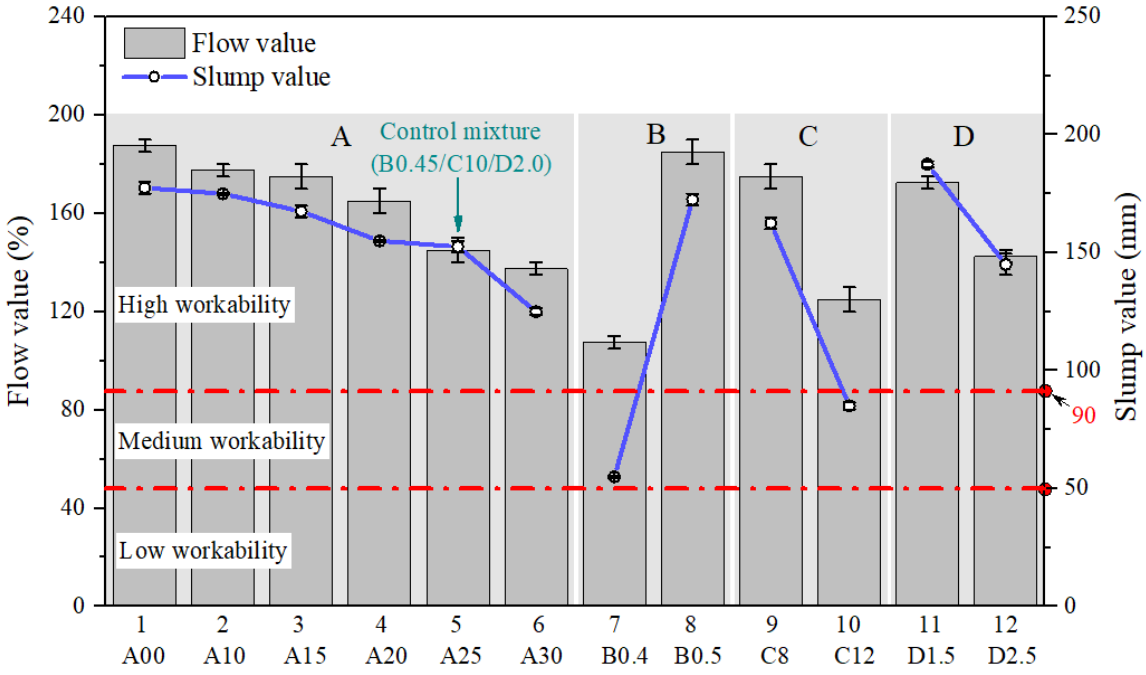

Figure 3-6 Flow value and slump value of AAFS paste and concrete

As shown in series A, the flow value of AAFS paste and the slump value of AAFS concrete are influenced by the replacement level of slag. The flow and slump values decrease with the increase of slag content in the mixture, which is consistent with previous research (Nath and Sarker, 2014; Deb et al., 2014). This is mainly because of the accelerated reaction of calcium-rich slag particles with angular shape compared to fly ash particles with spherical shape (Deb et al., 2014). More specifically, the slump values of A10, A15, A20, A25 and A30 decrease 1.41%, 5.63%, 12.68%, 14.08% and 29.58% respectively in comparison with the mixture without slag (A00). The effect of slag at a

30% replacement level appears to be more pronounced on the workability of AAFS concrete.

In series B, the AAFS mixture with AL/P ratio of 0.4 (B0.4) presents relatively low flow value and slump value as compared to mixtures with AL/P ratio of 0.45 (B0.45) and 0.5 (B0.5). The slump value of AAFS mixture is increased from 55 mm to 172 mm, when the AL/P ratio is increased from 0.4 to 0.5. The slump values of B0.45 and B0.5 are increased by 177.27% and 213.64% respectively as compared to B0.4. It indicates that the AL content plays a dominant role in the workability of AAFS concrete, which is consistent with other research (Nath and Sarker, 2014; Deb et al., 2014).

Considering the effect of SH molarity (see series C), the increase of SH molarity would decrease the workability of AAFS mixtures. The slump value of mixture is decreased from 162.5 mm to 152.5 mm and 85 mm, when the SH molarity is increased from 8 M (C8) to 10M (C10) and 12M (C12), respectively. This is mainly because the increase of SH molarity would improve the viscosity of the alkaline solution (Memon et al., 2013).

With respect to the effect of SS/SH ratio (see series D), the workability of AAFS decreases with the increase of SS/SH ratio, attributing to the high viscous of SS. When the SS/SH ratio is increased from 1.5 to 2.0, the flow value and slump value of D1.5 are decreased from 172.5% to 145%, and from 178.5 mm to 152.5 mm, respectively. However, the difference become less noticeable when the SS/SH is increased from 2.0 to 2.5 (see D2.0 and D2.5), where the flow value is decreased from 145% to 142.5% and the slump value is declined from 152.5 mm to 145 mm.

According to the classification of workability in AAC, the mixtures are divided into three different categories, i.e. high, medium and low workability (see Figure 3-6). For series A, all AAFS mixtures are classified as highly workable concrete as the slump values of these mixtures are higher than 90 mm. For series B, B0.5 is defined as highly workable concrete, while B0.4 is classified as medium workable concrete because its slump value is between 50 and 90 mm. In series C, C8 is classified as highly workable concrete, whereas C12 belongs to the medium workable concrete. The AAFS mixtures in series D are considered as highly workable concrete. In a conclusion, the AAFS concrete mixtures with slag replacement level from 0% to 30%, AL/P ratio in the range of 0.45 ~ 0.50, 8 ~ 10 M of SH, and SS/SH ratio of 1.5 ~ 2.5 can fulfil the requirement of workability.

3.3.2 Setting time

The requirement of setting time in the application of concrete generally depends on the strength classes. According to BS EN 197-1:2011 (2011), for example, it is mentioned that the initial setting time of PC concrete with the strength class of 42.5 should be longer than 60 min. Since the PC concrete with strength class of 42.5 is commonly used in civil engineering, this criterion is used as a reference to verify the feasibility of AAFS in terms of setting time. However, it should be noted that the criterion of setting time is not a single value to judge whether the AAFS concrete can fulfil the requirement of engineering application or not. It should be flexibly adjusted according to different requirements of engineering application of concrete structure. The setting time of AAFS paste is plotted in Figure 3-7.

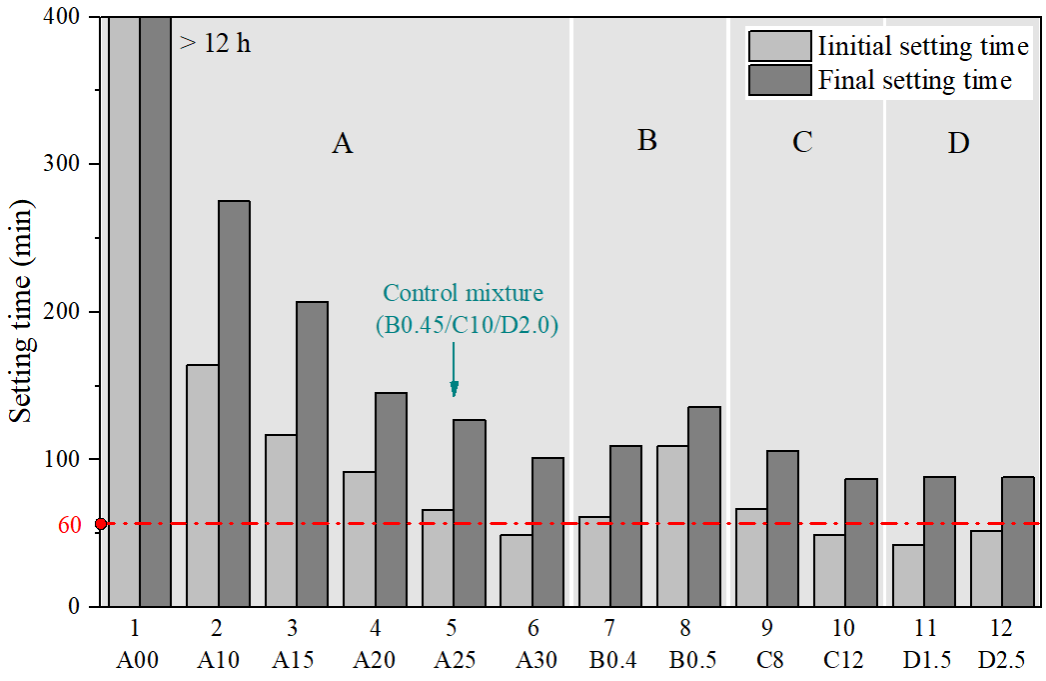

Figure 3-7 Setting time of AAFS paste

As shown in series A, the AAFS paste without slag (A0) takes a significantly long time (> 12h) to set due to the low chemical reactivity of fly ash at ambient curing condition (Nath and Sarker, 2014). When slag is added in the mixture, the setting time of AAFS paste is decreased significantly. With the addition of 10% slag (A10), the initial and final setting time of AAFS paste are decreased to 164 min and 275 min, respectively. The lowest setting time is obtained in the mixture with 30% slag (A30), in which the initial and final setting time are decreased to 49 min and 101 min, respectively. Additionally, the difference between the initial and final setting time is also reduced with the increase of slag content, which agrees well with other research (Nath and Sarker, 2014;

Kumar et al., 2010). These results indicate that the addition of slag would accelerate the chemical reaction of AAFS paste and reduce its setting time. This attributes to the soluble calcium from slag, which would enhance the dissolution of precursors and promote the formation of binding products (Temuujin et al., 2009a; Puligilla and Mondal, 2013).

In series B, when the AL/P ratio is increased from 0.4 (B0.4) to 0.45 (B0.45), the initial setting time is improved from 61 min to 66 min and the final setting time is increased from 109 min to 127 min. The mixture with the highest AL/P ratio of 0.5 (B0.5) has the longest setting time, with an initial setting time of 109 min and final setting time of 136 min. It indicates that the setting time of AAFS pastes increases with the increase of AL/P ratio. According to previous research, the low AL/P ratio has a low consistency of AAFS, which would lead to the accelerated reaction of raw materials and consequently the decrease of setting time (Rafeet et al., 2017).

As shown in series C, the effect of SH molarity on the setting time of AAFS paste seems not straightforward. The initial setting time of C10 (66 min) and C8 (67 min) is almost the same, while the final setting time of C10 (127 min) is higher than that of C8 (106 min). However, when the SH molarity increases to 12 M, the initial and final setting time decrease to 49 min and 87 min, respectively. Generally, with the increase of SH molarity, the setting time would be decreased if SH is solely used as alkaline activator because it would increase the hydroxide ion centration and accelerate the dissolution of raw materials (Somna et al., 2011). Nevertheless, when the activator is mixed by SH and SS, the increase of SH molarity would also affect the alkali modulus of AL (molar ratio of SiO_2/Na_2O in solution). In this study, the modulus of alkali solution was decreased from 1.25 (C8) to 1.13 (C10) and 1.04 (C12) when the SH molarity is increased from 8 M to 10 M and 12 M, respectively. A higher modulus of solution would accelerate the alkaline activation process and reduce the setting time (Siyal et al., 2016). Thus, a higher AL modulus of C8 (1.25) might be the reason for its relatively low final setting time in comparison with C10 (1.13).

Similar to the effect of SH molarity, the effect of SS/SH ratio on the setting time of AAFS paste is also not straightforward. When the SS/SH ratio is increased from 1.5 (D1.5) to 2.0 (D2.0), the initial and final setting time is increased from 42 min to 66 min and from 88 min to 127 min, respectively. Nevertheless, with the further increase of SS/SH ratio from 2.0 (D2.0) to 2.5 (D2.5), the initial and final setting time is decreased to 52 min and 88 min, respectively. The effect of SS/SH ratio on setting time can be attributed to the interaction between SS and SH (Lee and Lee, 2013). Both the dissolute silica from SS and hydroxide ion from SH would accelerate the chemical reaction of precursors and

reduce the setting time (Siyal et al., 2016; Gomaa et al., 2018). According to the mix proportion, the solution moduli of D1.5, D2.0 and D2.5 are calculated as 0.99, 1.13 and 1.9, respectively. It can be found that there is not much difference between the modulus of D1.5 and D2.0, which means that the dissolute silica content is not the main contributor for the increase of setting time when the SS/SH ratio is increased from 1.5 to 2.0. Thus, it can be attributed to the decrease of the relative amount of SH, which would inhibit the dissolution of raw materials and improve setting time (Gomaa et al., 2018). On the other hand, the modulus of D2.5 (1.9) is much higher than that of D2.0 (1.13), which might play an important role on the decrease of setting time of AAFS paste when the SS/SH ratio is increased from 2.0 to 2.5. The high content of dissolute silica would generally enhance the alkali activation process and reduce the time to complete the chemical reaction (Siyal et al., 2016).

According to BS EN 197-1:2011 (2011), the initial setting time of all mixtures in series A fulfil the requirement of engineering application (≥ 60 min) except A00 (> 12 h) and A30 (< 60 min). In series B, both B0.4 and B0.5 are acceptable for engineering application. However, for series C, only C8 is acceptable based on this criterion. For series D, both D1.5 and D2.5 are not acceptable for engineering application according to this criterion. In conclusion, the AAFS mixtures with slag replacement level from 10% to 25%, AL/P ratio in the range of 0.4 ~ 0.5, 8 ~ 10 M of SH, and SS/SH ratio of 2.0 can satisfy the engineering application of AAFS concrete in terms of setting time.

3.3.3 Compressive strength

The requirement of compressive strength is determined by the engineering application of concrete. According to the BS EN 206:2013+A1:2016 (2016), the 28-d compressive strength of concrete need to achieve at least 15 MPa for the basic engineering application without the risk of corrosion or attack. For the corrosion protection of reinforcement in concrete, the minimum compressive strength of concrete is 37 MPa. In this study, the minimum compressive strength of 37 MPa was used as a reference to evaluate the optimal mixtures of AAFS concrete. In addition, given that large volume of concrete is applied in non-structural structure, which has a relatively low requirement of compressive strength, the development of AAFS concrete should be able to be used for a wide range of engineering applications. Nevertheless, it should be noted that the characteristic strength of 37 MPa from BS EN standard cannot be directly compared with the measured strength.

Figure 3-8 shows the compressive strength of AAFS concrete with different slag replacement levels. The development of compressive strength of different mixtures

follows a similar trend but different magnitudes. It increases dramatically at early 28 d, but after that, the increasing rate becomes slow between 28 d and 56 d. The AAFS concrete without slag has the lowest compressive strength due to its low chemical reactivity in ambient curing condition. When slag is incorporated in the mixture, the strength increases significantly. This is because that the addition of slag would generate the space-filling binding products (i.e. C-A-S-H gels), which would reduce the porosity and condense the microstructure of AAFS matrix (Provis et al., 2012; Ye and Radlińska, 2016). The 28-d compressive strength is increased significantly from 23.8 to 61.4 MPa with the increase of slag content from 0% to 30%. Besides, it is discovered that the effect of slag at a 25% replacement level appeared to be more pronounced. After 28-d curing, the compressive strength of A10, A15, A20, A25 and A30 is increased by 63.13%, 77.85%, 93.90%, 131.08% and 157.95% respectively in comparison with the mixture without slag (A00), respectively.

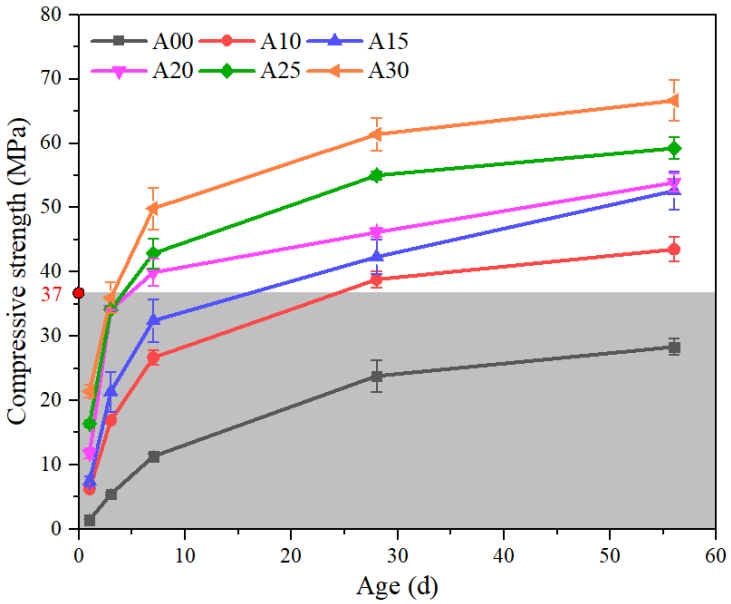

Figure 3-8 Compressive strength of AAFS concrete with different fly ash/slag ratio

The effect of AL/P ratio on the compressive strength is presented in Figure 3-9. The 1-d compressive strength of AAFS concrete with different AL/P ratio is almost identical. After 3 d, the compressive strength of mixture with AL/P of 0.4 (B0.4) and 0.45 (B0.45) keeps the similar value of 34 MPa, but it is higher than that of the mixture with AL/P ratio of 0.5 (B0.5). After 7 d, B0.4 has the highest compressive strength of 51 MPa, whereas the compressive strengths of B0.45 and B0.5 reach a similar value of 42 MPa. Afterwards, the compressive strengths of all mixtures become almost the same at 28 d and 56 d. It indicates that the amount of AL would strongly affect the compressive strength of AAFS

concrete at early-age (< 7 d), but it has no significant effect on the later-age strength (> 28 d). According to previous research, the reaction process of AAFS would be accelerated with the decrease of AL/P ratio due to the decrease of consistency of mixtures (Rafeet et al., 2017). The reaction products such as C-A-S-H gel and N-A-S-H gel can be produced quickly in the mixtures with low AL/P ratio, which would contribute to the development of early-age compressive strength (< 14 d) (Kumar et al., 2010; Lloyd et al., 2009b). Nevertheless, the reaction rate became slow after 14 d because most of the raw materials have been reacted.

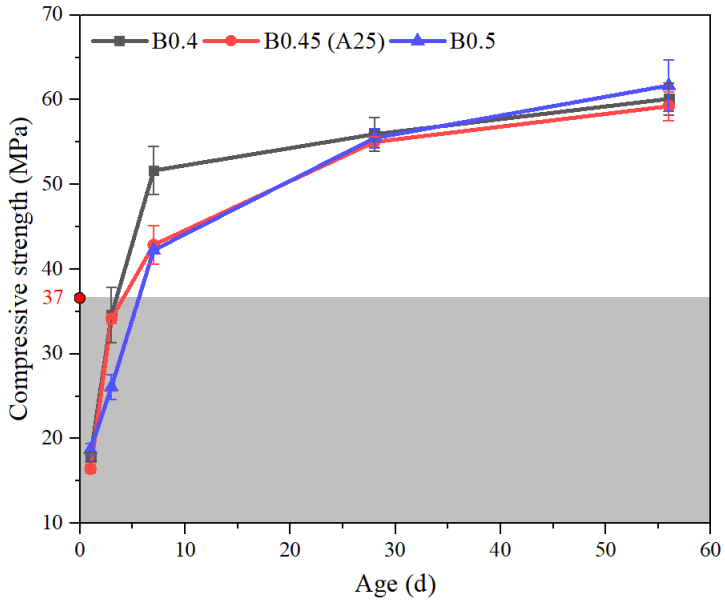

Figure 3-9 Compressive strength of AAFS concrete with different AL/P ratio

Figure 3-10 shows the compressive strength of AAFS concrete with different SH molarity. It is noted that the effect of SH molarity on the compressive strength at an early age (< 3 d) is not obvious. At 7 d, the mixture with highest SH molarity of 12 M (C12) has the highest compressive strength of 52 MPa, whereas C8 (8M) and C10 (10 M) have relatively low compressive strengths of 46 MPa and 43 MPa, respectively. Afterwards, the compressive strength of C10 and C12 becomes close with about 56 MPa at 28 d, while C8 has the lowest compressive strength of 49 MPa. This phenomenon can be explained by the reaction of the internal Si, Al and Ca components that caused by the increased breakage of the T-O-T bonds (T: Si or Al) in fly ash and the T-O bonds (T: Ca and Si) in slag, which itself is provoked by the high alkalinity resulting from the increasing molarity of SH (García-Lodeiro et al., 2013; Ryu et al., 2013). The strength of all mixtures becomes close at around 58 MPa at later age (56 d). It indicates that SH molarity would affect the early strength up to 28 d, but it becomes less significant at long-term age.

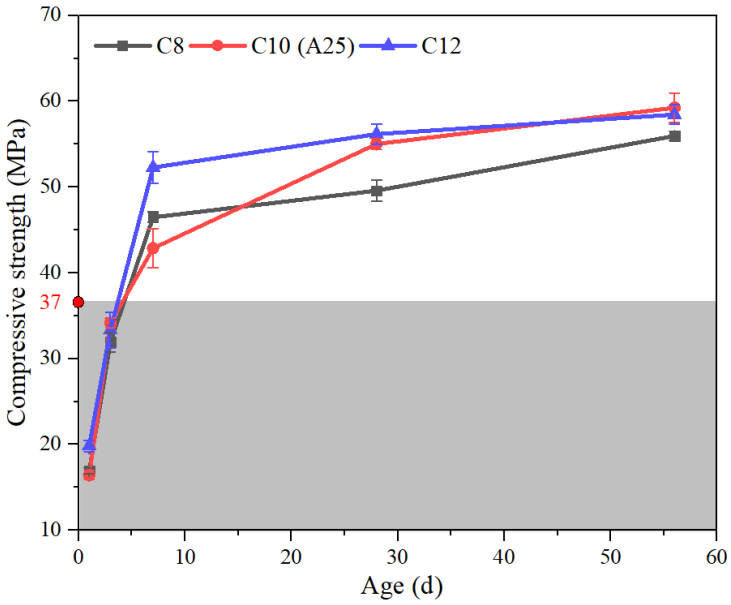

Figure 3-10 Compressive strength of AAFS concrete with different SH molarity

Finally, the compressive strength of AAFS concrete with different SS/SH ratio is presented in Figure 3-11. It can be found that the effect of SS/SH ratio on the development of compressive strength is not straightforward. The compressive strength of mixture with SS/SH ratio of 2.0 (D2.0) is slightly higher than the other two mixtures with SS/SH ratio of 1.5 (D1.5) and 2.5 (D2.5) at early 28 d. The strength of D1.5 and D2.5 is similar at early 7 d, while the strength of D2.5 is slightly higher than that of D1.5 after 28 d curing. After 56 d, the compressive strength of all three mixtures becomes close at around 55 MPa. These results indicate that SS/SH ratio would affect the compressive strength up to 28 d, but it has no obvious effects on the long-term strength.

According to the experimental results presented above, it is found that compressive strength of AAFS concrete is dominantly affected by the slag replacement level for fly ash and the content of AL. In addition, it is also found that the 28-d compressive strength of all mixtures except the AAFS mixture without slag is higher than 37 MPa and satisfy the basic requirement of normal and reinforced concrete. Thus, the mixtures with slag replacement level from 10% to 30%, AL/B ratio from 0.4 to 0.5, SH molarity from 8 M to 12 M, and SS/SH ratio in the range of 1.5 to 2.5 can be suggested as optimal mixtures for the sake of compressive strength.

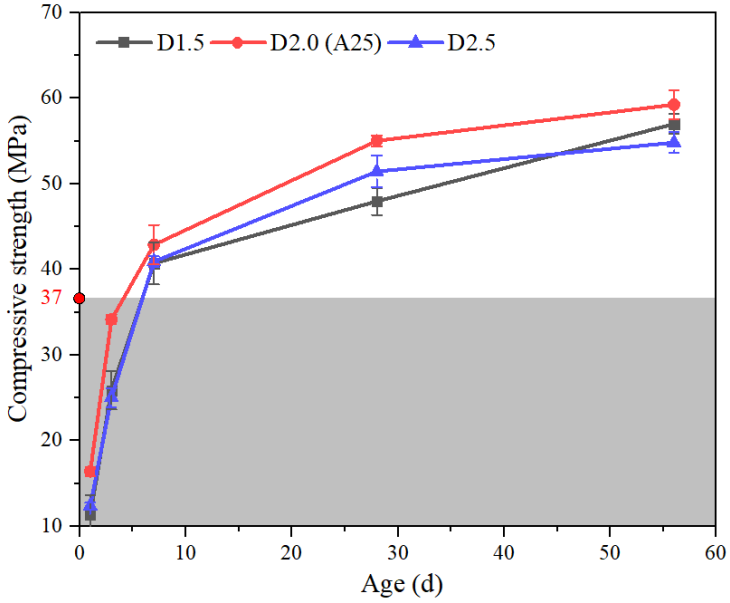

Figure 3-11 Compressive strength of AAFS concrete with different SS/SH ratio

3.3.4 Splitting tensile strength

Figure 3-12 shows the splitting tensile strength of AAFS concrete after 7 d and 28 d curing. The splitting tensile strength increases with the increase of curing age for all mixtures. As seen in series A, the splitting tensile strength increases with the increase of slag content, which is similar to the phenomenon found in the development of compressive strength. The 7-d and 28-d splitting tensile strength are improved from 0.81 to 3.0 MPa and from 3.46 to 4.08 MPa, respectively, when the slag content is increased from 0% (A0) to 30% (A30). This developing trend is agreed with the developing trend of compressive strength. Also, the split tensile strength decreases with the increase of AL/P ratio from 0.4 (B0.4) to 0.5 (B0.5) (see series B), consisting with the developing trend observed in compressive strength. The 7-d and 28-d splitting tensile strengths of B0.4 are 3.38 MPa and 4.48 MPa, respectively, which are higher than those of B0.5 (3.09 MPa at 7 d; 3.60 MPa at 28 d). Nevertheless, the effect of SH molarity on the split tensile strength is not obvious, in which only slight improvement can be found when the SH molarity is increased from 8 M (C8) to 12 M (C12) (see series C). This developing trend is different as compared to the development of compressive strength. Lastly, it is observed that the effect of SS/SH ratio on the splitting tensile strength is not straightforward (see series D). The 28-d splitting tensile strength increases from 3.29 MPa to 4.03 MPa with the increase of SS/SH ratio from 1.5 (D1.5) to 2.0 (D2.0), while it is reduced to 3.56 MPa when the SS/SH ratio is further increased to 2.5 (D2.5). This phenomenon is consistent with the developing trend of compressive strength.

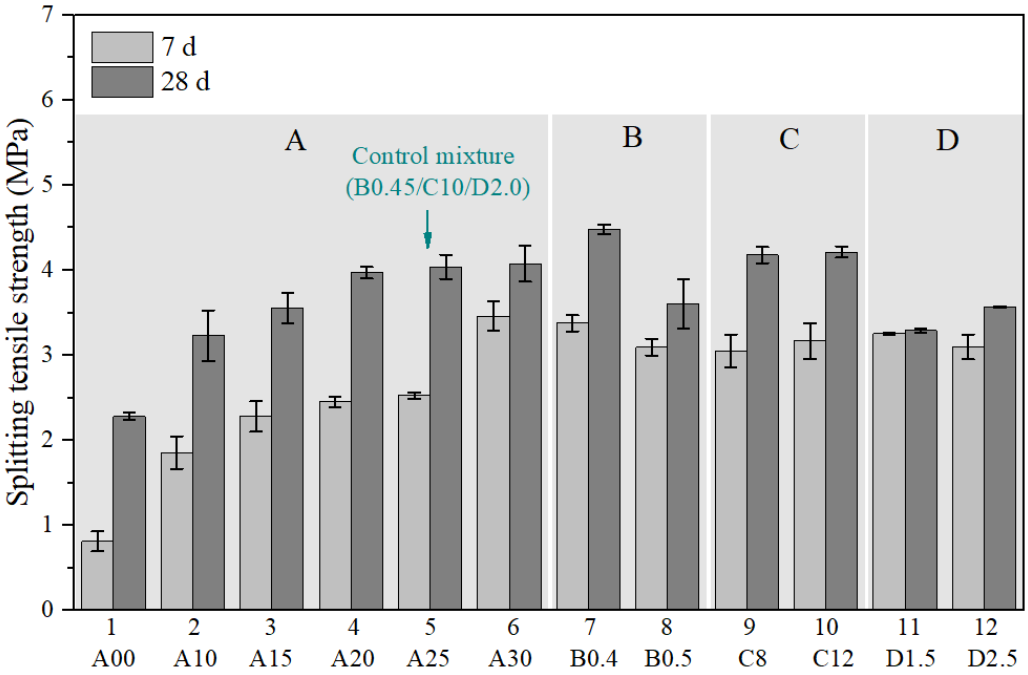

Figure 3-12 Splitting tensile strength of AAFS concrete

Additionally, the measured splitting tensile strength is compared with the predicted splitting tensile strength of PC concrete according to ACI M318-08 (2008) (Eq. 2-3) and Eurocode 2 (2004) (Eq. 2-4). It can be seen from Figure 3-13 that most of the measured splitting tensile strengths are lower than the predictions from these two codes. However, it is worthy noted that this simple comparison cannot predict the accurate relationship between measured results and existing formulas, because that the compressive strength used for the formulas is obtained from different types and sizes of specimens according to different standards, some of which are different from the specimens used in this study.

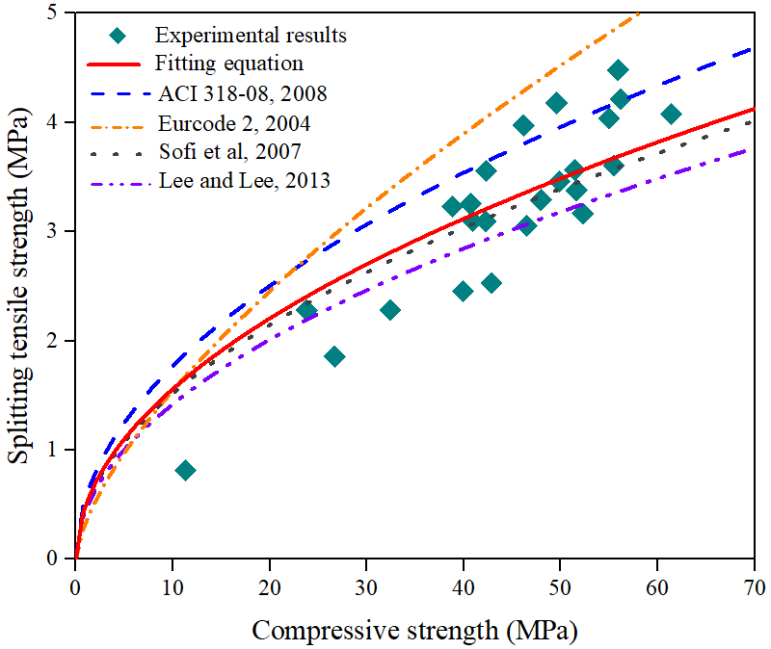

Figure 3-13 Comparison of measured and predicted splitting tensile strength of AAFS concrete

Based on these results, the relationship between splitting tensile strength and the compressive strength is identified as shown in the Eq. 3-1 with R^2 of 0.70. The constant of 0.49 in this equation is slightly higher than other previous research in AAFS concrete: ($0.48\sqrt{f_c}$) proposed by Lee and Lee (2013) and ($0.45\sqrt{f_c}$) proposed by Sofi et al (2007).

$$f_{ct} = 0.49\sqrt{f_c} \qquad (3-1)$$

where f_{ct} is the splitting tensile strength (MPa) and f_c is the compressive strength (MPa).

3.3.5 Elastic modulus

The elastic modulus of AAFS concrete is plotted in Figure 3-14. It can be found that the elastic modulus is improved obviously with the increase of curing age from 7 d to 28 d. As seen in series A, the elastic modulus is increased steadily with the increase of slag content, due to the formation of different types of reaction products. The main reaction products formed in the activation of slag are the C-A-S-H gels with an elastic modulus of 12 ~ 47 GPa (Puertas et al., 2011; Thomas et al., 2018), which is higher than the that of N-A-S-H gels (4.44 ~ 20 GPa) formed in activation of fly ash (Němeček et al., 2011; Lee et al., 2016; Ma et al., 2017). The 7-d and 28-d elastic moduli of AAFS concrete are increased significantly from 4.87 GPa to 30.85 GPa and from 11.75 GPa to 39.78 GPa, respectively, when the slag content is increased from 0% (A0) to 30% (A30). On the contrary, the effects of other factors such as AL/P ratio, SH molarity and SS/SH ratio on the elastic modulus of AAFS concrete are less significance, except the control mixture (A25). As the AL/P ratio increases from 0.4 (B0.4) to 0.5 (B0.5), the 7-d elastic modulus slightly decreases from 27.56 GPa to 24.82 GPa, whereas the 28-d elastic modulus slightly increases from 32.41 GPa to 34.85 GPa (see series B). It can be seen from series C that the 7-d and 28-d elastic moduli are increased slightly from 23.52 GPa to 25.37 GPa and from 31.16 GPa to 35.03 GPa, respectively, with the increase of SH molarity from 8 M to 12 M. The addition of SS/SH ratio would tend to slightly decrease the elastic modulus of AAFS concrete. The 7-d and 28-d elastic moduli are decreased from 24.66 GPa to 23.22 GPa and from 35.96 GPa to 32.13 GPa, respectively, with the increase of SS/SH ratio from 1.5 (D1.5) to 2.5 (D2.5).

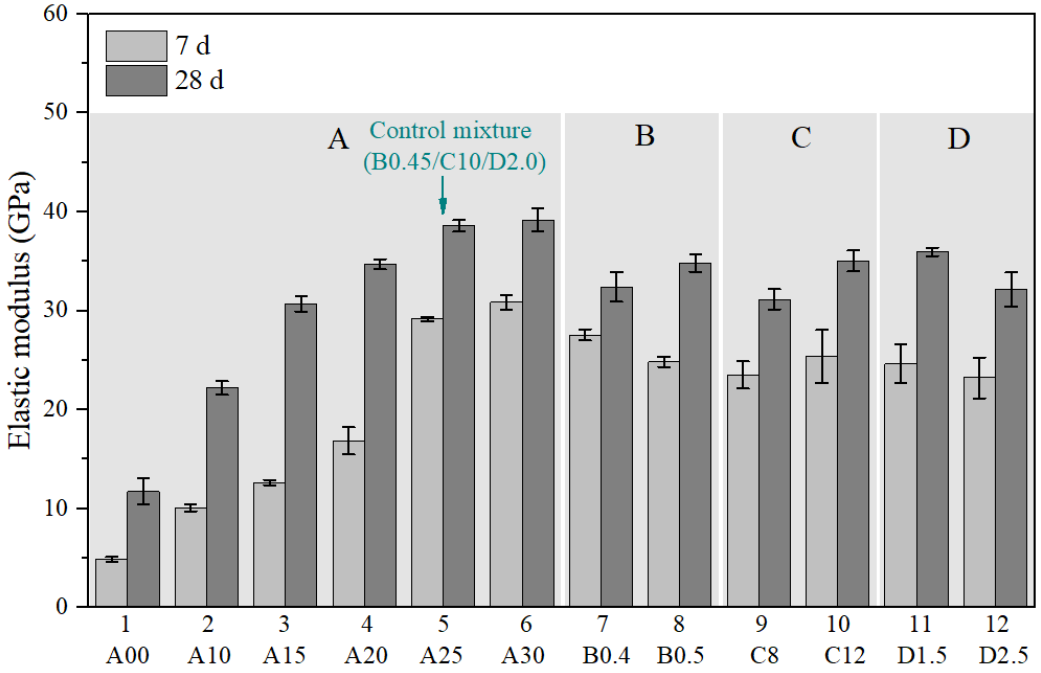

Figure 3-14 Elastic modulus of AAFS concrete

Figure 3-15 shows the measured elastic modulus of AAFS concrete as well as the predicted elastic modulus of PC concrete using CEM-FIP model code (1995) and ACI M318-08 building code (2008), and the predicted results of AAFS concrete by Lee and Lee ($E_C = 5300 \times (f_c)^{1/3}$) (2013). It is observed that the elastic modulus increases with the increase of compressive strength, consisting with other studies (Lee and Lee, 2013; Thomas and Peethamparan, 2015). The elastic modulus of AAFS concrete at 28 d is mostly higher than that of AAFS concrete at 7 d. In addition, it can be found that most of the 7-d elastic modulus in this study is lower than the prediction by these two codes but higher than the prediction obtained by Lee and Lee. However, these two codes show acceptable predictions for the 28-d elastic modulus. It indicates that the existing codes are more acceptable for predicting the high-strength types of AAFS concrete. Nevertheless, it should be noted that such comparison has some limitations which might be not provide the accurate prediction for this relationship. It is because that the elastic modulus measured for the CEM-FIP model code and the ACI M318-08 building code are based on different types of specimens, which might be different from the type of specimen used in this research.

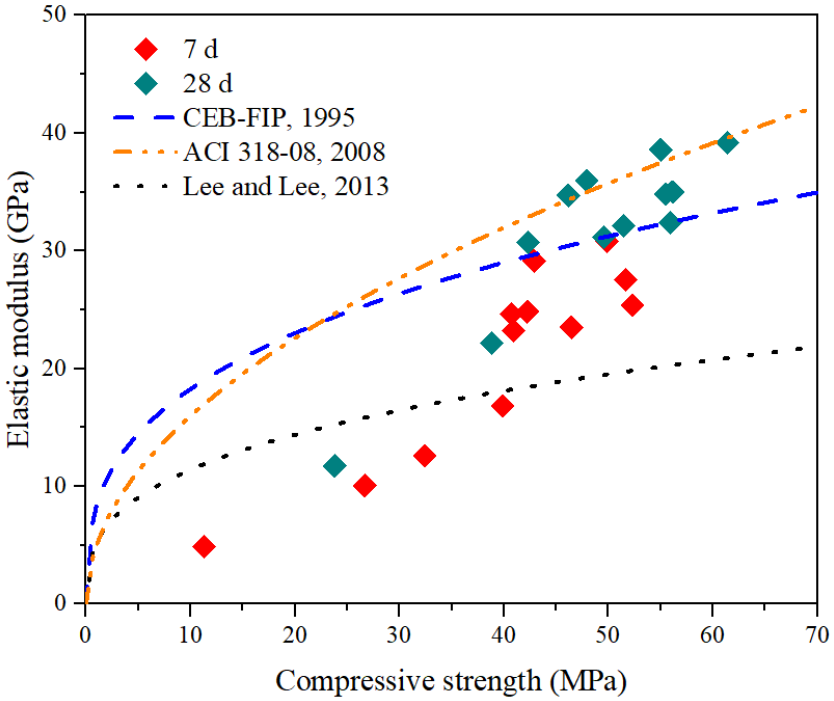

Figure 3-15 Comparison of measured and predicted elastic modulus of AAFS concrete

3.3.6 Fracture properties

Since the fracture properties of concrete are mainly characterised through the load-displacement curve, fracture toughness and fracture energy, the fracture properties of AAFS concrete will be discussed based on these three aspects.

3.3.6.1 Load-displacement curve

The load-displacement curve is a critical feature to reflect the fracture behaviour of concrete. Figure 3-16 shows the load-displacement curves of AAFS concrete regarding the effects of fly ash/slag ratio (slag content), AL/P ratio, SH molarity and SS/SH ratio. It should be noted that the load-displacement curves obtained here are based on the simply deflection control (LVDT measurement control) test rather than the crack mouth opening displacement (CMOD) controlled test. It can be found that the load-displacement curves of all mixtures follow a similar pattern. In the pre-peak curve, the load increases linearly at the beginning until the initiation of cracks, followed by a non-linear increase to the ultimate of peak load (P_U) that presents maximum load that is needed to split up the surfaces involving in the crack induced at the end of the extended crack tip. Afterwards, a downward post-peak curve occurs due to the continuous propagation of cracks, where the load decreases non-linearly until the final complete failure of concrete specimen. The slope of post-peak curve reflects the ductility of concrete.

As seen in Figure 3-16a, it can be observed that the slopes of pre-peak curves of mixtures with slag (A10 ~ A30) are steeper than the mixture without slag (A0). This indicates that the AAFS concrete without slag tends to deflect more than that with slag before the initiation of cracks. A similar phenomenon can be found in the slopes of post-peak curves, where the post-peak slope of A0 is more gentle than other mixtures, implying that A0 has a greater deflection behaviour after cracking. It reveals that the reduction of ductility of the AAFS concrete is associated with the addition of slag. This can be attributed to the variation of reaction products formed in these mixtures. For the AAFS mixture without slag, the main reaction products are N-A-S-H gels from the activation of fly ash, which have relatively low strengths but high ductility (Hou et al., 2018). With the addition of slag, a new type of reaction products called C-A-S-H gels is generated from the reaction of slag, which would generate a much stiff and brittle matrix in AAFS concrete (Thomas and Peethamparan, 2015; Kumarappa and Peethamparan, 2020). However, the formation of C-A-S-H gels would contribute to the increase of P_U, due to their high-strength characteristics. Evidently, P_U is generally increased with the addition of slag content, from 1.01 kN (A0) to 3.11 kN (A30).

The load-displacement curves of the mixture with various AL/P ratios, SH molarities and SS/SH ratios are presented in Figure 3-16b ~ d, respectively. It can be found that these mixtures show similar load-displacement behaviour, with a steep slope in both pre-peak and post-peak curves. Nevertheless, P_U of load-displacement curve is different among these mixtures. Regarding the effect of AL/P ratio, P_U is increased from 2.33 kN to 3.29 kN when the AL/P ratio is increased from 0.4 (B0.4) to 0.45 (B0.45), followed by a decrease to 2.64 kN at AL/P ratio of 0.5 (B0.5), as seen in Figure 3-16b. The effect of SH molarity on the development of peak load is straightforward, where P_U is increased steadily from 2.59 kN to 3.46 kN with the addition of SH molarity from 8 M (C8) to 12 M (C12) (Figure 3-16c). Lastly, it can be seen from Figure 3-16d that P_U increases significantly from 2.56 kN to 3.29 kN with the increase of SS/SH ratio from 1.5 (D.1.5) to 2.0 (D2.0), followed by a lightly decrease to 3.13 kN at 2.5 (D2.5).

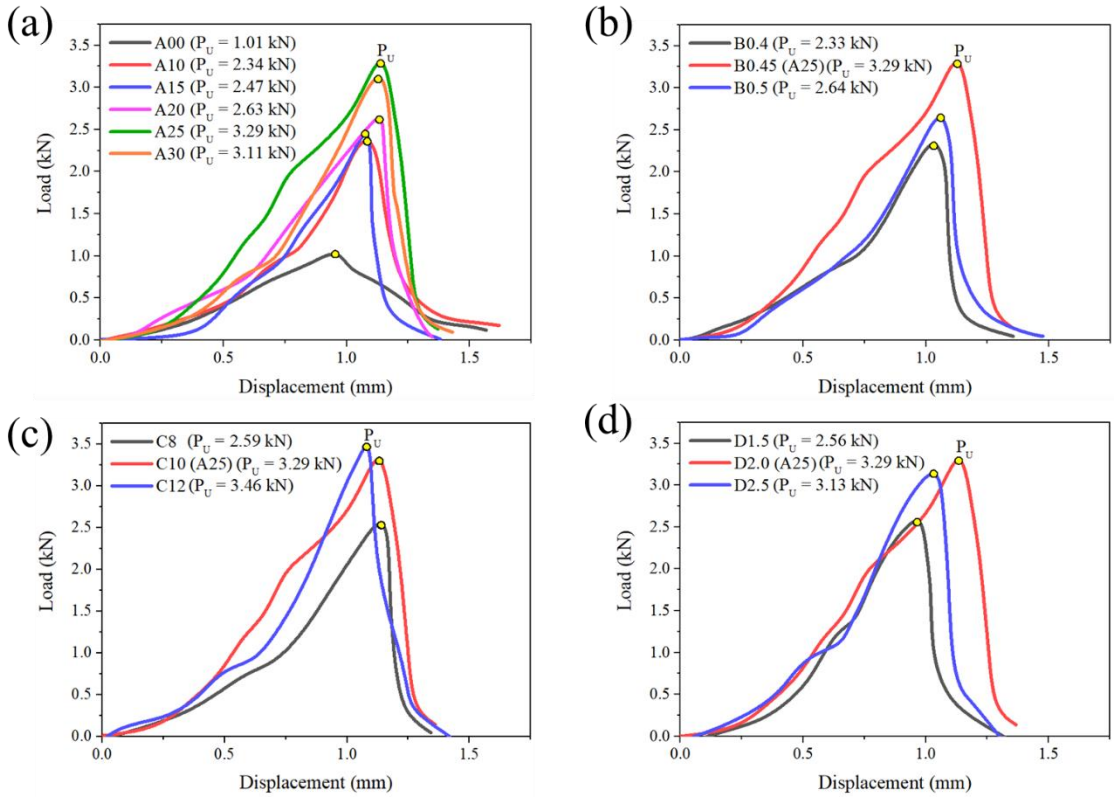

Figure 3-16 Load-displacement curve of AAFS concrete with different influencing factors ((a) fly ash/slag ratio, (b) AL/P ratio, (c) SH molarity and (d) SS/SH ratio)

3.3.6.2 Fracture toughness

Fracture toughness of concrete is defined as the critical stress intensity factor (K_{IC}), which is used to quantify the concrete's resistance to crack propagation. It is related to P_U and the geometric dimensions of the testing beam as the following equation (Peterson, 1980).

$$K_{IC} = \frac{3P_U l}{2wh^2}\sqrt{a_0}(1.93 - 3.07A + 14.53A^2 - 25.11A^3 + 25.8A^4) \quad (3-2)$$

where P_U is the peak load (N), l is the span of beam (300 mm), w is the width of beam (100 mm), h is the hight of beam (100 mm), a_0 is the depth of notch (40 mm), and $A=a_0/h$.

Figure 3-17 shows the influences of different factors on fracture toughness (K_{IC}) of AAFS concrete. The addition of slag content improves the fracture toughness of AAFS concrete (Figure 3-17a), corresponding well with the development of peak load. The fracture toughness of mixture is increased significantly from 0.2 MPa·m$^{1/2}$ to 0.58 MPa·m$^{1/2}$ with the increase of slag content from 0% to 15%, followed by a slight increase to 0.62 MPa·m$^{1/2}$ at mixture with 30% slag. In addition, it can be seen from Figure 3-17b ~ d that the effects of AL/P ratio, SH molarity and SS/SH ratio on the fracture toughness of AAFS concrete are less obvious, consisting with those effects on the peak load. With the increase of AL/P ratio from 0.4 to 0.45, the fracture toughness of mixture increases

slightly from 0.51 MPa·m$^{1/2}$ to 0.63 MPa·m$^{1/2}$, followed by a slight reduce to 0.55 MPa·m$^{1/2}$ at mixture with AL/P ratio of 0.5 (Figure 3-17b). The fracture toughness of mixture is improved from 0.47 MPa·m$^{1/2}$ to 0.63 MPa·m$^{1/2}$ when the SH molarity is increased from 8 M to 10 M but becomes stable with the further increase of SH molarity to 12 M (Figure 3-17c). Similarly, as shown in Figure 3-17d, the addition of SS/SH ratio from 1.5 to 2.0 would also improve the fracture toughness of mixture from 0.50 MPa·m$^{1/2}$ to 0.63 MPa·m$^{1/2}$. Nevertheless, the fracture toughness of mixture is slightly decreased to 0.54 MPa·m$^{1/2}$ with the further increase of SS/SH ratio up to 2.5.

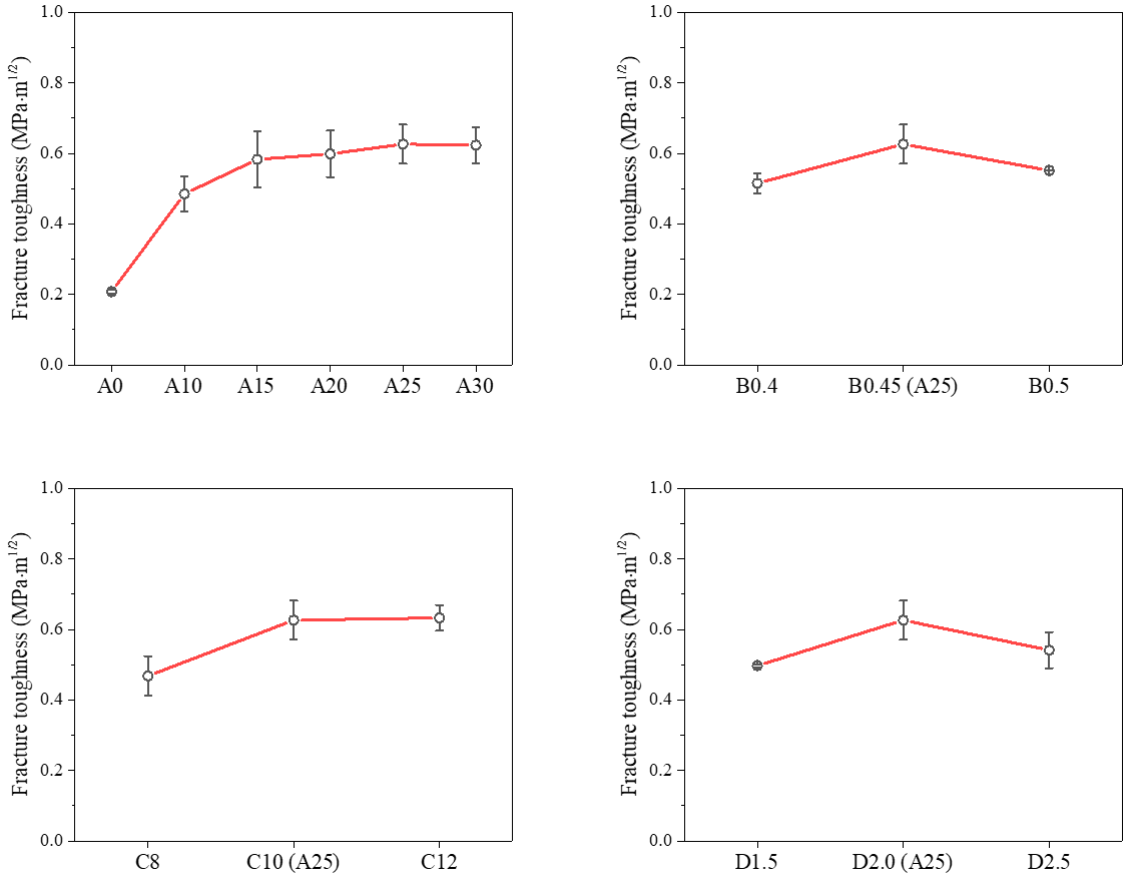

Figure 3-17 Fracture toughness of AAFS concrete with various (a) fly ash/slag ratio, (b) AL/P ratio, (c) SH molarity and (d) SS/SH ratio

3.3.6.3 Fracture energy

Fracture energy of concrete is an important parameter used to illustrate the energy dissipation capacity during the propagation of cracks, which can be calculated using the following equation given in RILEM TC 50-FMC guidelines (1985).

$$G_F = (W_0 + mgd)/A_{lig} \quad (3-3)$$

where G_F is the fracture energy (N/m), W_0 is the external work (N·m), m is the mass of beam between two testing supports (kg), g is the acceleration of gravity (9.81 m/s^2), d is the final mid-span displacement (m), $A_{lig} = w(h - a_0)$ is the ligament area (m^2), w is

the width of beam (0.1 m), h is the hight of beam (0.1 m) and a_0 is the depth of notch (0.04 m).

The influences of different factors on fracture energy of AAFS concrete are shown in Figure 3-18. The fracture energy of AAFS concrete increases with the slag replacement level. The fracture energy of mixture in series A augments from 151.29 N/m to 253.62 N/m with a 67.63% increase when the slag content rises from 0% (A0) to 30% (A30). This phenomenon is consistent with the developing trend observed in compressive strength, splitting tensile strength and elastic modulus. This might be because that the addition of slag content would release more calcium ions, which would promote the chemical reaction of raw material and the formation of reaction products, and consequently condense the microstructure. Similarly, with the addition of AL/P ratio from 0.4 (B0.4) to 0.5 (B0.5), the fracture energy of mixture is increased from 226.78 N/m to 235.95 N/m, i.e. an 11.98% increase. In addition, an increase of fracture energy from 245.26 N/m to 298.75 N/m can be found in C8 and C12, where the SH molarity is added from 8 M to 12 M. Lastly, the improvement of fracture energy is 16.14% from 201.52 N/m to 234.05 N/m with the increase of SS/SH ratio from 1.5 (D1.5) to 2.5 (D2.5). These phenomena are consistent with other research in terms of the effects of slag content, AL/P ratio, SH molarity and SS/SH ratio on the fracture energy of AAFS concrete (Nath and Sarker, 2016; Ding et al., 2018b).

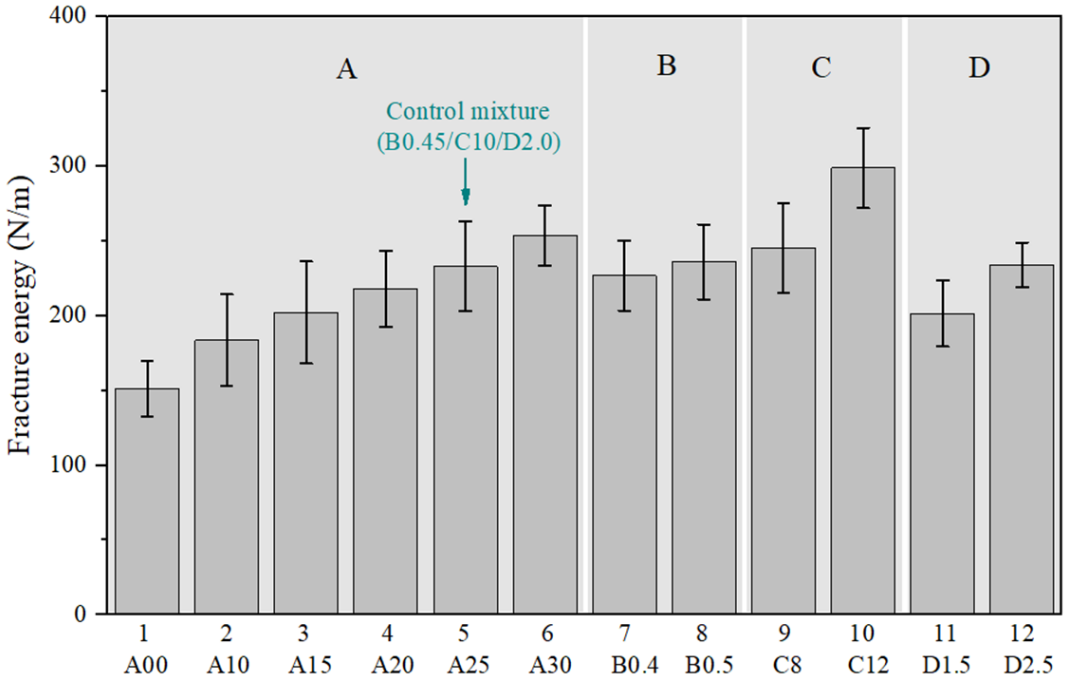

Figure 3-18 Fracture energy of AAFS concrete

Figure 3-19 shows the measured fracture energy of AAFS concrete and the predicted fracture energy of PC concrete using the CEB-FIP model (Eq. (2-7)) and the Bazant and Becq-Giraduon model (Eq. (2-8)) (CEB-FIP Model Code, 1995; Bažant and Becq-Giraudon, 2002). The fracture energy of AAFS concrete increases with the compressive strength, consisting of the results observed in PC concrete (Nath and Sarker, 2016; Ding et al., 2018a). Nevertheless, the measured fracture energy of AAFS concrete is significantly higher than the fracture energy of PC concrete predicted by the CEB-FIP model and the Bazant and Becq-Giraduon model. It indicates that AAFS concrete has a higher fracture energy than PC concrete with a similar compressive strength, which can be ascribed to the denser and stronger microstructure of AAFS concrete in comparison with PC concrete. It is worthy noted that the direct comparison of fracture energy between existing models and measured results might be not fully accurate, because that the measurements of fracture energy for different models are based on different types of specimens which might be different from the specimen used in this study.

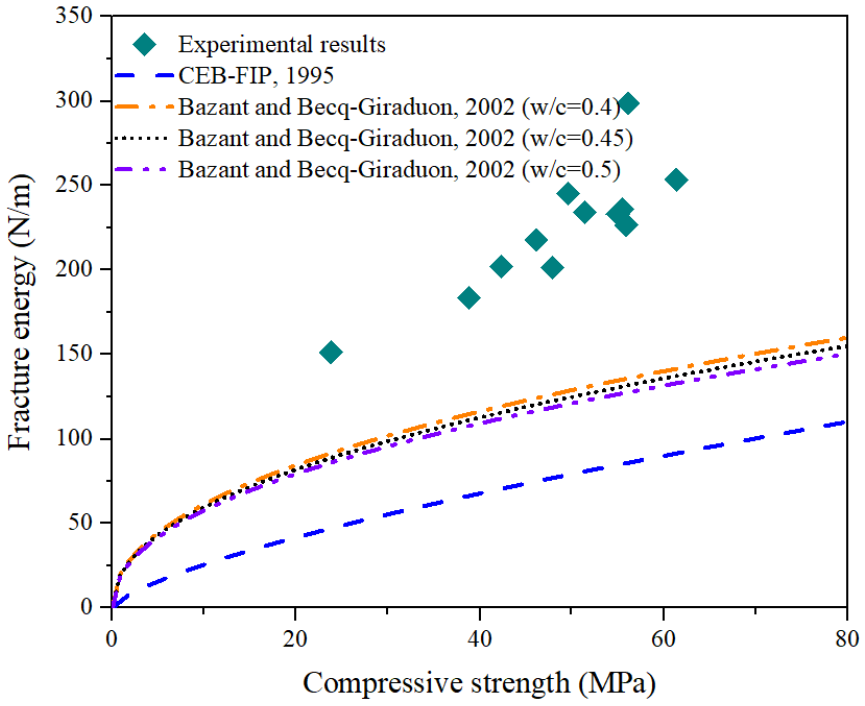

Figure 3-19 Comparison of measured and predicted fracture energy of AAFS concrete

3.3.7 Optimal mixtures

Figure 3-20 shows the obtained optimal mixtures of AAFS concrete according to the performance criteria of workability, setting time and compressive strength. Based on the discussion mentioned above, the optimal AAFS concrete should have high workability with a slump value of 90 mm or over (Talha Junaid et al., 2015), suitable setting time

with a minimum initial setting of 60 min (BS EN 197-1:2011, 2011) and high compressive strength with a minimum 28-d compressive strength of 37 MPa (BS EN 206:2013+A1:2016, 2016). Therefore, the mixtures with a slag replacement level from 10% to 25%, AL/B ratio in the range of 0.45 ~ 0.50, 8 ~ 10 M of SH, SS with a modulus of 2.0, and SS/SH ratio of 2.0 are suggested as optimal mixtures of AAFS concrete considering the balance of workability, setting time and compressive strength. The AAFS concrete with these mixtures is expected to fulfil the requirement of the engineering application, in which the AAFS concrete can be mixed easily, and has enough setting time for the casting, as well as can provide a high compressive strength for the structure.

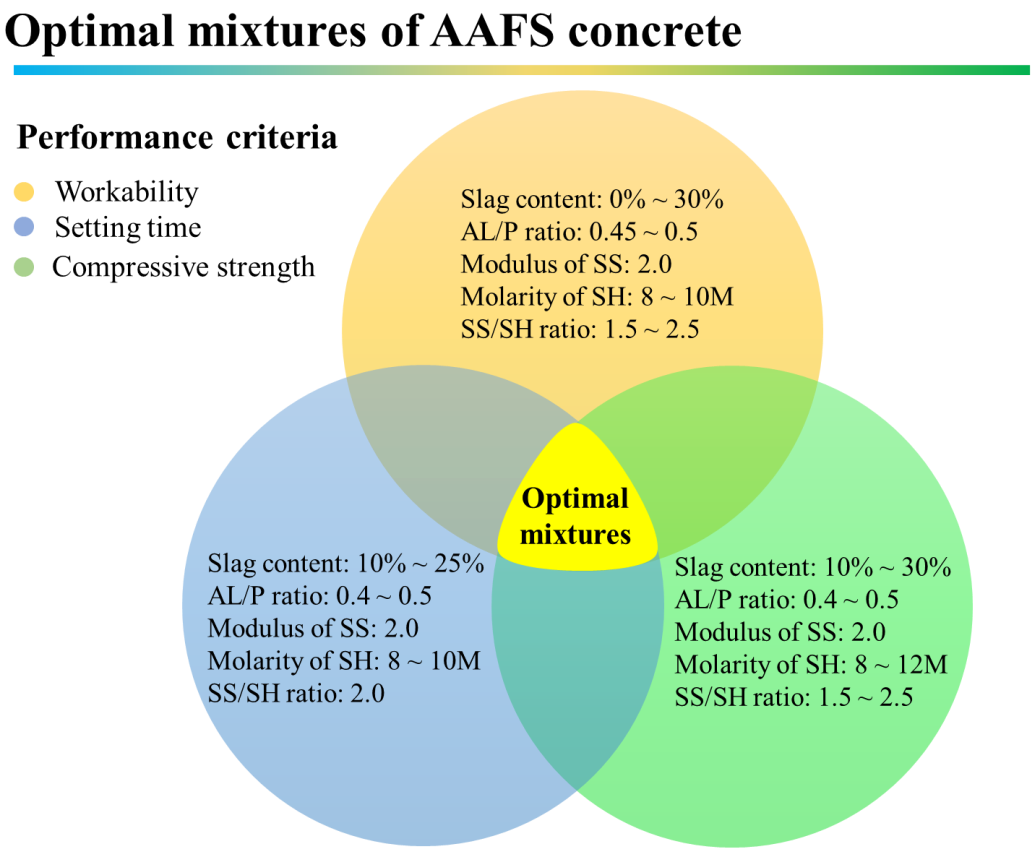

Figure 3-20 Schematic illustration of optimal mixtures of AAFS concrete in terms of workability, setting time and compressive strength

3.4 Concluding remarks

In this chapter, the workability, setting time and mechanical properties of AAFS concrete with different slag content, AL/P ratio, the molarity of SH and SS/SH ratio were investigated. Based on the experimental results, the main conclusions can be drawn as follows:

- Workability of AAFS concrete decreases with the increase of slag content, the molarity of SH and SS/SH ratio, as well as the decrease of AL/P ratio. It is found that

the effect of slag at 30% replacement level and AL/P ratio at 0.45 appears to be more pronounced.

- Setting time of AAFS concrete decreases with the increase of slag content and AL/P ratio. However, the effects of SH molarity and SS/SH ratio on setting time are not straightforward. The setting time of the mixture with 10 M SH is higher than the mixture with 8 M SH, whereas the setting time decreases to the lowest level when the SH molarity increases to 12 M. The setting time increases with the increase of SS/SH ratio from 1.5 to 2.0, but it decreases with the further increase of SS/SH ratio from 2.0 to 2.5.
- Compressive strength of AAFS concrete increases significantly with the increase of slag content, especially for the effect of slag at 25% replacement level. The amount of AL would strongly affect the compressive strength at early age (< 7 d), but the effect becomes less significance at later age (> 28 d). In addition, both SH molarity and SS/SH ratio would affect the early strength up to 28 d, but it becomes not obvious at long-term age.
- Spitting tensile strength of AAFS concrete increases with the increase of slag content and the decrease of AL/P ratio, which is similar to the phenomenon found in a compressive strength test. The effects of SH molarity and SS/SH ratio on splitting tensile strength is not obvious. Additionally, it is found that the existing equations provided by ACI 318-08 code and Eurocode 2 overestimate the values of splitting tensile strength of AAFS concrete. Accordingly, a more suitable equation is proposed based on the measured data.
- Elastic modulus of AAFS concrete increases with the increase of slag content and SH molarity, as well as the decrease of SS/SH ratio. The increase of AL/P ratio has a negative effect for early age development of elastic modulus (7 d), but it slightly increases the elastic modulus at a later age (28 d). In addition, the existing equations (CEB-FIP model code and ACI 318-08 code) are suitable to predict the 28-d elastic modulus, but these equations overestimate the 7-d elastic modulus in this study.
- Fracture toughness and peak load of the load-displacement curve of AAFS concrete are increased with the addition of slag content but are slightly affected by the changes of AL/P ratio, SH molarity and SS/SH ratio. Regarding the fracture energy of AAFS concrete, it is improved with the increase of slag content, AL/P ratio, SH molarity and SS/SH ratio. Besides, the measured fracture energy of AAFS concrete is significantly higher than the fracture energy of PC concrete predicted by the CEB-FIP model and the Bazant and Becq-Giraduon model, which implies that the AAFS concrete has

higher fracture energy than the PC concrete with a similar compressive strength.

- The mixtures of AAFS concrete with slag replacement level from 10% to 25%, AL/P ratio in the range of 0.45 ~ 0.50, 8 ~ 10 M of SH, SS with a modulus of 2.0, and SS/SH ratio of 2.0 are suggested as optimal mixtures regarding the performance criteria of workability, setting time and compressive strength.

Chapter 4 Multiscale microstructural characterisation of AAFS concrete

4.1 Introduction

In Chapter 3, the macroscopic engineering properties including workability, setting time and mechanical properties of AAFS concrete were investigated, considering the effects of different factors such as fly ash/slag ratio, and type and content of activator. In addition, the optimal mixtures of AAFS concrete were obtained to achieve a desired performance in terms of acceptable workability, suitable setting time and high compressive strength. In this chapter, the microstructure of AAFS concrete will be further characterised at four multiple length scales: Level 0 (solid gel particle), Level I (gel matrix), Level II (paste) and Level III (ITZ in concrete). As shown in Figure 4-1, the microstructure of AAFS concrete at different length scales was characterised using different testing methods. The nanostructure of solid gel particle at Level 0 was characterised by nuclear magnetic resonance (NMR). X-ray diffraction (XRD) and Fourier transform infrared spectroscopy (FTIR) were used to evaluate the chemical composition of gel matrix at Level I. The microstructure evolution of paste at Level II was characterised by means of X-ray microcomputed tomography (XCT), backscattered scanning electron microscopy (BSEM), energy dispersive spectrometry (EDS) and mercury intrusion porosimetry (MIP). Lastly, BSEM and EDS were utilised to investigate the microstructure development of ITZ in AAFS concrete at Level III. The details of the methodology for these microstructural tests will be given in the following sections. It should be noted that part of this chapter has been presented in the following publication: Guohao Fang and Mingzhong Zhang, The evolution of interfacial transition zone in alkali-activated fly ash-slag concrete, *Cement and Concrete Research*,129 (2020) 105963.

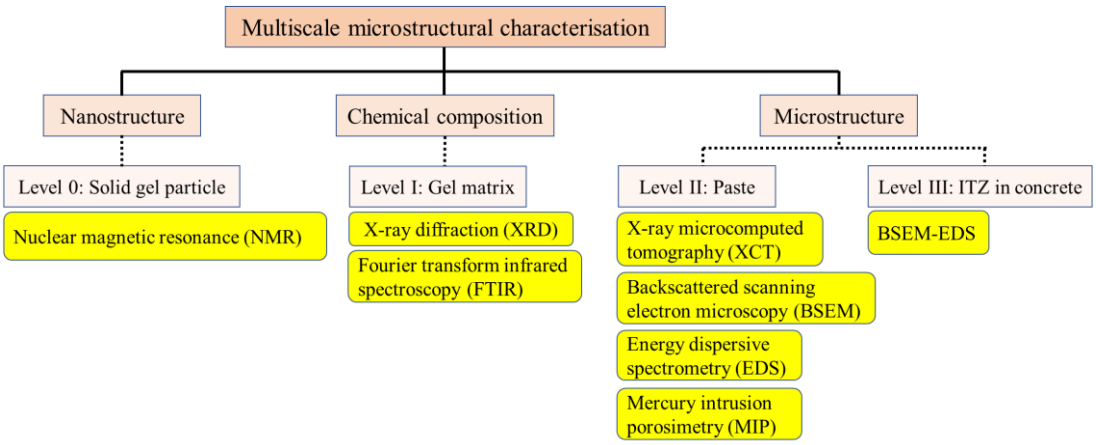

Figure 4-1 Multiscale microstructural characterisation of AAFS concrete

4.2 Representation of the multiscale microstructure of AAFS concrete

Informed by the microstructural features of AAFS concrete and the multiscale model of AAC and PC concrete developed by other researchers (Ulm et al., 2004; Šmilauer et al., 2011; Tatar et al., 2019), a schematic diagram for the multiscale microstructure of AAFS concrete is shown in Figure 4-2, where the transmission electron microscope (TEM) and SEM images were obtained from the literature (Garcia-Lodeiro et al., 2011; Puligilla and Mondal, 2013). The multiscale microstructure of AAFS concrete was identified based on four multiple length scales: Level 0, Level I, Level II and Level III.

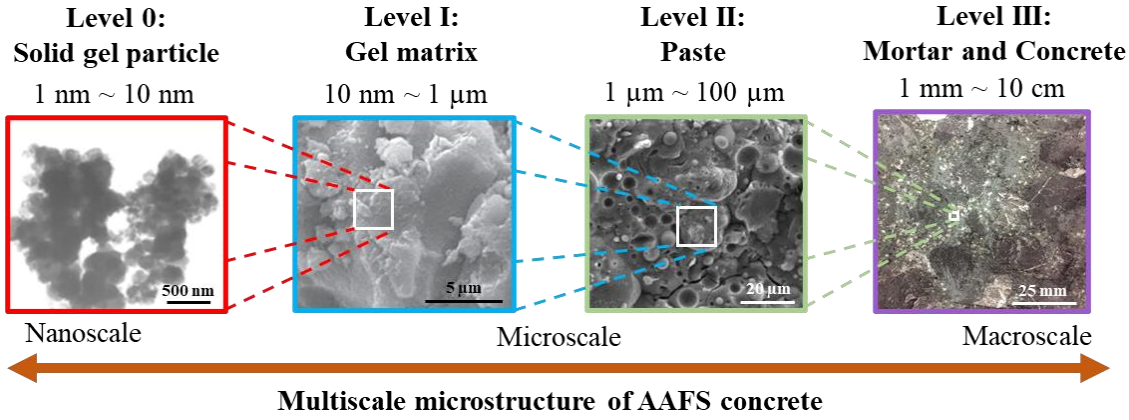

Figure 4-2 Schematic diagram of multiscale microstructure of AAFS concrete

4.2.1 Level 0 (L = 1 nm ~ 10 nm): Solid gel particle

Level 0 defines the length scale referred to the solid gel particles at nanoscale, which are mainly N-A-S-H, C-A-S-H and N-C-A-S-H sold gel particles in AAFS concrete. The N-A-S-H gel with a highly cross-linked disordered structure is generated from the reaction of fly ash, which has a three-dimensional framework of SiO_4 and AlO_4 tetrahedra linked through shared O atoms (Palomo et al., 1999). The N-A-S-H gel structure is closely related to a disordered zeolite-like structure, which has a length scale of 8 ~ 10 nm (Oh et al., 2014). The C-A-S-H gel consists of tetrahedrally coordinated silicate chains with a dreierkette structure, where each chain is composed of (3n-1) tetrahedra, similar to the C-S-H gel in PC paste (Fernández-Jiménez et al., 2003). Nevertheless, the chain length of C-A-S-H gel (up to 13 tetrahedra) is longer than that of C-S-H gel (three to five tetrahedra) (Puertas et al., 2011). It was reported that the structure of C-A-S-H gel is indicative of the co-existence of tobermorite 1.1 nm and tobermorite 1.4 nm (Puertas et al., 2011). Moreover, the hybrid solid gel called N-C-A-S-H can also be identified, as part of Na in N-A-S-H gel is replaced by the Ca released from slag (Ismail et al., 2014). The Ca-substituted N-A-S-H gel (N-C-A-S-H gel) may have a mineral feature between N-A-S-H gel and C-A-S-H gel, which retains the original 3D aluminosilicate framework structure

but tends to have a similar composition with C-A-S-H gel (Garcia-Lodeiro et al., 2011). The microstructural analysis above indicates that the size of solid gel particles of main reaction products is in the range of 1 nm ~ 10 nm, which is therefore considered as the characteristic size of Level 0 in this study.

4.2.2 Level I (L = 10 nm ~ 1 μm): Gel matrix

Level I represents the length scale corresponding to the generation of gel matrix which is agglomerated by the solid gel particles (with a length scale of 1 nm ~ 10 nm) along with the presence of gel pores with the size ranging from 2 nm to 50 nm (Keulen et al., 2018). During the alkaline activation of AAFS, the solid gel particles would appear and aggregate into clusters with the presence of gel pores. The agglomeration of these solid gel particles would create the gel-like matrix with a scale of tens to hundreds of nanometre (Šmilauer et al., 2011). Accordingly, the length scale of Level I is set in the range of 10 nm ~ 1 μm.

4.2.3 Level II (L = 1 μm ~ 100 μm): Paste

Level II denotes the length scale at paste level, which correlates to the AAFS paste consisting of the gel matrix from Level I (with a length scale of 10 nm ~ 1 μm), capillary pores and unreacted fly ash and slag particles. The capillary pores remain in the originally liquid-filled spaces with the size ranging from 10 nm to 1 μm in AAFS paste, as reported in the literature (Keulen et al., 2018). Besides, it was observed that the particle sizes of fly ash and slag cover the range between 1 μm and 100 μm (Tu et al., 2019). Therefore, the length scale of Level II is set in the range of 1 ~ 100 μm considering the microstructural features at this level.

4.2.4 Level III (L = 1 mm ~ 10 cm): Mortar and concrete

Level III stands for the length scale at mortar and concrete level, which consists of three phases: paste matrix from Level II (with a length scale of 1 μm ~ 100 μm), aggregate (fine and coarse aggregate) and the ITZ between them. The standard sands with a size of 0.08 ~ 2.00 mm manufactured according to BS EN 196-1:2016 (2016) are commonly used as fine aggregate, while the natural aggregates with size of 5 mm ~ 2 cm are generally chosen as coarse aggregates (Deb et al., 2014; Ding et al., 2018b). Accordingly, the length scale of Level III is set as between 1 mm and 10 cm regarding the microstructural features at this level.

4.3 Mix proportion

The mixture proportion of AAFS paste and concrete used in the microstructural studies was determined according to the optimal mixtures obtained in Chapter 3. Regarding the paste, the replacement ratio of slag for fly ash was 25 wt%, while the AL/P ratio, SS modulus, SH molarity, SS/SH ratio and SP/P ratio were set as 2.0, 10, 0.45, 2.0 and 0.01, respectively. In addition, the liquid/solid ratio was calculated as 0.23, where the liquid denotes the water content in SS and SH, while the solid includes the content of precursor and the solid content in SS and SH. Regarding the aggregate, the fine and coarse aggregates were set as 35% and 65% by the volume of total aggregates, respectively, in order to achieve an adequate consolidation of concrete (Kosmatka et al., 2002). It should be noted that the size of coarse aggregates was controlled between 5 mm and 10 mm, to minimise the size effects of aggregate on the microstructural studies. The mixture quantities of AAFS paste and concrete were calculated as shown in Table 4-1.

Table 4-1 Mix proportion and quantity (kg/m^3) of AAFS paste and concrete

Mixture proportion						Concrete mixture quantity						
						Paste mixture quantity						
Fly ash/ slag	AL/P ratio	SH molarity (M)	SS/SH ratio	SP/P ratio	Alkaline modulus of AL	Fly ash	Slag	SS	SH	SP	Fine aggregate	Coarse aggregate
75/25	0.45	10	2	0.01	1.13	300	100	120	60	4	622	1178

Note: AL (Alkaline activator); P (Precursor); SH (sodium hydroxide); SS (sodium silicate); SP (superplasticiser)

4.4 Mixing process

The mixing process of AAFS paste and concrete is described as follows. Firstly, fly ash, slag, fine and coarse aggregates (for concrete mixture) were dry mixed for 3 min. SS, SH and SP were then added into the mixture and mixed for another 3 min. After that, the fresh paste and concrete are immediately cast into three different moulds (see Table 4-2). The plastic cube moulds with a size of 20 × 20 × 20 mm were prepared for the NMR, XRD, BSEM, EDS and MIP tests of paste mixture, while the plastic cuboid moulds with a size of 1 × 1 × 10 mm were prepared for the XCT test of paste mixture. The plastic cylinder moulds with Φ25 × 100 mm were prepared for the BSEM and EDS test of concrete mixture. The moulds were put on the vibrating table for 2 min to remove the air bubbles and then sealed by the plastic sheet for first 24-h curing in room temperature (20 ± 2 °C). After that, the samples were demoulded and placed in the curing room (20 ± 2 °C, 95% RH) until the day of testing (see Table 4-2). It should be noted that the plastic cuboid

moulds for the XCT do not need to be demoulded because the X-ray can penetrate through the plastic mould to achieve the non-destructive test.

Table 4-2 Specimen preparations for microstructural characterisations

Mixtures	Sample	Shape	Size	Test performed	Curing age
Paste	Cube		20×20×20 mm	NMR/XRD/FTIR test BSEM/EDS/MIP test	1, 3, 7, 28 d
	Cuboid	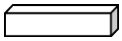	1×1×10 mm	XCT test	1, 3, 7, 28 d
Concrete	Cylinder		Φ25×100 mm	BSEM/EDS test	3, 12, 24 h 3, 7, 28 d

4.5 Sample preparation

The samples were prepared according to the requirement of different tests. For the XCT test, the samples do not need extra treatment due to its non-destructive nature, where the cuboid samples taken out from the curing room can be directly used for testing. Nevertheless, for other microstructural tests, the preparation of samples requires pre-treatment as shown in Figure 4-3, which can be divided into three steps: (i) sample cutting, (ii) reaction stopping and (iii) testing preparation.

In the first step, the small specimen in the centre of the sample was cut using a low-speed diamond saw which is equipped with a wet-cutting system. As shown in Figure 4-3a, the cuboid specimen with a size of 2 × 20 × 20 mm was cut from the paste sample, while the cylinder specimen with Φ25 × 3 mm was cut from the concrete sample.

After cutting, two different methods were applied to stop the hydration of testing samples according to their curing age (see Figure 4-3b). For the samples in the early few hours after casting (3 h), the freeze-drying method was used to stop their hydration. The indication is that this method is regarded as an effective method to instantly preserve the composition and microstructure at a specific time (Korpa and Trettin, 2006; Zhang and Scherer, 2011), which is crucial for the sample at the very early ages. Considering the experimental procedure, the specimens were immersed in the liquid nitrogen (-195 °C) for 5 min to freeze up, followed by the step that the specimens were transferred to the freeze-dryer system (-10 ± 1 °C) for 24-h drying. For the samples at the later curing ages (12 h, 24 h, 3 d, 7 d and 28 d), the solvent exchange method was applied to stop the hydration of testing samples. This method is commonly used to remove the free water inside the hardened sample without significant influences on its microstructure (Knapen

et al., 2009; Zhang and Scherer, 2011). Herein, the isopropanol solution was used as an organic solvent, which is regarded as the best-known solvent to minimize the effects on microstructure and component in cement (Zhang and Scherer, 2011). The samples were stored in the isopropanol solution for 2 d and then stored in the vacuum drying dish (20 ± 2 °C) for another 2 d.

Lastly, it can be seen from Figure 4-3c that the sample was further cut into smaller pieces of specimens and prepared for different tests. For the NMR/XRD/FTIR tests, the sample is needed to be grounded into a powder sample with a size smaller than 40 μm, whereas the MIP test needs the sample with a volume of 1 ~ 3 mm^3. For the BSEM-EDS test, the sample preparation is much more complicated, which should be well-polished to provide a smooth and flat surface. Firstly, the sample was put inside a cylinder plastic mould (with a diameter of 30 mm) and impregnated by epoxy solution (mass of epoxy resin: mass of hardening agent = 25: 3). The epoxy used here belongs to the low viscosity epoxy resin (EPO-TEK® 301-2, Epoxy Technology Inc., USA). The plastic mould was then put inside the vacuum mosaic to increase the impregnation depth of epoxy and remove the bubbles within the epoxy solution. The vacuum impregnation is essential to fill the pores of the specimen with epoxy solution before grinding and polishing, which would stabilize the microstructure and serve to withstand the stresses of grinding and polishing without alteration (Kjellsen et al., 2003). When the impregnation was finished, the plastic mould was put inside the vacuum drying dish under ambient condition (20 ± 2 °C) for the hardening of epoxy. After around 24 h, the sample with epoxy was demould and prepared for grinding and polishing. The automatic pressure polishing machine (BUEHLER, EcoMet™ 250, USA) was used to polish the sample. The rotation speed was set as 30 r/min while the loading increment was 5 N to minimize the damage on the sample during grinding and polishing. Herein, the ethyl alcohol was used as a cooling medium and lubricant. The sample was initially ground on the paper disks with a gradation of grits 400 (37 μm), 800 (19 μm), and 1200 (15.3 μm), respectively. Each grinding time was about 5 min. The sample was then polished on the polishing disks with grits of 2500 (5.5 μm), 3000 (5 μm), 5000 (2.7 μm) and 7000 (1.25 μm) with size from large to small. Each polishing step lasted approximately 15 min.

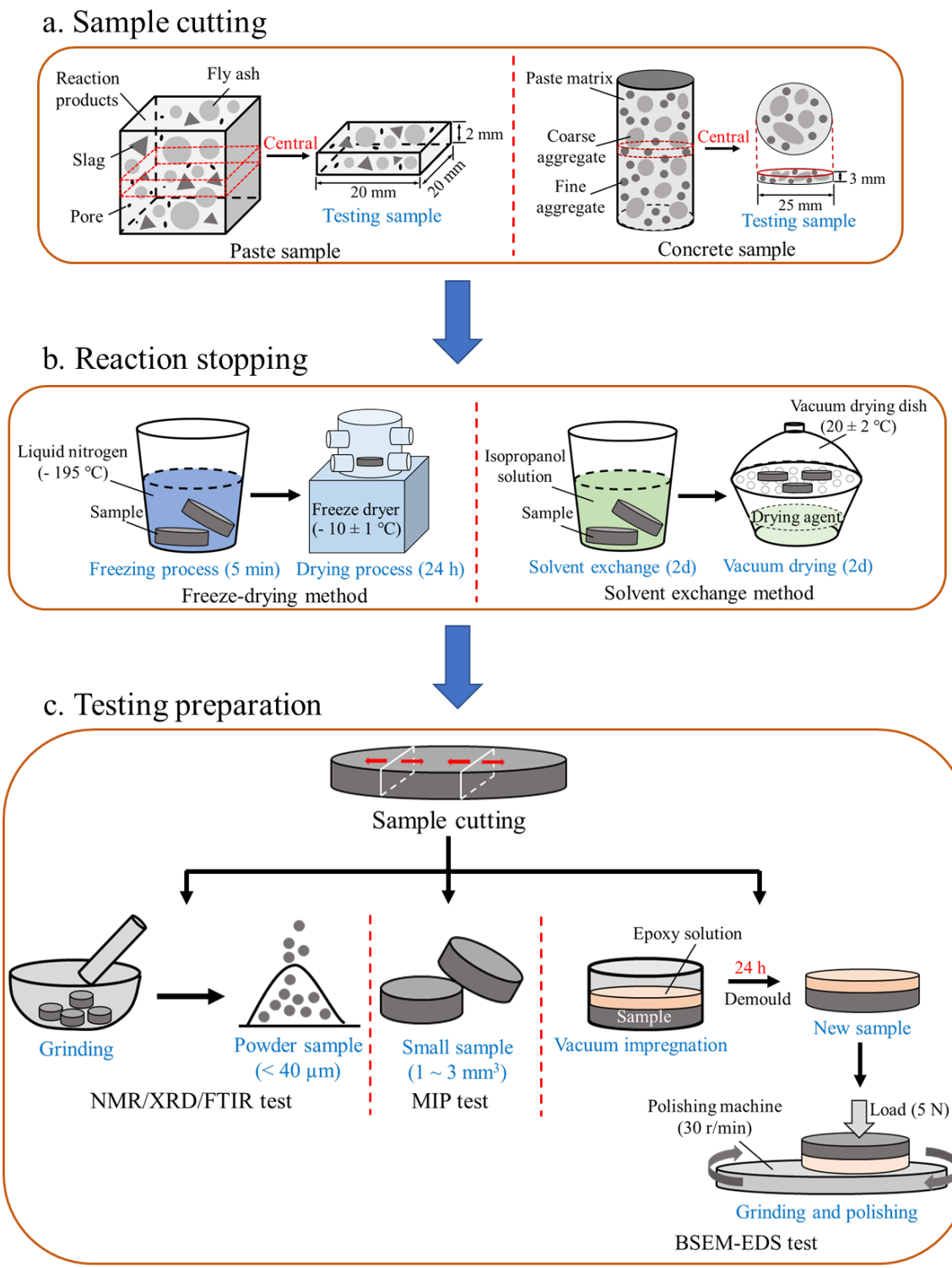

Figure 4-3 Schematic illustration of the sample preparation for microstructure tests

4.6 Test methods

4.6.1 Nuclear magnetic resonance

The nanostructure of solid gel particle was investigated using ^{29}Si NMR, which has been widely applied to qualitatively and quantitatively evaluate the nanostructure of cementitious materials (Girão et al., 2007; Justnes et al., 2020) and alkali-activated materials (Bernal et al., 2013; Gao et al., 2017b; Chen et al., 2018). The main advantage of this method is nuclear-spin selectivity, where one nuclear-spin isotope of the NMR periodic table (e.g. ^{1}H, ^{27}Al and ^{29}Si) is detected at the time, bringing informative spectra for complex multiphase systems. In addition, the resonances from these spin nuclei are sensitive to the local structural ordering and/or dynamic effects, which permits studies to not only crystalline phases but also amorphous components (Scrivener et al., 2016). ^{29}Si NMR can reveal the silicate structure in binding gels, contributing to understanding the structural compositions of reaction products at nanoscale (Gao et al., 2017b). Besides, the deconvolution of the obtained ^{29}Si NMR spectra provides a possible way for the quantitative analysis, bringing further information on the nanostructure changes, chain length and elements' ratios of binding gels (Bernal et al., 2013; Wang and Scrivener, 2003). As seen in Figure 4-4, the solid-state ^{29}Si NMR instrument (BRUKER, AVANCE 400WB, Germany) was utilized to investigate the nanostructure of solid gel particles, using the ^{29}Si resonance frequency of 79.48 MHz and the spinning speed of 5 kHz. The ^{29}Si NMR experiments applied a pulse length of 4.97 μs and a relaxation delay of 5 s with 2048 scans.

Figure 4-4 The instrument of nuclear magnetic resonance

4.6.2 X-ray diffraction

The chemical composition of gel matrix was characterised by XRD and quantified by the Rietveld refinement method, which is one of the most prominent analytical techniques in the characterisation of crystalline, fine-grained materials, such as cementitious materials (Scrivener et al., 2016). Based on this test, different phases can be qualitatively analysed according to a comparison of the peaks in a measured XRD pattern to a database called powder diffraction file containing peak patterns of known phases.

In addition, the Rietveld-based quantitative X-ray diffraction (QXRD) is mostly used for quantifying the mineralogical composition of the sample, which is based on qualitative phase analysis and the relative arithmetic. The principle of the Rietveld method is using the least-squares approach to refine a theoretical line profile until it matches the measured profile and to quantify the phase distribution based on the XRD pattern (Young et al., 1977). The internal standard method is regarded as the most common approach to QXRD analysis of samples containing amorphous phases (Scarlett et al., 2002). Here, the absolute concentration of the crystalline phases is determined, and the amorphous content is estimated by difference. The powder sample is required to be spiked with a known weight fraction of a crystalline standard material, accordingly, the quantitative phase analysis can be normalised (Madsen Ian et al., 2011). The standard material should be of known crystalline and should not be present in the sample. Thus, in this research, 10 wt.% corundum (α-Al_2O_3) was used as the crystalline standard materials, which is estimated to be ~99% crystalline. It should be noted that the sample and standard should be generally ground together along with the dispersion solvent to ensure the homogeneous mixing between these two materials. In this study, 4.5 g testing powder sample was mixed with 0.5 g corundum in the agate mortar and ground along with the addition of isopropyl alcohol solution, for 10 min. After that, the agate mortar with the sample is placed in the vacuum drying oven (25 °C) for 24 h to obtain the dried sample for QXRD test. As shown in Figure 4-5, a benchtop XRD instrument (Rigaku, Miniflex600, Japan) is utilised for the XRD and QXRD test, using CuKα X-ray (λ = 1.789Å) and 2θ configuration in the range of 5° ~ 65° with a step size of 0.02°.

Figure 4-5 The instrument of X-ray diffraction

4.6.3 Fourier transform infrared spectroscopy

The modification of amorphous phase in AAFS pastes was characterized with the help of FTIR, which can help to compensate for the phenomenon that cannot be analysed based on XRD (Zhang et al., 2012b; Ismail et al., 2014). FTIR is an analytical technique used to identify organic, polymeric and inorganic materials, in which the infrared light is utilised to scan test sample and observe its chemical properties (Griffiths and Haseth, 2007). When the infrared radiation passes through a sample, some radiation would be absorbed and some pass through. The absorbed radiation is converted into rotational and/or vibrational energy by the sample molecules. The resulting signal at the detector presents as a spectrum, typically from 4000 cm^{-1} to 400 cm^{-1}, which represents the molecular fingerprint of the sample (Griffiths and Haseth, 2007). Since the unique spectral fingerprint from each molecule or chemical structure is unique, FTIR is regarded as a great tool for chemical identification. Here, an FTIR instrument (Shimadzu, IRTracer-100, Japan) with 16 times scanning from 4000 to 400 cm^{-1} and a resolution of 4 cm^{-1} was used to characterise the gel matrices (see Figure 4-6). It should be noted that the powder sample should be further ground with a size smaller than 25 μm in order to avoid the scattering of mid-infrared.

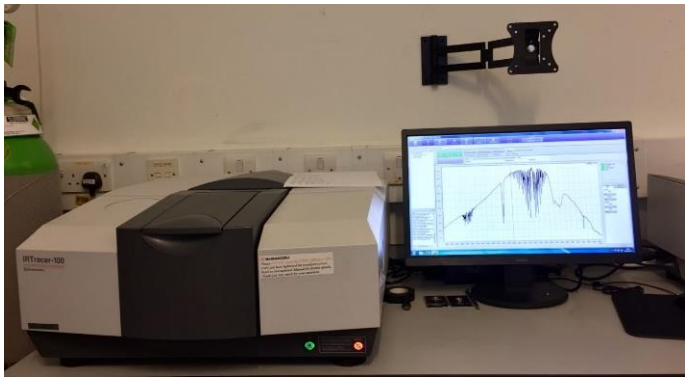

Figure 4-6 The instrument of Fourier transform infrared spectroscopy

4.6.4 X-ray microcomputed tomography

The microstructure evolution of paste matrix was in-situ monitored with the assistant of XCT, which provides a potential opportunity to non-destructively explore the reaction and microstructure of cementitious materials or alkali-activated materials, such as the time-dependent reaction process, dissolution of raw particles, subsequent formation and development of reaction products, and pore structure features (Gastaldi et al., 2012; Provis et al., 2012; Bossa et al., 2015; Hu et al., 2016). This testing method has been successfully demonstrated by the author's previous research to provide a platform for real-time monitoring without interfering with the chemistry or morphology of the inner microstructure, while offering 3D-imagery for comprehensive analysis (Dong et al., 2017; Fang et al., 2018; Fang et al., 2019).

The foundation of XCT is based on the X-ray attenuation, in which the x-ray attenuation is the function of the photon energy and the elemental composition of the material (McCullough, 1975). As shown in Figure 4-7, when a narrow beam of x-ray photons with a certain incident intensity passes through the testing specimen, the incident intensity is attenuated as transmitted intensity since the photons are absorbed and scattered by the specimen. The X-ray photons escaping from the sample are captured by the detector, from which the projection is created based on intensity measurements. Each projection is defined according to a specific angular position. From radiographs collected at different angles that compose a full rotation, a 3D reconstruction can be produced as a back-projection, the image of which is a 3D matrix composed of linear attenuation coefficients (voxels). In this way, the variation in voxel intensity with X-ray attenuation value (Hounsfield units), as reflected in the projected image, helps to distinguish structural and material characteristics. In addition, the X-ray attenuation value is quantified on a greyscale with 256 (0-255) intensity grades to provide a high-quality presentation.

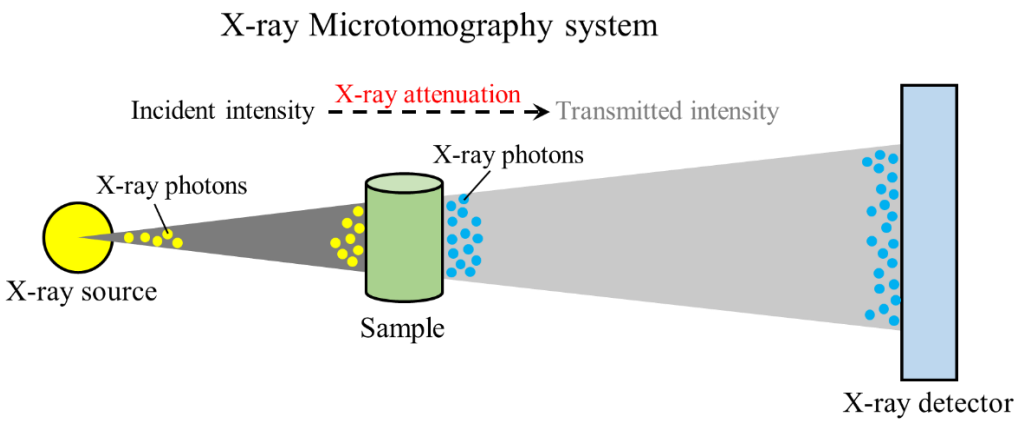

Figure 4-7 Fundamental concept of X-ray microcomputed tomography test

As seen in Figure 4-8, the XCT instrument called XRadia Micro XCT-400 scope (Zeiss, Germany) was used to make the XCT scans, which consists of a microfocus X-ray emitter, a rotation stage, and an image intensifier detector with charge-coupled device (CCD) camera. A special sample stage was used to tightly hold the testing sample, which can make sure the sample was set in the same position at each test. XCT scans were performed at 59 kV and 150 μA, while the magnification was 0.4×. The total scanning time for each test is about 7 h, in which 2501 projections (angle step of 0.144° from -180° to 180°) were acquired with a 10 s exposure time per projection. The field of view was 1.5 mm (x = y = z) and the spatial resolution (voxel size) was 1.56 μm (x = y = z).

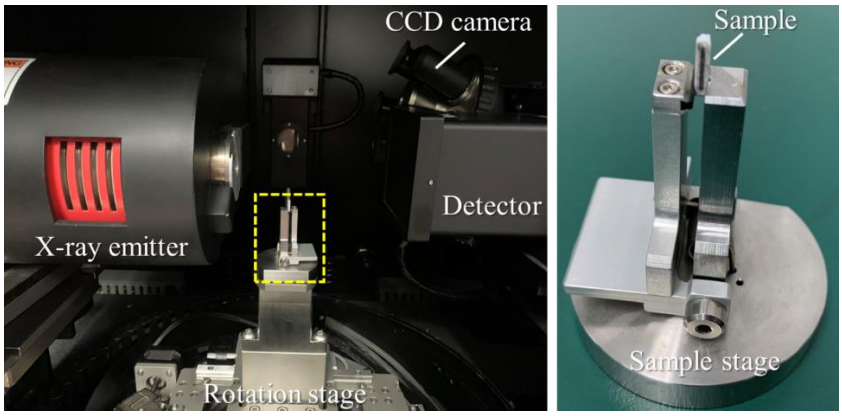

Figure 4-8 Experimental setup of X-ray microcomputed tomography test

4.6.5 Backscattered scanning electron microscopy - energy dispersive spectrometry

The phase composition and distribution within microstructure in paste and concrete were characterized with the help of BSEM along with EDS, which is the commonly used technique to study the microstructure of cementitious materials, including its surface morphology, composition and phase distribution (Scrivener et al., 2016). The principle for the formation of images in BSEM/EDS test is based on the interaction between the electron beam and the atoms in the sample (Goldstein et al., 2018). Three most important signals generated in scanning are secondary electrons (SE), back-scattered electrons (BSE) and characteristic X-rays, which corresponds to the three types of images: SEM images, BSEM images and elemental X-ray maps, respectively. Generally, SEM image and BSEM image are used in the microstructure analysis. SEM image is used to study the surface morphology as the intensity of SE depends on the local inclination of the specimen surface, accordingly, it can provide surface topographic data. BSEM image is used to detect chemical composition based on the difference of grey value since the intensity of BSE depends on the local atomic number of the specimen. Normally, each BSEM image is normalized to 8-bit grey values, which consists of 256 possible levels (0-

255) of grey value. The elements with a higher atomic number appear lighter grey in the image due to their higher backscatter electrons.

EDS is an analytical technique used for the elemental analysis or chemical characterization of a sample. The principle of EDS test is based on the interaction of X-ray excitation and a sample, which is similar to other X-ray instruments (e.g. XCT). Since each element has a unique atomic structure, a unique set of peaks is used to characterize the elemental composition of a sample. According to the scanning method, EDS can be divided as spot scanning, line scanning and map scanning.

As shown in Figure 4-9, a field emission scanning electron microscopy equipment (ZEISS, GeminiSEM, Germany) equipped with BSEM and EDS was used for microstructure examination. Before testing, the samples were sputter-coated with a layer of carbon under vacuum to increase conductivity. The BSE tests were operated at 10 kV voltages with a working distance of 8.9 mm. The BSEM images (1024×768 pixels, pixel size of 0.25 μm) with a magnification in the wide range of 30× and 4000× were captured at a constant brightness (53.9%) and contrast (54.3%) for reproducibility. The EDS analysis was performed at the beam energy of 15 keV with the probe current of 600 pA and the beam spot size of roughly 450 nm. The working distance of 8.5 mm and a take-off angle of 35° were used in this study. The counting rate of 50000 counts per analysis with dead times of about 30% and the acquisition time of 50 s were chosen.

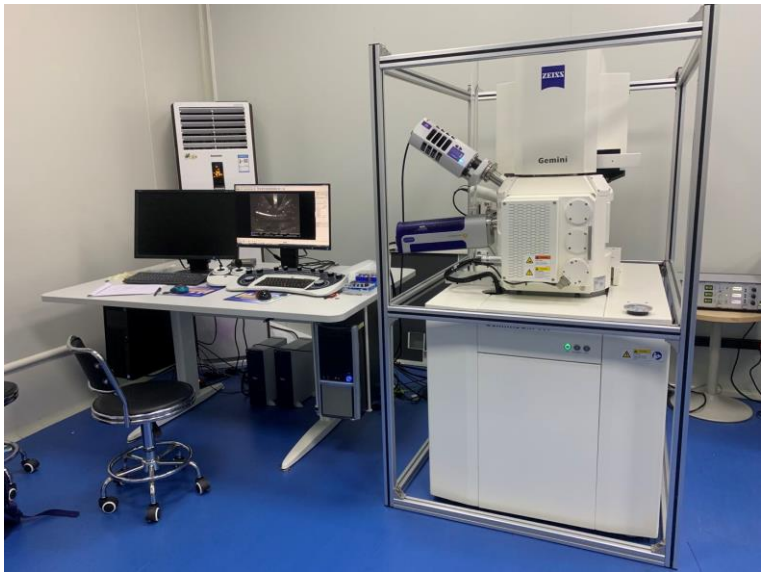

Figure 4-9 The instrument of scanning electron microscopy

4.6.6 Mercury intrusion porosimetry

The pore structure of paste matrix was characterised by MIP, which is commonly used to characterise the pore structure of porous materials (Zhou et al., 2010; Ma, 2014; Gu et al., 2019). The main advantages of this technique are its easy operation and the outcome data cover a wide range of pore size, from 6 nm to 350 μm. This technique is based on the intrusion of a nonwetting fluid (mercury) into porous structures under increasing pressure. As shown in Figure 4-10, the MIP instrument (Micrometitics Instrument Ltd, AutoPore IV 9500, USA) is used in this research, where the pressure between 0 and 420 MPa was applied. The surface tension of mercury was set as 0.485 N/m, while the contact angle between mercury and pore surface was set as 130° according to previous studies (Kaufmann et al., 2009; Ma, 2014).

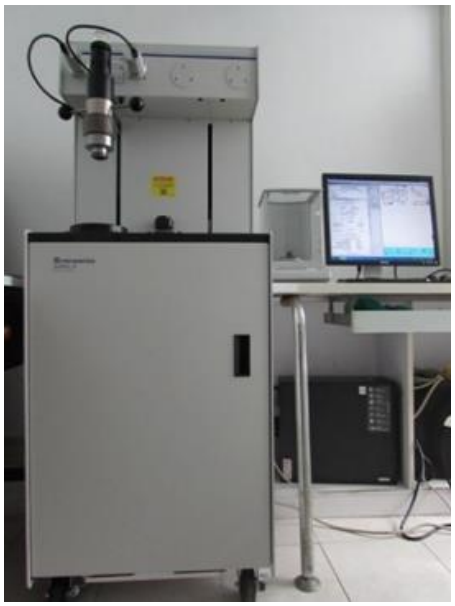

Figure 4-10 The instrument of mercury intrusion porosimetry

4.7 Results and discussion

4.7.1 Nanostructure of solid gel particle

Q^n(mAl) structural units are commonly used in ^{29}Si NMR spectra to identify the chemical environment of silicon tetrahedra of phases, where *n* represents the number of oxygen bridges between each silicon tetrahedral unit and other silicon atoms, and *m* is the number of aluminium tetrahedra taking place in bridging position (Singh et al., 2005). As shown in Figure 4-11, Q^0 unit represents the isolated silicon tetrahedron; Q^1 unit describes the silicon tetrahedron that only connects with another silicon tetrahedron; while Q^2 unit stands for the silicon tetrahedron connecting to other two silicon tetrahedrons; Q^3 unit denotes a silicon tetrahedron that connects with other three tetrahedrons, having a chain

branching, double-chain polymerisation, or a layered structure; and Q^4 unit represents a silicon tetrahedron linking with other three tetrahedrons to form a three-dimensional network (Lippmaa et al., 1980). The obtained spectra can be deconvolved to make a quantitative analysis and explore the changes in silicate structure of different reaction products (Gao et al., 2017b). Herein, the overlapped peaks were deconvolved using a statistical analysis software called 'PeakFit', where the Gaussian line model was applied.

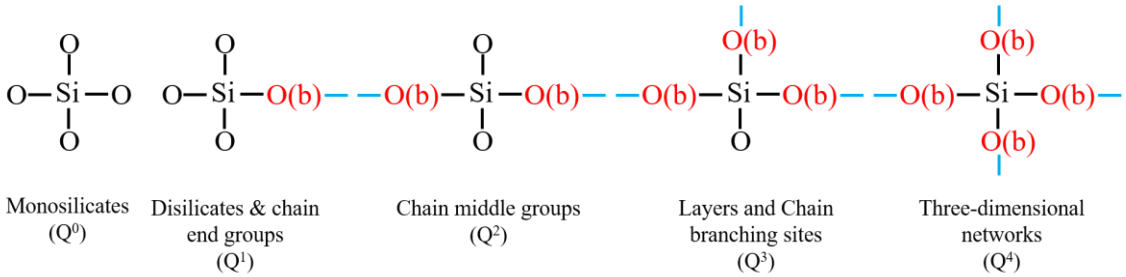

Figure 4-11 Structural schematic diagram of Q^n in solid silicates (O(b) represents bridging oxygen)

The ^{29}Si NMR spectra of raw materials, i.e. fly ash and slag, were presented and deconvolved in Figure 4-12a and b. The spectrum of fly ash shows an overlapped peak between -80 and -120 ppm, indicating the existence of different Q^4 structures (see Figure 4-12a). The overlapped peak can be deconvolved into five Q^4 structures of Q^4(4Al) (-87 ppm), Q^4(3Al) (-95 ppm), Q^4(2Al) (-103 ppm), Q^4(1Al) (-110 ppm), and Q^4(0Al) (-116 ppm). Different types of Q^4 structures can be attributed to the presence of amorphous and crystalline phases (Palomo et al., 2004). Regarding slag, only a broad peak between -55 and -95 ppm can be found, centred at around -75 ppm, which corresponds to the Q^0 and Q^1 sites, implying the presence of high proportion of amorphous phase and low content of crystalline phase (see Figure 4-12b) (Gao et al., 2017b).

Figure 4-12c presents the ^{29}Si NMR spectrum of AAFS paste, which was deconvolved into serval peaks based on the information available for AAFS (Bernal et al., 2013; Ismail et al., 2014; Gao et al., 2017b), and the peak positions were held constant for all mixtures. It should be noted that it is unlikely to separate the remnant precursors (i.e. fly ash and slag) and reaction products in ^{29}Si NMR spectrum due to the presence of vitreous phases within precursors which share the similar Q^n(mAl) structural units with reaction products. Nevertheless, since the Q sites from the original precursors can be assumed to be unchanged, the relative changes of Q sites at different curing ages can be considered as the development of reaction products. Using this observation, it is possible to characterise the evolution of reaction products in the ^{29}Si NMR spectrum.

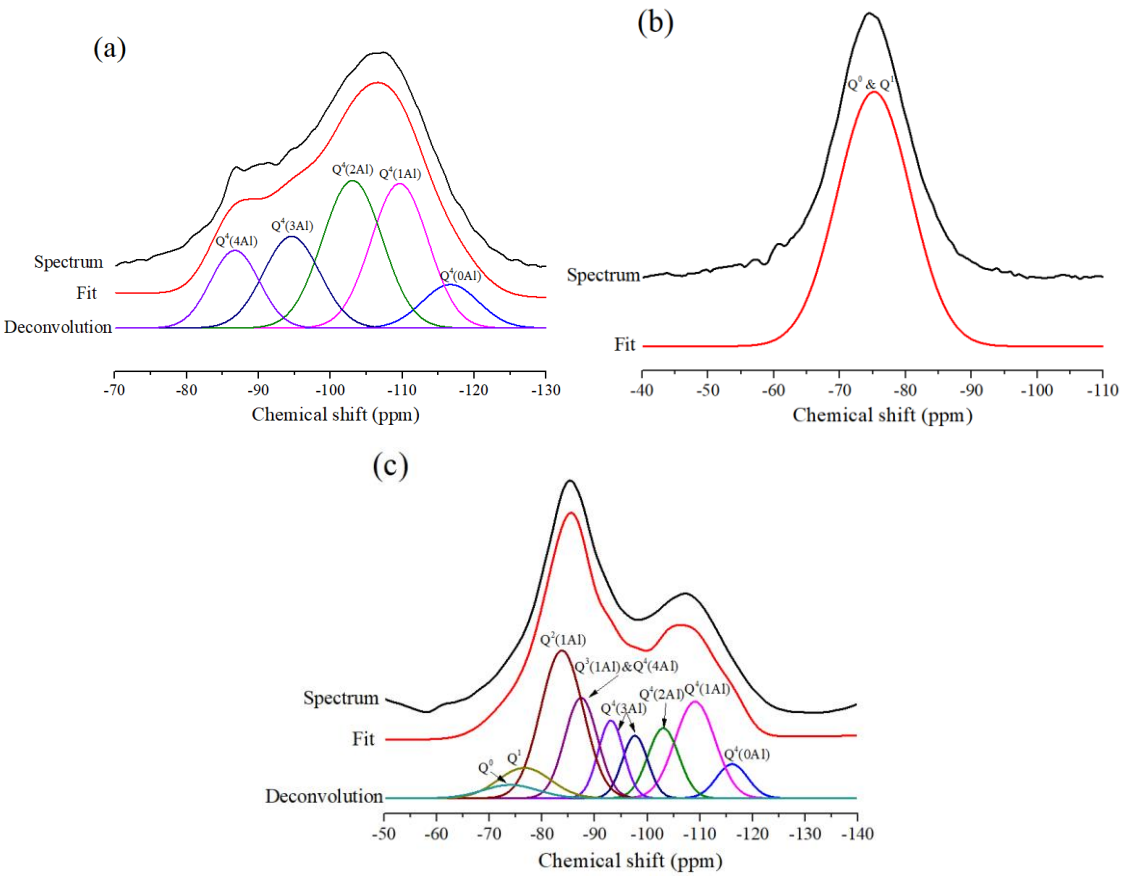

Figure 4-12 ^{29}Si NMR spectra of (a) fly ash, (b) slag, and (c) AAFS paste (t = 28 d)

The deconvolution results and relative quantification of all mixtures are summarised in Table 4-3. The Al/Si ratios of N-A-S-H gels, N-C-A-S-H gels and C-A-S-H gels were also calculated to evaluate the change in the chemical composition of solid gel particles (Myers et al., 2013; Gao et al., 2017b). Here, the AAFS mixture cured for 28 d is taken as an example to identify different Q^n(mAl) structural units in AAFS paste. The spectrum exhibits a broad peak between -60 and -90 ppm, representing a large amount of Q^0, Q^1 and Q^2 sites from the initial slag and the depolymerised reaction products. The wide coverage area with a range of -90 and -120 ppm corresponds to the Q^4 sites, which are mainly obtained from fly ash and its highly polymerised reaction products. More specifically, The peak at -74 ppm is associated with the Q^0 site, indicating the presence of unaltered crystalline phases (i.e. merwinite and melilite) in the original slag (Haha et al., 2011; Abdalqader et al., 2016; Gao et al., 2017b). The Q^1 site located at -77 ppm is assigned to the end-of-chain silicate tetrahedral within C-A-S-H gels (Gao et al., 2017b). The Q^2(1Al) site located at -83 ppm is corresponding to the middle-of-chain silicate within C-A-S-H gels (L'Hôpital et al., 2015). The peak at -88 ppm refers to the Q^3(1Al) and Q^4(4Al) sites due to the overlapping of resonances within this region (Engelhardt and Michel, 1987), which is assigned to the coexistence of C-A-S-H gels and N-A-S-H gels,

presenting as a highly cross-linked N-C-A-S-H gel (Engelhardt and Michel, 1987; Ismail et al., 2014). Normally, Q^3(1Al) site is related to the alumina-modified C-S-H gels (C-A-S-H gels) (Walkley et al., 2016a), while Q^4(4Al) site is assigned to the Al-rich N-A-S-H gels (Walkley et al., 2016b). Both peaks at -93 and -97 ppm are denoted as Q^4(3Al) and assigned to the Al-rich N-A-S-H gels, which belong to the reactive and highly polymerised aluminate phases (Gao et al., 2017b). The Q^4(2Al) and Q^4(1Al) sites represent the more stable Si-rich N-A-S-H types gels, which are located at -103 and -109 ppm, respectively (Park et al., 2018). Finally, the peak at -116 ppm is associated with the Q^4(0Al) site that corresponds to the presence of crystalline phases including quartz, mullite and maghemite in the original fly ash (Chancey et al., 2010; Ismail et al., 2014; Gao et al., 2017b).

Table 4-3 Deconvolution results (area percentage) of ^{29}Si NMR spectra of AAFS pastes

	Unreacted slag	Reaction products							Unreacted fly ash
		C-A-S-H		N-C-A-S-H	N-A-S-H (Al-rich)		N-A-S-H (Si-rich)		
Labels	Q^0	Q^1	Q^2(1Al)	Q^3(1Al) & Q^4(4Al)	Q^4(3Al)		Q^4(2Al)	Q^4(1Al)	Q^4(0Al)
	-74	-77	-83	-88	-93	-97	-103	-109	-116
1-d	3.45	18.15	25.41	11.14	6.69	5.21	9.09	14.87	5.99
3-d	3.12	15.69	27.24	10.40	8.36	4.68	9.20	17.90	3.41
7-d	3.38	10.24	27.79	13.75	10.03	3.76	8.88	16.96	5.21
28-d	3.22	7.04	27.87	14.57	8.73	7.03	9.66	17.17	4.71

Note: Unreacted slag corresponds to the unaltered phases in the original slag; Unreacted fly ash corresponds to the unaltered phases in the original fly ash.

The ^{29}Si NMR spectra of AAFS pastes at different curing ages are illustrated in Figure 4-13. As the curing age increases from 1 d to 28 d, the broad peak located at -84.23 ppm is slightly shifted to a higher value (-85.67 ppm), whereas the broad band centred at -107.2 ppm is slightly shifted to a lower value (-105.9 ppm). This indicates the increase of polymerisation degree and cross-linking of gels over time. More specifically, the Q^n(mAl) structural units of different phases are quantified and shown in Figure 4-14 to further evaluate the nanostructure change. It can be found that there is a relatively high amount of Q^1 sites (18.15%) within C-A-S-H gels at 1 d. As the reaction continues, it is decreased significantly to 7.09% at 28 d, while the content of Q^2(1Al) sites is increased steadily from 25.41% to 28.06%. This is mainly because of the dissolution of more silicon and aluminium monomers from fly ash and slag, which would enhance the gel polymerisation and lead to the chain in C-A-S-H gels with more links. Additionally, with the increase of

curing age from 1 d to 28 d, an increase in the amount of Q^3(1Al) and Q^4(4Al) sites from 11.14% to 14.57% can also be observed, which indicates a higher degree of polymerisation and cross-linking within N-C-A-S-H gels at later curing ages. Moreover, the polymerisation degree of N-A-S-H gels is also improved with the increase of curing age. The amount of Q^4(3Al) sites and Q^4(1Al) sites increases from 11.90% (1 d) to 15.76% (28 d) and from 14.87% (1 d) to 17.17% (28 d), respectively, while the Q^4(2Al) sites remain stable at around 9% during curing process. The content of Q^0 sites in unreacted slag is stable at around 3.2% at different curing ages, which is related to the presence of unaltered phases (i.e. crystalline phases) in the original slag. Nevertheless, the content of Q^4(0Al) sites in unreacted fly ash is fluctuant between 3.41% and 5.99% at these curing ages, which can be attributed to the heterogeneity of the unaltered phases in the original fly ash.

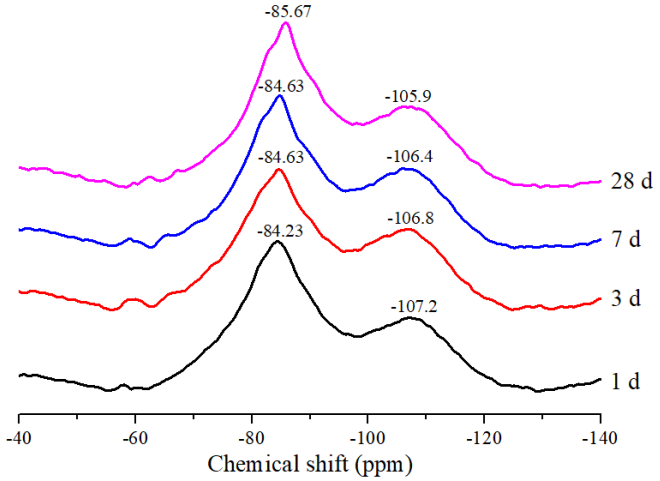

Figure 4-13 ^{29}Si NMR spectra of AAFS pastes at different curing ages

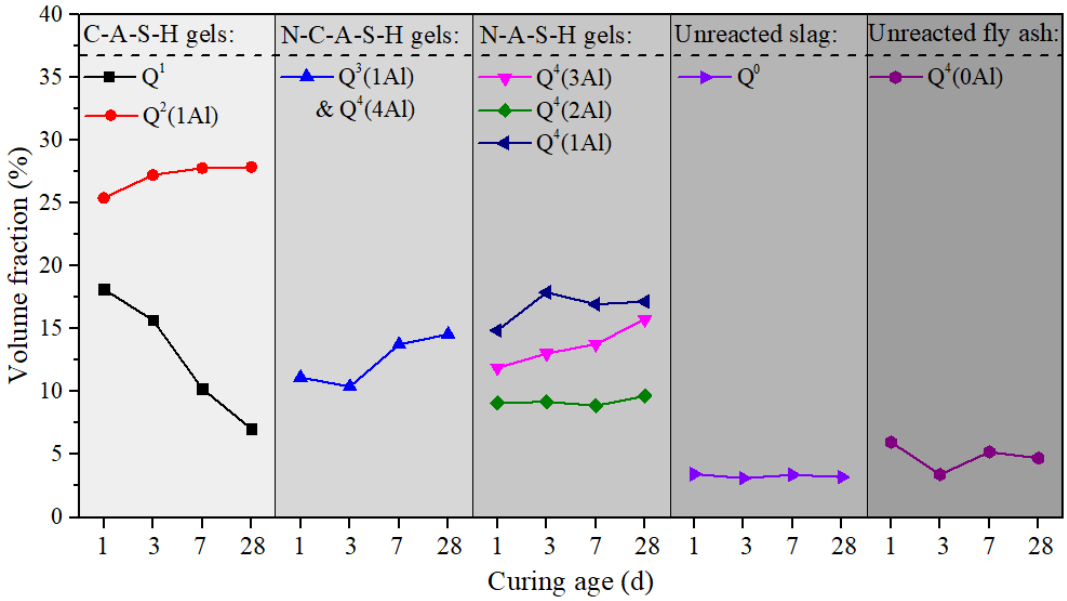

Figure 4-14 Deconvolution results of ^{29}Si NMR spectra of AAFS pastes at different curing ages

Finally, the Al/Si ratios of N-A-S-H gels, N-C-A-S-H gels and C-A-S-H gels can be calculated using the following equations (Myers et al., 2013; Gao et al., 2017b):

$$Al/Si_{(N\text{-}A\text{-}S\text{-}H)} = \frac{\sum_{n=0}^{4} \frac{n}{4} Q^4(nAl)}{\sum_{n=0}^{4} Q^4(nAl)} \quad (4-1)$$

$$Al/Si_{(N\text{-}C\text{-}A\text{-}S\text{-}H)} = \frac{Q^3(1Al)}{Q^1 + Q^2 + Q^2(1Al) + Q^3 + Q^3(1Al)} \quad (4-2)$$

$$Al/Si_{(C\text{-}A\text{-}S\text{-}H)} = \frac{\frac{1}{2} Q^2(1Al)}{Q^1 + Q^2 + Q^2(1Al)} \quad (4-3)$$

The Al/Si ratios of different reaction products are presented in Table 4-4. It can be observed that the Al/Si ratio of N-A-S-H gels is higher than that of C-A-S-H gels and N-C-A-S-H gels, regardless of curing age. Nevertheless, as the curing age increases from 1 d to 28 d, the Al/Si ratios of C-A-S-H gels and N-C-A-S-H gels are increased steadily from 0.29 to 0.40 and from 0.20 to 0.29, respectively, while the Al/Si ratio of N-A-S-H gels remains stable at around 0.5. This suggests that the chemical composition of N-A-S-H gels is stable during the curing process, while that of C-A-S-H gels and N-C-A-S-H gels are changed along with the substitute of aluminate species.

Table 4-4 Al/Si ratio of different reaction products in AAFS paste

Labels	Al/Si ratio of C-A-S-H	Al/Si ratio of N-C-A-S-H	Al/Si ratio of N-A-S-H
1-d	0.29	0.20	0.53
3-d	0.32	0.20	0.54
7-d	0.36	0.27	0.56
28-d	0.40	0.29	0.57

4.7.2 Chemical composition of gel matrix

The chemical composition of gel matrix was characterised by two different testing methods, including XRD and FTIR, as AAFS phase consists of crystalline (order) and amorphous (non-order) phases. Here, XRD was mainly used to characterise the crystalline phases, while FTIR was applied to study the bonding environments in non-crystalline (amorphous) phases.

4.7.2.1 X-ray diffraction

The XRD analysis can provide some information on the development of different crystalline phases and the total amount of amorphous phases, which helps to understand the chemical composition of gel matrix. Figure 4-15 shows the XRD patterns of raw materials (fly ash and slag) and reaction products, which are analysed by a software called

HighScore. Using this software, the peaks in XRD patterns can be searched and matched according to the known reference patterns. Afterwards, the relative fraction of identified phases was calculated according to related algorithms, as shown in Table 4-5. Firstly, the weight fraction W_α of the crystalline phases present in the testing sample (raw material + crystalline standard material) is estimated by the algorithm of Hill and Howard as shown in Eq. 4-4 (Hill and Howard, 1987).

$$W_\alpha = \frac{S_\alpha (ZMV)_\alpha}{\sum_{j=1}^{n} S_j (ZMV)_j} \qquad (4-4)$$

where S_α is the Rietveld scale factor for phase α, ZM is the mass of the unit cell contents, V is the volume of the unit cell and n is the number of phases in the analysis.

After that, the apparent weight fractions of different crystalline phases can be corrected proportionately according to Eq. 4-5.

$$W_{\alpha\,(correted)} = W_\alpha \frac{W_{s\,(known)}}{W_{s\,(measured)}} \qquad (4-5)$$

where $W_{\alpha\,(correted)}$ is the corrected weight fraction of phase α, W_α is the measured weigh fraction of phase α, $W_{s\,(known)}$ is the known weight fraction of the standard material in the sample, and $W_{s\,(measured)}$ is the measured weight fraction of the standard material.

Once the corrected weight fractions of crystalline phases have been calculated, the weight fraction of amorphous $W_{amorphous}$ can be derived from:

$$W_{amorphous} = 1 - \sum_{j=1}^{n} W_{j\,(corrected)} \qquad (4-6)$$

where $W_{amorphous}$ is the weight fraction of amorphous material in the testing sample (raw material + crystalline standard material) and $W_{j\,(correted)}$ is the corrected weight fraction of phase j.

Finally, the real weight fraction of phase in raw material can be calculated according to:

$$W_{\alpha\,(real)} = W_{\alpha\,(corrected)} \times \frac{1}{1 - W_{s\,(known)}} \qquad (4-7)$$

where $W_{\alpha\,(real)}$ is the real weight fraction of phase α in raw material, $W_{\alpha\,(correted)}$ is the corrected weight fraction of phase α and $W_{s\,(known)}$ is the known weight fraction of the standard material in the sample.

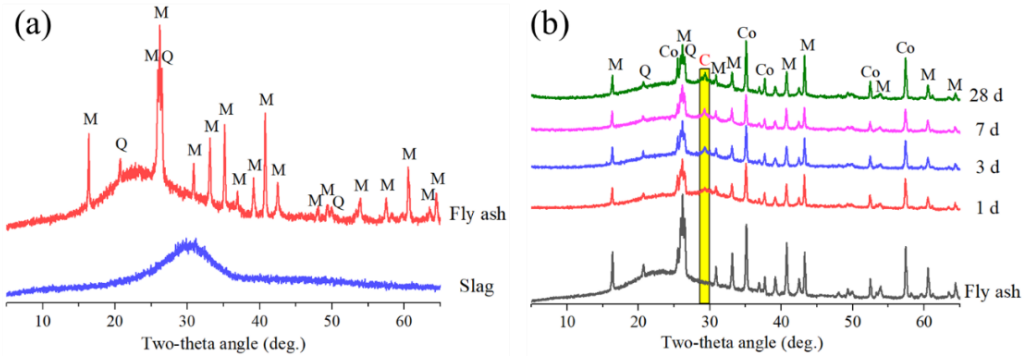

Figure 4-15 XRD pattern of (a) raw materials (fly ash and slag) and (b) AAFS pastes (M=mullite (PDF No: 01-070-3372), Q=quartz (PDF No: 01-089-8937), Co=corundum (PDF No: 01-075-0782), C=crystalline C-(A)-S-H gels)

Table 4-5 Mineralogical compositions of raw materials and AAFS paste

Labels	Phases			
	Mullite (PDF No. 01-070-3372)	Quartz (PDF No. 01-089-8937)	Crystalline C-(A)-S-H gels	Amorphous
Fly ash	39.24	7.89	-	52.87
Slag	-	-	-	> 95
1 d	24.77	4.30	1.55	69.38
3 d	24.90	4.54	2.68	67.88
7 d	31.76	8.62	2.71	56.91
28 d	19.79	3.79	2.10	74.32

Note: The amorphous phase includes the amorphous structures in the unreacted raw materials and the generated amorphous structures in the reaction products, mainly N-A-S-H and C-A-S-H gels

It can be seen from Figure 4-15a that fly ash consists of a majority of amorphous phases (see the broad 'hump' recorded between 2θ = 15° and 35°) and a minority of crystalline phases mainly with mullite ($Al_6Si_2O_{13}$, PDF No. 01-070-3372) and quartz (SiO_2, PDF No. 01-089-8937). Slag contains primarily amorphous phases corresponding to the 'hump' of 2θ = 25°~35°. The location of the amorphous hump is different between fly ash and slag due to the presence of different amorphous phases (Ismail et al., 2014).

The XRD patterns of AAFS paste at different curing ages are presented in Figure 4-15b. It can be observed that the crystalline phases (mullite and quartz) presented in raw fly ash are also identified in the reacted paste. Nevertheless, the relative intensities of these two crystalline phases are decrease in the reacted paste due to the formation of new amorphous phase and the mixing of slag with amorphous phases. In addition, a new broad and diffusive hump around 2θ = 29.5° is observed in the AAFS pastes, comparing with the XRD patterns of fly ash. This new hump is associated with the formation of crystalline C-(A)-S-H gels from the reaction of slag (Puligilla and Mondal, 2013; Walkley et al., 2016b; Nath and Kumar, 2017). The diffusive hump of crystalline C-(A)-S-H gels appears and magnifies as the curing age increases from 1 d to 7 d, where the percentage of crystalline C-(A)-S-H gels rises from 1.55% (1 d) to 2.71% (7d) (see Table 4-5). This

corresponds to the quick dissolution of slag at early ages, which would release the soluble calcium and lead to the formation of C-(A)-S-H gels. Nevertheless, the amount of crystalline C-(A)-S-H gels is declined to 2.10% at 28 d due to the relatively low amount of slag (25% of precursor), leading to the insufficient calcium for the formation of C-(A)-S-H gels. On the contrary, Table 4-5 shows that the content of amorphous phases is dropped from 69.38% to 56.91% during the early 7 d, relating to quick dissolution of slag which contains primarily amorphous phase (> 95%). However, it boosts up to 74.32% at 28 d, which might attribute to the ongoing polymerization progress would promote the formation of disorder products (e.g. N-A-S-H gels) since the high amount of fly ash (75% of precursor) can provide sufficient silicate and aluminate species for this reaction. It should be noted that it is impossible to differentiate the vitreous unreacted phase of precursors (fly ash and slag) from the amorphous reacted products (e.g. N-A-S-H and C-A-S-H gels) based solely on the XRD test.

4.7.2.2 Fourier transform infrared spectroscopy

Figure 4-16 presents the infrared spectra of raw materials (fly ash and slag) and the reacted paste at different curing ages. It can be seen from Figure 4-16a that the band between 1100 cm^{-1} and 900 cm^{-1} is related to the asymmetric stretching vibrations of Si-O-T bonds (T: tetrahedral Si or Al) (Abdalqader et al., 2016). The bands of fly ash and slag are centred at different positions (1050 cm^{-1} in fly ash and 900 cm^{-1} in slag), attributing to the chemical and structural differences between these two materials (Ismail et al., 2014). For fly ash, the band at 795 cm^{-1} correlates to the asymmetric stretch of quartz, while the shoulder at 545 cm^{-1} is associated with the Al-O stretch of mullite (Beran et al., 2001). The band at 435 cm^{-1} is related to the bending vibration of SiO_4. Regarding the spectra of slag, the band at 670 cm^{-1} represents the Si-O-Si bending vibration modes, while the band at 460 cm^{-1} is correlated to the SiO_4 bending modes.

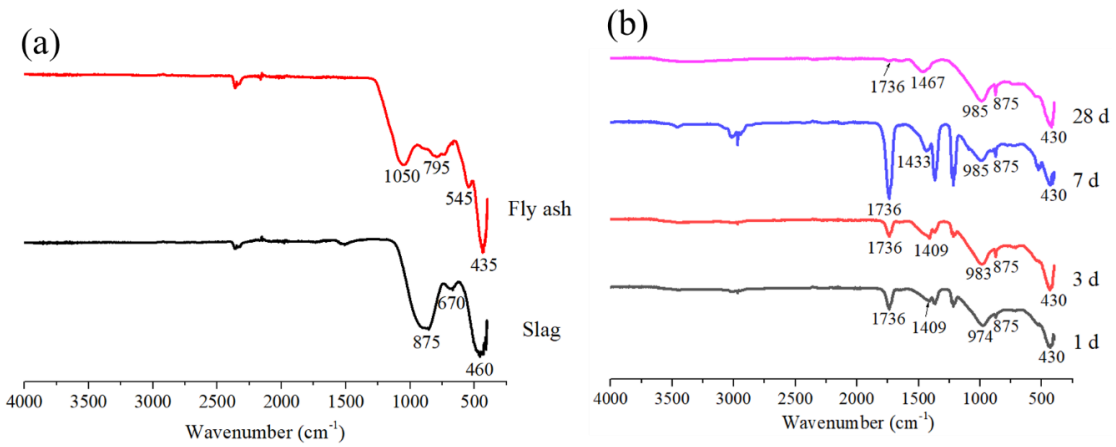

Figure 4-16 FTIR spectra of (a) raw materials (fly ash and slag) and (b) AAFS pastes

As shown in Figure 4-16b, the alkali-activation produces a broad intense band at around 980 cm^{-1} in the spectra, attributing to the asymmetric stretching vibrations of Si-O-T bonds (T: tetrahedral Si or Al) in the chain structure of reaction products (Abdalqader et al., 2016). The position of the main band for these reaction products (i.e. 980 cm^{-1}) is at a lower wavenumber than that for N-A-S-H gels (i.e. 1020 cm^{-1}) but at a higher wavenumber than that for C-A-S-H gels (i.e. 950 cm^{-1}) (Garcia-Lodeiro et al., 2011), indicating the coexistence of different reaction products (e.g. N-A-S-H gels and C-A-S-H gels) (Ismail et al., 2014). With the increase of curing age from 1 d to 28 d, the Si-O-T bonds within the reaction products shift towards higher wavenumber, from 974 cm^{-1} to 985 cm^{-1}. This suggests that the increase of curing age promotes the polymerisation and cross-linking of the gels, potentially through the initial formation of C-A-S-H gels followed by the gradual development of N-A-S-H gels with a higher cross-linking degree (Ismail et al., 2014). It is noticed that the final position of this band (985 cm^{-1}) in AAFS paste is at a lower wavenumber than that in AAF paste (1020 cm^{-1}), implying that the presence of Ca leads to the formation of N-C-A-S-H gels (Ismail et al., 2014).

A sharp band at 875 cm^{-1} in the spectra is associated with the asymmetric stretching of AlO_4^- group in Al-O-Si bonds within C-A-S-H gels (Bernal et al., 2011b), which becomes sharper with the increase of curing age. This indicates the increase of Al content within C-A-S-H gels, leading to a higher polymerisation and cross-linking degree of C-A-S-H gels. The intensive band between 1409 cm^{-1} and 1467 cm^{-1} is related to the asymmetric stretching model of O-C-O bonds of CO_3^{2-} groups (Bernal et al., 2011b), suggesting that some superficial carbonation of samples would happen during the curing. The intensive band at 1736 cm^{-1} is associated with the stretching model of C=O bonds of carboxylic acid group (Pereira et al., 2017), corresponding to the modified polycarboxylate-based SP in the mixture. Lastly, the band at 430 cm^{-1} is related to the bending vibration of SiO_4, indicating the presence of vitreous silica in the mixture (Szechyńska-Hebda et al., 2019). The evolution of chemical composition of gel matrix is consistent with the nanostructure development of solid gel particles presented in NMR results (see Section 4.7.1).

4.7.3 Microstructure evolution of fly ash and slag particles in AAFS paste

A systematic analysis based on in-situ XCT imaging was conducted to monitor the microstructure evolution of individual fly ash and slag particles with different sizes and structures (i.e. solid and hollow) in AAFS paste cured at ambient temperature and gain new insight into the reaction mechanism. The high-resolution reconstruction was

performed to visualize the time-dependent 3D microstructures of fly ash and slag particles in AAFS paste from 1 d to 28 d, indicating the morphology changes on the surface and interior of particles and the spatial distribution of reaction products, based on which the reaction process in terms of reaction depth, reaction degree and reaction rate was estimated. For comparison, SEM-EDS analysis was also undertaken, the results of which were used to validate the in-situ XCT findings and gain an in-depth understanding of reaction mechanism of AAFS paste.

4.7.3.1 XCT image analysis

Figure 4-17 shows a typical XCT image of AAFS paste, which is considered mathematically as a four-dimensional set, including the density and corresponding coordinates (x, y and z). As seen in Figure 4-17a, each pixel in the image is characterized by its greyscale value ranging from 0 to 255 for an 8-bit image, attributing to the X-ray attenuation of the testing material. A multiphase composite made up of unreacted particles (fly ash and slag), reaction products and pore space can be characterised in the 2D slice image due to the difference of X-ray absorption. To analyse the multiple phases in 2D or 3D images, the XCT images were processed based on four steps: (i) denoising, (ii) segmentation, (iii) labelling, and (iv) quantification.

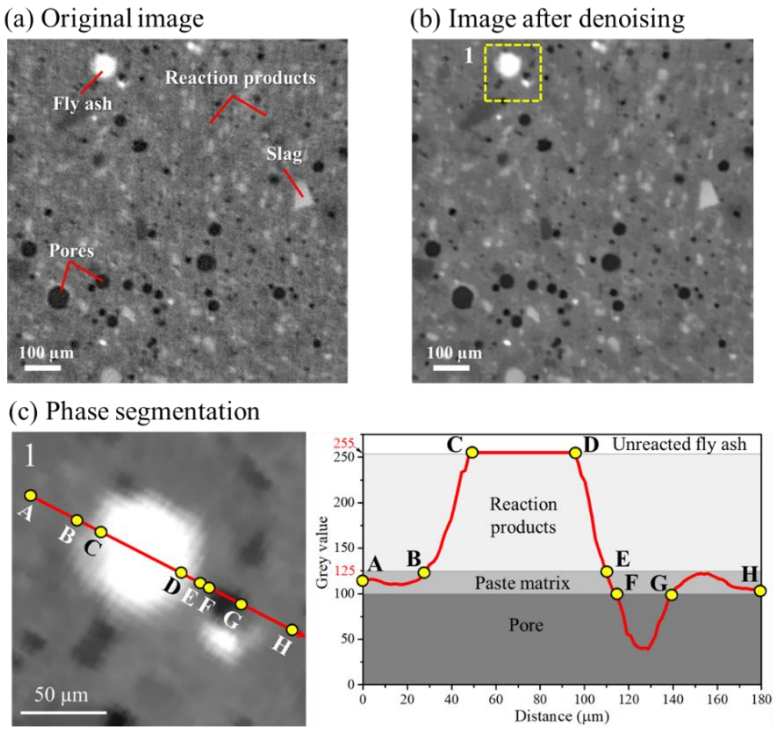

Figure 4-17 XCT image analysis (t = 1 d)

In the first step, image denoising was used to remove the noise of image data produced from the XCT test, which would help to improve the contrast between different phases.

In this study, the non-local means filtering method was applied for this purpose because this method can preserve both edges and textures (Buades et al., 2005). Accordingly, the noise within the original greyscale image was successfully removed as shown in Figure 4-17b.

The image was then segmented into different phases (unreacted particles, reaction products and pores) through local thresholding, which is commonly used to determine the threshold value of a specified region locally based on the histogram of grey value in a neighbourhood rather than the whole image (Sauvola and Pietikäinen, 2000). This method can avoid the problem of overlapping of grey value distribution, in which case the voxels within the overlap region cannot be identified (Brisard et al., 2020). Since this study aims at in-situ monitoring the microstructure evolution of a specified area, e.g. fly ash and slag particles, the local thresholding method is suitable. Taking the fly ash particle as an example, the grey value of different phases can be identified with the assistance of local linear threshold (Figure 4-17c). Herein, the red line across the fly ash particle indicates the location of grey value from point A to point H. The grey value is highest in the middle area of unreacted particle but drops sharply on the sides at the interface with paste matrix. The grey value of unreacted fly ash is measured to be 255, while that of paste mortar is in the range of 100-125. The reaction products accumulated at the interface between unreacted fly ash and paste matrix have a grey value between 125 and 255. The grey value under 100 represents the area of pores. It is worth noting that the determination of threshold values should be adjusted locally according to different particles due to the inherently heterogeneity of fly ash and slag particles. The additional information on phase segmentation for different fly ash and slag particles is presented in Appendixes A and B, respectively.

After segmentation, the identified phases were labelled as different connected clusters to characterise the morphological information, e.g. surface area and volume, considering the voxel connectivity. Three types of voxel connectivity (6-, 18- and 26- connectivity) are commonly used to analyse the morphological structure. The voxels share the same face are considered as connected in the type of 6-connectivity, while the 18-connectivity represents the connected voxels with a common edge. Regarding 26-connectivity, the voxels that share the same vertex are regarded to be connected. Here, the type of 26-connectivity is used to obtain accurate results.

Finally, the labelled clusters extracted from the image were quantified based on the voxel number of the labelled region and the voxel size of the image. For example, the volume of the labelled region can be calculated as:

$$V = N_v \times S_v \quad (4-8)$$

where V represents the volume of the labelled area (μm^3), N_v denotes the number of voxels (-), and S_v is the spatial resolution (voxel size) of the image (μm^3).

4.7.3.2 Microstructure evolution of fly ash particle

a. Phase identification

Figure 4-18 shows the local histogram of grey value of fly ash particle, which can be used to identify different phases in this particle. The red line across the fly ash particle from point A to point E indicates the location of grey value (Figure 4-18a). The linear grey value against distance from the core position of fly ash particle is illustrated in Figure 4-18b, where the grey value stays at the highest value of 255 between points A and B (located between 0 μm and 1.66 μm), representing the unreacted fly ash particle with the highest density among the phases in this local area. With the increase of distance from 1.66 μm to 30 μm (B – D), the grey value decreases sharply from 255 to 100, suggesting the presence of reaction products with various densities. The grey value at around 100 between point D and point E (located between 30 μm and 40 μm) corresponds to the area of paste matrix with the lowest density. The area of reaction products (B – D) can be further divided into inner products and outer products, based on their difference in grey value and their locations relative to the original boundary of fly ash particle. The linear area of inner products (B – C) covers the grey values between 178 and 255, while the linear area of outer products (C – D) belongs to the grey values between 100 and 178. The inner products with a relatively high grey value indicate that the density of inner products is higher than that of outer products. Also, a polychromatic image is used to visualize the distribution of different phases of fly ash particle. As seen in Figure 4-18c, the unreacted fly ash is labelled as yellow, while the inner products and outer products are labelled as red and green, respectively. The paste matrix is labelled as white.

It can be observed that there is a gradual transition of grey value at the boundary between unreacted particle and reaction products, as schematically illustrated in Figure 4-18d. It is the result of overlapping of these two phases at the boundary due to the limited resolution of XCT image, i.e. 1.56 μm, which is higher than the size of the elementary components of reaction product (gel matrix) with a length scale of 10 nm ~ 1 μm and thus the pixels at the boundary between particle and reaction products would tend to cover the grey values of both two phases. The gradual transition of grey value at the boundary is a common phenomenon existed in XCT imaging (Taiwo et al., 2016; Adrien et al., 2016), which would bring uncertainty regarding the selection of true boundary of phases. The

threshold value for reaction products may be either the upper, middle or lower end of the transition zone and accordingly the measured reaction products would be different. It has been demonstrated that a closer estimation of the threshold value can be obtained if selecting the grey value at the upper end of the transition region (Wong et al., 2006). Therefore, in this study, the grey value at the upper end of transition region is used to determine the boundary between unreacted particle and reaction products.

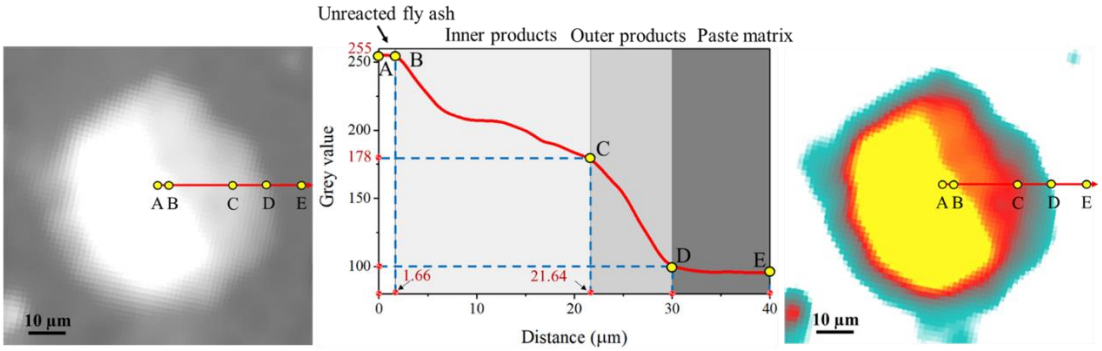

(a) Greyscale image (b) Grey value across fly ash particle (c) Polychromatic image

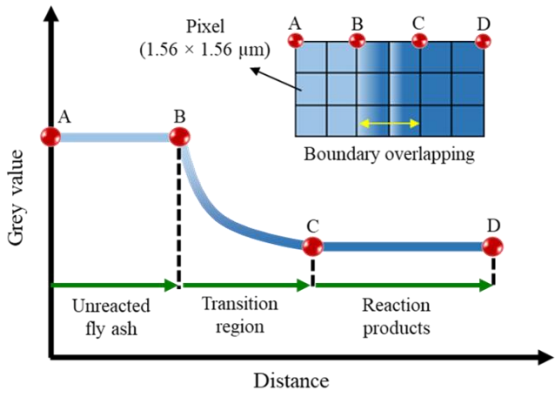

(d) Schematic illustration of the grey value transition region at the boundary between unreacted fly ash and reaction products

Figure 4-18 Phase identification of fly ash particle in AAFS paste (t = 28 d)

Figure 4-19 shows the chemical composition of fly ash particle characterised using BSEM-EDS, where the BSEM-EDS line analysis encompassing core particle-paste matrix is displayed in Figure 4-19a. There exists a slightly high grey value at the boundary of particle due to the charging effect of BSEM tests. The charging effect arising from electron/ion irradiation is unavoidable when a non-conductive specimen is tested using BSEM (Flatabø et al., 2017). The molar ratios of Ca/Si, Ca/Al and Ca/(Si+Al) along the distance from the core of fly ash particle are plotted in Figure 4-19b. These element ratios of the original fly ash particle are also provided to better separate the unreacted region and the reacted region of particle. Based on the chemical composition of fly ash particle (Table 3-1), the Ca/Si, Ca/Al and Ca/(Si+Al) molar ratios of original fly ash particle are calculated as 0.04, 0.07 and 0.026, respectively.

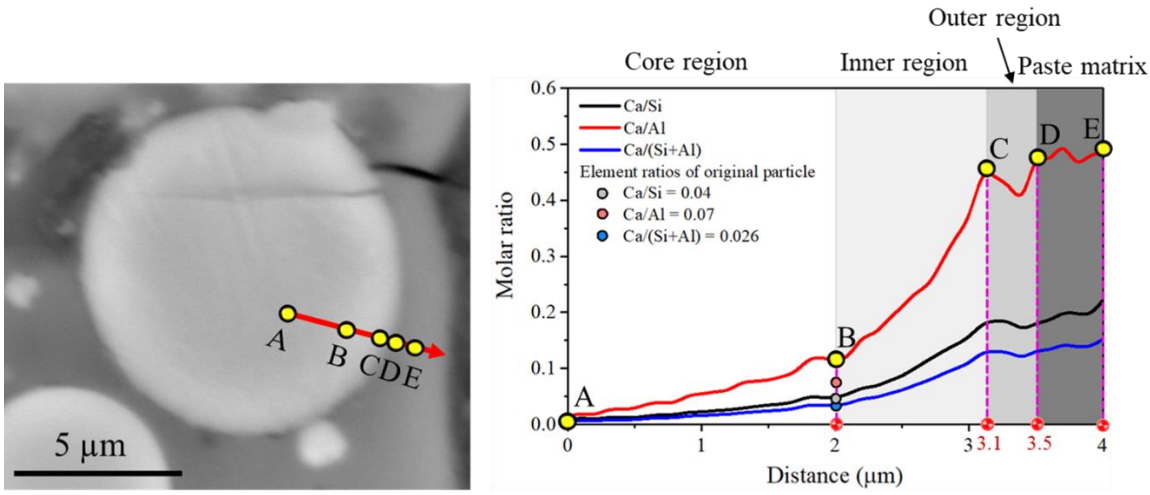

(a) BSEM image (b) Results of EDS line analysis

Figure 4-19 Chemical composition of fly ash particle in AAFS paste (t = 28 d)

It should be noted that it is challenging to make a comparison of the element ratios for the same particle over time based on BSEM-EDS test, as it is a destructive testing method and the sample needs to be cut, grinded, dried and polished. It can be found that the Ca/Si ratio stays at a low level (< 0.05) in the core region of particle (A – B), which is close to the Ca/Si ratio existed in the original fly ash particle (0.04). Such low Ca/Si ratio can be ascribed to the low content of Ca in the fly ash particle. The Ca/Si ratio is then increased rapidly from 0.1 to 0.45 in the inner region within the boundary of particle (B – C), attributing to the supply of Ca ions from the dissolution of outside particles, e.g. slag particles. The Ca/Si ratio becomes stable at a constant level between 0.4 and 0.5 in the outer region of particle (C – D) and the paste matrix (D – E) due to the relatively uniform distribution of Ca and Si ions. Similar trends can be observed in the distribution of Ca/Al and Ca/(Si+Al) ratios, suggesting the diffusion of ions from bulk solution into the fly ash particle, which would lead to the dissolution of particle and the formation of reaction products.

b. Reaction depth and reaction degree characterisation

Figure 4-20 shows the 3D internal structure of fly ash particle, which can be used to characterise the interior changes of particle structure. It can be seen from Figure 4-20a that the morphology of fly ash particle is modified along with the formation of reaction products. Here, the central slice of the fly ash particle is selected as the typical slice to quantify the interior changes of particle, i.e. reaction depth (Figure 4-20b). The reaction depth of fly ash particle is quantified by the distance between the boundary of outer products and the boundary of unreacted fly ash. The unreacted area labelled as yellow

gives the boundary of unreacted fly ash (see the black dash circle). The grey dash circle denotes the boundary of inner products, while the black solid cycle stands for the boundary of outer products. Figure 4-20c shows the reaction depths in the horizontal and vertical directions, which can be measured based on the difference of grey value in the linear local histogram of grey value. Accordingly, the reaction depths in horizontal and vertical directions are quantified as: D_1 = 11.37 μm, D_2 = 7.12 μm, D_3 = 7.21 μm, and D_4 = 6.68 μm. The reaction degree of fly ash can be calculated based on the volume change of fly ash particle as follows:

$$\alpha_{FA}=\left(1-\frac{V_{(t)FA}}{V_{(0)FA}}\right)\times 100\% \tag{4-9}$$

where α_{FA} is the reaction degree of fly ash particle, $V_{(t)FA}$ is the volume of unreacted fly ash at curing age *t*, and $V_{(0)FA}$ is the initial volume of fly ash particle before reaction.

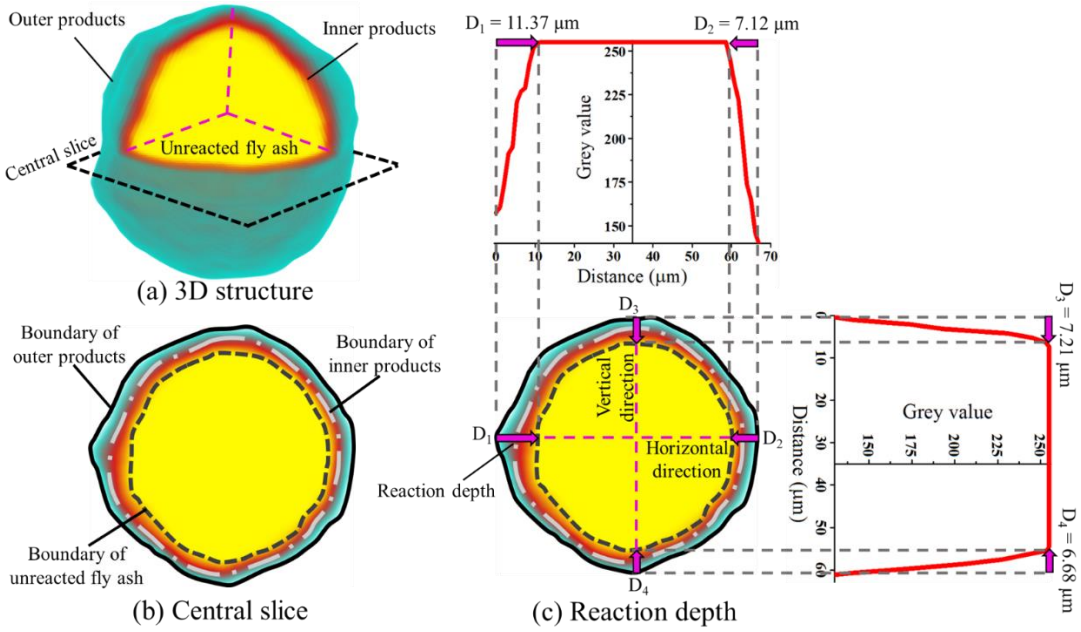

Figure 4-20 Feature identification of fly ash particle in AAFS paste (t = 1 d)

It should be noted that it is unlikely to obtain the "real" initial volume of fly ash particle due to the long testing time (~ 7 h). Nevertheless, since the formation of inner products is within the boundary of the original particle, the volume within the boundary of inner products can be assumed as the initial volume of fly ash particle. Accordingly, $V_{(0)FA}$ can be calculated based on the volume within the boundary of inner products in the fly ash particle at 1 d. Therefore, the relative volume change (i.e. reaction degree) of the same fly ash particle at different curing ages can be obtained and compared. The reaction rate of fly ash particle at different curing stages can be calculated as:

$$R_{FA} = \frac{\alpha_{(i+1)FA} - \alpha_{(i)FA}}{t_{(i+1)} - t_{(i)}} \quad (4\text{-}10)$$

where R_{FA} is the reaction rate of fly ash particle, $\alpha_{(i)FA}$ is the reaction degree of fly ash at stage i, $\alpha_{(i+1)FA}$ is the reaction degree of fly ash at stage i+1, $t_{(i)}$ is the curing age at stage i, and $t_{(i+1)}$ is the curing age at stage i+1. There are four curing stages, including stage 1 at 1 d, stage 2 at 3 d, stage 3 at 7 d, and stage 4 at 28 d corresponding to four curing ages, i.e. 1, 3, 7, and 28 d.

c. Microstructure evolution with curing age

Figure 4-21 shows the greyscale image of fly ash particle and its linear grey value histogram at different curing ages. The different morphology and grey values observed for different phases (e.g. unreacted fly ash and reaction products) allow us to explore how the fly ash particle is dissolved and how the reaction products are involved in its dissolution process. In the first image scanned at 1 d, rounded fly ash particle is visible in white, surrounded by a layer of reaction products in light grey and the paste matrix in dark grey. The grey value histogram highlights the presence of unreacted fly ash located between 38.42 µm and 77.73 µm (with the highest grey value of 255), surrounded by the reaction products with grey values of around 100-255. From 1 d to 28 d, the area of unreacted fly ash is decreased steadily, while the area of reaction products is increased (see greyscale image in Figure 4-21). This indicates that the fly ash particle is dissolved under the activation of alkaline activator along with the formation of reaction products. It is confirmed by the decrease of the grey value in the initial location of unreacted fly ash, as seen the grey value histogram in Figure 4-21. It is interesting to note that the dissolution of fly ash mainly results in the formation of inner products, indicating that most changes of fly ash microstructure are interior where the original boundary of fly ash is maintained during the dissolution process.

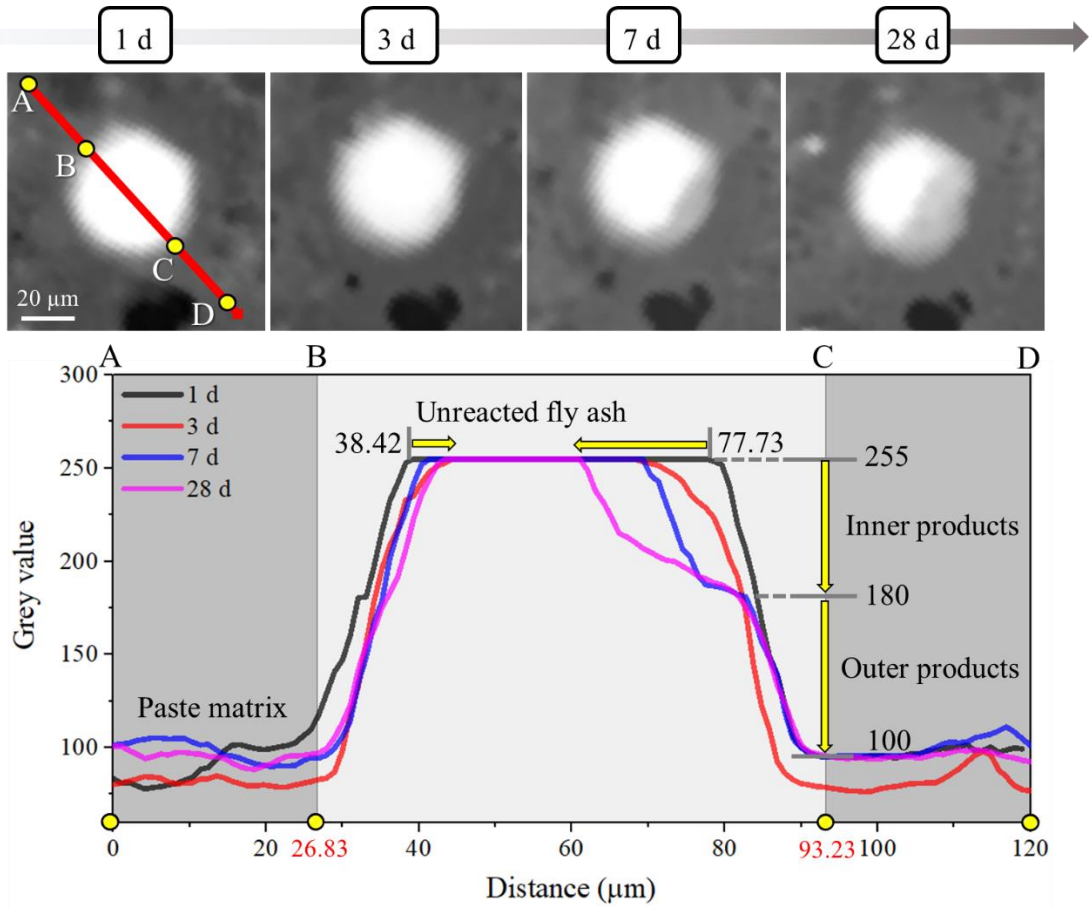

Figure 4-21 Grey value across fly ash particle in AAFS paste at different curing ages

As seen in Figure 4-22, the reaction depth and reaction degree of fly ash particle at different curing ages are quantified to further understand its microstructural evolution. The 3D microstructure evolution of fly ash particle is presented in Figure 4-22a. At 1 d, the fly ash particle changes within its original boundary along with the formation of inner products, but fewer outer products are formed outside its original boundary. This indicates that most ions from the dissolution of fly ash cannot diffuse into the surrounding regions, but are trapped inside the boundary of original particle, leading to the formation of inner products at this early age. Between 3 d and 28 d, more areas of fly ash particle are changed along with the precipitation of more inner products. In the meantime, more outer products are formed outside the boundary of fly ash particle, especially at 7 d and 28 d, which suggests that more dissolved ions have transported from the dissolution of fly ash particle to the outer region of particle, resulting in the precipitation of outer products. In addition, it is observed that the dissolution of fly ash particle is not uniform, where the particle dissolution along the X-direction is more obvious than that in Y- and Z-directions at 28 d.

To further characterise the microstructure evolution of fly ash particle, three central slices in different directions (i.e. X-Y, X-Z and Y-Z directions) is used to estimate its reaction depth, where eight directions from direction a to direction h in each slice are quantified, as shown in Figure 4-22b-d, the results of which are presented in Figure 4-22e. Regarding the X-Y central slice, the reaction depths in all directions are close to each other at the beginning (1 d), except for the reaction depth in direction g. The reaction depth in direction g is 11.37 μm higher than that in other directions (4.94 – 7.23 μm), implying the area in direction g is preferentially reacted in comparison with other areas. From 1 d to 3 d, the reaction depths in all directions are increased, especially for the reaction depths in directions c, d and e. At 3 d, the reaction depths in directions c, d and e are increased significantly from 6.89 μm, 4.93 μm and 6.66 μm to 9.19 μm, 12.17 μm and 10.11 μm, respectively. This suggests that the reaction levels at the bottom right area (from direction c to direction e) are higher than other areas during these curing ages. As the reaction continues from 3 d to 28 d, the reaction depths at the bottom right area are continuously increased, while the reaction depths at other areas are also increased steadily. At 28 d, it can be observed that the reaction depths in directions c, d, e and g are higher than those in other directions. Similar trends can also be found in the X-Z and Y-Z central slices, where the reaction depths in some areas are higher than others. This implies that the reaction of fly ash particle is not uniform but varies from one surface location to another.

Figure 4-22f shows the reaction degree and reaction rate of fly ash at different curing ages. The reaction degree of fly ash is increased slowly from 15.81% to 19.07% at the early ages between 1 d and 3 d. It is then increased dramatically from 19.07% to 33.80% at 7 d, and finally increases to 57.67% at 28 d. By contrast, it can be seen from Figure 4-22f that the reaction rate of fly ash is reduced dramatically from 15.81%/d to 1.63%/d between the first curing stage (0 – 1 d) and the second curing stage (1 – 3 d). And then, it is increased slightly to 3.68%/d at the third stage (3 – 7 d) and finally decreased to 1.14%/d at the last stage (7 – 28 d). This phenomenon can be attributed to the formation of inner products at 1 d, which would physically block the unreacted fly ash particle and the outside solution and thus reduce the transportation of dissolved ions, leading to the decrease of dissolving rate of fly ash particle and consequently the reaction rate (Bae et al., 2014).

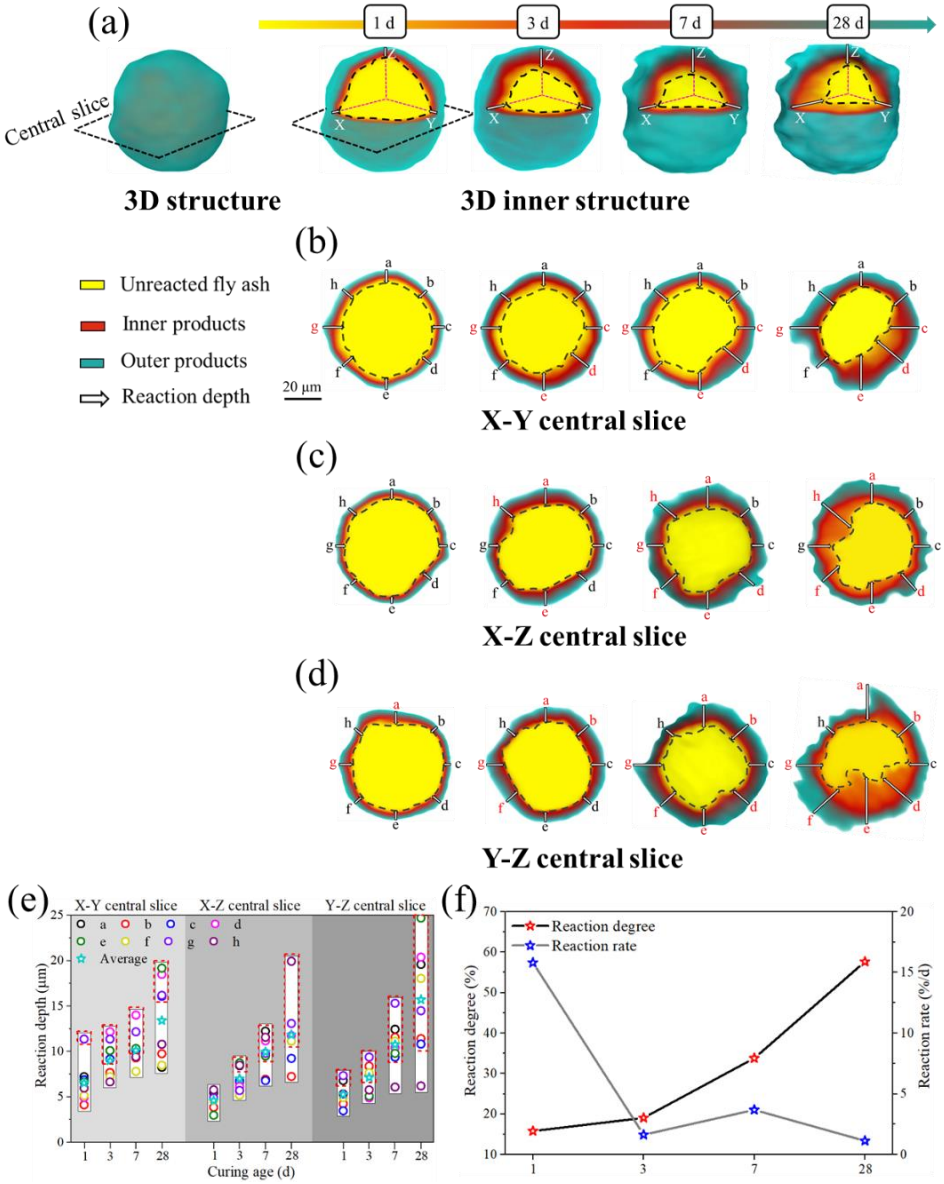

Figure 4-22 Reaction depth and reaction degree of fly ash particle in AAFS paste at different curing ages

d. Effect of particle structure

It is known that fly ash particles have two main structures, including the solid structure and the hollow structure. Thus, it is necessary to evaluate the effects of particle structure on the microstructure evolution of fly ash. The solid and hollow fly ash particles with a similar size were chosen to estimate these effects. Figure 4-23 shows the 3D structures and 2D slices of solid and hollow fly ash particles. The solid fly ash particle is found to be spherical and unbroken, while the hollow fly ash particle has a largely empty hollow core. In addition, the shape of the solid fly ash particle is more regular compared to the hollow fly ash particle. The greyscale slice and the linear grey value histogram of hollow fly ash are presented in Figure 4-24 to characterise its microstructure evolution. It can be observed that the reaction products formed during the reaction of hollow fly ash not only accumulate around the outer surface of particle but also accumulate inside the particle

due to the presence of hollow core. This indicates that the fly ash particle with a hollow structure would be activated simultaneously from the outside in and from the inside out, leading to the accelerated reaction process. The overall area of hollow fly ash particle is dissolved faster than that of solid fly ash particle, especially for the left side area which is fully reacted at 28 d. This phenomenon is confirmed by the relatively high reaction degree of fly ash particle with a hollow structure compared to that of solid fly ash particle, regardless of curing age (Figure 4-25a). Here, the reaction degrees of hollow fly ash at 1, 3, 7 and 28 d are found to 28.15%, 32.05%, 44.71% and 64.92%, respectively, which are higher than that of solid fly ash at the same curing ages, i.e., 15.81%, 19.07%, 33.8% and 57.67% at 1, 3, 7 and 28 d, respectively. As seen in Figure 4-25b, the changing trend of reaction rate of hollow fly ash particle is similar to that of solid fly ash particle, both of which are gradually decreased with the increase of curing age.

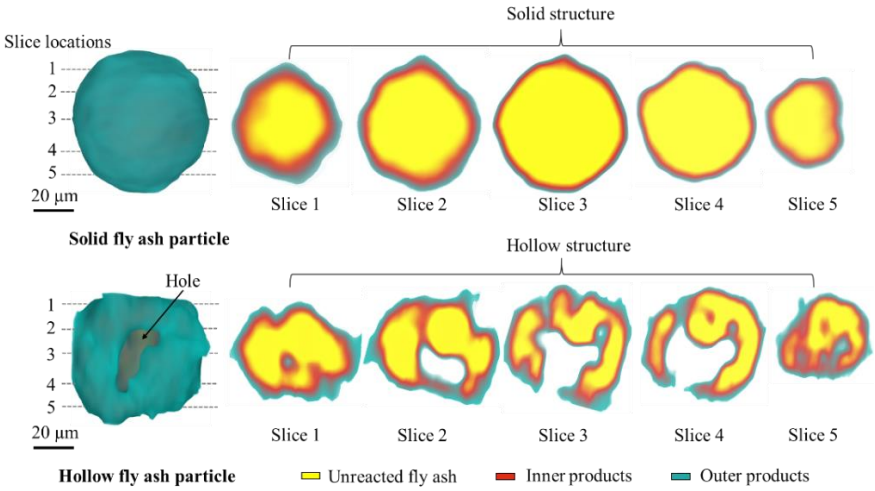

Figure 4-23 2D/3D structure of solid fly ash particle and hollow fly ash particle in AAFS paste (t = 1 d)

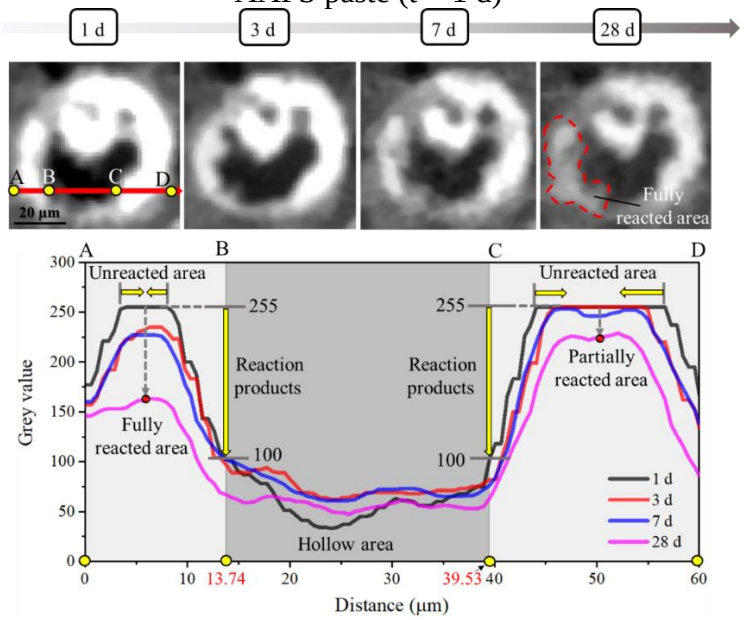

Figure 4-24 Grey value across hollow fly ash particle in AAFS paste at different curing ages

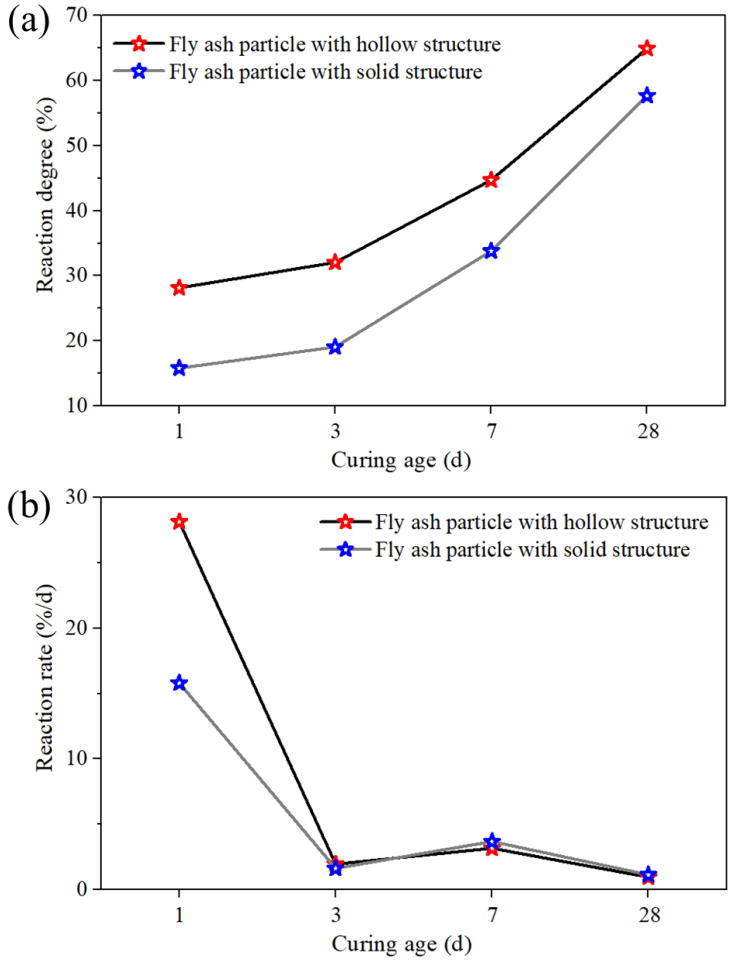

Figure 4-25 Reaction degree and reaction rate of solid and hollow fly ash particles in AAFS paste at different curing ages

e. Effect of particle size

The particle size of the initial fly ash particle would influence its microstructure evolution. To evaluate such effect, five fly ash particles with different diameters ranging from about 50 μm to 10 μm are chosen and the evolution of their microstructures is investigated. The selection of the typical size of fly ash particle is based on the particle size distribution, where the size of 95% fly ash is smaller than 45 μm and 50% fly ash has a size larger than 10 μm (Figure 3-3). In addition, the limitation of the XCT image resolution (1.56 μm) would also affect the selection of fly ash particle. Here, the size of fly ash particle is measured as the spherical equivalent diameter (d_{Eq}) that is calculated based on the volume of fly ash particle. The obtained d_{eq} of these five fly ash particles from particle 1 to particle 5 are 56.59 μm, 41.30 μm, 28.14 μm, 16.63 μm and 12.93 μm, respectively.

Figure 4-26 shows the microstructure evolution of five fly ash particles (particle 1 to particle 5). The central slice of each particle is used to characterise the development of reaction depths, in which eight directions (from direction a to direction h) are quantified as illustrated in Figure 4-26a and b. At 1 d, the reaction depths in all directions of each

particle are close to each other, except that in the direction g in particle 1, which indicates that most particles are activated uniformly around the spherical fly ash particle at 1 d. At this stage, the order of average reaction depth for different particles is particle 1 > particle 3 > particle 4 > particle 2 > particle 5, which is different with the order of particle size from particle 1 to particle 5, implying there is no obvious positive relationship between the particle size and reaction depth of fly ash particle. At 3 d, the reaction depths in different directions for all particles are increased, but at different levels. For particles 1, 2 and 3, the reaction depths in some directions are higher than that in other directions, i.e. directions c, d, e and g in particle 1, direction h in particle 2, and directions f, g and h in particle 3. However, the reaction depths in all directions are still close to each other in particles 4 and 5. With the increase of curing age from 3 d to 28 d, the discrepancy of reaction depths in different directions in particles 1, 2 and 3 becomes more obvious, while the reaction of particles 4 and 5 is still uniform. This indicates that the reaction of fly ash particle with a relatively large size is easier to become asymmetrical than that of the particle with a smaller size.

It can be seen from Figure 4-26c that the reaction degrees of all particles are increased steadily with the increase of curing age, which generally follow an order of particle 1 < particle 2 < particle 3 < particle 4 < particle 5. This suggests that the fly ash particle with a smaller size would be easier activated due to its relatively high specific area. As seen in Figure 4-26a, the fly ash particle with the smallest size (particle 5) is fully reacted at 28 d, while the reaction degree of particle 2 (45.64%) is lower than that of particle 1 (57.67%) at 28 d, which can be ascribed to the heterogeneous characteristics between these two particles, where particle 2 may have a relatively high content of crystal phases, resulting in a relatively low reaction degree. Moreover, the reaction rates of all particles are decreased dramatically after 1 d, which implies that the formation of inner products would indeed prevent the contact between unreacted fly ash and alkaline solution and inhibit the further reaction of fly ash particle, regardless of its size.

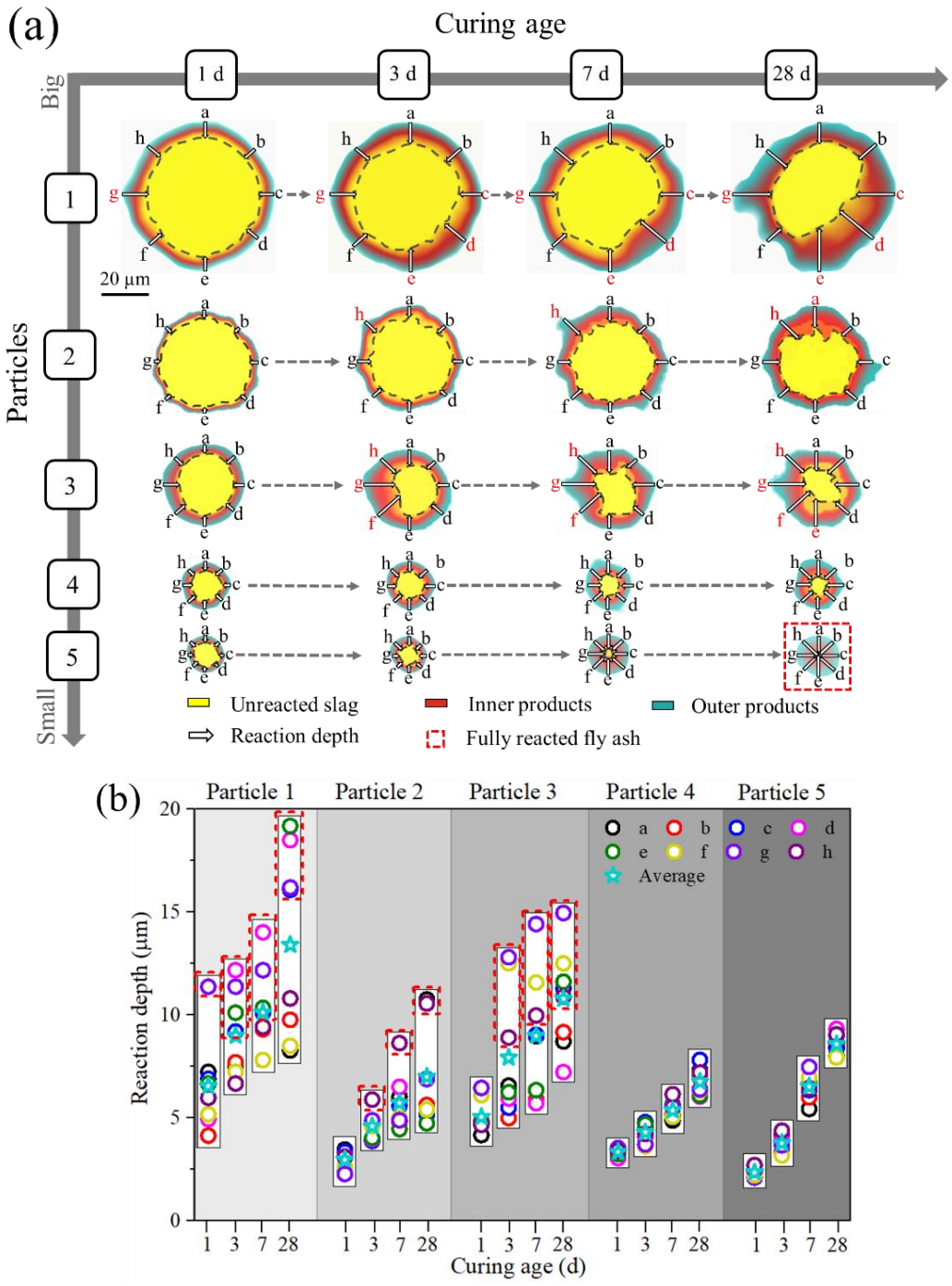
(a)
Curing age
1 d
3 d
7 d
28 d
Big
Small
Particles
1
2
3
4
5
20 μm
Unreacted slag
Inner products
Outer products
Reaction depth
Fully reacted fly ash
(b)
Particle 1
Particle 2
Particle 3
Particle 4
Particle 5
a
b
c
d
e
f
g
h
Average
Reaction depth (μm)
Curing age (d)

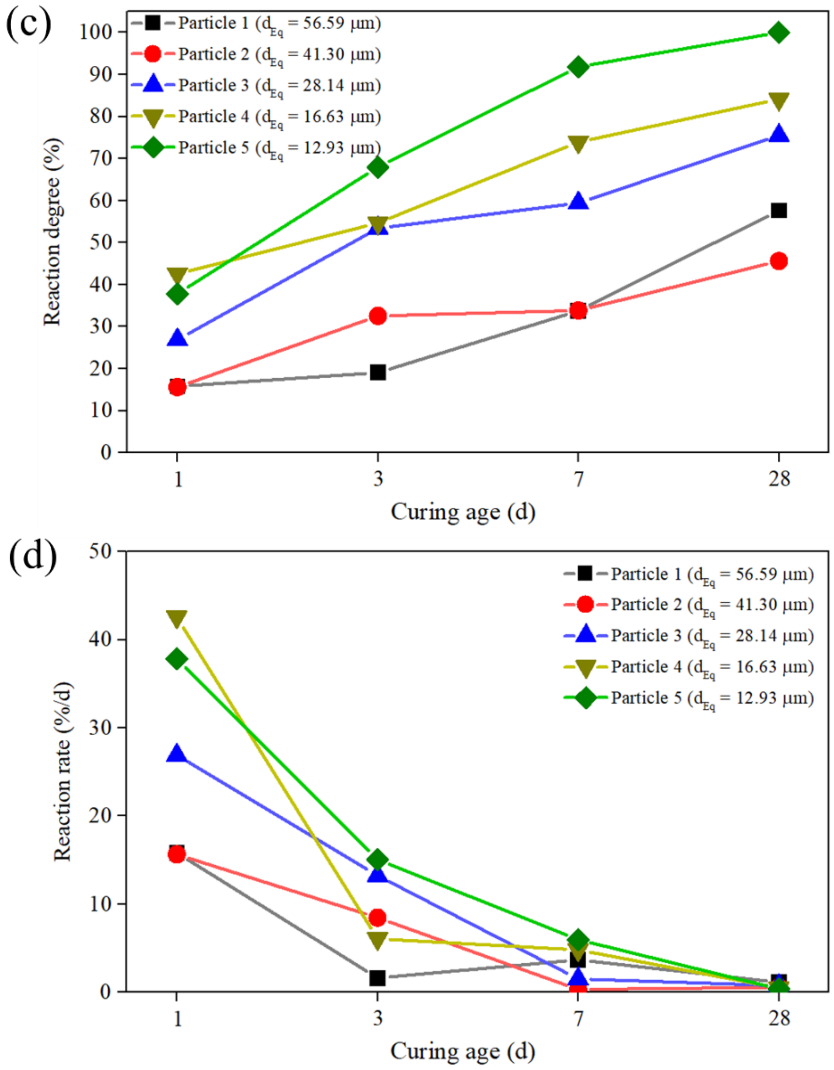

Figure 4-26 Reaction depth and reaction degree of fly ash particles with different size in AAFS paste at different curing ages

f. Mechanism of microstructure evolution

The microstructure evolution of fly ash particle can be divided into two parts: the dissolution of particle and the formation of reaction products, as shown in Figure 4-27. It can be seen from Figure 4-27a that the fly ash particle is dissolved upon the activation of alkaline activator (SS and SH) via rupture the Si-O-Si and Al-O-Al bonds in fly ash. An irregular shape can be observed in the reacted fly ash particle, indicating that the reaction of fly ash is not uniform, which varies from point to point on the surface. It can be attributed to the inherently heterogeneous characteristics of fly ash particle that consists of relatively inert crystal phases and highly reactive amorphous phases (Chancey et al., 2010). This suggests that the area of fly ash particle with a high proportion of amorphous phases could be easier activated, resulting in a rapid localized dissolution.

Once the fly ash particle is dissolved, a variety of dissolved species are generated, including silica monomers (e.g. $Si(OH)_4$) and alumina monomers (e.g. $Al(OH)_4^-$)). With

the increase of monomer species, the monomers would react with each other to form dimers such as silica dimers and silica-alumina dimers. Afterwards, the reaction products start to form and precipitate in the dissolved area of fly ash particle. The reaction products can be typically classified as inner products and outer products, according to the location relative to the original boundary of fly ash particle and the difference in density and composition, as discussed in Section 4.1.1. It can be seen from Figure 4-27b that the reaction products region is asymmetrically distributed around the unreacted fly ash particle, due to the inhomogeneous dissolution of fly ash particle.

Besides, most reaction products accumulate within the boundary of the original particle, suggesting the formation of inner products as a result of the reaction process of fly ash. Once the region of fly ash particle reacts with the solution, etch pits start to form on the surface, leading to the locally rapid dissolution inside the pits. This rapid dissolution would greatly increase the ionic concentration inside the pits, which would make the supersaturation in these pit areas and promote the nucleation of reaction products. Afterwards, the nuclei of reaction products would start to grow and fill the pits, until they reach the original surface of particle. And then, the growth would become slow when the reaction products reach the boundary of original particle due to the relatively low ionic concentration in the surrounding regions.

Furthermore, as shown in Figure 4-27b, the early formation of inner products would naturally build a physical barrier between the unreacted particle and the outside solution, which would prohibit the diffusion of ions from bulk solution to the core particle (Bae et al., 2014). Consequently, the diffusion of ions from bulk solution to the unreacted particle would become difficult as the ions need to penetrate through the porous reaction products (e.g. N-A-S-H gels (Duxson et al., 2005)) or the microcracks in the precipitation layer instead of the direct contact with the unreacted particle (Yin et al., 2018). The formation of microcracks in the precipitation layer can be attributed to the nonuniform reaction on the surface of particle, which leads to the variation of products precipitation from one surface location to another. Accordingly, the diffusion rate of ions from bulk solution to the unreacted particle would be decreased, and consequently slow down the reaction process of fly ash. It is confirmed by the significant decrease of reaction rate of fly ash particle after 1 d, regardless of particle shape and particle size (Figure 4-25b and 4-26d), and agrees well with the descriptive model presented in previous research (Fernández-Jiménez et al., 2005).

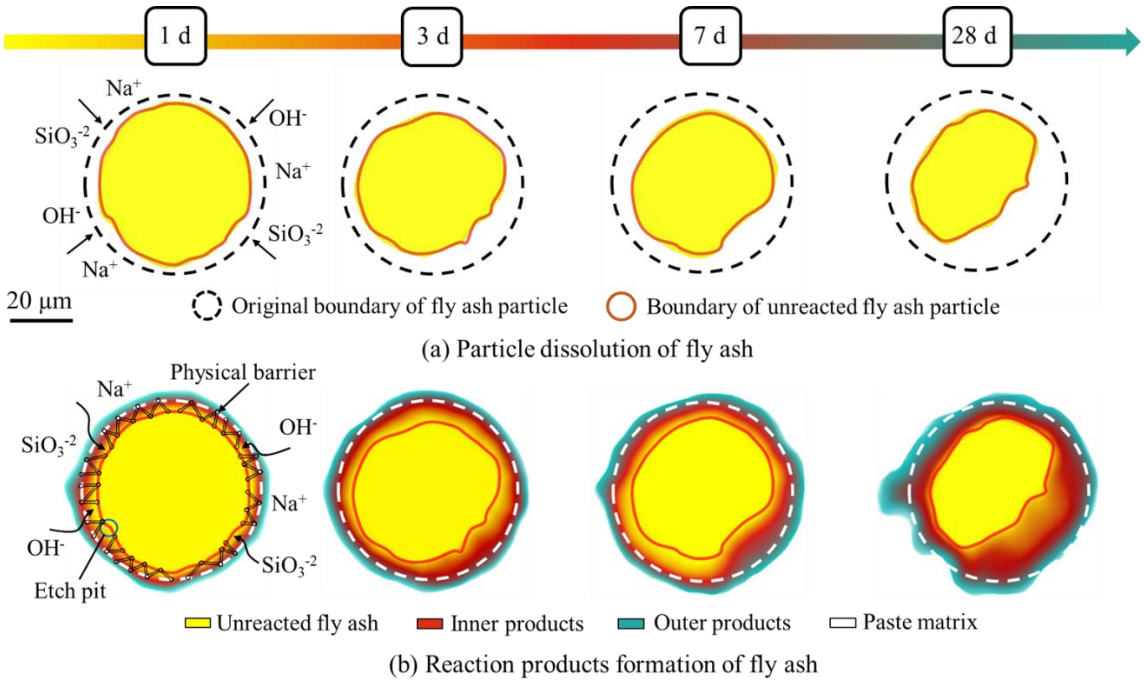

Figure 4-27 Microstructure evolution of fly ash particle in AAFS paste

4.7.3.3 Microstructure evolution of slag particle

a. Phase identification and characteristics

Figure 4-28 shows the linear grey value against distance from the core position of slag, based on which different phases in slag particle can be identified. As seen in Figure 4-28a and b, the grey value of unreacted slag is measured to be 160 between point A and point B (located between 0 μm and 10.58 μm). The location between 10.58 μm and 26.20 μm (B – C) represents the region of inner products, covering the grey values of 132 – 160. The outer products (C – D) have grey values of 94 – 132, while the paste matrix (D – E) covers the grey values around 94. Accordingly, the different phases in slag particle can be labelled as different colours in Figure 4-28c, where unreacted slag, inner products, outer products, and paste matrix are displayed in yellow, red, green, and white, respectively.

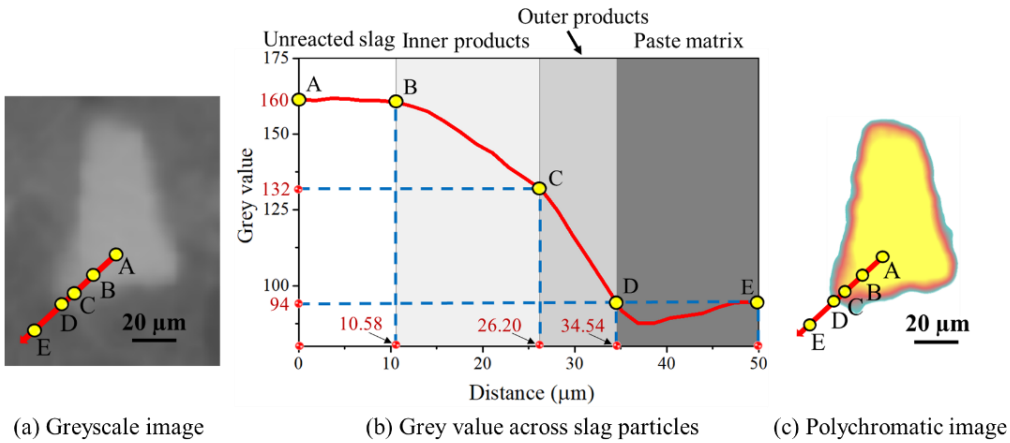

Figure 4-28 Phase identification of slag particle in AAFS paste (t = 1 d)

Figure 4-29 illustrates the chemical composition of slag particle characterised using the BSEM-EDS line scanning from the core position of slag to the paste matrix. The molar ratios of Ca/Si, Ca/Al and Ca/(Si+Al) against the distance from the core position of slag are quantified and presented in Figure 4-29a and b. In addition, these element ratios of the original slag particle are also obtained based on its chemical composition (Table 3-1), where the molar ratios of Ca/Si, Ca/Al and Ca/(Si+Al) are found to be 1.34, 2.85 and 0.91, respectively. The Ca/Al ratio stays at a high level (> 1.8) at the core region of particle (A – B), consisting with the high Ca/Al ratio in the original slag particle, which can be ascribed to the high content of Ca in the slag particle. The Ca/Al ratio is decreased significantly from 1.8 to 0.6 in the inner region of particle (B – C), which can be attributed to the supply of Al ions from the dissolution of outside particles, e.g. fly ash particles. The Ca/Al becomes stable between 0.6 and 0.8 in the outer region of particle (C – D) and the paste matrix (D – E), due to the relatively uniform distribution of Ca and Al ions. Similar trends can be observed in the distribution of Ca/Si and Ca/(Si+Al) ratios. The diffusion of ions into the slag particle indicates that the slag would be dissolved under the activation of bulk solution, leading to the formation of reaction products.

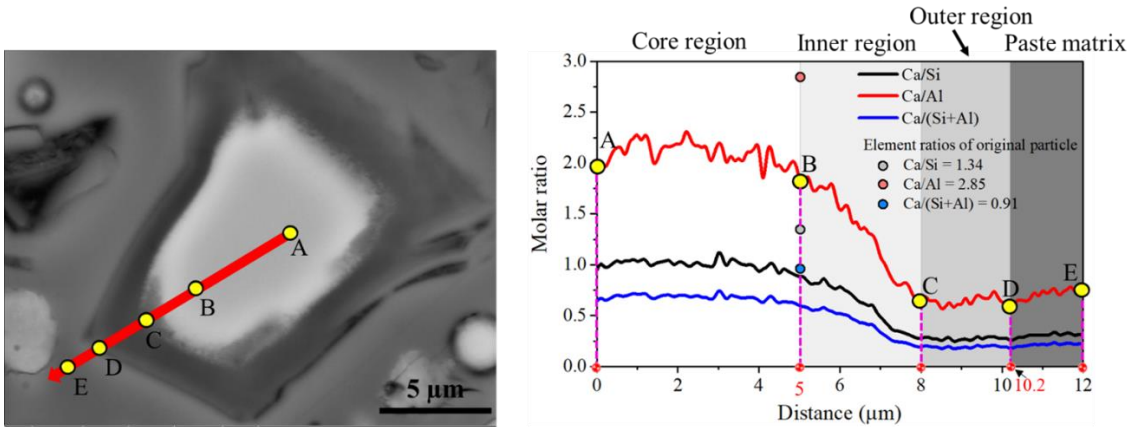

(a) BSEM image (b) Results of EDS line analysis

Figure 4-29 Chemical composition of slag particle in AAFS paste (t = 1 d)

The estimations of reaction depth and reaction degree slag follow a similar approach for fly ash as mentioned above. The distance between the boundary of the outer products and the boundary of the unreacted slag is regarded as the reaction depth. The reaction degree of slag can be calculated based on the volume change of the slag particle as follows:

$$\alpha_{slag} = \left(1 - \frac{V_{(t)slag}}{V_{(0)slag}}\right) \times 100\% \quad (4\text{-}11)$$

where α_{slag} is the reaction degree of fly ash particle, $V_{(t)slag}$ is the volume of unreacted fly ash at curing age *t*, and $V_{(0)slag}$ is the initial volume of fly ash particle calculated from the volume within the boundary of inner products at 1 d.

The reaction rate of slag particle at different curing stages can be calculated as:

$$R_{slag} = \frac{\alpha_{(i+1)slag} - \alpha_{(i)slag}}{t_{(i+1)} - t_{(i)}} \quad (4\text{-}12)$$

where R_{slag} is the reaction rate of fly ash particle, $\alpha_{(i)slag}$ is the reaction degree of fly ash at stage i, $\alpha_{(i+1)slag}$ is the reaction degree of fly ash at stage i+1, $t_{(i)}$ is the curing age at stage i and $t_{(i+1)}$ is the curing age at stage i+1.

Similarly, four curing stages including stage 1 at 1 d, stage 2 at 3 d, stage 3 at 7 d and stage 4 at 28 d corresponding to four curing ages of 1, 3, 7 and 28 d, respectively are considered for further analysis.

b. Microstructure evolution with curing age

As seen in Figure 4-30, the microstructure evolution of slag particle is characterised with the assistant of the greyscale image and its linear grey-value histogram. At 1 d, the unreacted slag covers a relatively wide area located between 17.58 μm and 42.40 μm, surrounded by a thin layer of reaction products. Between 3 d and 28 d, the region of unreacted slag is reduced steadily, while the region of reaction products is increased, confirmed by the grey value histogram, which suggests the dissolution of slag particle and the formation of reaction products under the activation of alkaline activator.

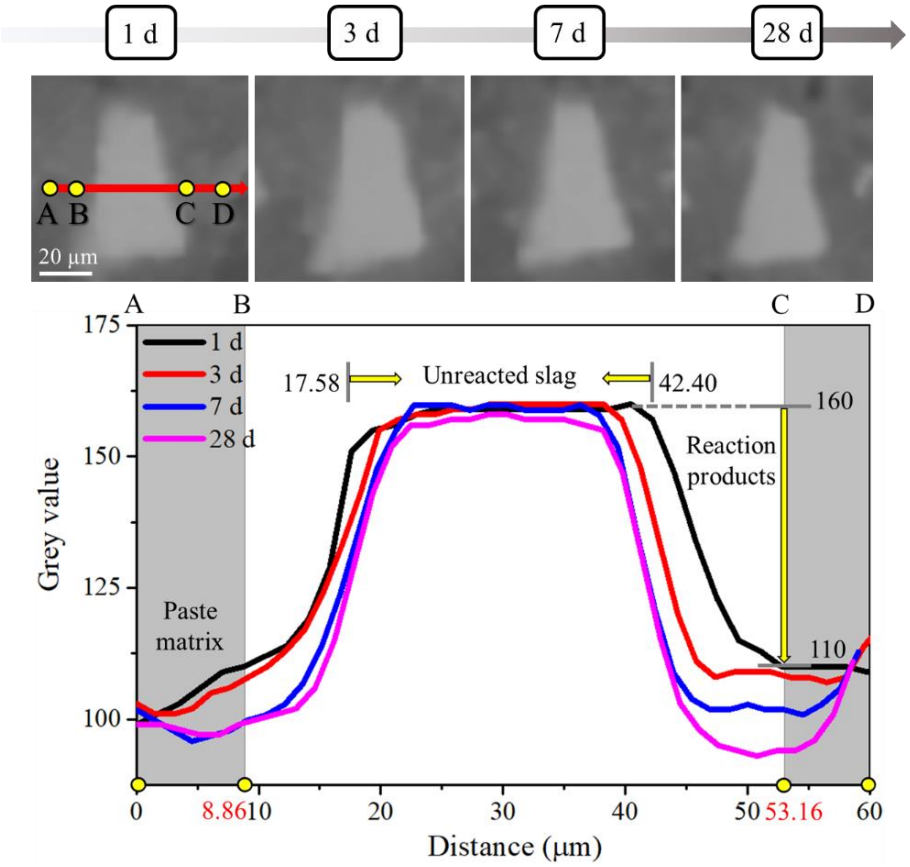

Figure 4-30 Grey value across slag particle in AAFS paste at different curing ages

Figure 4-31 shows the internal microstructural changes of slag particle with increasing curing ages. It can be seen from Figure 4-31a that the slag particle is heterogeneously varied and covered by the reaction products, where the reactions of some regions are more extensive than others at 1 d. The 3D inner structure indicates that most regions of slag particle evolve within its original boundary along with the formation of inner products and fewer products can be observed outside its original boundary (i.e. the formation of outer products). It implies that the dissolved region of slag accumulates a higher concentration of ions compared to the surrounding regions, which would result in a rapid reaction and promote the formation of reaction products in this region (i.e. inner products). From 3 d to 28 d, the slag particle is continually reacted accompanied by the formation of more inner products. In addition, more outer products are also found at later curing ages (7 d and 28 d), attributing to the transport of more dissolved ions from inner region to outer region of slag particle.

The microstructure evolution of slag particle along different directions (i.e. X-Y, X-Z and Y-Z directions) at three central slices is shown in Figure 4-31b-d, respectively. The reaction depths of these slices in eight directions from direction a to direction h are quantified and presented in Figure 4-31e. For the X-Y central slice, the reaction depth in direction f is higher than that in other directions at 1 d. The reaction depth in direction f is 17.24 μm, while the reaction depths in other directions are in the range of 4.37 – 8.44 μm. It is indicated that the reaction of slag particle is not uniform, and the area in direction f is preferentially activated. As the curing age increases from 3 d to 28 d, the heterogeneous reaction of slag particle proceeds, which leads to the relatively high reaction depths in directions a, f and h at 28 d. Similar developing trend of reaction depth can also be observed in the X-Z and Y-Z central slices, suggesting that some areas of slag particle are preferentially activated than other areas.

The reaction degree and reaction rate of slag particle at different curing ages are quantified and shown in Figure 4-31f. It can be found that the reaction degree of slag is increased steadily from 25.19% to 61.31% between 1 d and 28 d. Nevertheless, its reaction rate is decreased dramatically from 25.19%/d to 6.63%/d between first curing stage (0 – 1 d) and second curing stage (1 – 3 d), followed by a continuous reduction to 0.59%/d at the last stage (7 – 28 d), which suggests that the early formation of inner products at 1 d would influence the reaction rate at later curing ages. Once the inner products are formed on the surface of slag particle, they would physically block the unreacted slag and the surround solution, leading to a reduction of the further dissolution of slag.

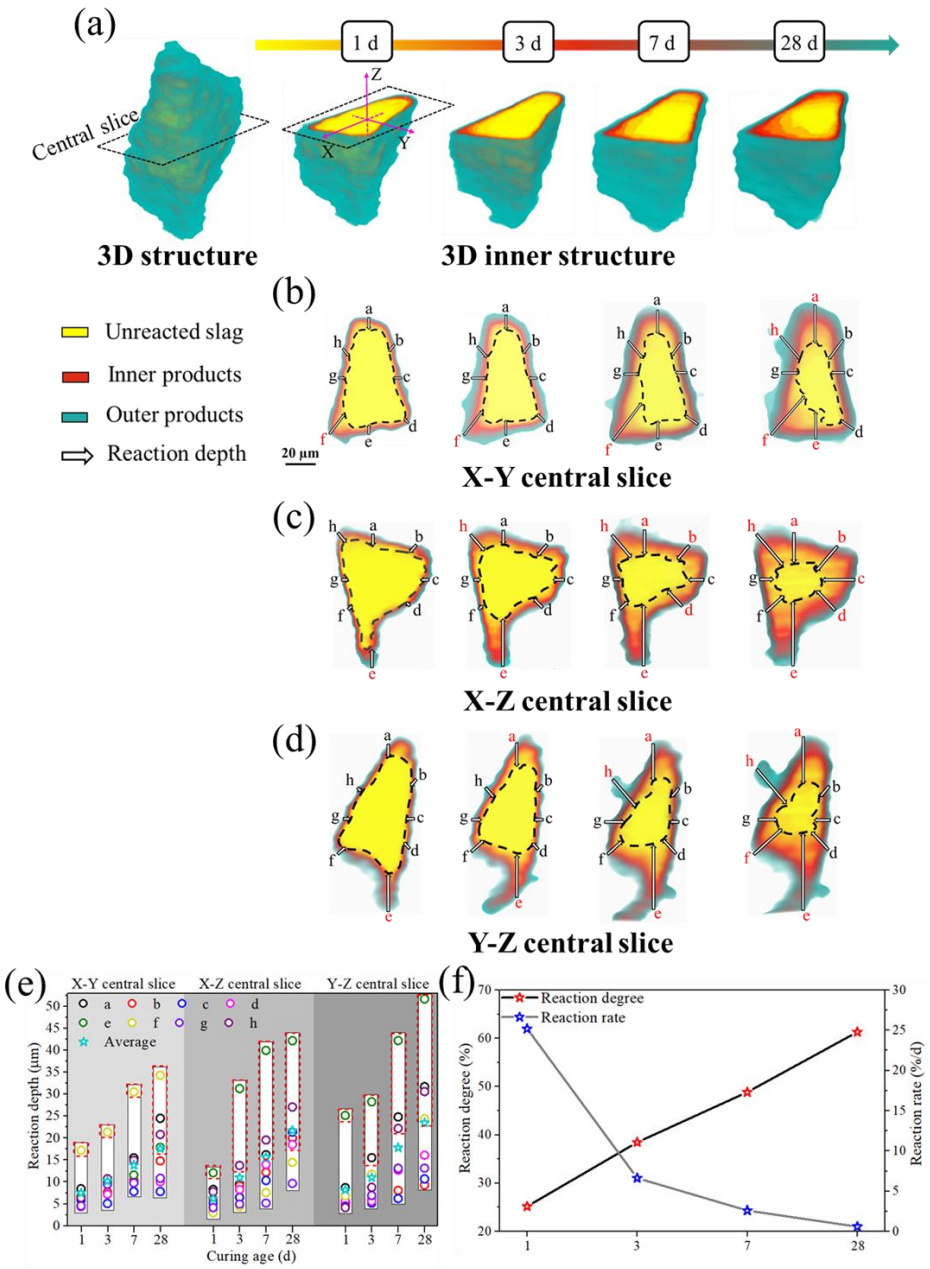

Figure 4-31 Reaction depth and reaction degree of slag particle in AAFS paste at different curing ages

c. Effect of particle size

To estimate the effect of particle size on microstructure evolution of slag particle in AAFS, five slag particles with a diameter ranging from about 75 μm to 10 μm are selected, which mostly covers the particle size distribution of slag used in this study (Table 3-3). The size of slag particle is referred to as the maximum diameter (d_{max}) that is measured as the maximum distance between two points in the original boundary of the central slice in X-Y direction. The d_{max} values of the five slag particles from particle 1 to particle 5 are found to be 74.76 μm, 64.22 μm, 36.04 μm, 21.42 μm and 9.48 μm, respectively.

Figure 4-32 shows the microstructure evolution of five slag particles (particle 1 to particle 5) at different curing ages. The reaction depths of different particles at eight

directions are quantified and shown in Figure 4-32a and b. The average reaction depths for different particles follow an order of particle 1 > particle 2 > particle 3 > particle 4 > particle 5, which is consistent with the order of particle size from particles 1 to 5. This implies that the size of slag particle has a positive influence on its reaction depth. At the beginning (1 d), there exists a close reaction depth at all directions in each particle, except for the direction f in particle 1, which suggests that most particles are activated uniformly around the slag particle at 1 d. At 3 d, the reaction depths at different directions for all slag particles are increased, but at different levels. The reaction depths in direction f in particle 1 and direction g in particle 2 are higher than those at other directions, while the reaction depths at all directions are still close to each other in particles 3, 4 and 5. At 7 d, the heterogeneous reaction can also be observed in particles 3 and 4, where the reaction depths in some directions are higher than those in other directions, e.g. the directions a, b and c in particle 3 and direction a in particle 4. With the increase of curing age from 7 d to 28 d, the discrepancy of reaction depths in different directions in particles 1, 2 and 3 becomes more obvious, while the reaction of particles 4 and 5 is uniform. This implies that the slag particle with a relatively large size tends to experience a non-uniform reaction compared to that with a smaller size.

The reaction degrees and reaction rates of all slag particles are quantified and shown in Figure 4-32c and d. As seen in Figure 4-32c, the reaction degrees of all slag particles are increased steadily with the increase of curing age. At 1 d, it can be found that the slag particles with a smaller size have a higher reaction degree, where the reaction degree follows an order of particle 5 (70.91%) > particle 4 (49.74%) > particle 3 (41.88%) > particle 2 (27.44%) > particle 1 (25.19%). This indicates that the size of slag particle would indeed significantly affect its chemical reaction and microstructural evolution in AAFS. The slag particles with smaller size would be activated more easily due to the relatively high specific area. However, the reaction degree of particle 2 (29.66%) becomes smaller than that of particle 1 (38.46%) at 3 d, which implies that the reaction of slag particle may also be affected by other factors, such as the morphology and chemical composition of slag. With the increase of curing age from 3 d to 28 d, the difference of reaction degree between the small slag particle (particle 4 and particle 5) and the large slag particle (particles 1, 2 and 3) becomes more obvious. Particle 5 and particle 4 are fully reacted at 7 d and 28 d, respectively, while the other particles share a similar reaction degree of about 60% at 28 d. As seen in Figure 4-32d that the reaction rates of all slag particles are reduced significantly after 1 d, which suggests that the initially formed inner products would indeed prevent the further reaction of slag particle, regardless of its size.

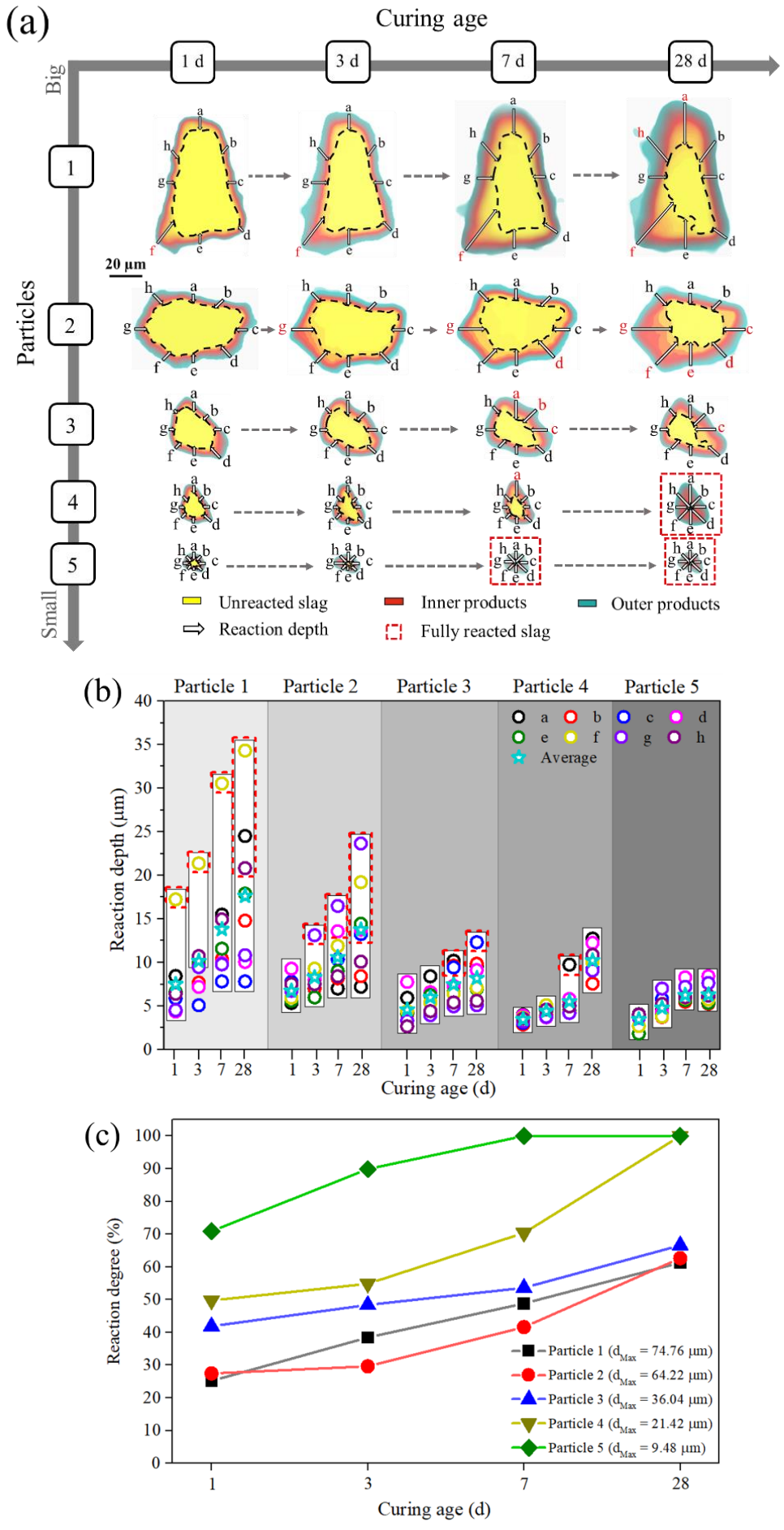
(a)
Curing age
1 d
3 d
7 d
28 d
Big
Small
Particles
1
2
3
4
5
20 μm
Unreacted slag
Reaction depth
Inner products
Fully reacted slag
Outer products
(b)
Particle 1
Particle 2
Particle 3
Particle 4
Particle 5
Average
Reaction depth (μm)
Curing age (d)
(c)
Reaction degree (%)
Curing age (d)
Particle 1 (d_Max = 74.76 μm)
Particle 2 (d_Max = 64.22 μm)
Particle 3 (d_Max = 36.04 μm)
Particle 4 (d_Max = 21.42 μm)
Particle 5 (d_Max = 9.48 μm)

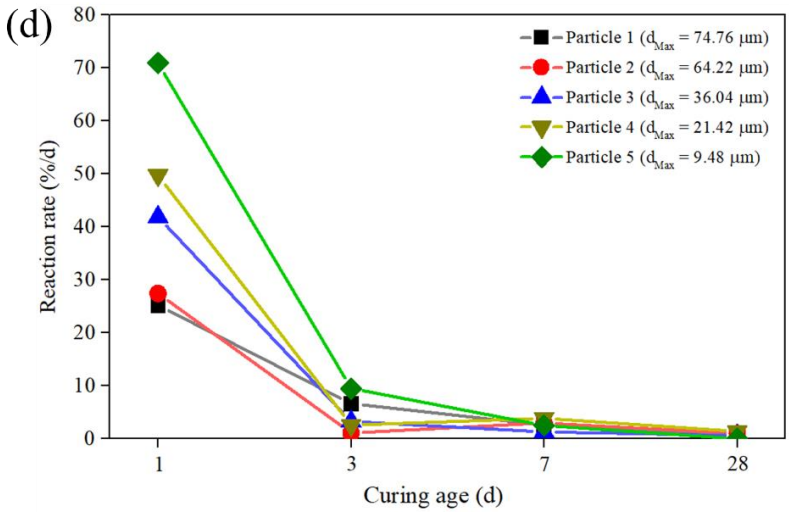

Figure 4-32 Reaction depth and reaction degree of slag particles with different size in AAFS paste at different curing ages

d. Mechanism of microstructure evolution

Figure 4-33 shows the microstructural changes of slag particle with curing ages, in terms of the dissolution of particle and the formation of reaction products. In the beginning, the diffusion of alkaline solution into the slag particle would rupture the Ca-O and Si-O-Si bonds in slag, thereby dissolving the slag particle and reducing its size. It can be seen from Figure 4-33a that the original slag particle is dissolved and an irregular sharp of the unreacted particle is formed due to the non-uniform dissolution. Some regions of the slag particle experience more dissolution than others, which can be attributed to the heterogeneous distribution of chemical composition of slag and the initial defects induced by the mechanical damage during the grounding process of AAFS sample. These special regions would promote the formation of etch pits and result in the rapid localized dissolution. A similar phenomenon can also be observed in the dissolution of fly ash particle in AAFS mixes as discussed in Section 4.1.6.

After the dissolution of slag particle, a thin layer of reaction products is formed around the unreacted slag particle, as shown in Figure 4-33b. It can be found that the distribution of reaction products is not uniform around the slag surface, attributing to the non-uniform dissolution of slag. The reaction products can be divided into inner products and outer products. The proportion of inner products is higher than that of outer products, as a result of the rapid reaction in the dissolved region of slag, where the high ionic concentration would promote the formation of reaction products, filling the dissolved region. When the dissolved region of slag is filled with the inner products, the growth of reaction products would drop due to the relatively low ionic concentration surrounding the outside particle. Besides, it can be seen from Figure 4-33b that the formation of inner products (e.g. C-A-

S-H gels (Puertas et al., 2011)) would also act as a physical barrier, preventing the diffusion of ions between unreacted slag and the surrounding region and thus slowing down the reaction process. It is responsible for the sharp decrease of reaction rate of slag particle after 1 d, regardless of particle size (Figure 4-32). A similar phenomenon can be found in the formation of reaction products of fly ash particle in AAFS as mentioned above.

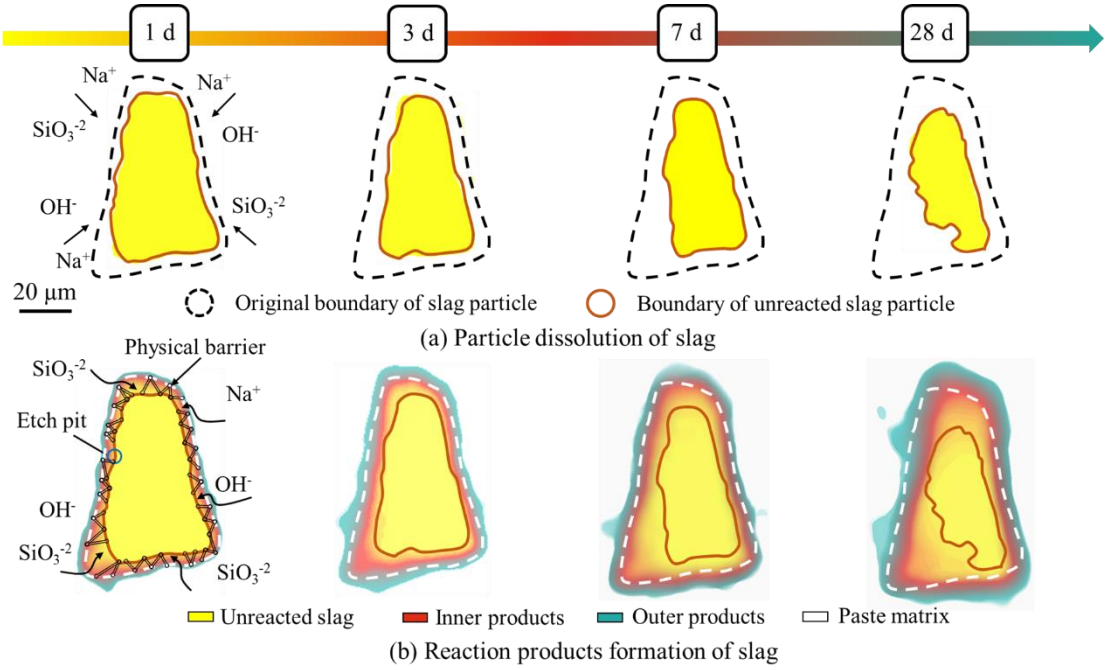

Figure 4-33 Microstructure evolution of slag particle in AAFS paste

4.7.3.4 Interaction between fly ash and slag particles

a. Phase identification

Figure 4-34 demonstrates the linear grey value across the adjacent slag and fly ash particles. The unreacted slag with a grey value of 230 (C – D) and unreacted fly ash with a grey value of 255 (G – H) are surrounded by the reaction products and paste matrix. The reaction products of slag (B – C; D – E) cover the grey values of 120 – 230, while the reaction products of fly ash (F – G; H – I) correspond to the grey values of 108 – 255. The reaction products of slag and fly ash can also be divided into inner and outer products based on their difference in grey value and their relative locations to the original boundary of particle, as mentioned in Sections 4.7.3.2 and 4.7.3.3. Similarly, different phases in slag and fly ash particles are also labelled as different colours (unreacted particle: yellow; inner products: red; outer products: green; paste matrix: white).

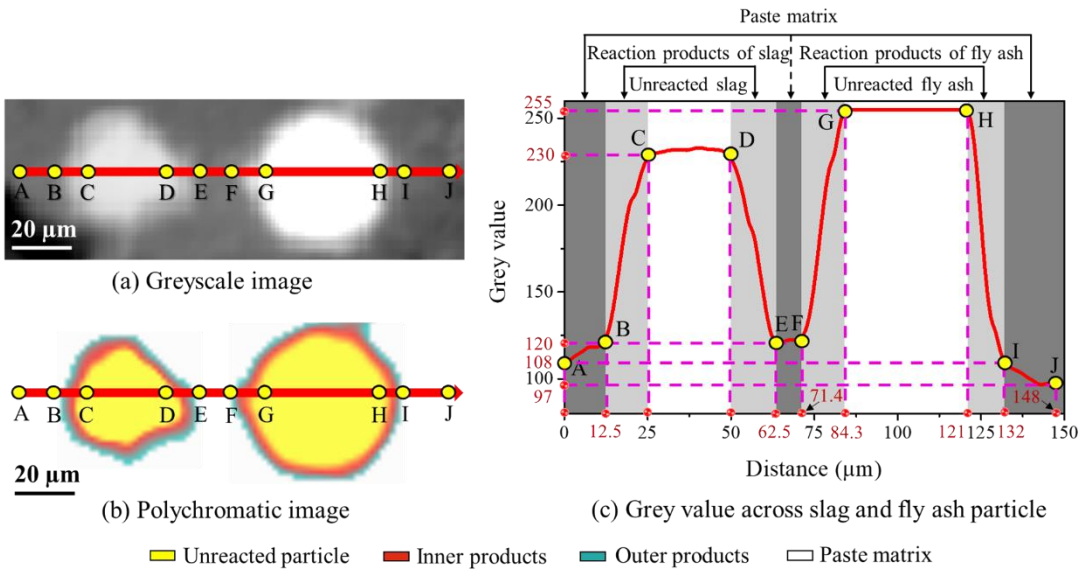

Figure 4-34 Phase identification of slag and fly ash particles in AAFS paste (t = 1 d)

Figure 4-35 shows the chemical composition across slag and fly ash particles characterised by means of the BSEM-EDS line scanning from slag to fly ash. The molar ratios of Ca/Si, Ca/Al and Ca/(Si+Al) against the distance from slag to fly ash are calculated and plotted in Figure 4-35a and b. The Ca/Al ratio stays at a relatively high level (> 1.0) at the core region of slag (A – B) and reduces from 1.0 to 0.43 at the outer region of slag (B – C), followed by a further slight reduction from 0.43 to 0.26 in the region of paste matrix between slag and fly ash (C – D). The Ca/Al ratio drops from 0.26 to 0.03 in the outer region of fly ash (D – E) but becomes stable at around 0.03 in the core region of fly ash (E – F). The continuous decrease of Ca/Al ratio from the region of unreacted slag fly ash can be attributed to the decline of Ca content and the increase of Al content due to the ion transport during the dissolution of slag and fly ash. The Ca dissolved from slag particle would diffuse to the region close to fly ash particle due to the gradient of ionic concentration. Similarly, the dissolution of Al from fly ash would also diffuse to the slag region. Similar trends can be observed in the distribution of Ca/Si and Ca/(Si+Al) ratios.

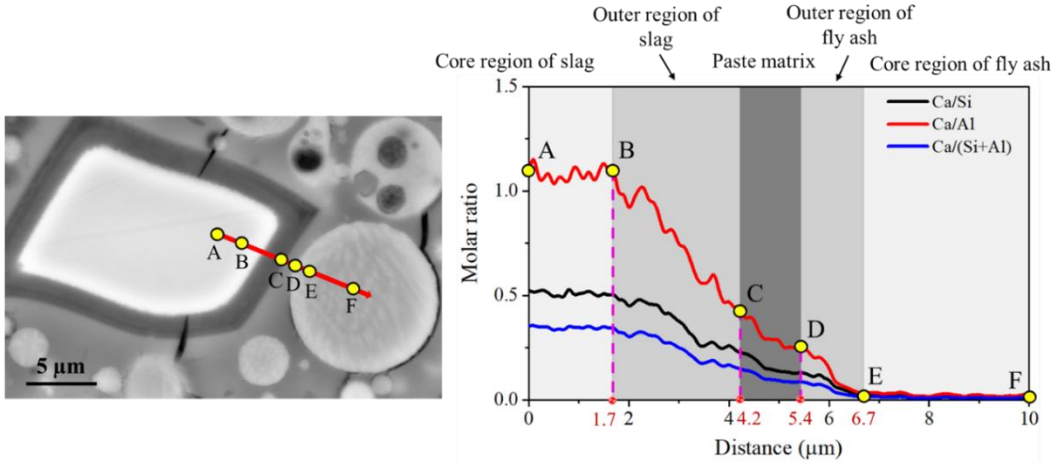

(a) BSEM image (b) Results of EDS line analysis

Figure 4-35 Chemical composition across slag and fly ash particle in AAFS paste (t = 28 d)

b. Interaction of fly ash and slag at various curing ages

Figure 4-36 displays the interaction between fly ash and slag particles at different curing ages, characterised using the greyscale image and the linear grey value histogram. At the beginning (1 d), both unreacted slag and fly ash particles occupy a relatively wide area, surrounded by a thin layer of reaction products. At 3 d, the areas of unreacted slag and fly ash are both slightly reduced, while the areas of reaction products of slag and fly ash are increased accordingly. However, the microstructure evolution of slag and fly ash becomes different after 3 d. Between 7 d and 28 d, the area of unreacted slag is reduced steadily, following a similar changing trend observed in the isolated slag. This indicates that the presence of fly ash has a slight effect on the microstructure evolution of slag. Nevertheless, the area of unreacted fly ash is reduced significantly between 7 d and 28 d. At 7 d, fly ash particle is dissolved quickly, leading to an irregular shape of unreacted fly ash, as confirmed by the obvious decrease of grey value. At 28 d, the fly ash particle is completely dissolved, resulting in a fully reacted area with reaction products. This implies that the presence of slag would strongly accelerate the chemical reaction and microstructure evolution of fly ash in AAFS, which is completely different from the microstructure evolution of isolated fly ash.

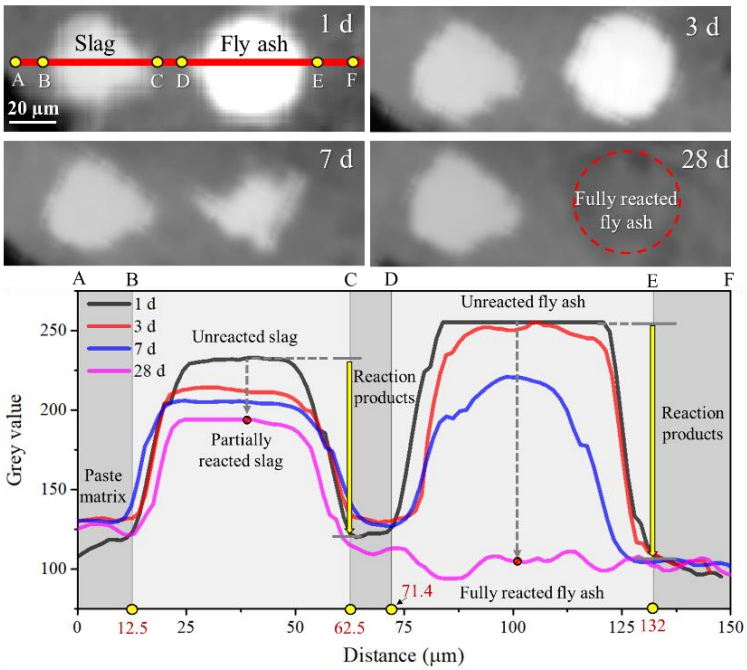

Figure 4-36 Grey value across slag and fly ash particles in AAFS paste at different curing ages

The reaction degree and reaction rate of slag and fly ash at different curing ages are quantified and presented in Figure 4-37 to understand the interaction between slag and fly ash particles in AAFS. As seen in Figure 4-37a, the microstructure evolution of slag particle close to fly ash particle is similar to that of isolated slag particle (Figure 4-31a), where the slag particle is dissolved steadily accompanied by the formation of inner products. Nevertheless, the microstructure evolution of fly ash particle close to slag particle is different compared to the isolated fly ash particle (Figure 4-22a). The original boundary of fly ash disappears after 7 d along with the formation of outer products in paste matrix, which can be attributed to the accelerated reaction of fly ash particle. It can be seen from Figure 4-37b that the reaction degree of slag is increased steadily from 36.28% to 62.89% between 1 d and 28 d, following a similar changing trend of isolated slag (Figure 4-31f), while, the change of reaction degree of fly ash is different from that of isolated fly ash, which is increased steadily with increasing curing age from 1 d to 28 d (Figure 4-22f). Here, the reaction degree of fly ash is increased slightly from 22.56% to 28.80% with the increase of curing age from 1 d to 3 d, but then increased significantly to 72.50% at 7 d and eventually reaches 100% at 28 d. Besides, it can be found that the reaction degree of slag (36.28% ~ 47.05%) is higher than that of fly ash (22.56% ~ 28.80%) at early ages (1 ~ 3 d). Afterwards, the reaction degree of slag (53.50% ~ 62.89%) becomes lower than that of fly ash (72.50% – 100%) between 7 d and 28 d. Furthermore, it can be seen from Figure 4-37c that the change of reaction rate of slag near the fly ash particle in AAFS is similar to that of isolated slag (Figure 4-31f), where the reaction rate

reduces from 36.28%/d to 5.39%/d during the first curing stage (0 ~ 1 d) and the second curing stage (1 ~ 3 d) and continually drops to 0.45%/d at the last stage (7 ~ 28 d). However, the changing trend of reaction rate of fly ash near the slag particle in AAFS is different from that of isolated fly ash (Figure 4-22f). The reaction rate of fly ash is decreased significantly from 22.56%/d to 3.12%/d during the first and second stages, followed by a sharp increase to 10.92%/d at the third stage (3 ~ 7 d) and a sharp decrease to 1.30%/d at the last stage (7 ~ 28 d).

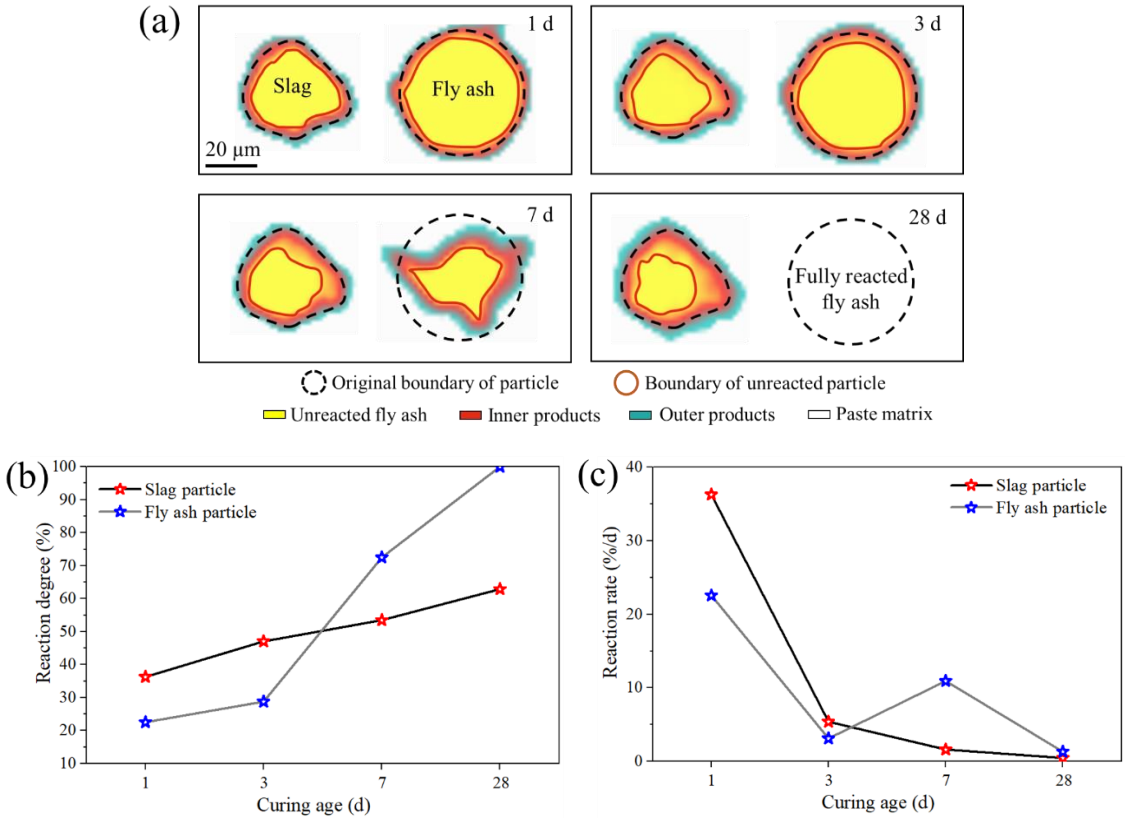

Figure 4-37 Reaction degree and reaction rate of slag and fly ash particles in AAFS paste at different curing ages

c. Mechanism of interaction between fly ash and slag

The interaction between fly ash and slag in AAFS can be associated with their different reaction mechanism. During the alkaline activation, different types of chemical elements would be dissolved from fly ash and slag particles, leading to the formation of different reaction products (Ye and Radlińska, 2016). The Si and Al ions would be dissolved from fly ash to form N-A-S-H gels, while the Ca, Si and Al ions would be dissolved from slag to form C-A-S-H gels. Therefore, it is likely to occur interaction and reaction of dissolved ions, which would further affect the surrounding aqueous environment of fly ash and slag, resulting in the interaction between them in terms of microstructure evolution (Puligilla and Mondal, 2013).

As shown in Figure 4-37, the microstructure evolution of fly ash and slag at early ages (1 – 3 d) is similar to that of isolated fly ash (Figure 4-27) and slag (Figure 4-33), respectively, which indicates that the interaction between fly ash and slag is not obvious at early ages. This can be ascribed to the limited movement of the dissolved ions between fly ash and slag particles. At these early ages, the reaction degree of fly ash is smaller than that of slag due to its relatively low reactivity. At later curing ages (7 – 28 d), the trend of microstructure evolution of fly ash becomes different from that of slag. The microstructure of fly ash exhibits a significant change with the increase of curing age from 7 d to 28 d, indicating the existence of interaction between fly ash and slag. This can be attributed to the diffusion of Ca ions from the dissolved slag to the unreacted fly ash, which would enhance the rate and the extent of fly ash dissolution and the formation of reaction products (Puligilla and Mondal, 2013). The presence of Ca ions would facilitate and promote the precipitation of Ca-based products (C-A-S-H gels), which would act as nucleation sites and trigger the rapid formation of Na-based products (N-A-S-H gels) (Yip et al., 2008). Besides, since Si ions existing around the fly ash particle would preferentially react with Ca ions to form (C, N)-A-S-H gels, the dissolution rate of fly ash is accelerated to maintain the concentration of Si ions (Puligilla and Mondal, 2013). The formation of (C, N)-A-S-H gels would also consume water, and thus increase the alkalinity of solution around fly ash particle and further encourage its dissolution (Puligilla and Mondal, 2013). Nevertheless, the presence of fly ash has no obvious effect on the microstructure evolution of slag even at later curing ages (7 – 28 d), where the microstructure of slag close to the fly ash particle in AAFS changes steadily, in consistence with the microstructure evolution of isolated slag.

4.7.4 Microstructure evolution of AAFS paste

Figure 4-38 shows the microstructure of AAFS paste. Based on the difference in morphology and grey value, different phases can be clearly identified in Figure 4-38a, which can be roughly classified into two groups: (1) pore phase including cracks and pores, both of which are presented as black due to the low atomic number, and (2) solid phase including unreacted particles (i.e. fly ash and slag) and reaction products, which appear as light grey and dark grey, respectively. In order to subdivide different phases in AAFS paste, the greyscale histogram is subtracted from Figure 4-38a and deconvolved into four Gaussian curves using a statistical analysis software called Peakfit (see Figure 4-38b). The first Gaussian curve is assigned to pores, while the second Gaussian curve corresponds to reaction products. The third and fourth Gaussian curves are related to

unreacted fly ash and slag, respectively. The point of interaction between Gauss 1 (Pores) and Gauss 2 (reaction products) is defined as the threshold value to determine the boundary between pores and reaction products. Similarly, the threshold value of frontier between reaction products and unreacted fly ash is set as the interaction point between Gauss 2 (reaction products) and Gauss 3 (unreacted fly ash). Unreacted fly ash and slag are separated based on the interaction point between Gauss 3 (unreacted fly ash) and Gauss 4 (unreacted slag). Here, the threshold values of 43, 155 and 184 are obtained to segment pores, reaction products, unreacted fly ash and unreacted slag (see Figure 4-38b). Accordingly, as shown in Figure 4-38c, different phases including unreacted slag, unreacted fly ash, reaction products and pores are distinguished and labelled in different colours. The unreacted slag is labelled in red, while the unreacted fly ash is presented as yellow (see Figure 4-38d). It is interesting to note that the reaction products cover a wide range of colours from light blue to light green, which indicates that different types of reaction products form together within the AAFS paste (see Figure 4-38e). The pores are labelled in blue (see Figure 4-38f).

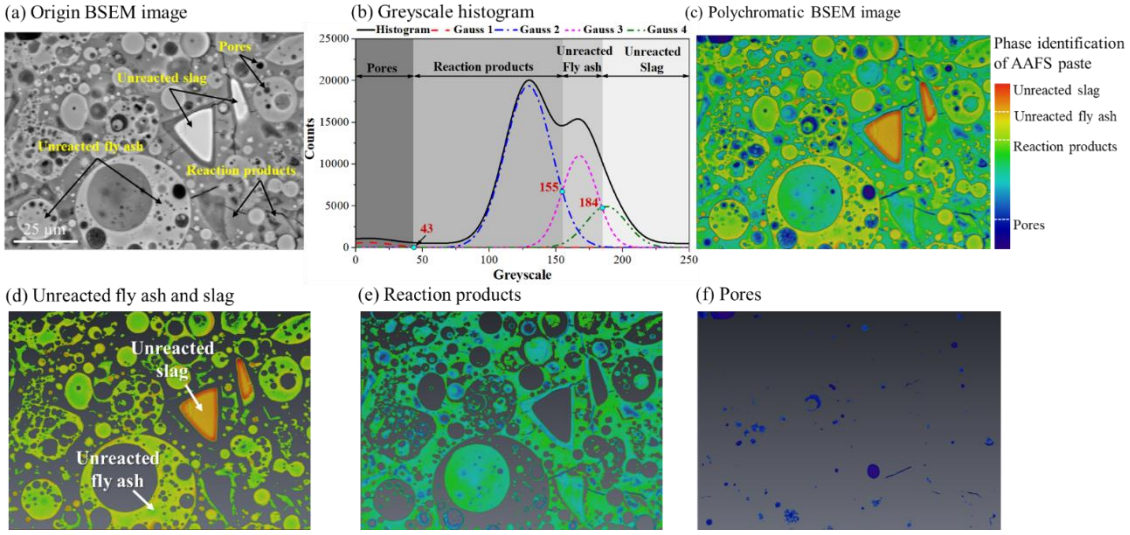

Figure 4-38 Typical polychromatic greyscale image of AAFS paste (t = 28 d)

Figure 4-39 shows the BSEM images of AAFS pastes at different curing ages. The microstructure of solid AAFS pastes is significantly changed with the increase of curing age. Initially, the morphology of most precursors (fly ash and slag) at 1 d is not altered by the alkaline activator, except for the morphology change in some small particles (see Figure 4-39a). This is mainly because the finer particles are easier to be activated at early curing ages (Wang et al., 2005; Kumar et al., 2007). Additionally, the reaction products are presented as dark grey, which implies that the density of their structures is relatively low. This is because of the low reaction degree at early curing ages. As the curing age

increases to 3 d, the change in morphology of fly ash and slag becomes obvious, even for the relatively large particles (see Figure 4-39b). At this stage, the change in morphology of slag is more significant than that of fly ash due to its higher reactivity. Normally, slag has over 90% vitreous phase which contributes to alkaline activation, while fly ash only has about 50% vitreous phase and the remaining constituents (crystalline phase) in fly ash are difficult to be activated and thus need longer time for reaction (Kumar et al., 2007). As the reaction proceeds with time from 7 d to 28 d (see Figure 4-39c and d), the change in morphology of slag becomes more obvious, along with a significant reduction in the size of original slag particles, and some fully reacted slag can be found. During the activation of fly ash, its morphology is also changed significantly, with the filling of reaction products into the original hallow within fly ash. Furthermore, the reaction products at later curing ages are presented as a lighter grey than that at early curing ages (1 d and 3 d), suggesting that the microstructure becomes compact at later curing ages.

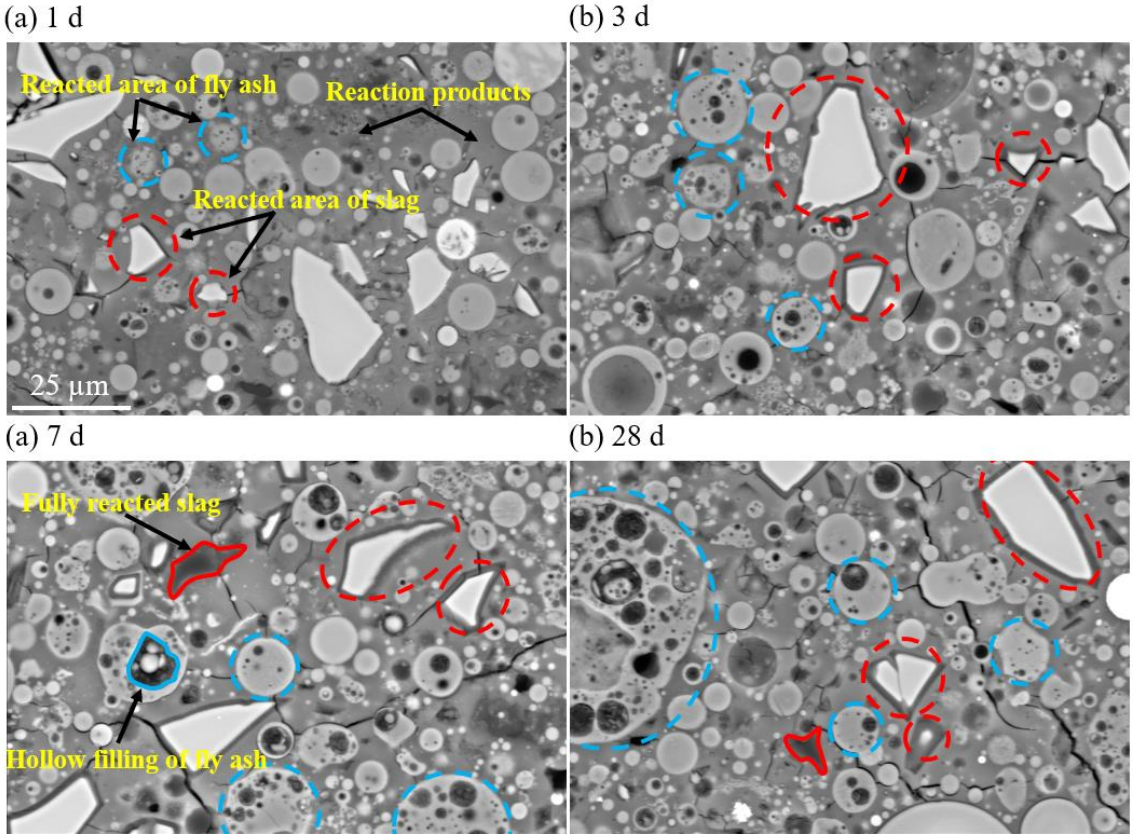

Figure 4-39 BSEM images of AAFS pastes at different curing ages

To further understand the evolution of microstructure, the reaction degrees of fly ash and slag were calculated based on a series of analysis on 10 BSEM images (magnification: 250×) of each sample. Combined with the image analysis mentioned in Figure 4-38, unreacted fly ash and slag were distinguished from each image, and their volume fractions were characterised using an open-source image analysis software called Fiji (Schindelin

et al., 2012). Subsequently, the reaction degrees of fly ash and slag can be calculated as follows:

$$\alpha_{fly\text{-}ash} = \left(1 - \frac{V_{(t)fly\ ash}}{V_{(0)fly\ ash}}\right) \times 100\% \quad (4-13)$$

$$\alpha_{slag} = \left(1 - \frac{V_{(t)slag}}{V_{(0)slag}}\right) \times 100\% \quad (4-14)$$

where $\alpha_{fly\text{-}ash}$ is the reaction degree of fly ash, $V_{(t)fly\text{-}ash}$ is the volume fraction of unreacted fly ash at age *t* obtained from the BSEM image analysis, $V_{(0)fly\ ash}$ is the initial volume fraction of fly ash (before reaction) calculated based on the mixture quantity in Table 4-1 (i.e. 43.28%), α_{slag} is the reaction degree of slag, $V_{(t)slag}$ is the volume fraction of unreacted slag at age *t* obtained from the BSEM image analysis, and $V_{(0)slag}$ is the initial volume fraction of slag (before reaction) (i.e. 11.19%).

Figure 4-40 shows the reaction degree of fly ash and slag at different curing ages. It can be found that the reaction degree of slag is higher than that of fly ash, especially at early 7 d. Within the first 7 d, the reaction degree of slag (46.66% ~ 58.96%) is obviously higher than that of fly ash (30.48% ~ 44.83%), which can be attributed to the high content of vitreous phase within slag. The high reaction degree of slag is related to the high dissolution of calcium silicates from slag, which would promote the formation of C-A-S-H gels and N-C-A-S-H gels in AAFS paste. In comparison, there is less dissolution of aluminate silicates from fly ash due to its relatively low reaction degree. Between 7 d and 28 d, the difference of reaction degree between slag and fly ash becomes less, where the reaction degree of slag (74.36%) is 10% higher than that of fly ash (64.52%). This indicates that the dissolution rate of calcium silicates from slag becomes slow, while the dissolution rate of aluminate silicates from fly ash increases, which would promote the formation of N-A-S-H gels.

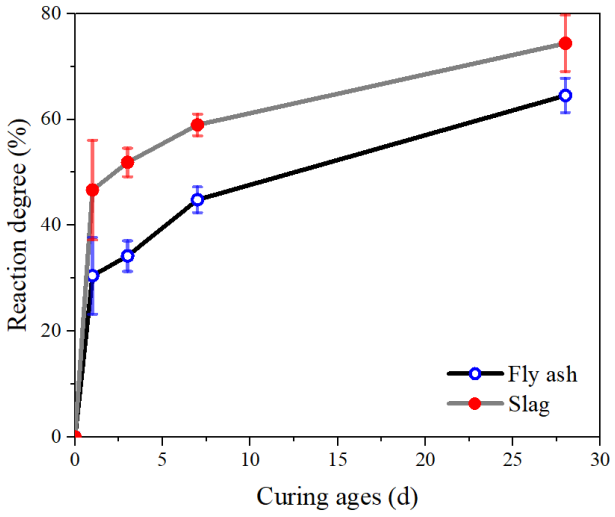

Figure 4-40 Reaction degree of fly ash and slag at different curing ages

Figure 4-41 shows the pore size distribution of AAFS pastes at different curing ages obtained from MIP tests. The pore size decreases dramatically in the early 7 d and then decreases slightly with increasing curing age from 7 d to 28 d (see Figure 4-41a). The pores with size between 5 and 30 nm exhibit obvious changes compared to other pores. Generally, the pores with size between 2.5 and 10 nm belong to small gel pores, while the pores with size in the range of 10 and 50 nm can be assigned to medium capillary pores (Aligizaki, 2005). Hence, it is suggested that both gel pores and capillary pores in AAFS pastes would be changed and refined due to the newly formed reaction products. Additionally, the total porosity of AAFS pastes is decreased significantly from about 28% to 10% with the increase of curing age from 1 d to 28 d, leading to a compact microstructure of AAFS pastes at later curing ages (see Figure 4-41b).

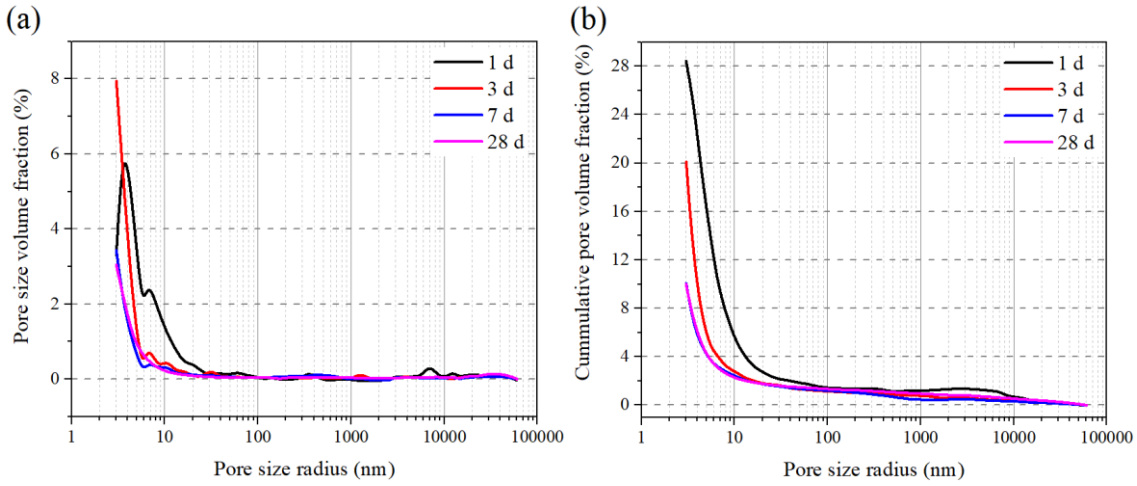

Figure 4-41 Pore size distribution of AAFS pastes at different curing ages

4.7.5 Microstructure evolution of ITZ in AAFS concrete

A systematic analysis of the microstructure evolution of ITZ in AAFS concrete from the very early age (3 h) to the later curing age (28 d) was made based on BSEM and EDS test, providing needed insight into the mechanisms, by which it evolves over time. Firstly, the interfacial features between aggregates and paste were characterised to identify the ITZ. Afterwards, the formation and development of ITZ were studied through the quantitative analysis of physical packing of fly ash and slag grains against aggregates, reaction process, and pore structure evolution. Finally, the mechanisms of ITZ's evolution were discussed in detail based on the experimental results.

4.7.5.1 BSEM image analysis

After the BSEM images were obtained, a series of image analysis was carried out, which can be divided into four steps, including aggregate boundary delineation, phases identification, strip delineation, and quantitative analysis.

Aggregate boundary delineation

A typical BSEM image of AAFS concrete after 24 h of curing is shown in Figure 4-42. To specify the interface between aggregates and paste matrix, it is essential to delineate the boundary of aggregates. However, it is not possible to automatically specify the aggregate boundary due to the close grey scale between aggregates and reaction products in the BSE images and the irregular shape of aggregates (see Figure 4-42a). Therefore, an artificial method is required to accurately specify the boundary of aggregates. The aggregate boundary delineation mainly includes three steps: (i) detecting the boundary of aggregate, (ii) labelling the edge of aggregate, and (iii) getting rid of aggregate area. In the first step, the original BSEM image was magnified to make sure that the boundary between aggregates and paste matrix can be clearly recognized (see Figure 4-42b). The triple magnification was used in this study. As shown in Figure 4-42c, the boundary of aggregates can be clearly recognized. Afterwards, the irregular curve was used to label the boundary of aggregates, where the distance between two points was controlled under 3 μm to ensure the accuracy of labelling (see Figure 4-42d). Next, the labelled aggregate area was cut (see Figure 4-42e). Finally, as shown in Figure 4-42f, the boundary of aggregate in the whole image was clearly specified. Here, an in-house MATLAB code along with the image processing software called ImageJ was used.

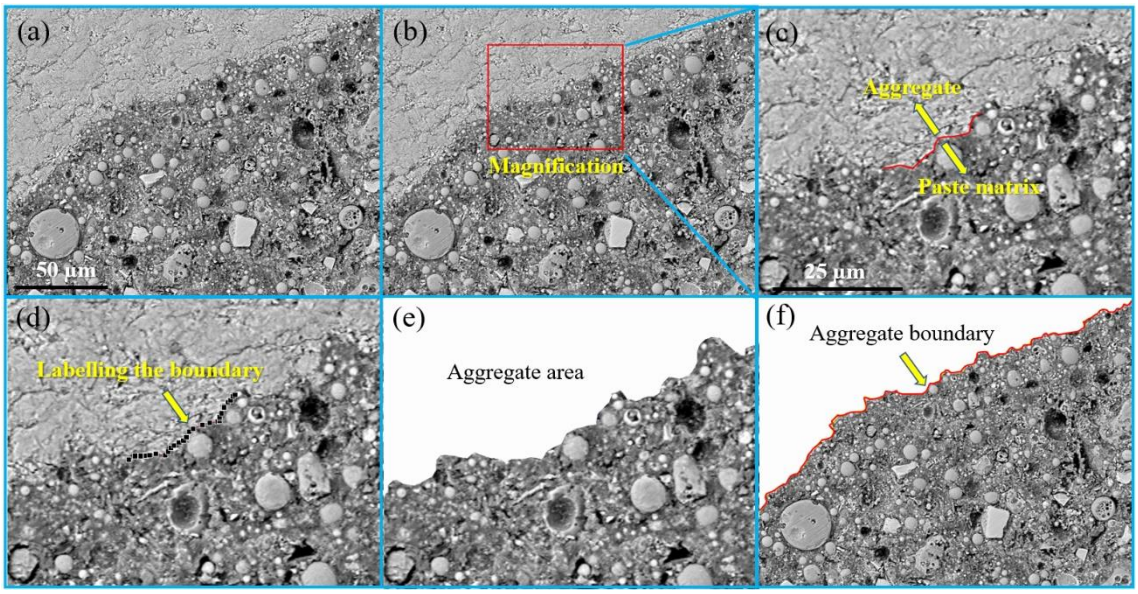

Figure 4-42 A schematic diagram for the aggregate boundary delineation (t = 24 h)

Phases identification

To characterise the interfacial properties of AAFS concrete, it is vital to identify different phases including pores, reaction products and unreacted particles. It should be noted that the term 'pores' used here is regarded as a general term for epoxy-filled voids in the sample, which includes capillary pores, cracks and hollow reaction shells, referring to previous research (Wong et al., 2006). Figure 4-43 shows a typical greyscale histogram subtracted from a 24-h cured AAFS concrete. The histogram was deconvolved into three Gaussian curves using a statistical analysis software called PeakFit, in which the Gaussian line model was applied. The first Gaussian curve corresponds to the pores, and the second Gaussian curve is attributed to the reaction products while the third Gaussian curve is assigned to the unreacted particles. The threshold value defining the frontier between pores and reaction products was set as the point of intersection between Gauss 1 (pores) and Gauss 2 (reaction products). Similarity, the intersection between Gauss 2 (reaction products) and Gauss 3 (unreacted particles) was defined as the threshold value to specify the boundary between reaction products and unreacted particles. Accordingly, the threshold values of 25 and 132 were determined to distinguish pores, reaction products and unreacted particles, which are shown in Figure 4-43. With this method, the threshold values of all testing samples were obtained as listed in Table 4-6. It is worth mentioning that the determination of threshold values should be adjusted according to each sample, since there is a deviation of this value between different samples. Although all the testing parameters are set as constant values, some deviations between different samples are difficult to be avoided. More details about the phase segmentation for different samples are presented in Appendix C.

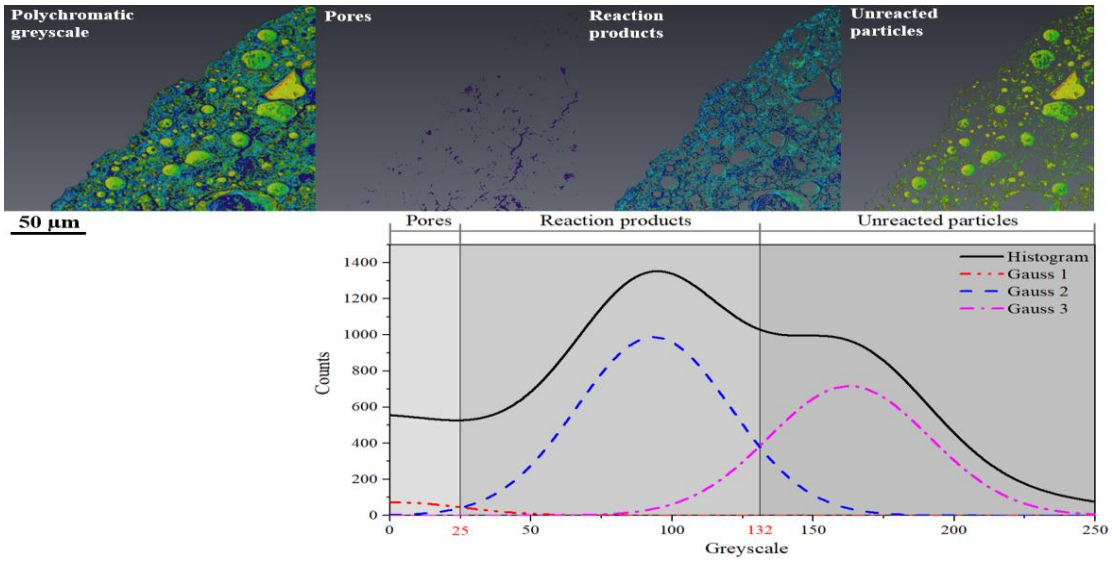

Figure 4-43 A typical polychromatic greyscale histogram of different phases in AAFS concrete (t = 24 h)

Table 4-6 Threshold values for identifying different phases in AAFS concrete

Mix no.	Pores	Reaction products	Unreacted particles
3-h	0~27	27~134	134~255
12-h	0~27	27~135	135~255
24-h	0~25	25~132	132~255
3-d	0~27	27~137	137~255
7-d	0~27	27~145	145~255
28-d	0~30	30~140	140~255

Strip delineation

In order to characterise the interfacial properties along the distance from the aggregate surface, some successive strips with specified distance were delineated based on the strip delineation method called "concentric expansion" (Gao et al., 2013). Therefore, 20 successive strips of 5-μm width were delineated per image and repeated on 30 images for each specimen. A typical example is shown in Figure 4-44a. It should be noted that the ITZ with width below 5 μm cannot be detected in this research.

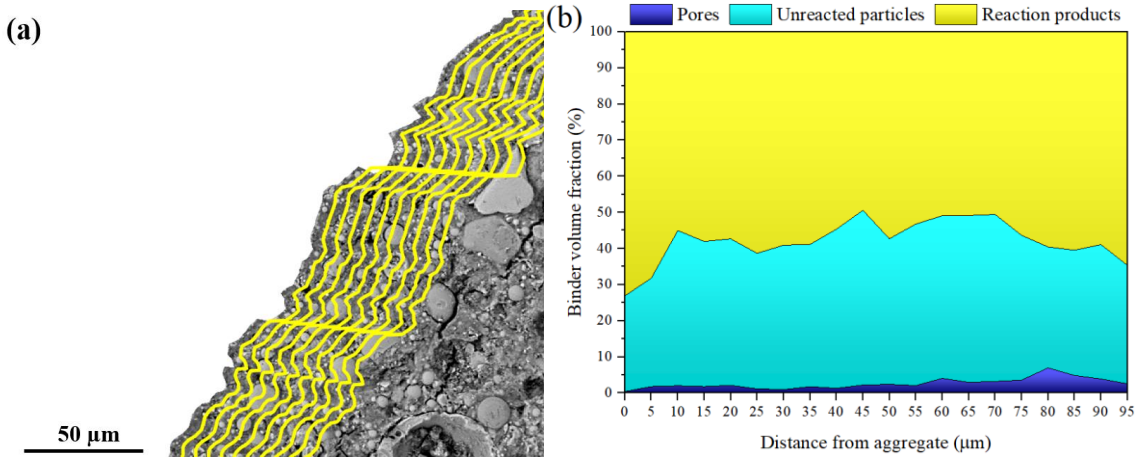

Figure 4-44 An example of strip lineation (a) and quantitative analysis using concentric expansion method (b) (t = 24 h)

Quantitative analysis

The properties of each strip can then be quantified with the assistance of phase identification mentioned above. Figure 4-44b shows the volume fractions of different phases, i.e., pores, reaction products and unreacted particles. It should be noted that the segmented pores here are assigned to the porous patches with the greyscale below the threshold defined for pores instead of the single pores. The porous patches mainly consist of interconnected capillary pores, microcracks and hollow shells (Wong and Buenfeld, 2006). This is mainly due to the size limitation of the BSEM images (Diamond and Leeman, 2011). In this study, the BSEM images with a resolution of 0.25 μm cannot

provide the direct information of the single pores, because the pore size in AAFS system (typically < 0.1 μm (Nedeljković et al., 2018)) is smaller than 0.25 μm. Therefore, in BSEM analysis, a cluster of interconnected pores is generally classified as a single pore during the characterisation of pore structures, as it cannot further segment individual pore chambers and throats (Yio et al., 2019). Thus, the porosity obtained here is only referred to the pores larger than 0.25 μm.

Statistical analysis

In addition, the statistical data of the volume fraction of different phases were analysed using the one-way analysis of variance (ANOVA) method. One-way ANOVA is a type of statistical method that can be used to determine whether there are any statistically significant differences between the means of two or more groups (Bewick et al., 2004). Within this method, two parameters including *F*-value and *p*-value were provided to evaluate the statistical significance. The *F*-value represents the ratio of the variation between group means to the variation within the groups. The *p*-value is the probability value associated with the *F*-value, which is used to evaluate whether the result of *F*-value between different groups is statistically significant. The *p*-value is compared with the significance level to determine whether the observed groups have significant difference. Significance level indicates the risk of conclusion that a difference exists when no actual difference is happen (Bewick et al., 2004). Here, the significance level was set as 0.05 which is typically used in statistical analysis (Salkind, 2007). If the *p*-value is more than 0.05, there is no significant difference between the observed groups. Otherwise, if the *p*-value is less than 0.05 the observed groups have a significant difference. Furthermore, if the *p*-value is less than 0.01, it indicates a strong significant difference between the observed groups.

4.7.5.2 Characterisation of the interfacial features between aggregate and paste

The characterisation of interfacial features between aggregates and paste was performed based on the statistical analysis, where multiple regions (at 30 regions in each sample) have been imaged and analysed to ensure that the results obtained can possibly represent the whole specimen. In the analysis, the volume percentage corresponding to each of the identified phases (i.e., pores, unreacted particles and reaction products) was compiled for the strip (with 20 successive 5-μm strips). The mean values of percentage volume calculated from 30 different locations were used to characterise the variation of phases with distance from the aggregate surface. Figure 4-45 shows the mean values of

volume fraction of different phases against distance from the aggregate surface at different curing ages. As shown in Figure 4-45a, the microstructural gradients between the region close to the surface of aggregate and the region far away can be observed at 3 h, which are less distinct than those in the case of PC system (Scrivener et al., 2004). At 12 h, the similar microstructural gradients are observed in comparison with 3 h. Nevertheless, the content of reaction products at 12 h is increased dramatically regardless of the distance from aggregate. This can be attributed to the significant reaction process taken place at this very early age, and consequently the volume fraction of pores is decreased dramatically (see Figure 4-45b). During the curing ages from 24 h to 7 d, the content of reaction products is increased slightly regardless of the distance from aggregate, while the content of unreacted particles and pores is decreased slightly (see Figure 4-45c to e). Similarly, the less distinct microstructural gradients are also identified during these curing ages. However, at 28 d, the gradients of reaction products and unreacted particles become conspicuous (see Figure 4-45f). The content of reaction products close to the surface of aggregate is higher than the region far away, while the relative low content of unreacted particles can be found in the region close to the aggregate surface. Simultaneously, the content of reaction products is much higher than that at 7 d, while the content of unreacted particles is obviously lower than that at 7 d.

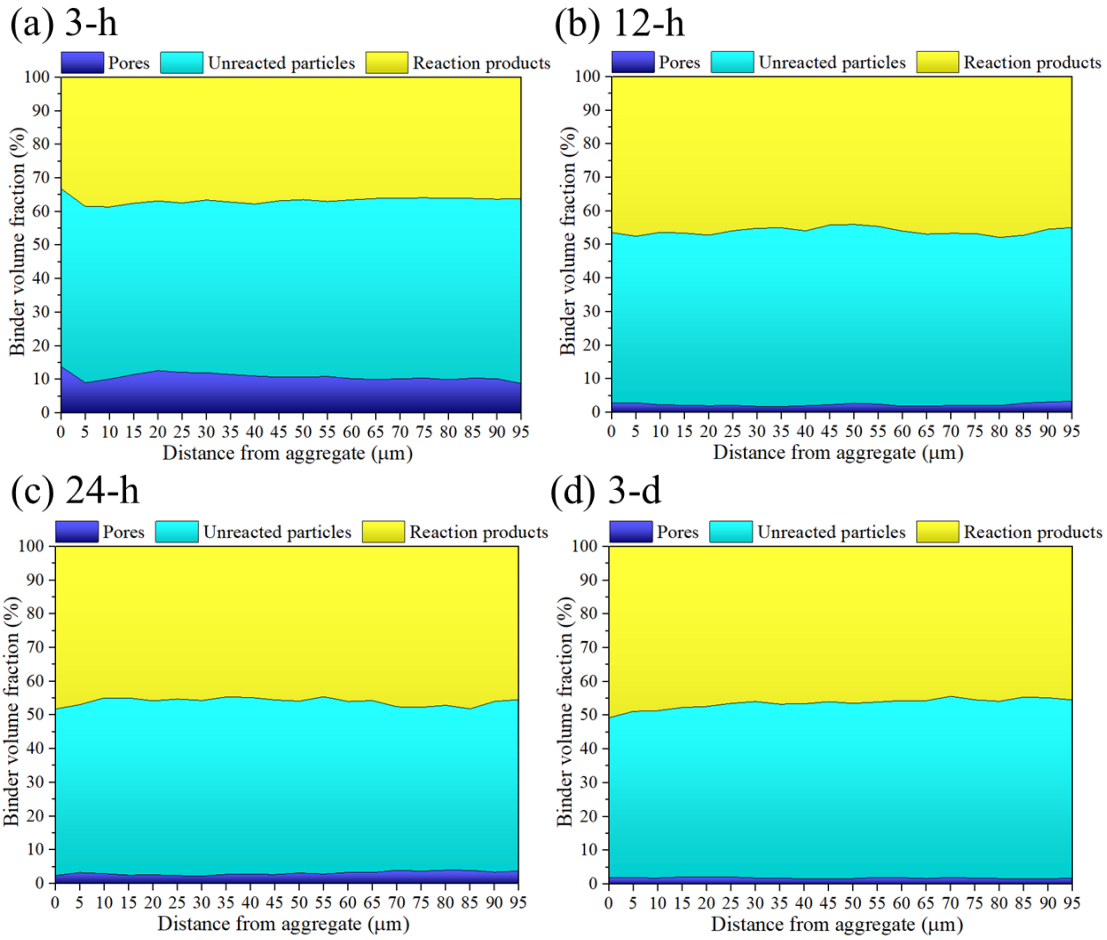

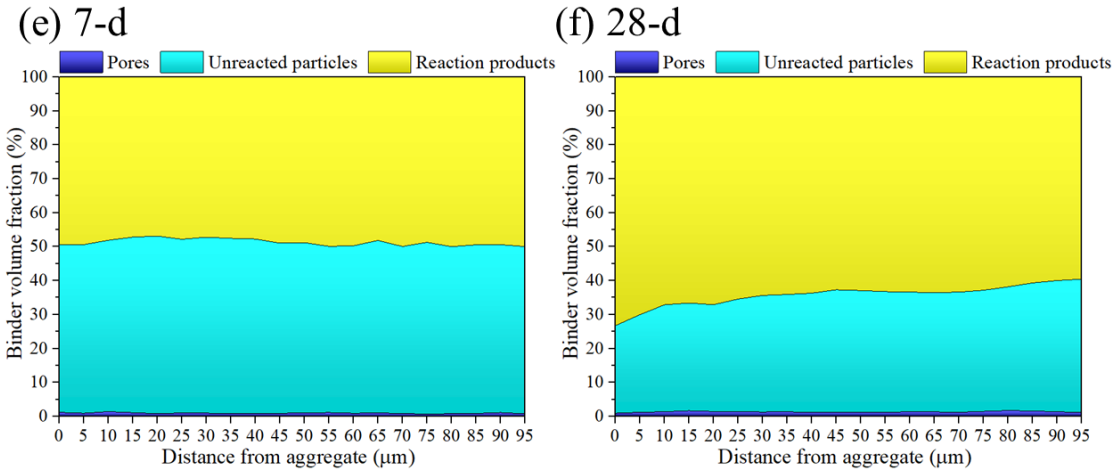

Figure 4-45 Volume fractions of different phases against distance from aggregate surface at different curing ages

In addition, it is desirable to statistically evaluate the degree of lateral variation for successive narrow strips at a fixed distance from aggregate surface. The lateral variation is normally expressed in terms of standard deviation or the coefficient of variation, which helps to better understand the statistical analysis of mean values (Diamond, 2001). The coefficient of variation was used in this study. Figure 4-46 shows the coefficient of variation for the mean volume fraction of different phases against distance from aggregate surface at different curing ages. It can be observed that the coefficient of variation for unreacted particles and reaction products ranges approximately from 10% to 30%, indicating a relatively low degree of variability from different locations taken at the same distance from aggregate. With this acceptable variation between individual locations, a mean value does adequately describe the situation at the fixed distance from aggregate. Meanwhile, the change in volume fractions of unreacted particles and reaction products corresponds to the key feature of ITZ, as demonstrated in PC system (Scrivener et al., 2004) and AAC system (Nicolas and Provis, 2015). Therefore, the mean values of unreacted particles and reaction products content are used to identify the region of ITZ in this study. In addition, the coefficient of variation for pores ranges widely from 20% to 100%, implying a large degree of non-uniformity in terms of pore content. This is due to their relatively low concentration and the complicated components including capillary pores, cracks and reaction hollow shells, which would induce great uncertainty between different locations even at the same distance from aggregate. Thus, the change in mean value of pores is superimposed on a complex pattern of irregular variations, which is a normal and inescapable characteristic in the microstructure of cementitious materials (Diamond, 2001).

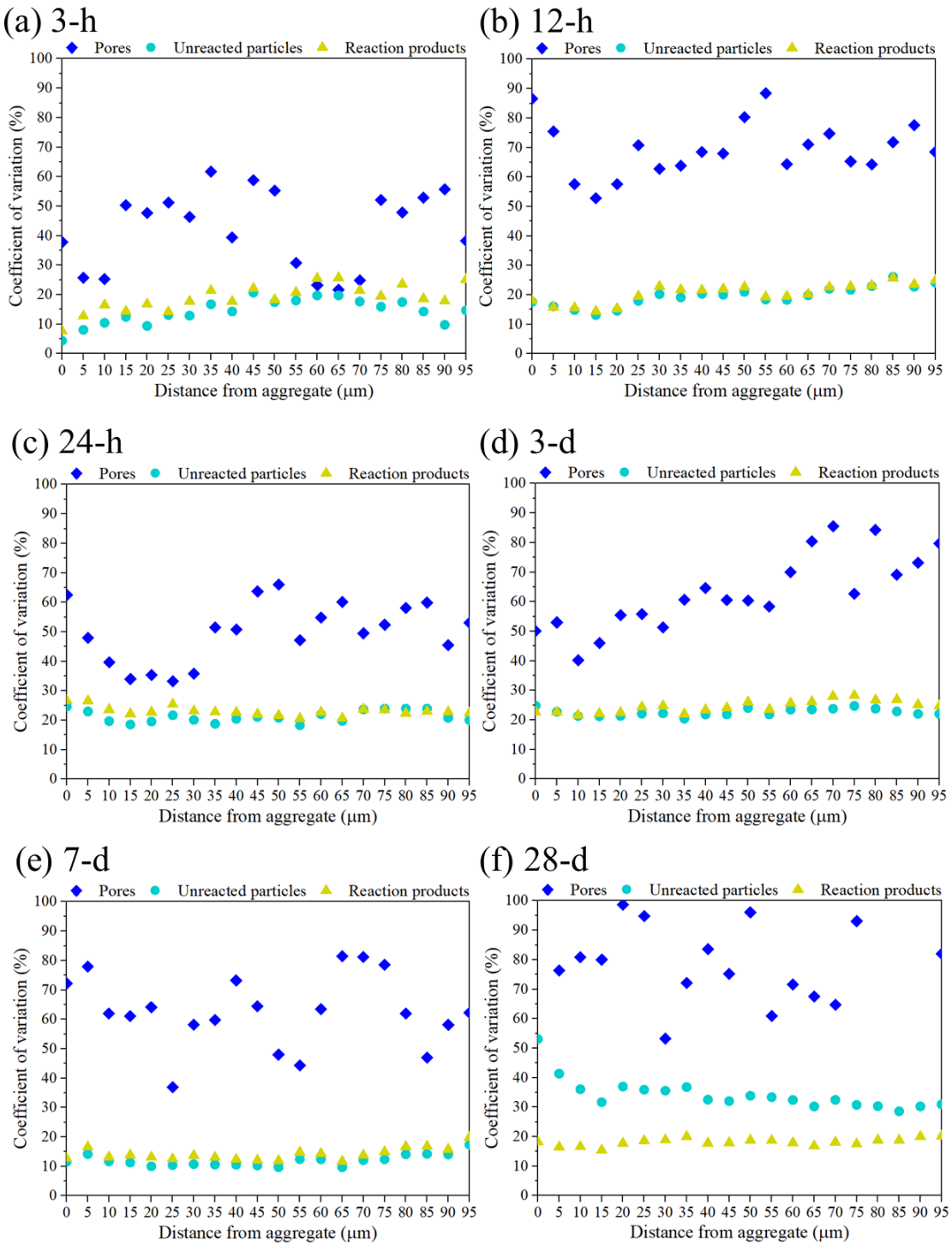

Figure 4-46 Coefficients of variation for the volume fractions of different phases against distance from the aggregate surface at different curing ages

Furthermore, a detailed statistical analysis of the mean values is also crucial to investigate the variation of composition with distance from the aggregate. According to the lateral variation analysis mentioned above, the mean values of unreacted particles and reaction products content were used to define the boundary between ITZ and paste matrix. In order to statistically characterise the variation of composition (i.e. difference of the

adjacent data), the coefficients of difference for unreacted particles (D_u) and reaction products (D_r) were introduced as:

$$D_u = \frac{|U_i - U_0|}{U_0} \times 100\% \quad (4-15)$$

$$D_r = \frac{|R_i - R_0|}{R_0} \times 100\% \quad (4-16)$$

where U_0 is the volume fraction of unreacted particles in the first strip (5 μm far from aggregate surface), U_i is the volume fraction of unreacted particles in the i^{th} strip (up to 20 strips with 5 μm), R_0 is the volume fraction of reaction products in the first strip, and R_i is the volume fraction of reaction products in the i^{th} strip.

Figure 4-47 shows the coefficients of difference for unreacted particles and reaction products against distance from aggregate surface at different curing ages. At 3 h, the coefficients of difference for unreacted particles and reaction products are increased steadily from 0% to 23% and from 0% to 41% respectively with increasing distance from 0 μm to 45 μm, and then fluctuate at around 20% and 35% respectively between the distance of 45 μm and 95 μm (see Figure 4-47a). This might suggest that the microstructure close to the aggregate surface is different compared to the region far away. This microstructurally distinct region that is different from the paste matrix can be regarded as the ITZ. As the curing age increases to 12 h, the boundary between unreacted particles and reaction products becomes fuzzy, which is found to be at 40 μm from the aggregate surface (see Figure 4-47b). Similar phenomena can be observed for the curing ages between 24 h and 7 d (see Figure 4-47c to e), where the boundaries are defined at 50 μm, 40 μm and 40 μm, respectively. However, the boundary becomes obvious again at 28 d (see Figure 4-47f), where the coefficients of different for unreacted particles and reaction products are increased dramatically within the distance between 0 μm and 45 μm and become relatively stable at 45 μm from the aggregate surface.

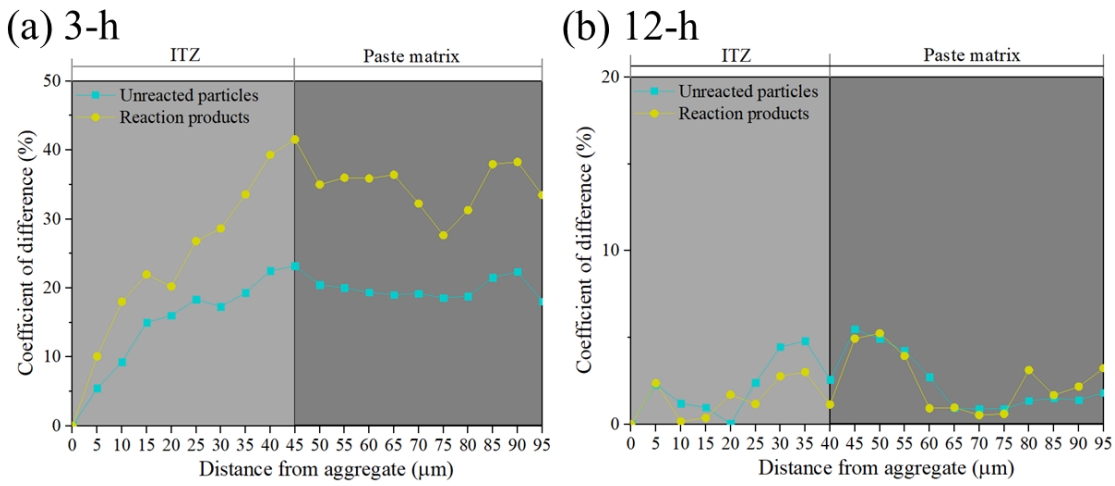

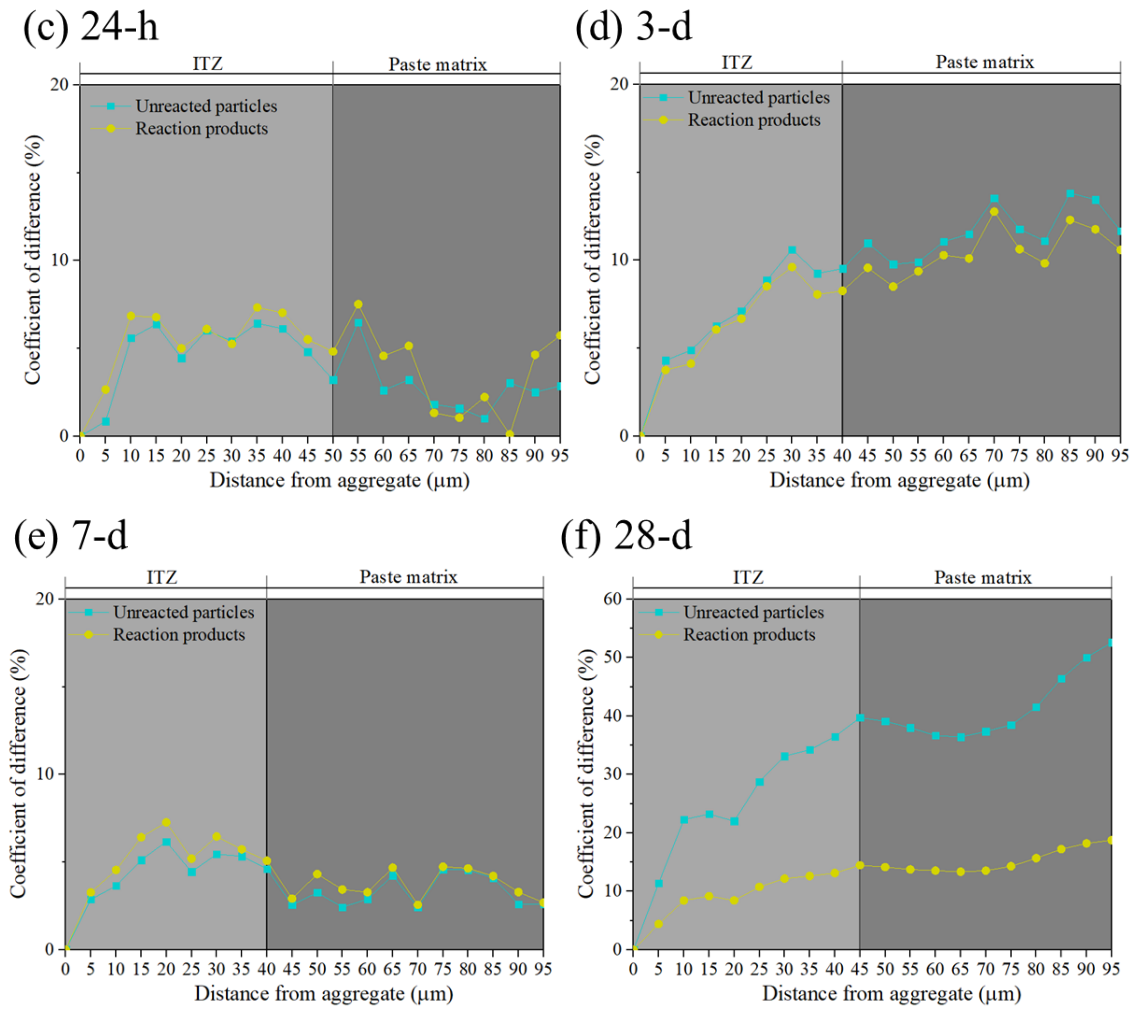

Figure 4-47 Coefficients of difference for the volume fractions of unreacted particles and reaction products against distance from the aggregate surface at different curing ages

Microcracking induced by shrinkage is another key interfacial feature between aggregates and paste, which would initiate and propagate preferentially in the ITZ. As seen in the BSEM images in Figure 4-48, the microcracks existing in ITZ can be divided into two types, including bond cracks and matrix cracks (Wong et al., 2009). The bond cracks appear at the interface between aggregates and paste, while the matrix cracks exist across from aggregate surface to paste matrix. As shown in Figure 4-48a, a clear bond crack exists near the interface between aggregate and paste at 3 h. At 12 h, although the interfacial debonding area can be observed, the paste starts to adhere closely to the aggregate at this stage (see Figure 4-48b). With the further curing at 24 h, the bond cracks become finer than that at 12 h, while some matrix cracks initiate in the interphase region (see Figure 4-48c). As shown in Figure 4-48d, a tight bonding between aggregate and paste can be clearly observed at 3 d, where the bond cracks almost disappear. At 7 d, both bond cracks and matrix cracks are difficult to be identified (see Figure 4-48e). Finally,

the tight bonding between aggregate and paste can also be observed at 28 d, whereas the matrix cracks reappear and propagate from aggregate surface across the paste matrix (see Figure 4-48f).

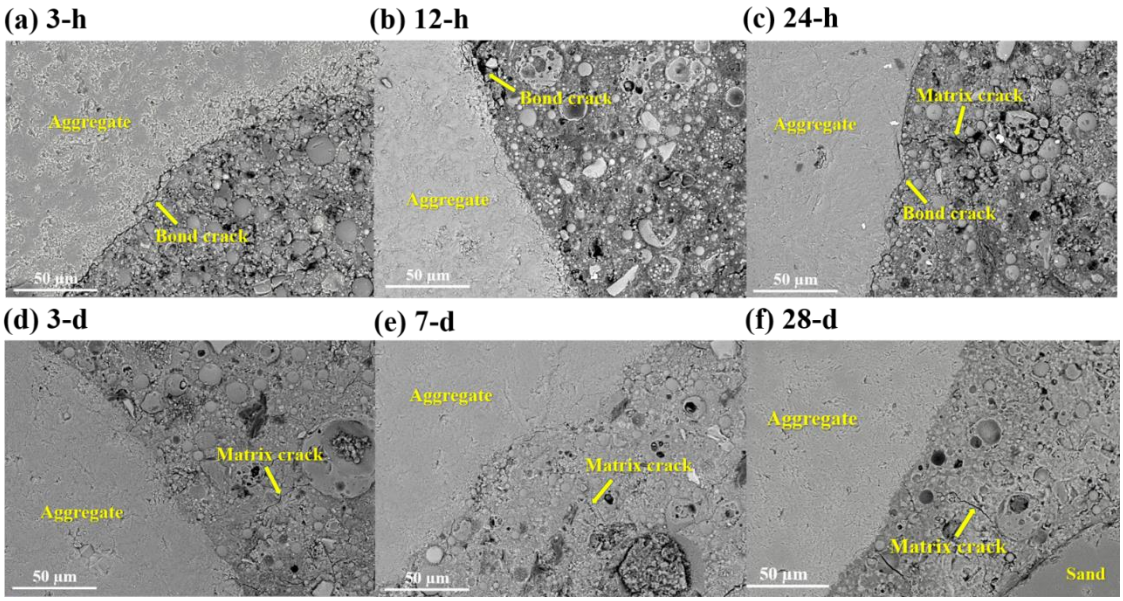

Figure 4-48 BSEM images of interface between aggregate and paste at different curing ages

4.7.5.3 Formation and development of ITZ

In the aforementioned literature, the original ITZ is found to be highly dependent on the packing of raw particles, e.g. cement, fly ash and slag, against the flat surface of aggregates (Scrivener et al., 2004). This phenomenon is called "wall effect", which is responsible for the feature of ITZ, since it would directly affect the grading of unreacted particles, the reaction process and thus the microstructure revolution (especially pore structure). Accordingly, the formation and development of ITZ are discussed from three points of view, including physical packing of unreacted particles, reaction process and pore structure evolution.

Physical packing of fly ash and slag grains in the ITZ

Figure 4-49 presents the grain distribution of fly ash and slag near the surface of aggregate. It can be seen from Figure 4-49a that the small particles play a dominant role in the region close to the surface of aggregate, while the large particles can be found further out of the aggregate surface. This phenomenon can be attributed to the obvious difference in size between precursors (fly ash and slag) grains and aggregates. Normally, the size of fly ash and slag is in the range between 0.1 μm and 100 μm, while the size of aggregate is several orders of magnitude larger than that of fly ash and slag. Thus, each

aggregate exists like a mini “wall” in concrete. During the mixing process, the packing of grains through the surface of aggregate would be disrupted, leading to the so-called “wall effect” (Scrivener et al., 2004). Accordingly, the zone with a deficit of large grains that cannot physically pack adjacent to the aggregate is generated, which is the origin of ITZ (see Figure 4-49b). The particle size distribution of precursors in ITZ and paste matrix was calculated and shown in Figure 4-49c. It can be observed that the diameter of grains in ITZ is much smaller than that in paste matrix. The particle size of precursors in ITZ ranges from 0.5 μm to 11.5 μm, while that in paste matrix covers a larger range between 2.5 μm and 62.5 μm. Nevertheless, it should be mentioned that the particle size distribution would be slightly different due to the random packing of grains even in the same sample (see Figure 4-50).

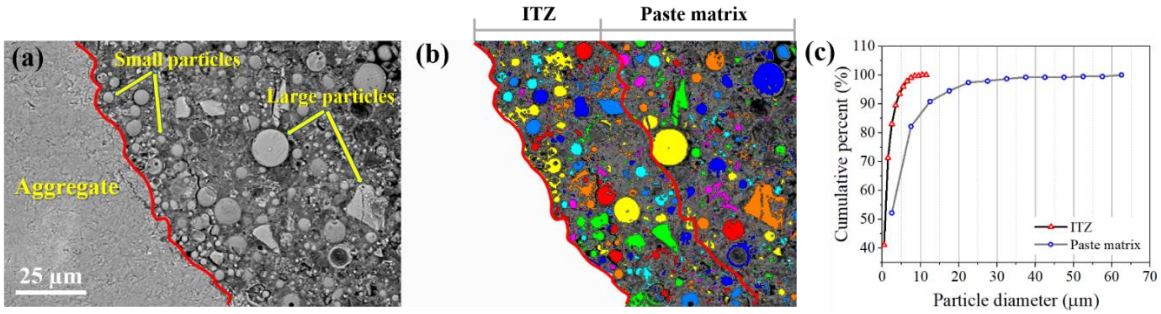

Figure 4-49 Particle distribution of fly ash and slag near the surface of aggregate

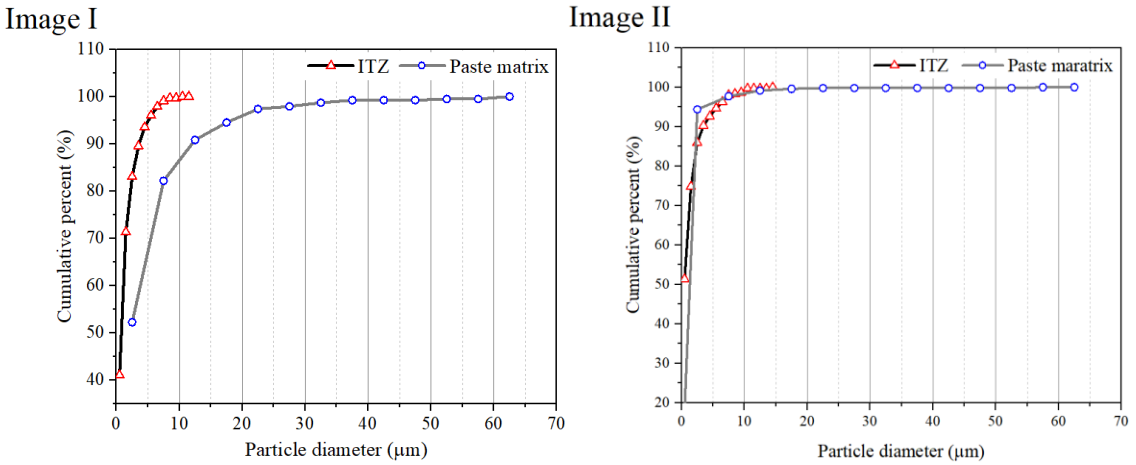

Figure 4-50 Particle size distribution of fly ash and slag obtained from two different images for the same sample

In addition, the physical packing of precursors would lead to a deficit of large particles that cannot physically pack close to the aggregate, and consequently results in a relatively low content of precursors in the ITZ. Such features would bring a higher effective alkaline activator/precursor ratio in the ITZ than that in the paste matrix, and eventually induce the differences in physical and chemical properties. As seen in Figure 4-51, the mean

content of unreacted particles in the ITZ is 51.88% which is lower than that in the paste matrix (i.e. 53.75%) at 3 h. The statistical analysis also reveals a strong significance difference (p-value < 0.01) between the content of unreacted particles in the ITZ and paste matrix at this age (see Table 4-7). As the curing age increases from 3 h to 7 d, the contents of unreacted particles in the ITZ and paste matrix are decreased slightly due to the alkaline reaction, followed by a dramatic drop at 28 d, where the contents of unreacted particles in the ITZ and paste matrix are decreased to 32.30% and 36.21%, respectively.

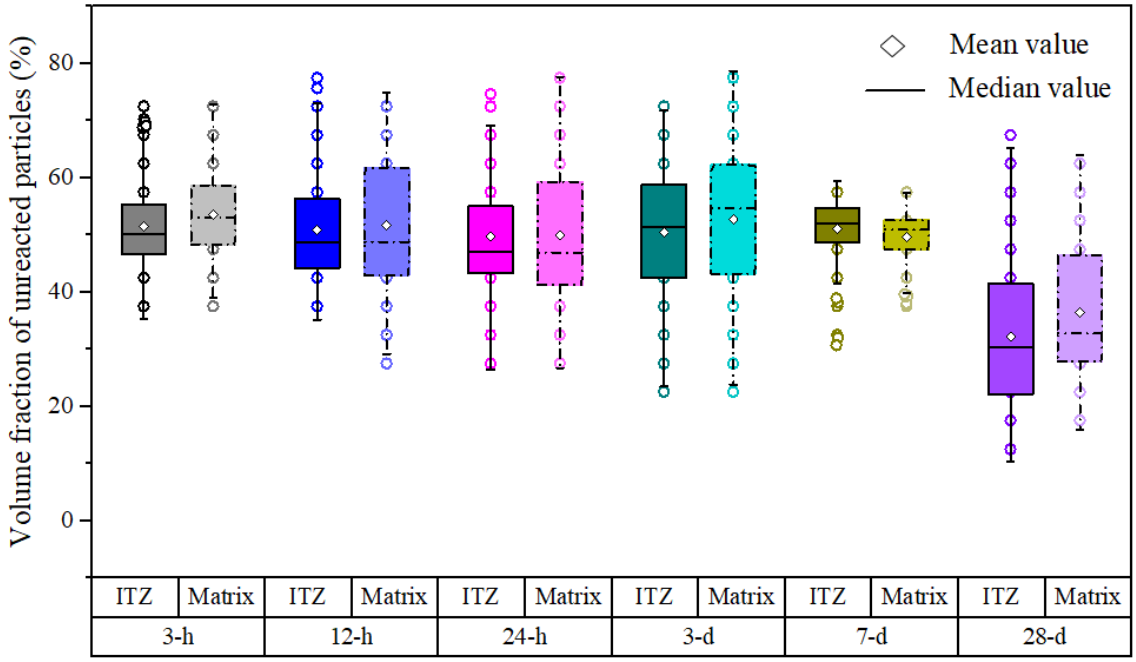

Figure 4-51 Volume fractions of unreacted particles in ITZ and paste matrix at different curing ages

Table 4-7 Statistical significance of the volume fraction of unreacted particles

		F-value	p-value	Significance
3-h	ITZ / Paste matrix	8.4499	0.0038	**
12-h	ITZ / Paste matrix	0.7188	0.3970	-
24-h	ITZ / Paste matrix	0.0346	0.8526	-
3-d	ITZ / Paste matrix	5.0210	0.0255	*
7-d	ITZ / Paste matrix	3.8475	0.0512	-
28-d	ITZ / Paste matrix	16.9626	0.4558×10^{-4}	**

\- No significant difference
* Significant difference
** Strong significant difference

Reaction process in the ITZ

The origin of ITZ lies in the "wall effect" of packing of precursors against the aggregate surface, but its microstructure is also associated with the chemical reactions occurred in this region. Figure 4-52 shows the volume fraction of reaction products in the ITZ and paste matrix at different curing ages. At the beginning (3 h), the mean value of volume fraction of reaction products in the ITZ (37.5%) is slightly higher than that in the paste matrix (36%). With the increase of curing age from 3 h to 12 h, the contents of reaction products in the ITZ and paste matrix are increased significantly from 37.5% to 46% and from 36% to 45.5%, respectively. As the reaction continues from 12 h to 7 d, the contents of reaction products in the ITZ and paste matrix become stable, with a slight increase from 46% to 48% and from 45.5% to 49%, respectively. However, as the curing age changes from 7 d to 28 d, the volume fractions of reaction products in the ITZ and paste matrix are increased dramatically again from 48% to 66% and from 49% to 62%, respectively. There are more reaction products in the ITZ than in the paste matrix at this stage. Accordingly, the difference of reaction products content in the ITZ and paste matrix becomes obvious at 28 d, where these two regions show a strong significant difference (p-value < 0.01) in the statistical analysis (see Table 4-8). These results are mainly ascribed to the different reaction process happened in the ITZ and paste matrix, which is discussed in detail below.

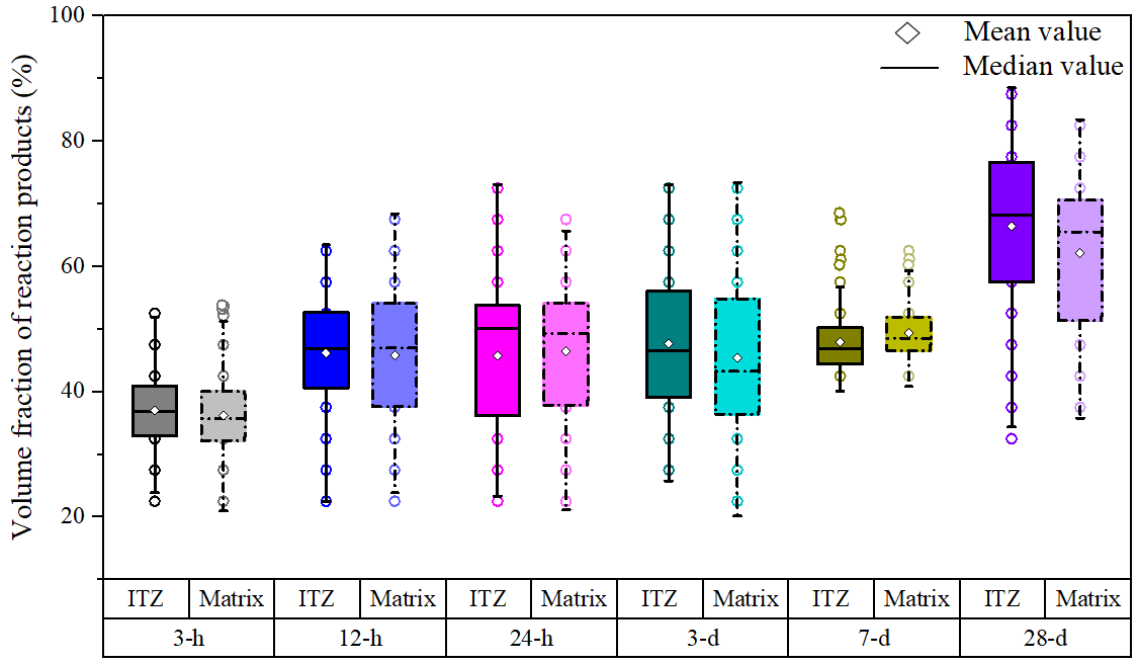

Figure 4-52 Volume fractions of reaction products in ITZ and paste matrix at different curing ages

Table 4-8 Statistical significance of the volume fraction of reaction products

		F-value	*p*-value	Significance
3-h	ITZ / Paste matrix	1.7427	0.1875	-
12-h	ITZ / Paste matrix	0.1563	0.6928	-
24-h	ITZ / Paste matrix	0.5743	0.4490	-
3-d	ITZ / Paste matrix	4.8685	0.0278	*
7-d	ITZ / Paste matrix	0.3387	0.5610	-
28-d	ITZ / Paste matrix	14.9629	1.2553×10^{-4}	**

- No significant difference
* Significant difference
** Strong significant difference

Figure 4-53 presents the local elemental maps of key elements (Na, Ca, Si and Al) near the interface between aggregates and paste at different curing ages. In the element maps of Na, the distinction between the region close to the aggregate and the region far away from the aggregate is not obvious at all curing ages. This is confirmed by the EDS spot analysis shown in Figure 4-54a, where the difference in the mean value of Na percentage between ITZ and paste matrix is smaller than 1% for all the AAFS samples. This is also revealed by the statistical analysis, in which there is no significant difference of Na content in the ITZ and paste matrix (p-value > 0.05) (see Table 4-9). The uniform distribution of Na implies that the content of Na within the reaction products in the ITZ and paste matrix is similar regardless of curing age.

Table 4-9 Statistical significance of the atomic percentage of Na

		F-value	*p*-value	Significance
3-h	ITZ / Paste matrix	0.5348	0.4752	-
12-h	ITZ / Paste matrix	0.8341	0.3826	-
24-h	ITZ / Paste matrix	0.0085	0.9278	-
3-d	ITZ / Paste matrix	0.3540	0.5597	-
7-d	ITZ / Paste matrix	0.0747	0.7881	-
28-d	ITZ / Paste matrix	0.0585	0.8124	-

- No significant difference

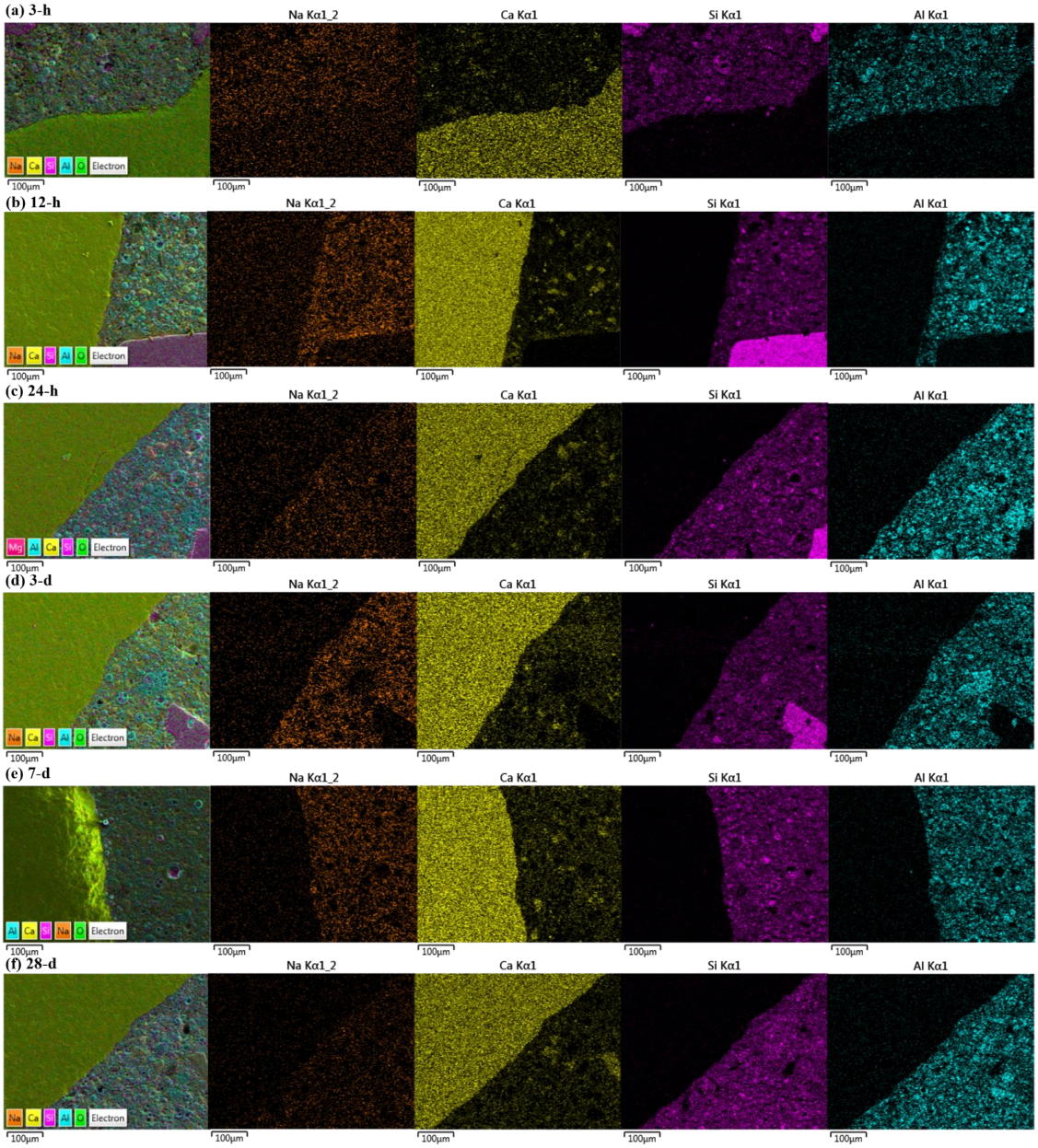

Figure 4-53 Element maps (Na, Ca, Si and Al) of the interface between aggregate and paste at different curing ages (based on weight percentages)

In the element maps of Ca, the homogeneous intensity can be observed in the interface between aggregate and paste matrix at all curing ages, while the overall intensity of Ca seems to increase with increasing curing ages. These are consistent with the statistical analysis of the Ca percentages in the ITZ and paste matrix (Figure 4-54b). The difference in the Ca percentage ranges from 0.13% to 1.52%, which suggests that the gradient of Ca between ITZ and paste matrix is not obvious. These two regions do not show a significant difference (p-value > 0.05) in the statistical analysis (see Table 4-10). This can be attributed to the relatively low content of Ca in the unreacted particles, where CaO only occupies 9.7% of total binding materials according to the chemical composition of CaO in fly ash and slag.

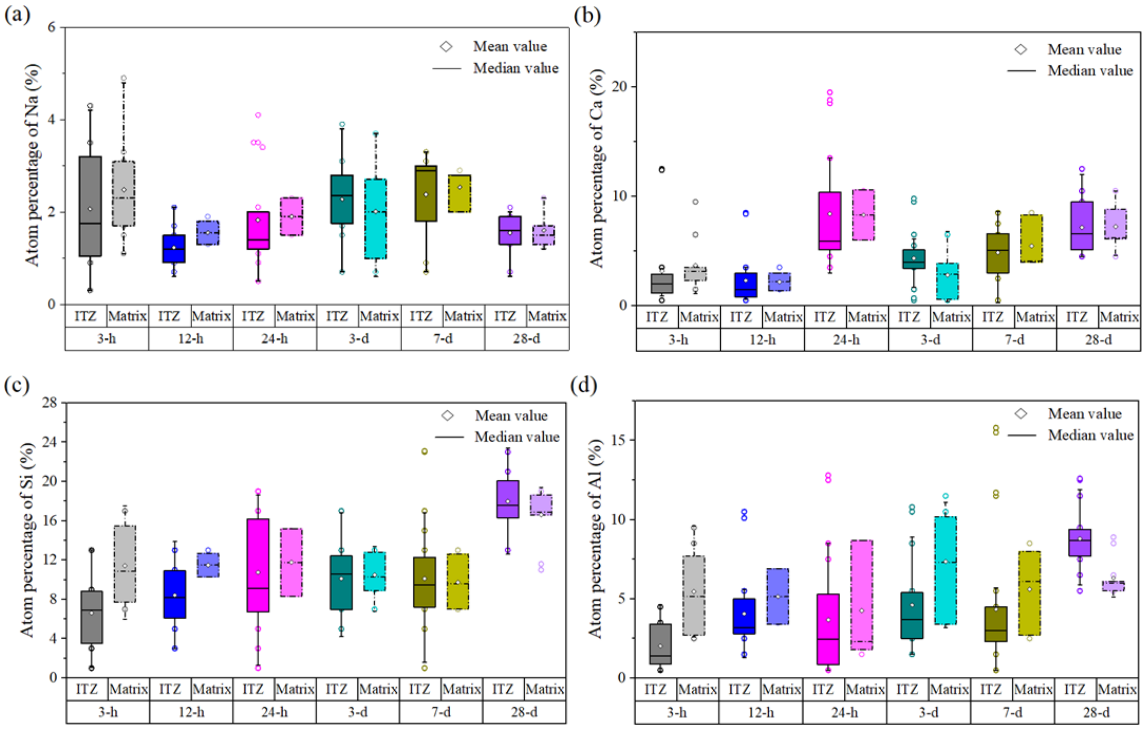

Figure 4-54 Atomic percentages (Na, Ca, Si and Al) in ITZ and paste matrix at different curing ages

Table 4-10 Statistical significance of the atomic percentage of Ca

		F-value	*p*-value	Significance
3-h	ITZ / Paste matrix	0.1291	0.7241	-
12-h	ITZ / Paste matrix	0.0056	0.9420	-
24-h	ITZ / Paste matrix	5.7108×10^{-4}	0.9813	-
3-d	ITZ / Paste matrix	1.7122	0.2104	-
7-d	ITZ / Paste matrix	0.1378	0.7157	-
28-d	ITZ / Paste matrix	0.0041	0.9502	-

- No significant difference

In the element maps of Si, the intensity of Si in the region close to the aggregate is lower than that in the region further out at 3 h. As the reaction proceeds, the difference between these two regions becomes less especially at later curing ages. It can be observed from the EDS spot analysis in Figure 4-54c, in which the mean value of Si content in the ITZ is obviously lower than that in paste matrix at 3-h curing. A significant difference (*p*-value < 0.05) between the Si content in the ITZ and paste matrix at this age is also found in the statistical analysis (see Table 4-11). This is consistent with the finding of less fly ash and slag close to the interface of aggregate (see Figure 4-51). As the curing age increases from 3 h to 12 h, the content of Si in the ITZ increases significantly from 6.5%

to 8.43%, whereas the content of Si in the paste matrix only slightly increases from 11.25% to 11.5%. This indicates that the reaction process in the ITZ is faster than that in the paste matrix because of the higher content of AL/P ratio in this zone, as confirmed by the relatively low content of unreacted particles in the ITZ (Figure 4-51). In addition, the difference in the size of gains would also affect the reaction process in the ITZ, where the particle size in the ITZ is smaller than that in the paste matrix due to the "wall effect" (Figure 4-49). The smaller particles would be reacted quickly and completely, while the larger particles would be reacted relatively slowly due to the existence of a core of unreacted grains. As a result, the increasing rate of the mobile ions such as Si in the ITZ is higher than that in the paste matrix, and thus the reaction process is fast in this zone. With the increase of curing age from 12 h to 24 h, the content of Si in the ITZ increases from 8.43% to 10.77%, while that in the paste matrix only increases slightly from 11.5% to 11.75%. For the curing ages between 3 d and 7 d, the percentage of Si in both ITZ and paste matrix becomes stable. However, at 28 d, the content of Si is increased dramatically again, where the Si percentages in ITZ and paste matrix are increased from 10.5% to 18% and from 10% to 16.5%, respectively. The Si content in the ITZ is higher than that in paste matrix in this stage, suggesting that the reaction products formed in the ITZ at 28 d are rich with Si than the rest of paste, which is consistent with the development of reaction products shown in Figure 4-52. Given that the quantity of initial particle of fly ash and slag in the ITZ is lower than that in the paste matrix, some of the mobile ions might come from the dissolution of fly ash and slag outside the ITZ due to the concentration gradient developed with the progress of chemical reactions.

Table 4-11 Statistical significance of the atomic percentage of Si

		F-value	*p*-value	Significance
3-h	ITZ / Paste matrix	5.6218	0.0316	*
12-h	ITZ / Paste matrix	1.3289	0.2758	-
24-h	ITZ / Paste matrix	0.0470	0.8318	-
3-d	ITZ / Paste matrix	0.0530	0.8207	-
7-d	ITZ / Paste matrix	0.0162	0.9005	-
28-d	ITZ / Paste matrix	0.6095	0.4480	-

\- No significant difference
* Significant difference

In the element maps of Al, a relatively low intensity adjacent to the surface of aggregate is found at 3 h. As can be seen in Figure 4-54d that the mean value of Al content in the ITZ is obviously lower than that in paste matrix at this age. This is agreed with the statistical analysis, in which the Al content in the ITZ and paste matrix has a strong significant difference (p-value < 0.01) (see Table 4-12). As the curing age increases, the homogeneous intensity of Al can be observed regardless of the distance from aggregate. The percentage of Al in the ITZ is increased dramatically during the curing age from 3 h to 12 h, while in paste matrix it is changed slightly in this period (see Figure 4-54d). After that, it is increased steadily with the increase of curing age regardless of ITZ and paste matrix because of the ongoing reaction in AAFS paste (from 12 h to 3 d). During these ages, there is no significant difference (p-value > 0.05) between the Al content in the ITZ and paste matrix (see Table 4-12). Besides, the content of Al in the ITZ is lower than that in paste matrix at early 7 d but it is higher than that in paste matrix at 28 d, which is consistent with the development of reaction products shown in Figure 4-52 and the release process of Si (see Figure 4-54c). Accordingly, a significant difference (p-value < 0.05) between Al content in the ITZ and paste matrix at 28 d can be observed in the statistical analysis (see Table 4-12). A relatively high Al content in the ITZ at a later curing age (28 d) was also reported in previous research (Singh et al., 2016), where the Si/Al ratio in the ITZ was found to be around 1.51 which is lower than that in the paste matrix (i.e. ~ 2.39). Here, the low Al content in the ITZ at early ages (< 7 d) indicates that the reaction products with low Al are generated, while Al-rich reaction products are expected to be formed in the ITZ at later curing ages, e.g. 28 d.

Table 4-12 Statistical significance of the atomic percentage of Al

		F-value	*p*-value	Significance
3-h	ITZ / Paste matrix	9.1735	0.0085	**
12-h	ITZ / Paste matrix	0.3230	0.5824	-
24-h	ITZ / Paste matrix	0.0567	0.8155	-
3-d	ITZ / Paste matrix	3.4518	0.0817	-
7-d	ITZ / Paste matrix	0.2571	0.6190	-
28-d	ITZ / Paste matrix	5.9474	0.0287	*

\- No significant difference
* Significant difference
** Strong significant difference

To further investigate the reaction process in ITZ, the development of different types of reaction products was discussed based on the ternary CaO-Al_2O_3-SiO_2 diagram plotted in Figure 4-55, which was normalised by the content of these oxides by neglecting any other constituents. The chemistry of ITZ at a very early age (3 h ~ 12 h) mainly lies within the region commonly associated with low Ca C-(N)-A-S-H gels, clustered along with the boundary of the region with high Ca C-(N)-A-S-H gels (van Deventer et al., 2015). Nevertheless, it is difficult to find the pure N-A-S-H gels in the ITZ due to the presence of Ca which would hinder the formation of this product (Garcia-Lodeiro et al., 2011; van Deventer et al., 2015). As the reaction continues (24 h to 7 d), the chemistry of ITZ is mainly within the region assigned with high Ca C-(N)-A-S-H gels. This is mainly because of the further dissolution of Ca from slag. Some data points lie in the region containing C-A-S-H gels (Garcia-Lodeiro et al., 2011), suggesting that some of the Na in C-(N)-A-S-H gels have been fully replaced by the Ca. With the curing age increases from 7 d to 28 d, the chemistry of ITZ mainly lies in a stable region of high Ca C-(N)-A-S-H gels with rich Si and Al, which is in a good agreement with the release process of Si and Al shown in Figure 4-54c and d. This would contribute to the continuous dissolution of fly ash and slag. Given that the content of fly ash is much higher than that of slag, the higher amount of Si and Al can be supplied for producing the well-densified and thermodynamically stable reaction products with rich Si and Al (C-(N)-A-S-H gels) (Myers et al., 2014; Ismail et al., 2014), which might contribute to increasing strength and interfacial binding (Nicolas and Provis, 2015).

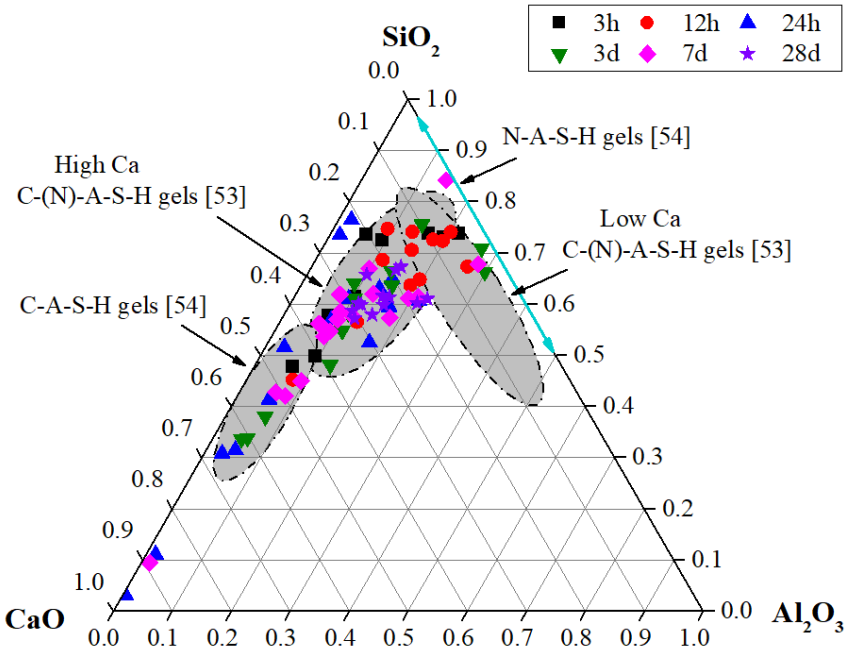

Figure 4-55 Ternary CaO-Al_2O_3-SiO_2 diagram of ITZ at different curing ages (based on molar ratios)

Pore structure evolution in the ITZ

The pore structure of ITZ is another key feature that would strongly determine the properties in this region, such as mechanical properties and transport properties. Figure 4-56 shows the porosity of ITZ and paste matrix at different curing ages. The difference in porosity between ITZ and paste matrix in the AAFS system is not obvious, which is in contrast to that in PC system (Xie et al., 1991; Pope and Jennings, 1992). At 3 h, the porosity of ITZ (11.45%) is higher than that of paste matrix (10.20%) due to the initial packing of fly ash and slag grains and the presence of bond cracks at the interface between aggregate and paste (see Figure 4-48a). This is also revealed by a strong significant difference (p-value < 0.01) between the porosity in the ITZ and paste matrix (see Table 4-13). Afterwards, there is a sharp decrease in porosity with the increase of curing age due to the redistribution of reaction products. At 12 h, the porosity of ITZ and paste matrix is decreased significantly to 2.22% and 2.45%, respectively. This is the result of the vigorous reaction during the very early age between 3 h and 12 h, where the space-filling products, i.e. C-(N)-A-S-H gels, are formed in this region, instead of the distinct large crystallites, i.e. calcium hydroxide (CH), formed in the PC system. CH crystallites are commonly formed close to the aggregate surface in the PC system, which would lead to a relatively high porosity in ITZ (Scrivener et al., 2004). Afterwards, the porosities of ITZ and paste matrix are increased slightly from 2.22% to 2.45% and from 2.45% to 2.74% respectively during the curing age increasing from 12 h to 24 h, which can be attributed to the presence of matrix cracks (see Figure 4-48c). As the curing continues from 24 h to 7 d, the porosities of ITZ and paste matrix are decreased steadily from 2.45% to 1.05% and from 2.74% to 0.96%, respectively. This can be ascribed to the continue chemical reaction which would generate the space-filling products (i.e. C-(N)-A-S-H gels) to modify the microstructure and lead to the continuous refinement of pores as well as the improvement of interfacial bonding between aggregate and paste. During these curing ages, the bond cracks and the matrix cracks become finer, and these cracks are almost disappeared at 7 d (see Figure 4-48e). Finally, the porosity of ITZ increases slightly from 1.05% to 1.35% as the curing age increases from 7 d to 28 d, while the porosity of paste matrix increases from 0.96% to 1.40%. This is probably because of the reappearance of matrix cracks, as shown in Figure 4-48f.

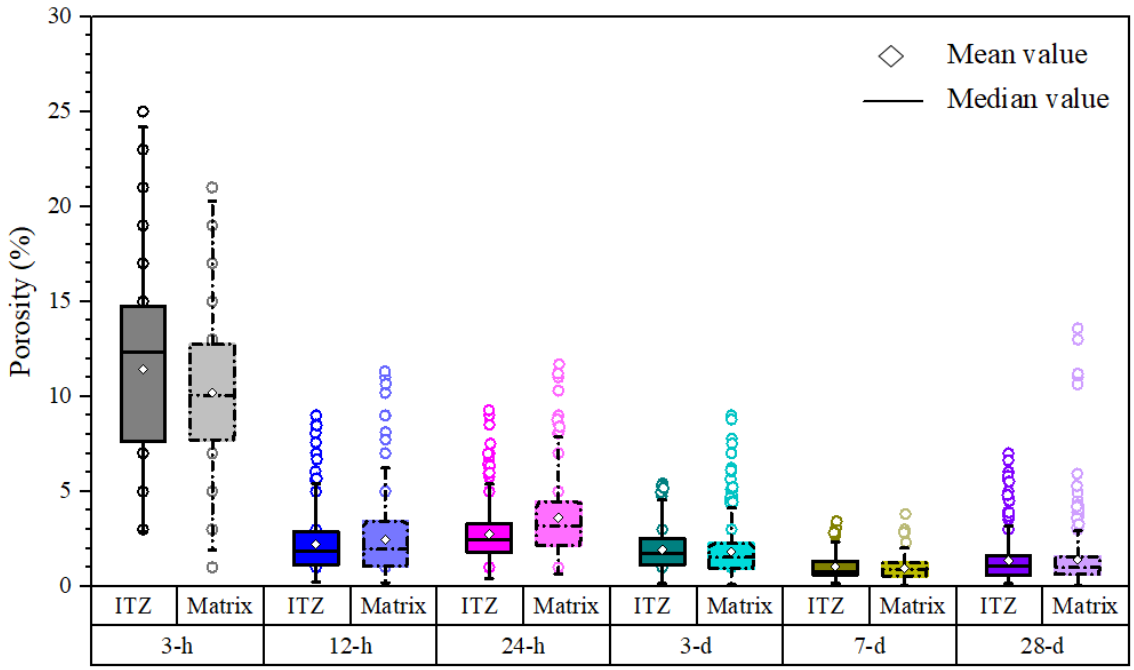

Figure 4-56 Porosity of ITZ and paste matrix at different curing ages

Table 4-13 Statistical significance of porosity

		F-value	*p*-value	Significance
3-h	ITZ / Paste matrix	9.7708	0.0019	**
12-h	ITZ / Paste matrix	1.7168	0.1908	-
24-h	ITZ / Paste matrix	28.5291	1.4863×10^{-7}	**
3-d	ITZ / Paste matrix	0.8043	0.3702	-
7-d	ITZ / Paste matrix	1.4140	0.2353	-
28-d	ITZ / Paste matrix	0.1893	0.6637	-

- No significant difference
** Strong significant difference

To further understand the pore structure evolution, the size distribution of pores in ITZ and paste matrix was analysed. As shown in Figure 4-57, the typical images in each sample were used to illustrate the distribution of pore size. The pore size was measured as the circle-equivalent diameter using Fiji (an open source image processing package) with the 'Analyze Particles' function (Schindelin et al., 2012), in which a cluster of interconnected pores was regarded as a single pore for calculation (Yio et al., 2019). A similar trend regarding pore size distribution for ITZ and paste matrix in different images can be recognized (see Figure 4-58). As seen in Figure 4-57a, most pores in the ITZ are larger than those in paste matrix at 3 h (1~17 μm for ITZ and 0.5~17.5 μm for paste matrix), which can be attributed to the deficit of large grains in the ITZ due to the packing of fly ash and slag particles against aggregates. This would induce a relatively high AL/P

ratio in ITZ and lead to the presence of larger pores. A sharp decrease in the size of pores in ITZ and paste matrix (0.25~6.75 μm for ITZ and 0.3~4.1 μm for paste matrix) can be found at 12 h (see Figure 4-57b), which can be ascribed to the quick alkaline activation of fly ash and slag. This finding is consistent with the EDS analysis shown in Figure 4-54. In this stage, although similar small pores (0.25 ~ 4.1 μm) can be found in ITZ and paste matrix, the large pores with size from 4.1 μm to 6.75 μm only exist in the ITZ, which can be attributed to the fewer precursors remaining in the ITZ and thus the newly formed reaction products are not enough to fill the large pores in this region. Nevertheless, as the curing age increases from 24 h to 7 d, the distribution of pore size in the ITZ is found to be similar to that in the paste matrix due to the redistribution of reaction products (see Figure 4-57c to e). As the reaction proceeds at 28 d, the pore size in ITZ becomes smaller than that in paste matrix (see Figure 4-57f) due to the further redistribution of reaction products through the migration of ions from the dissolution of particles outside the ITZ, which can also be observed from the EDS analysis shown in Figure 4-54. As seen in Figure 4-57g and h, the pore size in ITZ is decreased steadily with the increase of curing age, while the pore size development in paste matrix is not obvious after 12 h due to the presence of large fly ash and slag grains in paste matrix. This suggests that ITZ might not be the weak link providing a preferred pathway for aggressive species to pass through the AAFS materials.

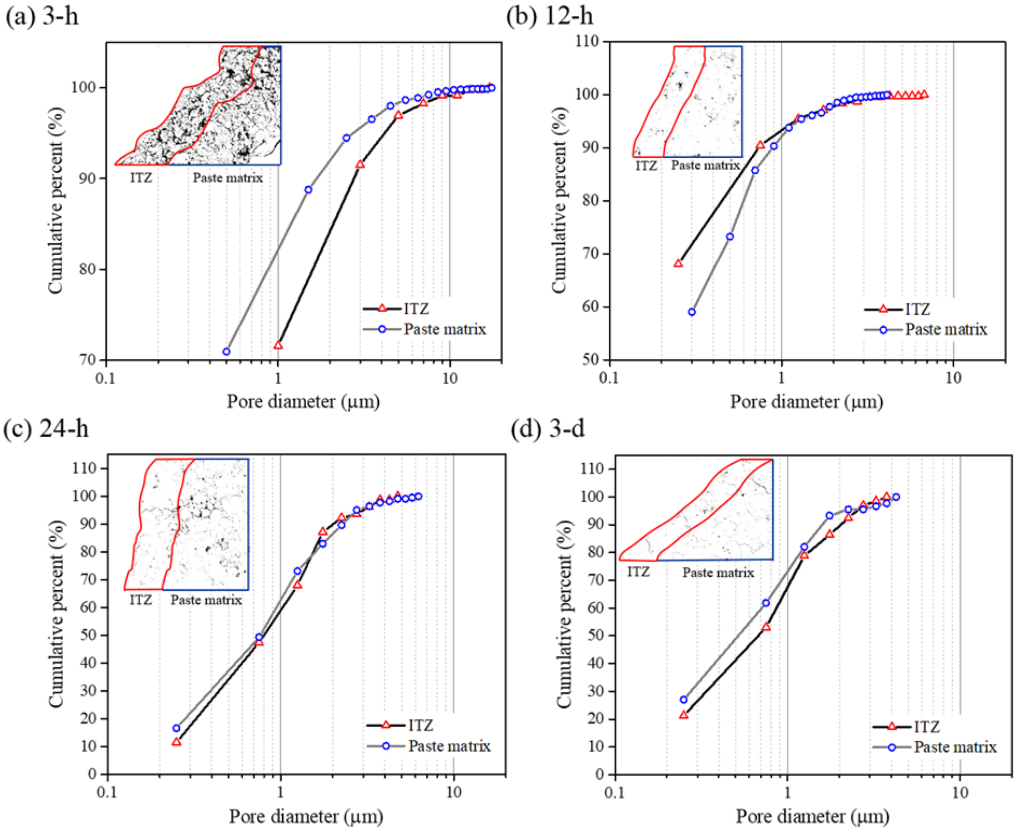

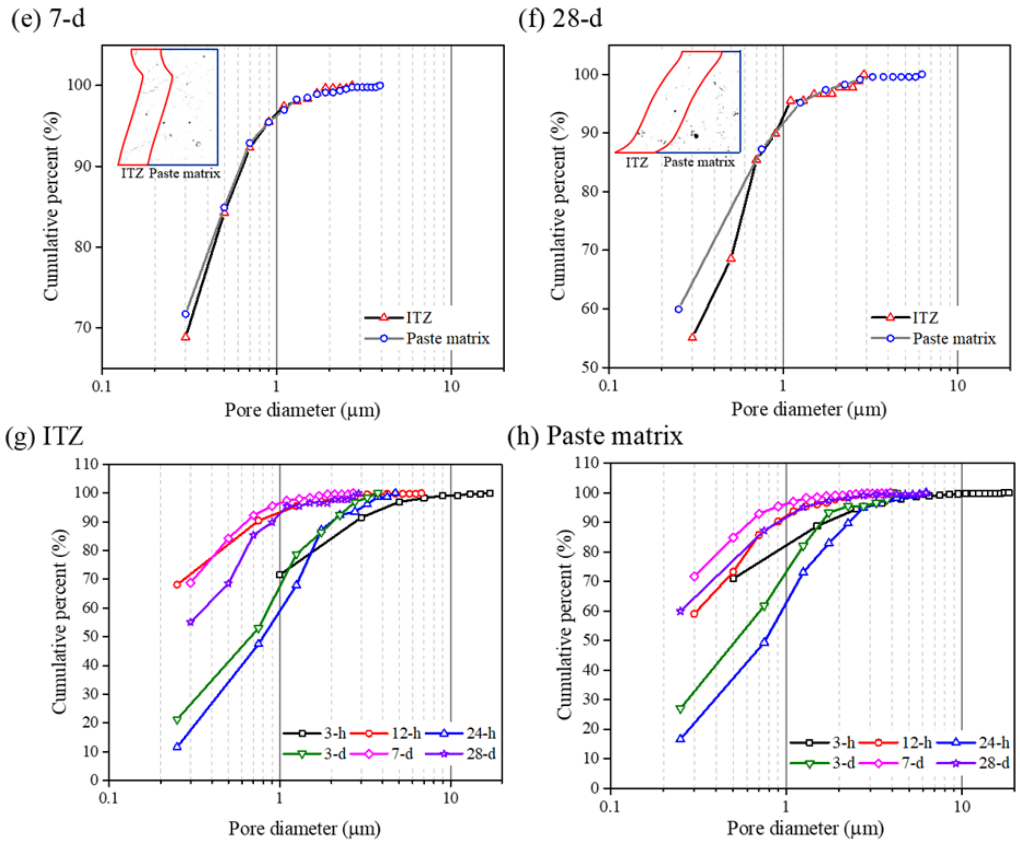

Figure 4-57 Pore size distribution in ITZ and paste matrix at different curing ages (Note: a cluster of interconnected pores is classified as a single pore in the characterization of pore structure)

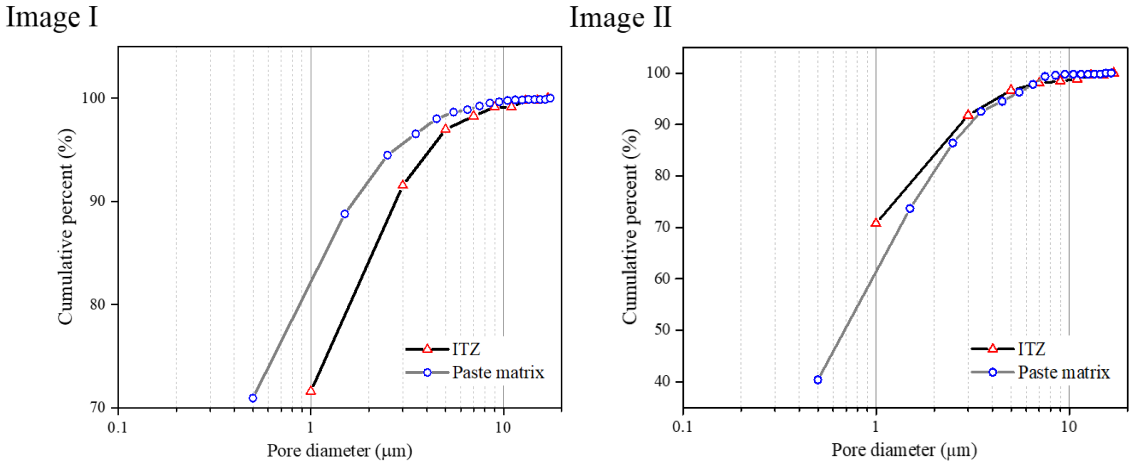

Figure 4-58 Pore size distribution in ITZ and paste matrix obtained from two different images at the same sample (t = 3 h)

4.7.5.4 Mechanism of ITZ evolution

The formation of ITZ in AAFS concrete is started from the so-called “wall effect”, where the fly ash and slag grains are disrupted when they pack through the flat surface of aggregate. This effect would induce the formation of a special region close to aggregate

(i.e. the origin of ITZ), where the large grains are deficient in this region (see Figure 4-49), leading to a higher effective AL/P ratio than that in paste matrix.

Initially, the precursors in the ITZ and paste matrix are dissolved upon the alkaline activation, generating a variety of dissolved species such as Si, Al and Ca. As the quantity of precursors in ITZ is lower than that in paste matrix, the content of dissolved species in ITZ would be lower than that in paste matrix, especially in the initial stage. This explains why the content of Ca, Si and Al in ITZ is lower than that in paste matrix at 3 h (near final setting time), confirmed by the EDS atomic percentage shown in Figure 4-54.

As the reaction continues, much more species are dissolved from precursors and reacted together to form low Ca C-(N)-A-S-H gels at the very early ages from 3 h to 12 h (see Figure 4-55). In this stage, the dissolved rate in the ITZ is higher than that in the paste matrix due to the higher effective AL/P ratio and the smaller precursor grains in this region. This is consistent with the higher dissolution of Si and Al in the ITZ at 12 h, as shown in Figure 4-54. The relatively high dissolution rate would help accelerate the formation of reaction products (see Figure 4-52) and reduce the porosity (see Figure 4-56). Additionally, it would also modify the pore structure in ITZ, where the pore size in ITZ at 12 h is smaller than that at 3 h (see Figure 4-57).

As a result of the further reaction, the content of dissolved species in ITZ increases steadily along with the formation of high Ca C-(N)-A-S-H gels and C-A-S-H gels due to the release of more Ca from slag, during the curing ages between 12 h and 7 d (see Figures 4-54 and 4-55). Consequently, the porosity and pore size are decreased steadily in these curing ages (see Figures 4-56 and 4-57).

Finally, at a later age, the amount of dissolved species in ITZ is increased significantly and becomes higher than that in paste matrix (see Figure 4-54). Given that the quantity of initial particle of fly ash and slag in ITZ is lower than that in paste matrix, some species (e.g. Si and Al) might come from the dissolution of precursors in paste matrix rather than ITZ. The relatively high amount of dissolved species would contribute to generating more reaction products (see Figure 4-52), refining the pore structure (see Figure 4-57) and consequently bringing a more compact and mature microstructure in the ITZ. This is similar to the ITZ formed in AAS or AAF concrete (Lee and van Deventer, 2004; Ji et al., 2017), but it is different from the ITZ formed in PC concrete (Scrivener et al., 2004). Normally, the ITZ in PC concrete is regarded as the “weak link” due to the higher proportions of pores and CH crystals in this region (Larbi and Bijen, 1990; Pope and Jennings, 1992). Nevertheless, there is no distinct large crystallites (CH crystals) formed in the ITZ of AAFS concrete but rather the C-(N)-A-S-H gels which would improve the

strength and interfacial binding (Nicolas and Provis, 2015),which is potentially important for the long-term performance of concrete.

According to the discussion above, the microstructure evolution of ITZ can be primarily divided into three stages: (i) formation of reaction products via quick alkaline activation at very early curing ages (< 12 h); (ii) modification of microstructure via the redistribution of reaction products at early curing ages (12 h ~ 7 d); (iii) reorganisation of microstructure via further redistribution of reaction products at later curing ages (7 d ~ 28 d).

4.8 Concluding remarks

In this chapter, the microstructures of AAFS concrete at multiple length scales from nano- to macro-scale were systematically studied based on various testing methods including NMR, XRD, FTIR, XCT, BSEM-EDS and MIP. According to the experimental results, the main conclusions can be drawn as follows:

(i) Nanostructure and chemical composition of solid gels

- The polymerisation degree and cross-linking of gels are improved over curing ages, potentially through the initial formation of C-A-S-H gels followed by the gradual development of N-A-S-H and N-C-A-S-H gels with a higher cross-linking degree. This is mainly attributed to the dissolution of more silicon and aluminium monomers from fly ash and slag, which would enhance the gel polymerisation and lead to the chain in gels with more links.
- The chemical composition of N-A-S-H gels is stable with the Al/Si ratio of around 0.5 during the curing process, while that of C-A-S-H gels and N-C-A-S-H gels are changed from 0.29 to 0.40 and from 0.20 to 0.29, respectively, along with the substitute of aluminate species.

(ii) Microstructure evolution of individual phases in paste

- The dissolution of fly ash and slag particles is not uniform due to their inherently heterogeneous characteristics, which is consistent with the descriptive model presented in previous research. The non-uniform dissolution of fly ash particle can be mainly attributed to the heterogeneous chemical composition, while the preferential dissolution of slag can be associated with the initial defects induced during the preparation of slag.
- The formation of reaction products mostly accumulates within the boundary of the original fly ash and slag particles, i.e. the formation of inner products, as a result of the rapid dissolution of etch pits on the particle surface, which would increase the

ionic concentration inside the pits and promote the formation of inner products. The inner reaction products would naturally build a physical barrier between the unreacted particles and the outside solution, which would inhibit the further reactions of fly ash and slag particles in AAFS.

- The microstructure evolution of fly ash and slag particles is significantly affected by their structure and size. The dissolution of hollow fly ash particle is faster than that of solid fly ash particle, due to the simultaneous reactions from the outside in and from the inside out. The fly ash and slag particles with a smaller size exhibit a faster dissolution compared to the larger particles because of the relatively high specific area.
- The interactions between fly ash and slag particles exist in AAFS during chemical reactions with the increase of curing age. The presence of slag would strongly accelerate the microstructure evolution of fly ash at later curing ages (7 d ~ 28 d), which can be ascribed to the diffusion of Ca ions from the dissolved slag to the unreacted fly ash, promoting the reaction rate and the extent of fly ash.

(iii) Microstructure evolution of ITZ in concrete

- The ITZ in AAFS concrete originates from the so-called “wall effect”, where the packing of fly ash and slag grains would be disrupted through the flat surface of aggregate, leading to the deficit of large grains adjacent to aggregate and a higher effective activator to precursor ratio in the ITZ than that in the paste matrix.
- The microstructure evolution of ITZ can be mainly divided into three stages: (i) formation of reaction products via quick alkaline activation at very early curing ages (< 12 h); (ii) modification of microstructure via the redistribution of reaction products at early curing ages (12 h ~ 7 d); (iii) reorganisation of microstructure via further redistribution of reaction products at later curing ages (7 d ~ 28 d).

Chapter 5 Multiscale micromechanical analysis of AAFS concrete

5.1 Introduction

In Chapter 4, the microstructure of AAFS concrete at multiple length scales from nano- to macro-scale was systematically investigated. Following the multiscale microstructural features identified in Chapter 4, the multiscale micromechanical properties of AAFS concrete will be further investigated in this chapter, to offer the first-hand information of the micromechanical properties of individual phases in this concrete and their contributions to the overall mechanical properties. Here, the mixture proportion and sample preparation are consistent with those used in the microstructural characterisation of paste and concrete (see Chapter 4). As shown in Figure 5-1, experimental tests and predictions using continuum micromechanics model were carried out to investigate the micromechanical properties of AAFS concrete at multiple length scales from Level I to Level III. The micromechanical properties (i.e. elastic modulus and hardness) of individual phases at Level I were measured by means of nanoindentation. The self-consistent continuum micromechanics model was used to estimate the effective mechanical properties of paste matrix at Level II. The micromechanical properties of ITZ in AAFS concrete were evaluated through a series of statistical analysis. It should be noted that the micromechanical properties of solid gel particle at Level 0 are still cannot be measured to date due to the limitation the testing technique. It should be noted that part of this chapter has been presented in the following publication: Guohao Fang and Mingzhong Zhang, Multiscale micromechanical analysis of alkali-activated fly ash-slag paste, *Cement and Concrete Research*, 135 (2020) 106141.

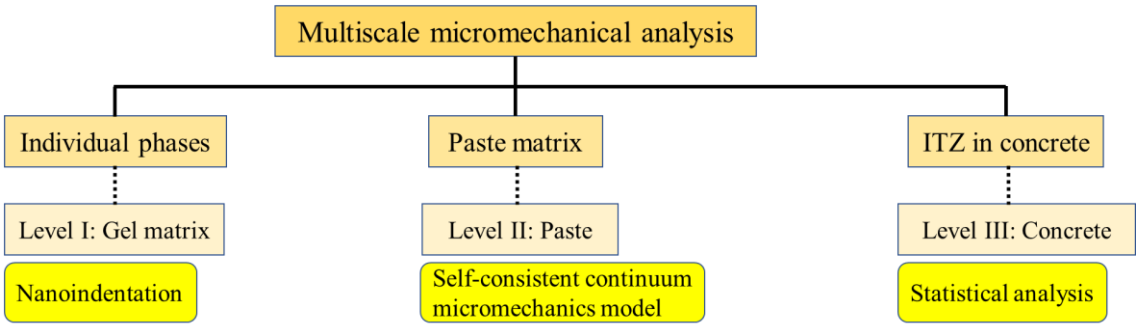

Figure 5-1 Multiscale micromechanical analysis of AAFS concrete

5.2 Fundamental concept of multiscale micromechanical analysis

The foundation of multiscale micromechanical analysis is based on the concept of continuum micromechanics, by which the AAFS concrete as a heterogeneous material can be split into different phases with average continuous material properties (Aboudi et al., 2013). The analysis of multiscale micromechanical properties mainly includes two steps: homogenization and localization (see Figure 5-2). As seen in Figure 5-2a, the transition from low level (bottom) to high level (top) is called homogenization, where the macroscopic mechanical properties of 'composite' are the function of microscopic properties of individual 'constituents' including their mechanical properties, volume fractions and specific morphologies. Conversely, the localization from high level to low level is to establish the link between microscopic mechanical properties of individual 'constituents' and macroscopic mechanical properties of 'composite'. The relationship between 'constituents' and 'composite' can be simplified as presented in Figure 5-2b. The combination (i.e. homogenization) of constituents A and B at Level I would become constituent C at Level II, which is subsequently combined with constituent D to produce composite E at Level III. The labelling of 'constituent' and 'composite' corresponds to the selection of length scale. For instance, the component C can be regarded as a constituent for Level III, while it also can be considered as a composite for Level I.

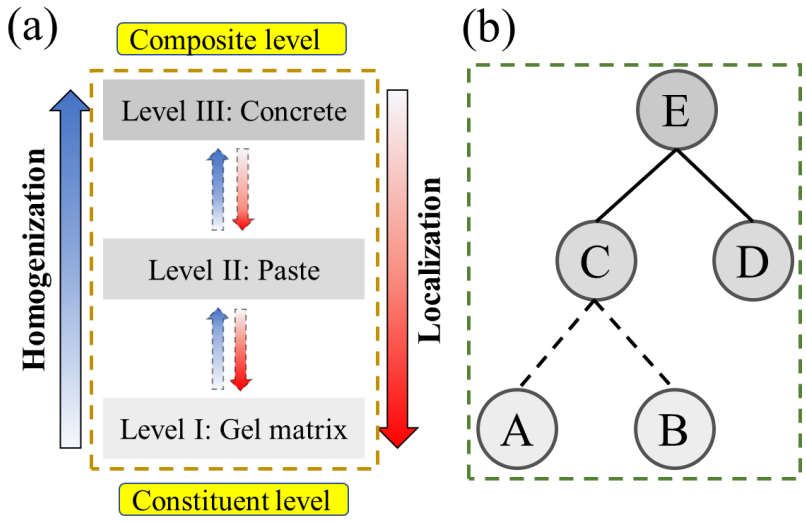

Figure 5-2 Fundamental concept of multiple micromechanical analysis

5.3 Test methods

5.3.1 Atomic force microscopy

The surface topographic of polished specimens was measured using atomic force microscopy (AFM) (Bruker, Dimension ICON, USA), in order to make sure that the

polished samples can fulfil the requirement of nanoindentation test (see Figure 5-3). The specimens were scanned under the Peakforce mode to collect a topographic map. The scanning was operated with an engage setpoint of 0.85 V, a peak force amplitude of 300 mV and a scan rate of 1.0 Hz. The scanning size at the interface was 50 × 50 μm. The digital analysis was then conducted on each image to obtain the roughness value. Here the root-mean-squared roughness number (RMS) was used to describe the surface roughness (Xiao et al., 2013b; Hu and Li, 2015b). The RMS roughness of AAFS samples at different curing ages was calculated and presented in Table 5-1.

Figure 5-3 Instrument of atomic force microscopy

Table 5-1 RMS roughness (nm) of AAFS paste and concrete at different curing ages

Scanning age		3 h	12 h	1 d	3 d	7 d	28 d
Paste sample		-	-	119	165	96	99
Concrete sample	Aggregate	51	75	93	60	72	54
	ITZ	132	122	124	103	97	138

5.3.2 Nanoindentation

Nanoindentation is an effective method to detect the micromechanical properties (e.g. the local elastic modulus and hardness) of materials at micro-level (Hu and Li, 2015a). The basic principle of nanoindentation is to measure the mechanical properties of the testing material from the response of the press of a sharp tip (Hu and Li, 2015a). Figure 5-4 shows a typical load-depth curve that starts with a constantly increasing loading, followed by a constant holding and a constantly decreasing loading (Hu and Li, 2015b). According to the initial slope of the elastic unloading curve, two mechanical properties

including indentation modulus (M) and hardness (H) can be obtained as follows (Oliver and Pharr, 2011; Hu, 2014):

$$M = \frac{1}{2}\left(\frac{dp}{dh}\sqrt{\frac{\pi}{A}}\right)|h = h_{max} \quad (5-1)$$

$$H = \frac{P_{max}}{A} \quad (5-2)$$

where p is the indentation load, p_{max} is the maximum indentation load, h is the indentation depth, h_{max} is the maximum indentation depth, and A is the projected area of the elastic contact.

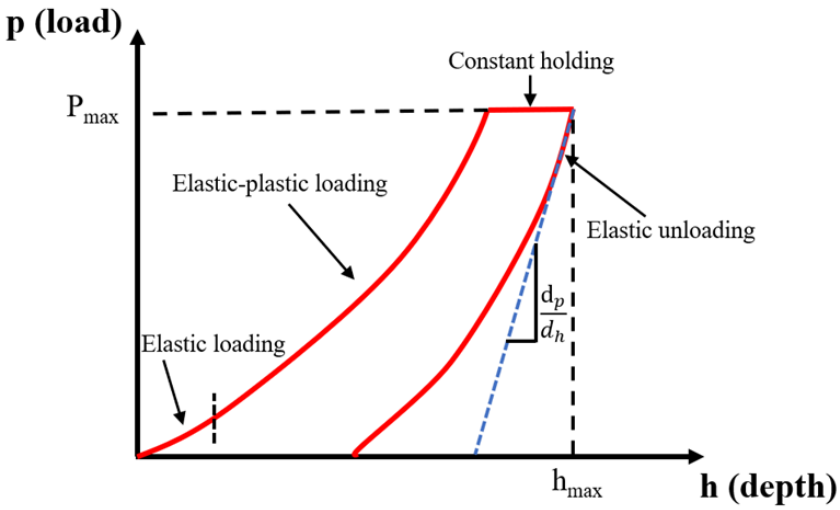

Figure 5-4 A typical load-depth curve of nanoindentation test

The indentation modulus (M) is associated with the elastic properties of the testing material (E) and the indenter tip (E_{tip}) as (Fischer-Cripps, 2004):

$$\frac{1}{M} = \frac{1-\nu^2}{E} + \frac{1-\nu_{tip}^2}{E_{tip}} \quad (5-3)$$

where ν is the Poisson's ratio of the testing material, and ν_{tip} is the Poisson's ratio of the indenter tip.

For the diamond indenter used in this study, the values of E_{tip} and ν_{tip} are 1140 GPa and 0.07, respectively. For AAC, the value of Poisson's ratio (ν) is in the range of 0.13 and 0.26 (Sofi et al., 2007; Thomas and Peethamparan, 2015). Since the change of ν from 0.13 to 0.26 would not significantly affect the results according to Eq. 5-3, the suggested ν for the testing material was set as 0.2 in this study. Accordingly, the elastic modulus (E) can be calculated as (Zhu et al., 2017):

$$E = (1-\nu^2) \times \left[\frac{1}{M} - \frac{\left(1-\nu_{tip}^2\right)}{E_{tip}}\right]^{-1} \quad (5-4)$$

As shown in Figure 5-5, the nanoindentation instrument with a Berkovich indenter tip (BRUKER, Hysitron TI 950, Germany) was used in this study. Nanoindentation test started with the loading at a constant increasing rate of 400 μN/s until it reached the maximum load of 2 mN. Afterwards, the load was held for 2 s followed by the unloading at a similar constant rate. The maximum load of 2 mN corresponded to the average indentation depth of 300 nm. The average indentation depth (300 nm) was over 2 times greater than the RMS roughness of testing samples, which allows avoiding the effect of roughness on the measured properties (see Table 5-1).

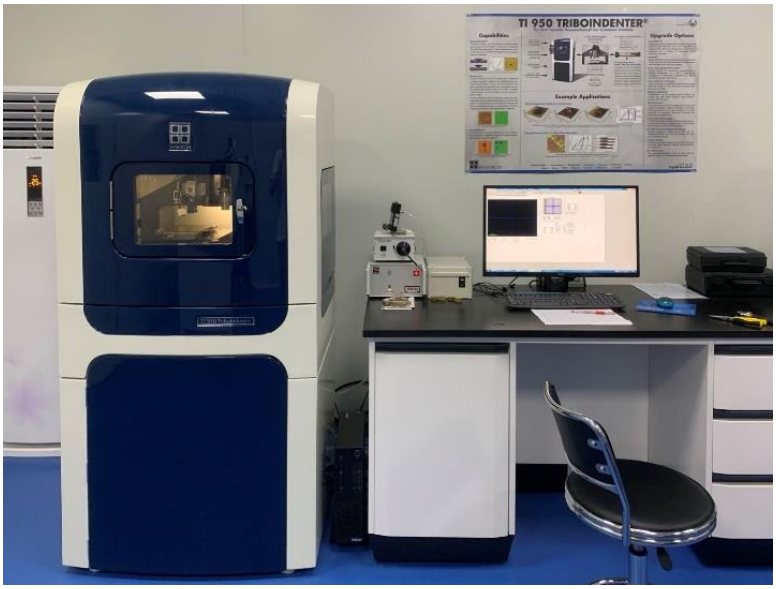

Figure 5-5 Instrument of nanoindentation

The classical nanoindentation mode and grid nanoindentation mode were applied in this work. The classical nanoindentation mode was used to describe the relationship between the load of nanoindentation test and the displacement of indented area, while the grid nanoindentation was utilised to map the micromechanical properties and provide the dataset for statistical analysis (Fischer-Cripps, 2004; Randall et al., 2011; Hu and Li, 2015b). Regarding the classical nanoindentation, for each phase including unreacted fly ash, unreacted slag and reaction products, 10 indentation tests were conducted on different locations in paste sample. In terms of grid nanoindentation, a grid of 100 × 100 μm with 10 μm space between indents was given in the paste sample (see Figure 5-6a). For the concrete sample (see Figure 5-6b), the grid nanoindentation area covered the dimension of 50 × 100 μm across the interface between aggregate and paste matrix. The space between the indented points was set as 10 μm and 5 μm in the lateral and vertical directions, respectively. It can be observed that the distance between indented points was over 16 times larger than the indentation depth (300 nm), which should be sufficient to

avoid the effects of interaction microvolume during nanoindentation tests (normally about 3 ~ 5 times the indentation depth (Buckle, 1973)).

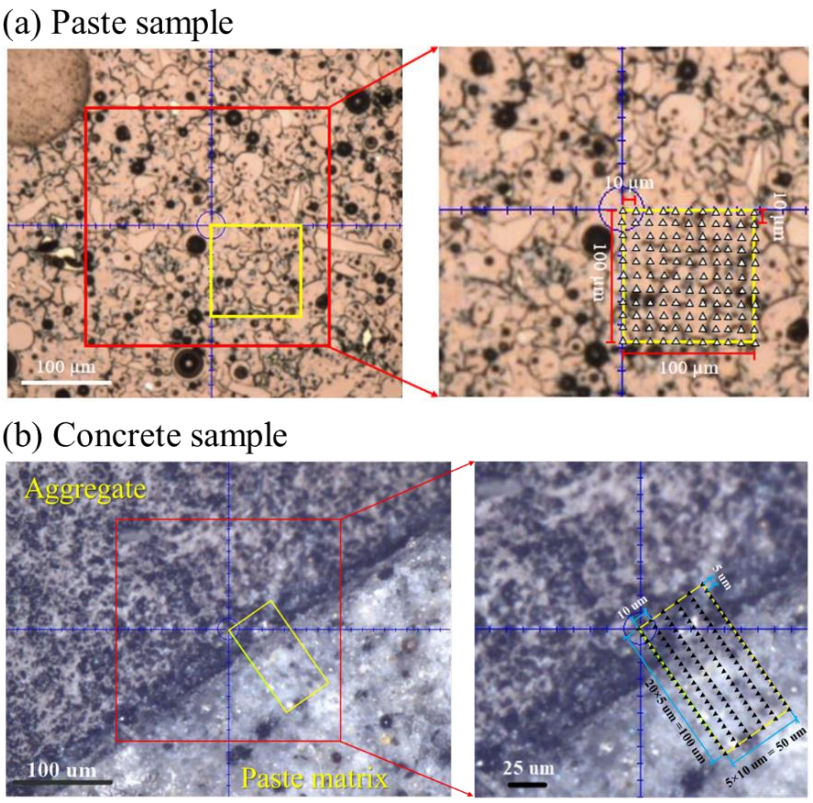

Figure 5-6 Schematic illustration of the indented area

5.4 Results and discussion

5.4.1 Micromechanical properties of individual solid phases in AAFS paste

5.4.1.1 Identification of individual solid phases

The characterisation of mechanical properties of different solid phases, i.e., unreacted fly ash, unreacted slag and reaction products, was performed based on the nanoindentation test, where the classical nanoindentation test and grid nanoindentation test have been made. The classical nanoindentation test helps to characterise the load-displacement behaviour of different phases and understand the difference in their mechanical properties. In this study, the classical nanoindentation test of each phase was performed on 10 different locations to ensure the results can possibly represent the load-displacement behaviour of each phase. Figure 5-7 shows the load-displacement curves of unreacted fly ash, unreacted slag and reaction products. A significant difference in the displacement and the slope of unloading portion between these phases can be well recognised due to the dissimilarity in elastic modulus and hardness among the corresponding material phases. The displacement of unreacted fly ash is generally lower than that of unreacted slag and reaction products, but the slopes of the curves for unreacted fly ash are higher than that of unreacted slag and reaction products. This

suggests that the unreacted fly ash has the highest elastic modulus and hardness, followed by unreacted slag and reaction products. In addition, it can be observed that the same phase exhibits different load-displacement behaviour. Regarding unreacted particles, the displacement of unreacted fly ash and slag is changed in the range of 176 ~ 385 nm and 176 ~ 449 nm, respectively, which is related to the heterogeneity of fly ash and slag. In the terms of reaction products, the displacement is changed from 416 nm to 706 nm, corresponding to the formation of different reaction products.

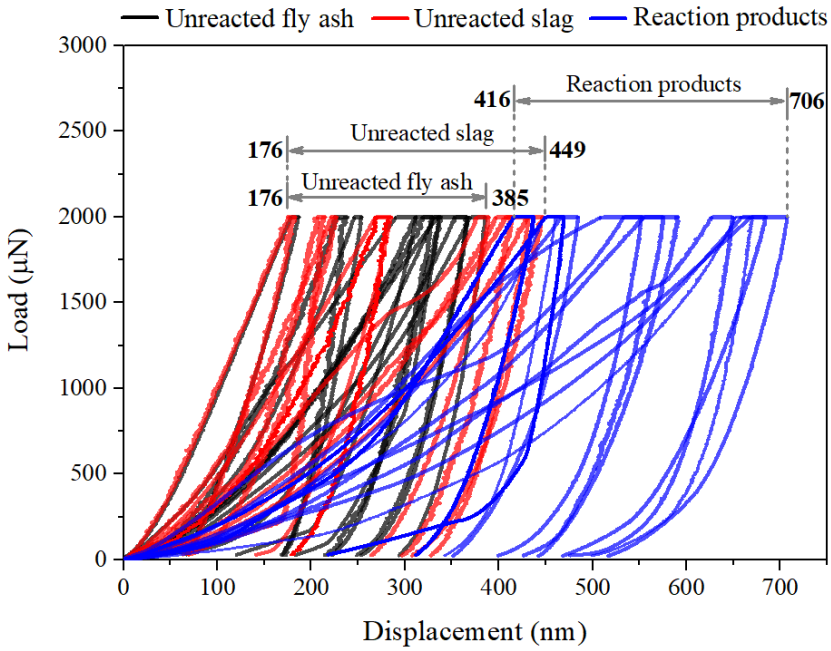

Figure 5-7 Load-displacement curves of different solid phases in AAFS paste (t = 1 d).

5.4.1.2 Visualization of the distribution of individual solid phases

Regarding the grid nanoindentation test, it can be used to reflect the mechanical properties and provide the dataset for statistical analysis. The obtained discrete data can be converted into a mapping of micromechanical properties by linearly interpolating the nodal values over the 100 μm × 100 μm grid region with spacing of 10 μm (Constantinides and Ulm, 2007). As shown in Figure 5-8, the elastic modulus and hardness were calculated and plotted in two-dimensional contour maps according to the load-displacement curves. It can be observed that there exists a good correlation between elastic modulus and hardness. Thus, the discussion will be mainly focused on the elastic modulus in the following sections. Within the contour maps of elastic modulus, the red area represents the hard matrix with a relatively high elastic modulus, while the blue area stands for the soft matrix with a relatively low elastic modulus. Combined with the analysis of microstructure (see Section 4.7.4) and load-displacement curves above (see

Figure 5-7), the contour maps of elastic modulus can be separated into three categories, i.e., unreacted particles, reaction products, and pores. Herein, the unreacted particles (fly ash and slag) cover the colours from green to red due to their relatively high elastic modulus, while the pores with the lowest elastic modulus (< 0.1 GPa) are represented as deep blue. The area with middle elastic modulus is assigned to reaction products, which cover the colours from blue to light green. Similar to the microstructure characterisation in Section 4.7.4, the reaction products also cover a wide range of colours in the mechanical property map. It also suggests the existence of complex reaction products, including N-A-S-H gels, N-C-A-S-H gels and C-A-S-H gels. It can be seen from the contour map in Figure 5-8 that the area with unreacted particles is obvious in the map of elastic modulus at early curing ages (< 3 d), while most part of contour map are occupied by the reaction products at later curing ages (> 7 d).

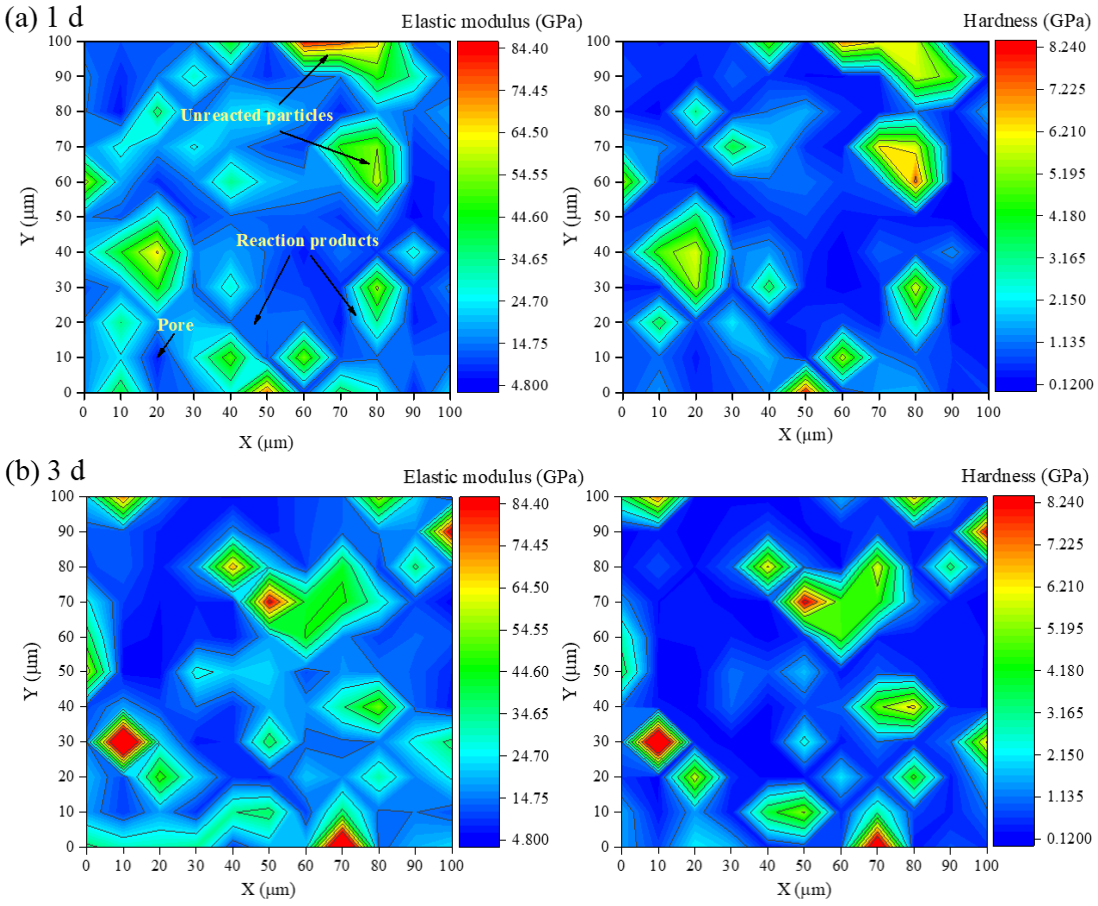

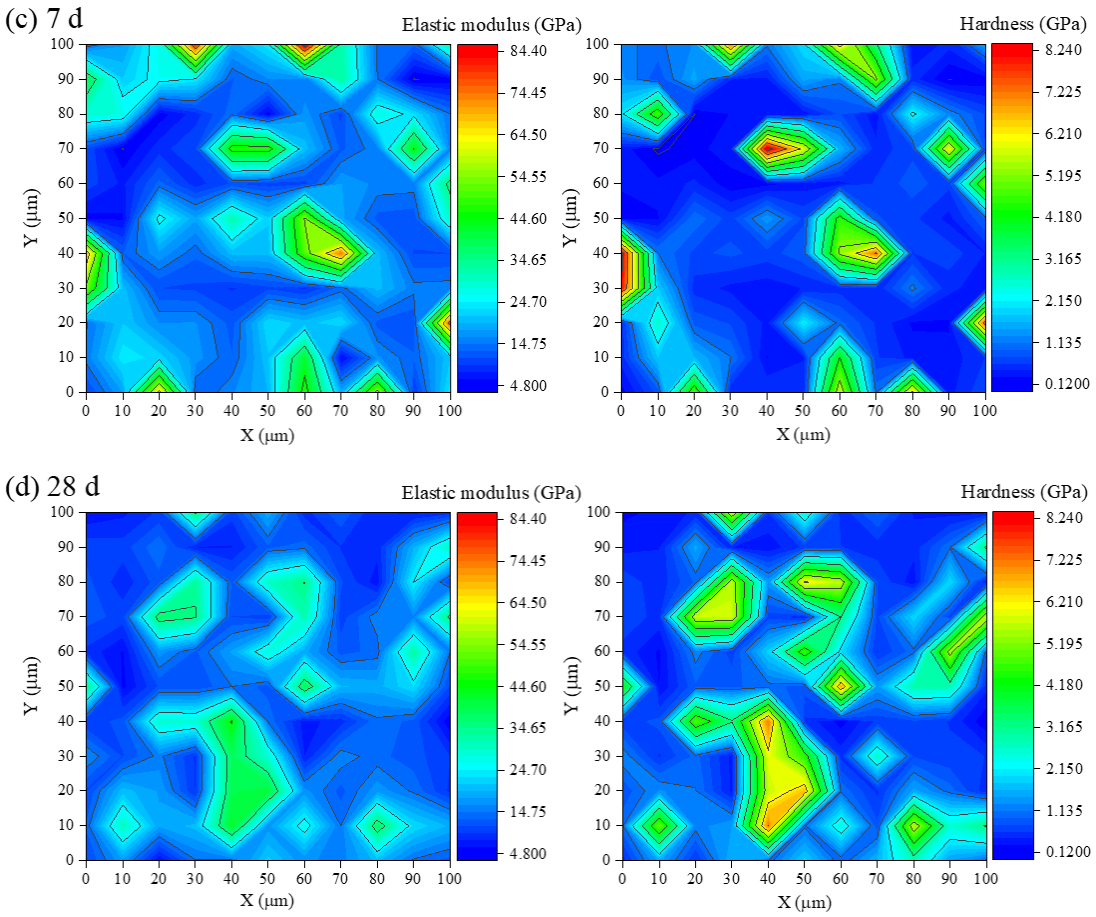

Figure 5-8 Contour map of elastic modulus and hardness of AAFS pastes

5.4.1.3 Statistical analysis of individual solid phases

To further investigate the micromechanical properties of AAFS paste, a statistical Gaussian deconvolution method was subsequently used to determine the elastic moduli of different phases in AAFS paste. Gaussian deconvolution method is commonly adopted to identify clusters of data with distinct micromechanical properties based on the obtained experimental data (Tatar et al., 2019). As shown in Figure 5-9, the determination of elastic moduli of different phases includes four steps: (i) experimental fitting, (ii) Gaussian deconvolution, (iii) phases identification, and (iv) data analysis. Firstly, as seen in Figure 5-9a, the frequency density (normalised histogram with a bin size of 5 GPa) of the experimental data in terms of elastic modulus is fit by the probability density function (PDF) using a statistical analysis software called OriginPro. Since the PDF can be assumed as Gaussian distribution (Constantinides et al., 2006; Randall et al., 2011), the experimental PDF is then deconvolved by the Gaussian distribution curves to generate the theoretical PDF for experimental data (see Figure 5-9b). The number of Gaussian distribution curves is determined based on the microstructural and chemical analysis mentioned in Sections 4.7.1 ~ 4.7.4. Here, six phases including pores, three types of reaction products, and two types of unreacted particles were identified. Nevertheless, the

elastic modulus of pore phase (< 0.1 GPa) was not considered in the deconvolution process because its frequency density of the measured quantity is too small to quantify. Thus, five phases including unreacted fly ash, unreacted slag, N-A-S-H gels, N-C-A-S-H gels, and C-A-S-H gels were considered in the Gaussian deconvolution. Accordingly, the dataset of elastic modulus can be segmented into five different mechanically distinct phases (see Figure 5-9b). Afterwards, as shown in Figure 5-9c, these five different phases can be further identified based on the literature of typical elastic modulus ranges for alkali-activated materials (Němecek et al., 2010; Thomas et al., 2018; Nedeljković et al., 2018), where the typical order of elastic modulus for different phases is N-A-S-H < N-C-A-S-H < C-A-S-H < slag < fly ash. Finally, the mean values of elastic modulus and volume fraction of each phase can be characterised based on the Gaussian distribution curves (see Figure 5-9d).

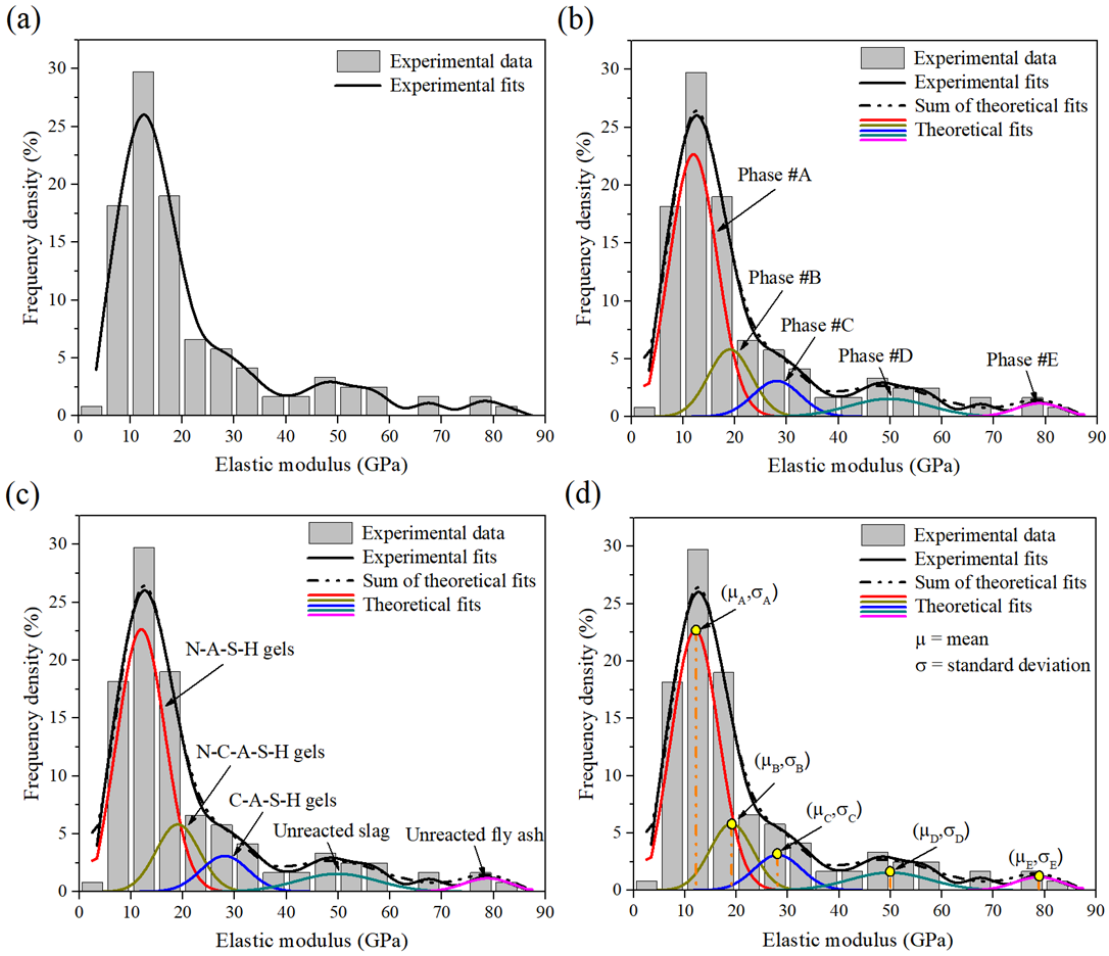

Figure 5-9 Schematic diagram for the determination of elastic modulus of different phases in AAFS paste (t = 1 d).

As shown in Figure 5-10, the Gaussian deconvolution was successfully undertaken to identify the clusters of data with distinct elastic modulus and separate different phases in the gel matrix. Taking the AAFS sample cured for 1 d as an example (Figure 5-10a), the

first peak with the largest and most frequent region is corresponding to N-A-S-H gels with elastic modulus of around 10 GPa. The second peak is assigned to the hybrid type gels called N-C-A-S-H with elastic modulus of around 20 GPa. The third peak with the highest elastic modulus of around 30 GPa among reaction products is associated with the C-A-S-H gels due to their very densely packed structure (Puertas et al., 2011). The fourth peak of around 50 GPa is related to the unreacted slag, while the fifth peak of around 75 GPa is associated with the unreacted fly ash. These findings are in good agreement with the nanoindentation load-displacement curves presented in Figure 5-7, where the unreacted fly ash has the highest stiffness, followed by unreacted slag and reaction products. The distinction of micromechanical properties between these five phases is also clearly presented in the cluster allocation of elastic modulus and hardness (see Figure 5-10a). Based on the Gaussian deconvolution above, the mean elastic modulus and the volume fraction of individual solid phases are summarised in Table 5-2. In addition, a statistical analysis is performed using one-way analysis of variance (ANOVA) method to determine whether there is any significant difference in elastic modulus between different phases. In this method, the probability value (i.e. *P*-value) is compared with the significance level to determine whether the observed groups have significant differences (Bewick et al., 2004). The significance level is commonly set as 0.05 (Salkind, 2007). If the *P*-value is lower than 0.05, there is a significant difference between the observed groups. Otherwise, the observed groups have no significant difference (i.e. *P*-value > 0.05). Moreover, if the *P*-value is lower than 0.01, it means that the observed groups have a strong significant difference with each other. The results of ANOVA tests are presented in Tables 5-3 and 5-4.

Table 5-2 Elastic modulus (GPa) and volume fraction of individual solid phases in AAFS paste at different curing ages

Phases	1 d	3 d	7 d	28 d
A. N-A-S-H gels	11.96 ± 1.42 (65.01%)	10.66 ± 0.10 (63.44%)	12.57 ± 0.17 (54.76%)	12.22 ± 0.17 (77.98%)
B. N-C-A-S-H gels	18.99 ± 3.44 (15.24%)	21.45 ± 0.22 (16.62%)	21.40 ± 0.34 (37.72%)	22.72 ± 1.13 (9.43%)
C. C-A-S-H gels	28.02 ± 2.79 (8.89%)	34.53 ± 0. 28 (14.79%)	33.06 ± 0.37 (3.28%)	34.94 ± 0.57 (12.59%)
D. Unreacted slag	49.75 ± 0.69 (7.53%)	49.14 ± 0.69 (3.43%)	48.20 ± 0.30 (2.48%)	-
E. Unreacted fly ash	78.68 ± 0.52 (3.33%)	74.70 ± 0.97 (1.72%)	70.69 ± 0.94 (1.76%)	-

Note: Volume fraction is the frequency of occurrence in the solid phase of AAFS paste

Table 5-3 Statistical significance of elastic modulus between N-A-S-H gels (A), N-C-A-S-H gels (B) and C-A-S-H gels (C)

Curing age (d)	Groups	*F*-value	*p*-value	Significance
1	A&B	19.86	1.51×10^{-5}	**
	B&C	33.51	5.95×10^{-8}	**
	A&C	101.06	0	**
3	A&B	32.77	4.82×10^{-8}	**
	B&C	54.02	3.86×10^{-11}	**
	A&C	198.89	0	**
7	A&B	16.87	6.03×10^{-5}	**
	B&C	53.69	5.03×10^{-11}	**
	A&C	144.78	0	**
28	A&B	44.69	3.79×10^{-10}	**
	B&C	87.70	4.11×10^{-15}	**
	A&C	416.56	0	**

** Strong significant difference.

Table 5-4 Statistical significance of elastic modulus between unreacted fly ash and slag

Curing age (d)	*F*-value	*p*-value	Significance
1	35.95	1.45×10^{-5}	**
3	21.44	4.71×10^{-4}	**
7	30.80	5.56×10^{-5}	**

** Strong significant difference.

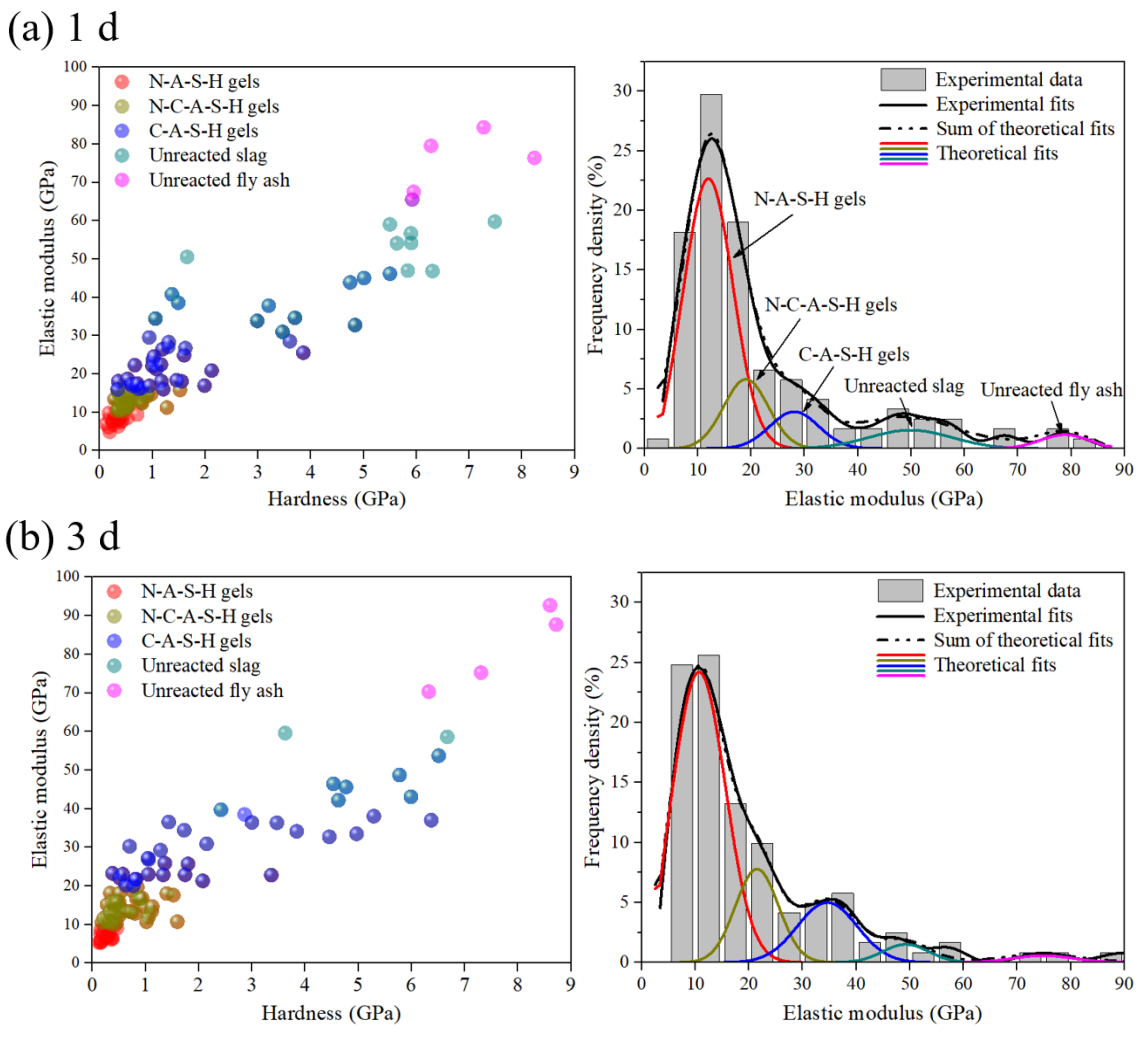

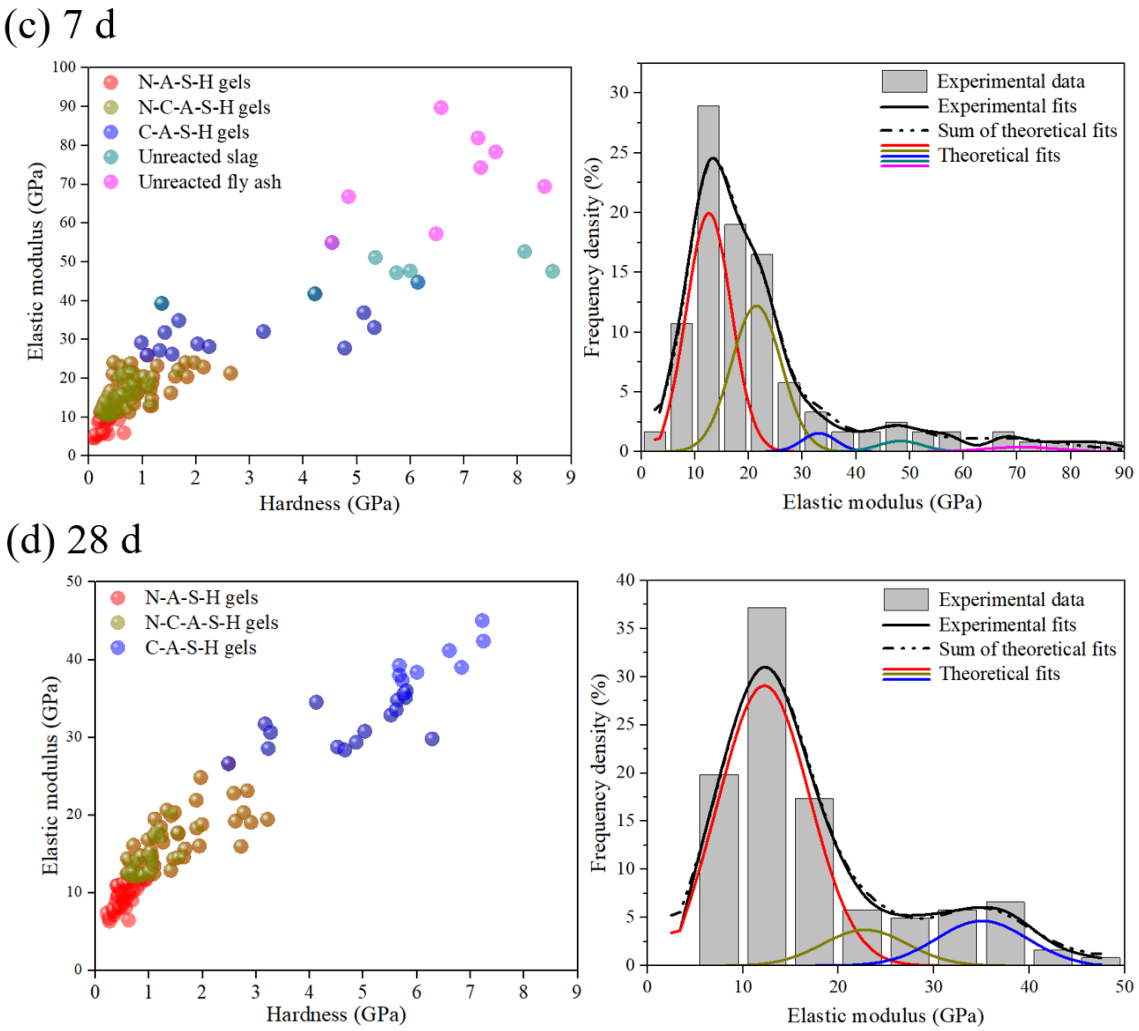

Figure 5-10 Gaussian mixtures deconvolution of elastic modulus of AAFS pastes at different curing ages (left – cluster allocation of elastic modulus and hardness; right – deconvolved elastic modulus corresponding to different phases)

Figure 5-11 shows the elastic moduli of different phases in AAFS paste at different curing ages. There exists an obvious distinction of elastic modulus between different phases, regardless of curing ages. The statistical analysis also indicates a strong significant difference (P-value < 0.01) of elastic modulus between different phases (see Tables 5-3 and 5-4). The order of elastic modulus among these five phases is N-A-S-H gels < N-C-A-S-H gels < C-A-S-H gels < unreacted slag < unreacted fly ash. The elastic modulus of N-A-S-H gels is stable at 11-12 GPa during the curing process. Regarding the N-C-A-S-H gels, the elastic modulus is relatively low, which is about 19 GPa at 1 d and then increases slightly to 23 GPa at 28 d. Consequently, the difference of elastic modulus between N-A-S-H gels and N-C-A-S-H gels becomes more obvious at later curing ages. This phenomenon can also be recognised in the cluster allocation of elastic modulus and hardness in Figure 5-10. The cluster of N-A-S-H gels is almost overlapped with that of N-C-A-S-H gels at 1 d (see Figure 5-10a). However, the overlap area between these two

gels becomes smaller and the boundary between them tends to be clear at later curing ages (see Figure 5-10b to d). Regarding the elastic modulus of C-A-S-H gels, it is obviously higher than that of N-A-S-H gels and N-C-A-S-H gels, regardless of curing age. In addition, the elastic modulus of C-A-S-H gels is increased steadily from 28 GPa to 35 GPa with increasing curing age from 1 d to 28 d. Regarding the unreacted particles, the elastic modulus of unreacted slag is decreased from 50 GPa to 48 GPa, while that of unreacted fly ash is decreased from 78 GPa to 71 GPa. As the unreacted slag and fly ash cannot be found in the testing area at 28 d, only the 7-d data are plotted here.

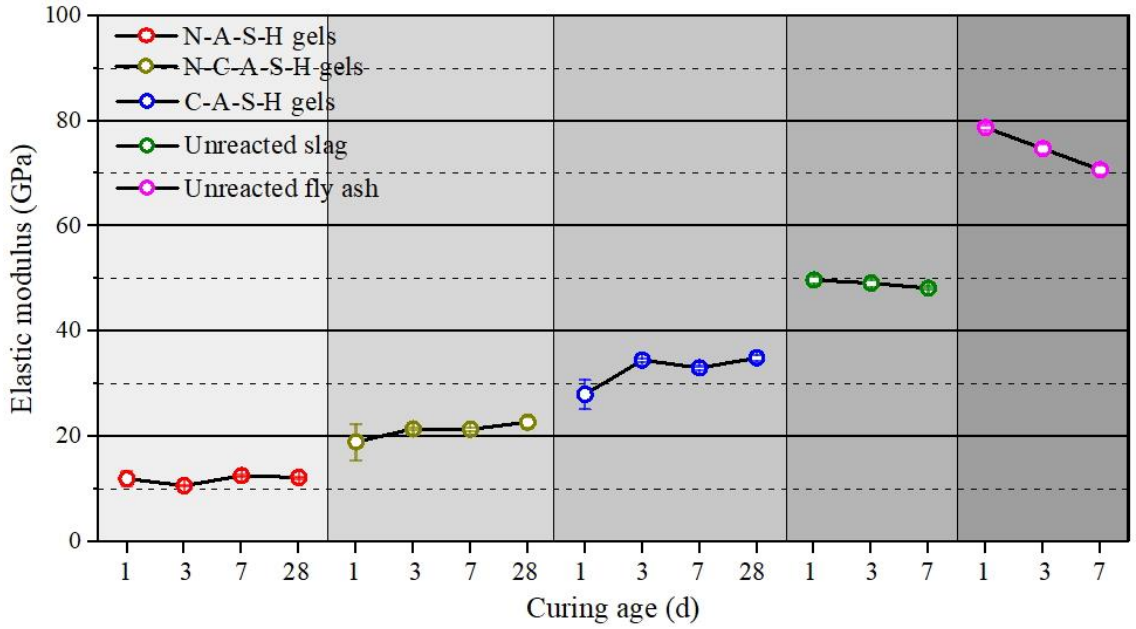

Figure 5-11 Elastic modulus of different phases in AAFS paste at different curing ages

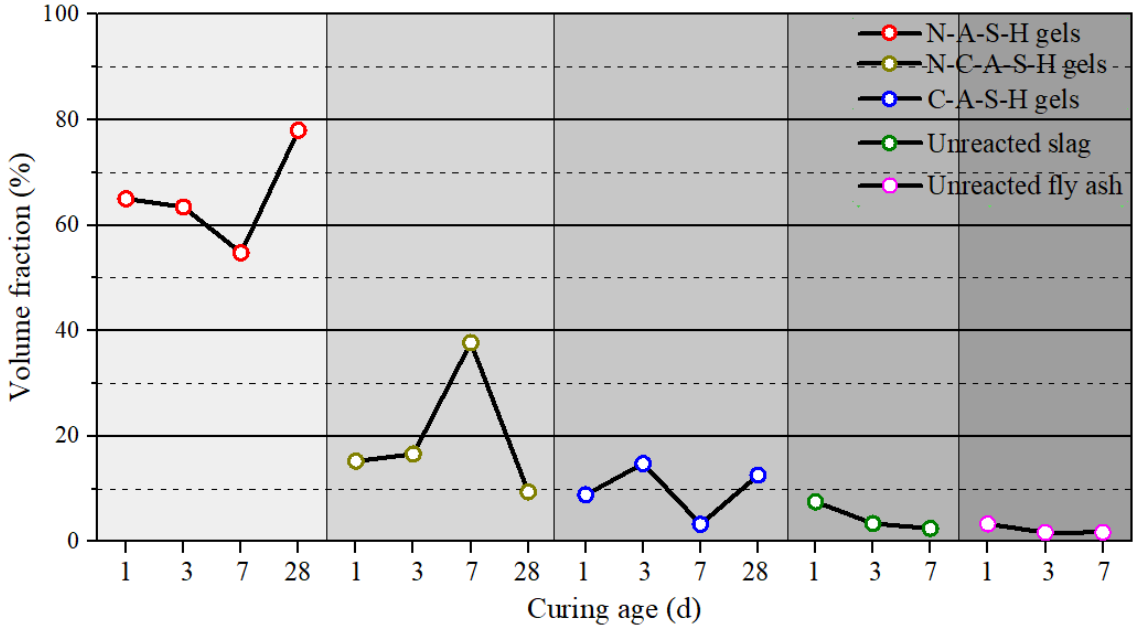

Figure 5-12 Volume fraction of elastic modulus of different phases in AAFS paste at different curing ages

Figure 5-12 presents the change in volume fraction of different phases in terms of elastic modulus against curing age. This information would help further understand the evolution of elastic moduli of different phases and their contribution to the overall elastic modulus of AAFS. It can be found that the volume fraction of N-A-S-H gels is obviously higher than that of N-C-A-S-H gels and C-A-S-H gels, regardless of curing age. Besides, it can be observed that the volume fraction of each phase is changed with the increase of curing age. For N-A-S-H gels, the content decreases steadily from 65.01% to 54.76% at early 7 d, but increases significantly at later curing ages, reaching 77.98% at 28 d. In contrast, the amount of N-C-A-S-H gels increases steadily from 15.24% to 37.72% with the increase of curing age from 1d to 7 d and then decreases dramatically to 9.43% at 28 d. The volume fraction of C-A-S-H gels is fluctuant at around 9%. The nonlinear development of micromechanical properties of different reaction products implies that the interaction between fly ash and slag exists during the reaction process. This phenomenon has also been found in other studies on chemical characterisation of AAFS (Ye and Radlińska, 2016). The content of unreacted slag and fly ash decreases steadily with the increase of curing age.

5.4.2 Micromechanical properties of AAFS paste

Continuum micromechanics provides a link between the mechanical properties of individual phases at micro-scale and AAFS paste at macro-scale. Here, the effective mechanical properties of AAFS paste including effective bulk modulus (K_{eff}) and effective shear modulus (G_{eff}) were calculated using the self-consistent continuum micromechanics model given as follows (Zaoui, 2002). The self-consistent continuum micromechanical model is used to estimate the effective micromechanical properties of a homogenized phase based on the volume fraction and micromechanical properties of individual phases. However, it should be noted that this model does not consider the effect of interaction between phases in the space. The interaction and configuration of different phases exists in the "composite" space, which might affect the overall mechanical properties. Therefore, it is of importance to investigate new simulating models which can consider the effect of phases' interaction and provide a more accurate prediction of overall mechanical properties.

$$K_{eff}=\frac{\sum_{i=1}^{n} f_i K_i\left[1+\alpha\left(\frac{K_i}{K_0}-1\right)\right]^{-1}}{\sum_{i=1}^{n} f_i\left[1+\alpha\left(\frac{K_i}{K_0}-1\right)\right]^{-1}} \qquad (5-5)$$

$$G_{eff}=\frac{\sum_{i=1}^{n} f_i G_i\left[1+\beta\left(\frac{G_i}{G_0}-1\right)\right]^{-1}}{\sum_{i=1}^{n} f_i\left[1+\beta\left(\frac{G_i}{G_0}-1\right)\right]^{-1}} \quad (5-6)$$

$$\alpha=\frac{3K_0}{3K_0+4G_0} \quad (5-7)$$

$$\beta=\frac{6K_0+12G_0}{15K_0+20G_0} \quad (5-8)$$

where f_i is the volume fraction of the i^{th} phase, K_i is its bulk modulus, and G_i is its shear modulus. A reference medium is regarded as the 0^{th} phase, which is equal to the homogenised medium itself in the self-consistent model, leading to $K_0 = K_{eff}$ and $G_0 = G_{eff}$ after several iterations. Additionally, the bulk modulus (K) and shear modulus (G) can be calculated as: $K=\frac{E}{3(1-2v)}$ and $G=\frac{E}{2(1+v)}$, respectively.

In addition, the effective elastic modulus (E_{eff}) for AAFS paste can be calculated based on its K_{eff} and G_{eff} as:

$$E_{eff}=\frac{9K_{eff}G_{eff}}{3K_{eff}+G_{eff}} \quad (5-9)$$

Here, five different phases were identified and conducted to homogenise the effective modulus of AAFS paste. Based on the obtained K and G of individual phases (see Table 5-5), K_{eff} and G_{eff} of AAFS pastes at various curing ages were calculated and presented in Table 5-6. E_{eff} was also calculated based on K_{eff} and G_{eff} (see Table 5-6). It can be observed that E_{eff} and K_{eff} are fluctuant in the range of 14.69 ~ 16.80 GPa and 8.16 ~ 9.33 GPa, respectively, while G_{eff} is stable between 6.12 GPa and 7 GPa.

Table 5-5 Bulk modulus (K) and shear modulus (G) of individual solid phases in AAFS paste at different curing ages (GPa)

Phases	1-d		3-d		7-d		28-d	
	K	G	K	G	K	G	K	G
A. N-A-S-H gels	6.64	4.98	5.92	4.44	6.98	5.24	6.79	5.09
B. N-C-A-S-H gels	10.55	7.91	11.92	8.94	11.89	8.92	12.62	9.47
C. C-A-S-H gels	15.57	11.68	19.18	14.39	18.37	13.78	19.41	14.56
D. Unreacted slag	27.64	20.73	27.30	20.48	26.78	20.08	-	-
E. Unreacted fly ash	43.71	32.78	41.50	31.13	39.27	29.45	-	-

Table 5-6 Effective elastic modulus (E_{eff}), effective bulk modulus (K_{eff}) and effective shear modulus (G_{eff}) of AAFS paste at different curing ages (GPa)

	1-d	3-d	7-d	28-d
E_{eff}	16.13	15.33	16.80	14.69
K_{eff}	8.96	8.51	9.33	8.16
G_{eff}	6.72	6.39	7.00	6.12

5.4.3 Micromechanical properties of ITZ in AAFS concrete

5.4.3.1 Identification of ITZ

Figure 5-13 shows the results of classical nanoindentation test on AAFS concrete. The line area near the edge of coarse aggregate was chosen for the nanoindentation test, where 10 points with space of 10 μm along a testing line from aggregate to paste matrix were tested (see Figure 5-13a). Figure 5-13b depicts the load-depth curves of the testing points. Three different regions including aggregate, ITZ and paste matrix can be well distinguished, where the differences in the indentation depth and the slope of unloading portion among these curves can be clearly recognized. This can be attributed to the differences in hardness and stiffness among the corresponding material phases. The indentation depth is associated with the hardness, while the slope of unloading portion is related to the elastic modulus. The order of indentation depth among these regions is aggregate < ITZ < paste matrix, while the order of slope is aggregate > ITZ > paste matrix. This suggests that aggregate has the highest hardness and highest elastic modulus, followed by ITZ and paste matrix.

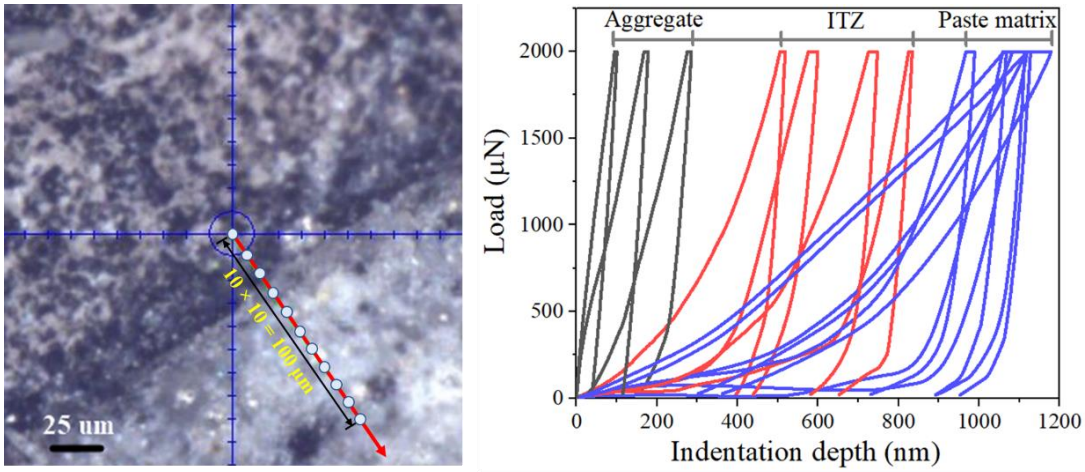

(a) Indent line area (b) Load-depth curves of indent area

Figure 5-13 Testing results of grid nanoindentation of AAFS concrete (t = 3h)

5.4.3.2 Evolution of micromechanical properties in ITZ

The characterisation of micromechanical properties of ITZ and paste matrix was performed based on a series of statistical analysis, where 126 indentations given on a grid of 50 × 100 μm in each sample were analysed. In the analysis, the micromechanical properties including elastic modulus and hardness were obtained from 20 strips with 5-μm width. To estimate the variation of elastic modulus and hardness against the distance from the aggregate surface, the mean values of these properties were calculated using 6 grid points in each strip. Additionally, the elastic modulus and hardness were plotted in the counter map to visualize the phase distribution in the testing area. Figure 5-14 shows

the mean values of elastic modulus and hardness against the distance from aggregate and the counter maps of elastic modulus and hardness at different curing ages. It should be noted that the elastic modulus was mainly discussed in the following sections considering the similar trend between curves of elastic modulus and hardness.

As seen in Figure 5-14a, the elastic modulus is generally reduced by increasing the distance from aggregate at 3 h. Aggregate has the highest elastic modulus (> 30 GPa), followed by ITZ and paste matrix, whose elastic moduli are in the range of 10 ~ 20 GPa and 0-10 GPa, respectively. A similar trend of elastic modulus can be observed at 12 h (Figure 5-14b), where the elastic modulus of different regions follows an order of aggregate (> 30 GPa) > ITZ (10 ~ 30 GPa) > paste matrix (0 ~ 20 GPa). Between 1 d and 3 d, the elastic modulus of ITZ is stable at 10-30 GPa (Figure 5-14c and d), while the elastic modulus of paste matrix increases from 0 ~ 20 GPa to 10 ~ 30 GPa at 1 d and then decreases to 0 ~ 10 GPa at 3 d. As the curing age increases from 7 d to 28 d, the elastic moduli of ITZ and paste matrix become close to each other and have a similar value of 10 ~ 20 GPa (Figure 5-14e and f).

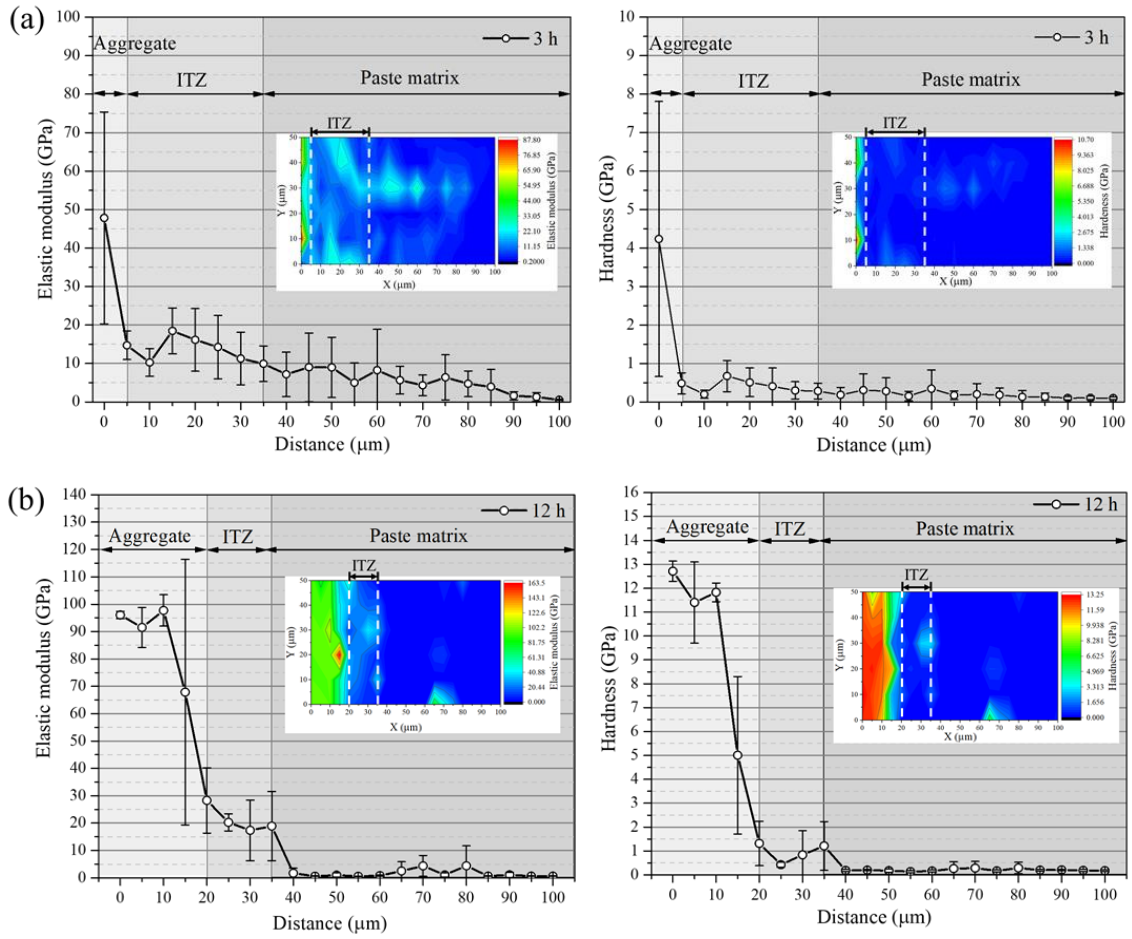

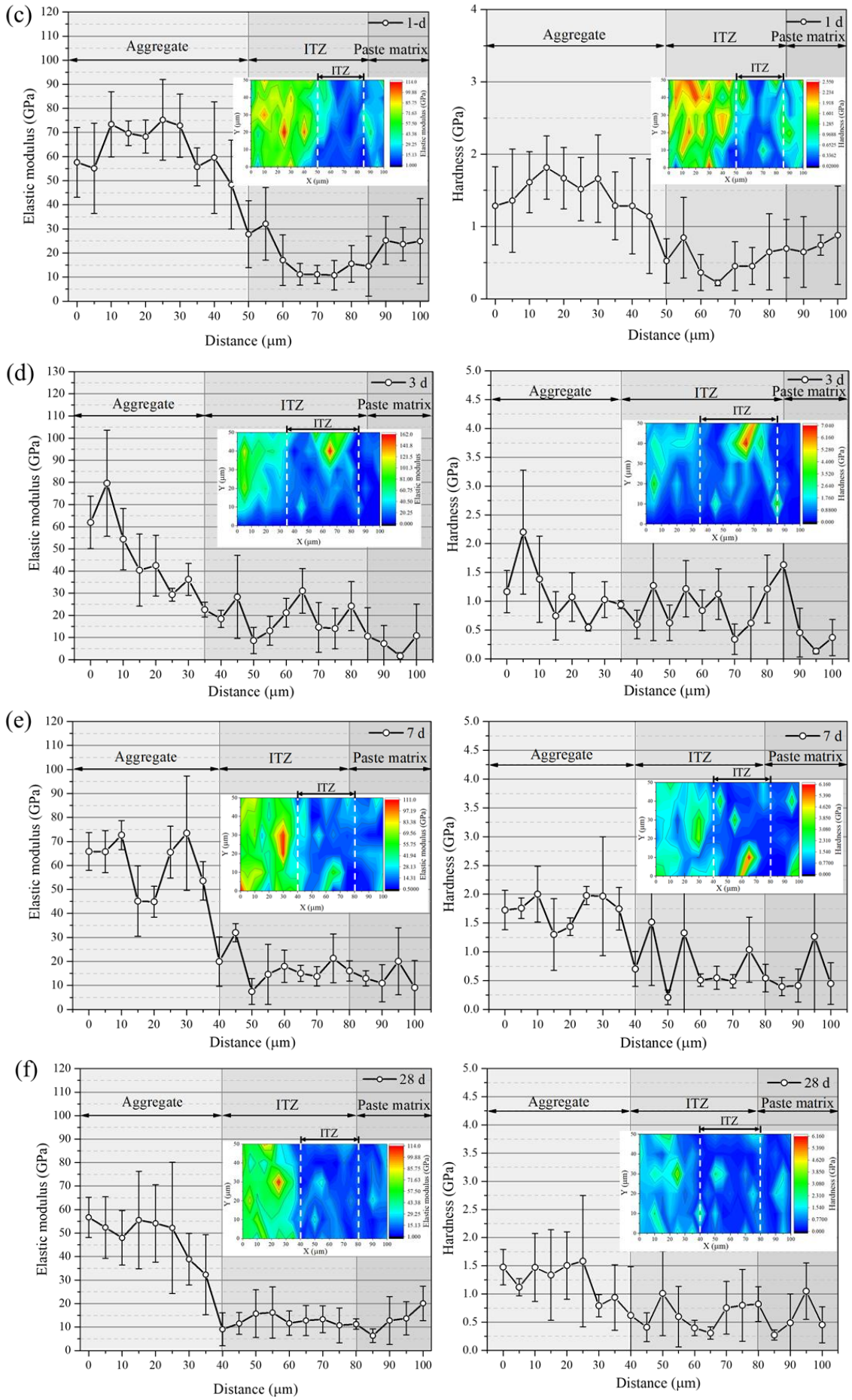

Figure 5-14 Histogram of elastic modulus and hardness of AAFS concrete at different curing ages

Figure 5-15 shows the mean values of elastic modulus and hardness in ITZ and paste matrix of AAFS concrete at different curing ages. As seen in Figure 5-15a, the elastic modulus of ITZ is 13.58 GPa at 3 h, which is higher than that of paste matrix, i.e. 5.11 GPa. With the increase of curing age from 3 h to 12 h, the elastic modulus of ITZ tends to be much higher than that of paste matrix and increases significantly from 13.58 GPa to 21.21 GPa, while the elastic modulus of paste matrix is stable at around 5 GPa. At 1 d, the elastic modulus of ITZ is slightly decreased to 18.37 GPa, while that of paste matrix approaches 19.59 GPa, implying that ITZ and paste matrix have a similar elastic modulus. Afterwards, the elastic modulus of paste matrix reduces obviously to 11.33 GPa at 3 d, making it lower than the elastic modulus of ITZ again. With increasing curing age from 3 d to 28 d, the elastic modulus of ITZ is decreased steadily from 18.5 GPa to 13.20 GPa, while that of paste matrix is increased slightly from 11.33 GPa to 13 GPa, leading to a similar elastic modulus of these two regions at 28 d. A similar trend can also be observed in the evolution of hardness, as shown in Figure 5-15b.

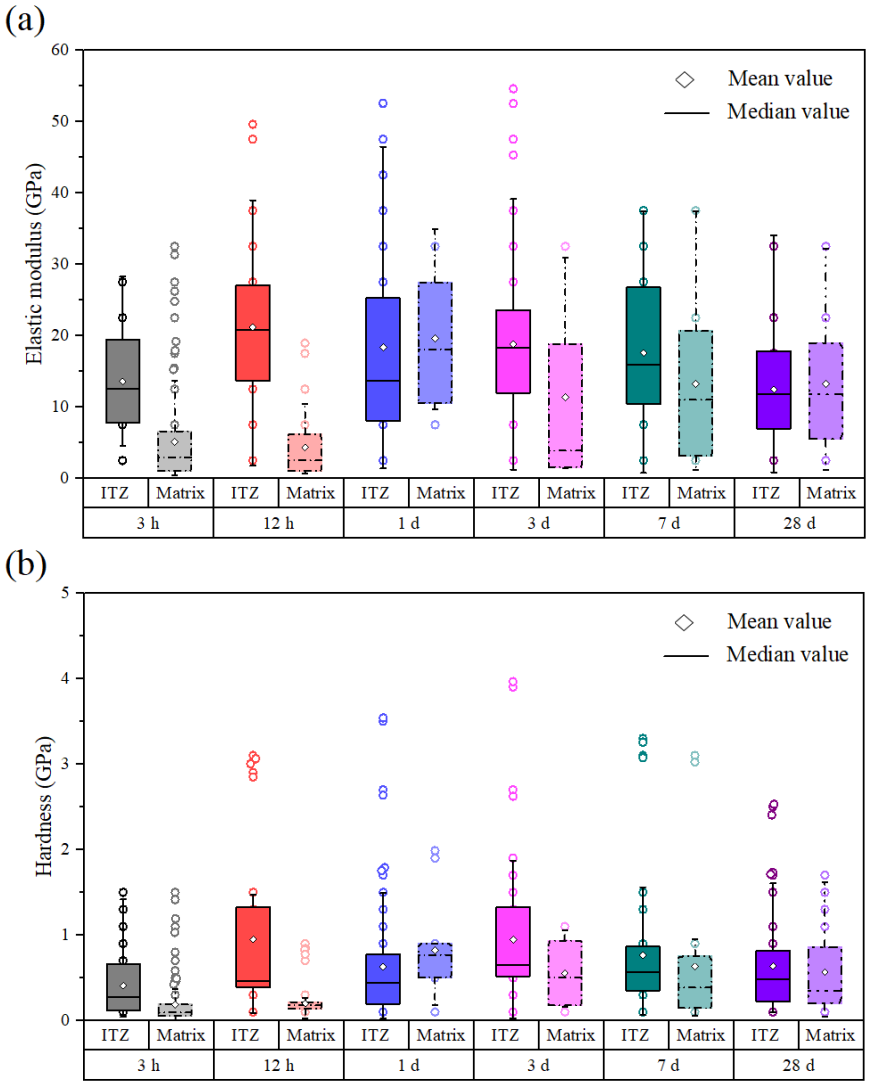

Figure 5-15 Elastic modulus (a) and hardness (b) of ITZ and paste matrix of AAFS concrete at different curing ages

5.4.3.3 Micromechanical properties of reaction products in ITZ

It is known that reaction products are the main components in ITZ, which would directly affect the micromechanical properties of ITZ. Thus, the micromechanical properties of reaction products were analysed to investigate the mechanism behind the development of micromechanical properties of ITZ. Gaussian deconvolution method is commonly used to characterise the clusters of experimental data with distinct mechanical properties (Tatar et al., 2019). As shown in Figure 5-16, the frequency density of elastic modulus (normalised histogram with a bin size of 2.5 GPa) was fit by three Gaussian distribution functions using the statistical analysis software called PeakFit (Constantinides et al., 2006; Randall et al., 2011). Five Gaussian distribution curves representing the five solid phases including three types of reaction products (N-A-S-H, N-C-A-S-H and C-A-S-H gels) and two type of unreacted particles (fly ash and slag) are considered in the Gaussian deconvolution . According to the literature (Němecek et al., 2010; Nedeljković et al., 2018; Thomas et al., 2018) and the identification of solid phases in Section 5.4.1, the elastic modulus of reaction products is lower than 50 GPa while that of unreacted particles is generally higher than 50 GPa. Therefore, the three deconvoluted phases with elastic modulus of < 35 GPa are associated with the existence of three types of reaction products, followed by the order of elastic modulus: N-A-S-H < N-C-A-S-H < C-A-S-H (Figure 5-16). The first peak was assigned to the N-A-S-H gels with elastic modulus of around 10 GPa, while the second and third peak were corresponding to the N-C-A-S-H gels (~ 20 GPa) and C-A-S-H gels (~ 30 GPa), respectively. The threshold value defining the frontier between N-A-S-H gels and N-C-A-S-H gels was set as the point of intersection between Gauss 1 (N-A-S-H gels) and Gauss 2 (N-C-A-S-H gels). Similarity, the intersection between Gauss 2 (N-C-A-S-H gels) and Gauss 3 (C-A-S-H gels) was considered as the threshold value to specify the boundary between N-C-A-S-H gels and C-A-S-H gels. Accordingly, the threshold values of 15 GPa and 26 GPa were used to determine the distinguish N-A-S-H, N-C-A-S-H and C-A-S-H gels in terms of elastic modulus (Figure 5-16). The determination of threshold value should be slightly adjusted according to different sample due to the value deviation between different samples. Lastly, the volume fraction of each phase can be statistically characterised based on the total frequency density within each threshold value. It is noted that the volume fraction used here is the frequency of occurrence in the solid phase, since the elastic modulus of gas phase (< 0.1 GPa) is not considered in the deconvolution process.

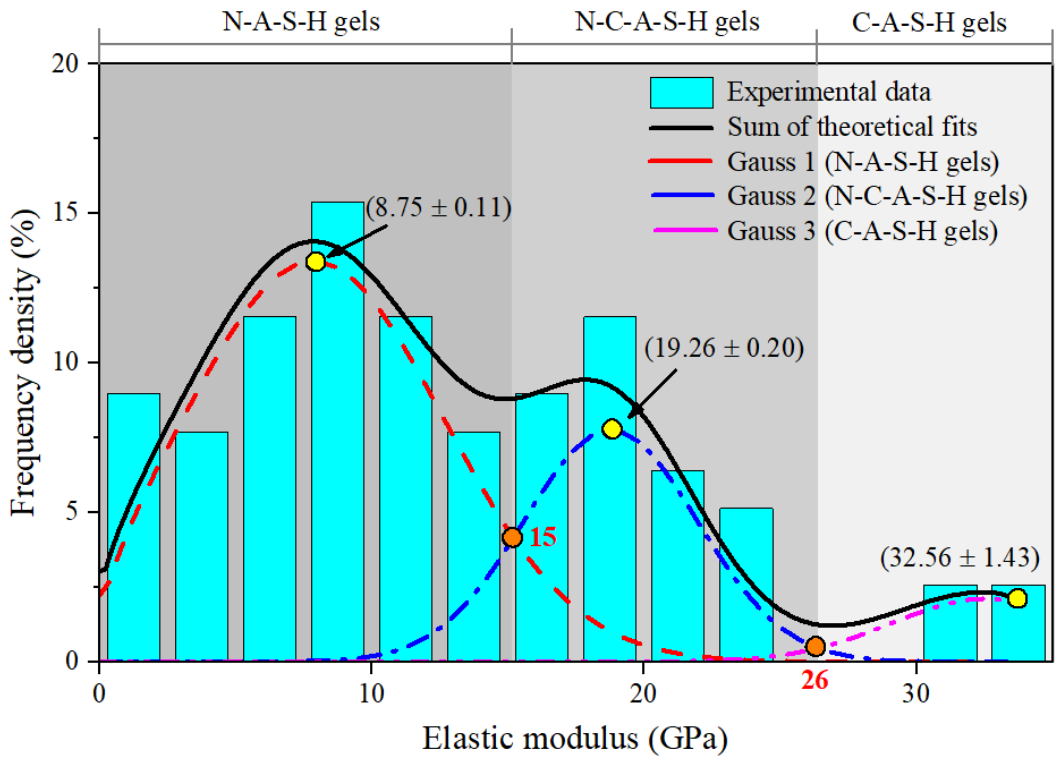

Figure 5-16 Gaussian deconvolution of frequency density for elastic modulus of reaction products in AAFS concrete (t = 28 d)

As shown in Figure 5-17, the cluster allocation and volume fractions of different reaction products in ITZ and paste matrix at different ages are successfully characterised. At early ages (3 ~ 12 h), the volume fraction of N-A-S-H gels in ITZ is much lower than that in paste matrix, while the volume fractions of N-C-A-S-H gels and C-A-S-H gels are obviously higher than those in paste matrix (Figure 5-17a and b). At 1 d, the volume fraction of N-A-S-H gels in ITZ becomes higher than that in paste matrix, but the volume fractions of N-C-A-S-H gels and C-A-S-H gels are lower than those in paste matrix at this stage (Figure 5-17c). At later curing ages (3 ~ 28 d), the volume fractions of all types of reaction products in ITZ become close to those in paste matrix (Figure 5-17d ~ f). The lack of any significant difference in the distribution of reaction products in ITZ and paste matrix at 28 days indicates that ITZ is not the weakest region in AAFS concrete. It means that AAFS concrete can be regarded as a "two-phase medium" comprising aggregate and paste, which is expected to achieve a desired mechanical property due to the lack of weakest region.

(a) 3 h

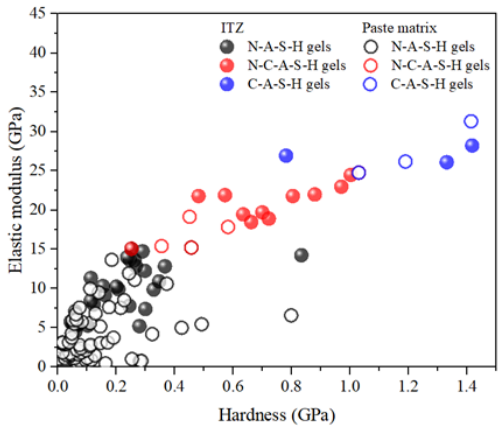

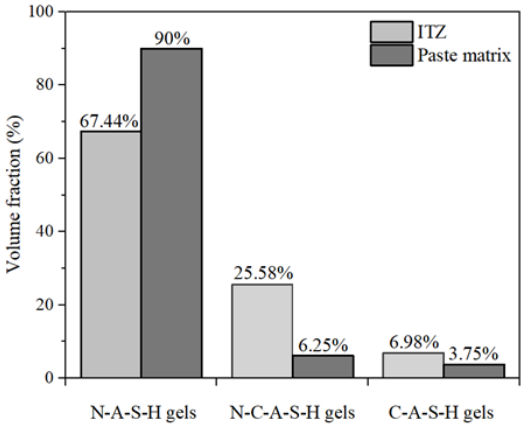

(b) 12 h

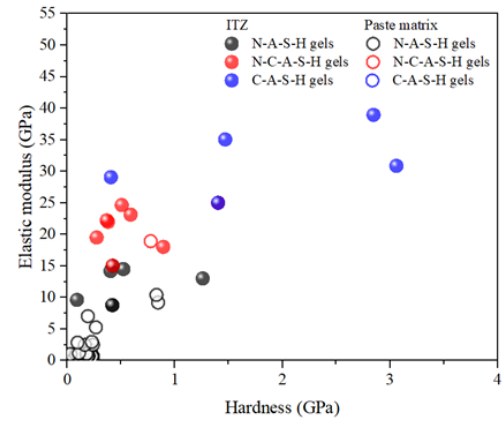

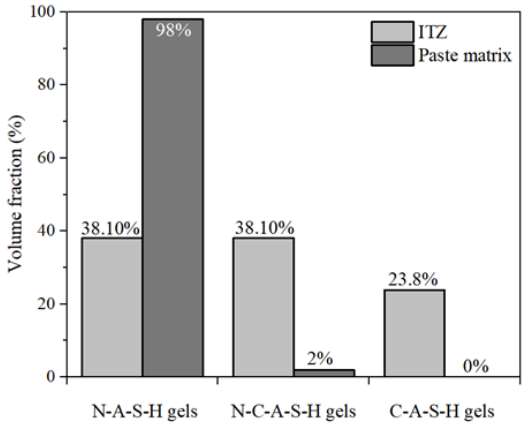

(c) 1 d

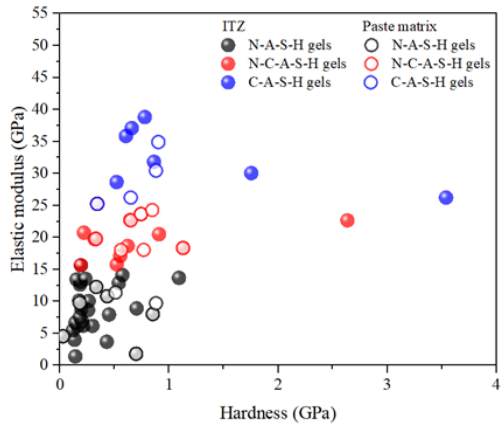

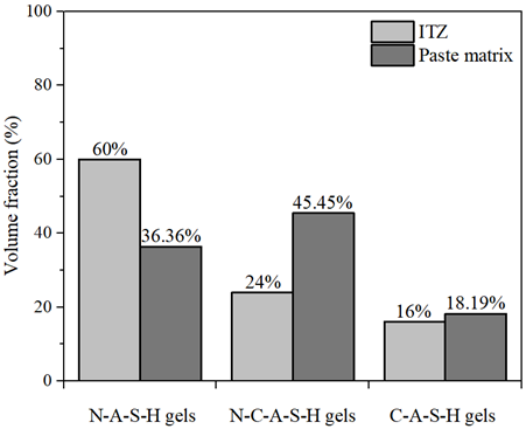

(d) 3 d

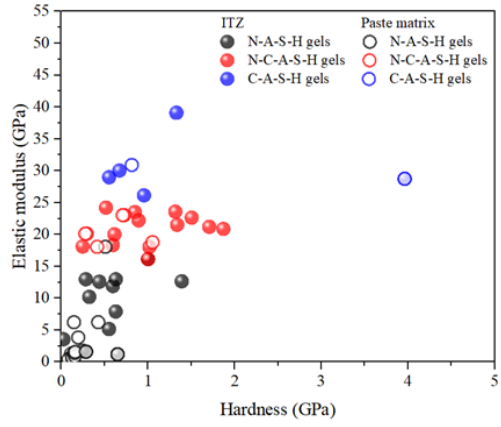

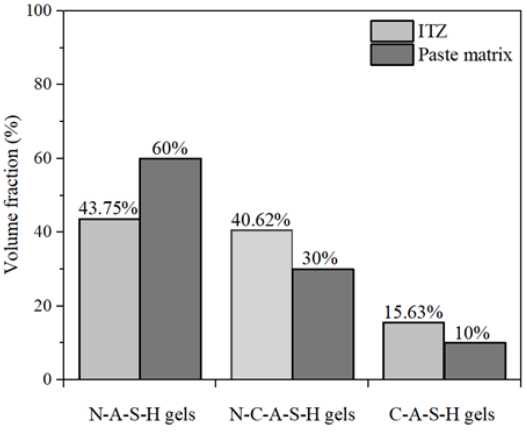

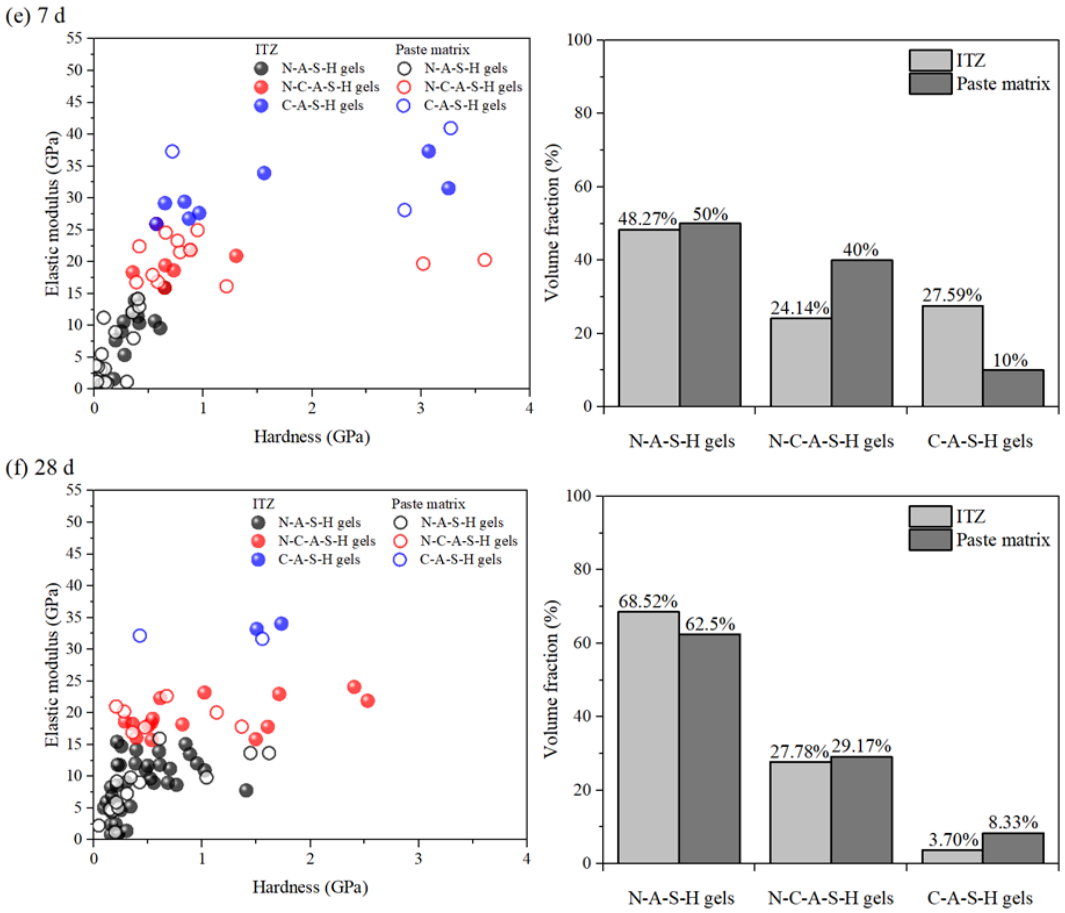

Figure 5-17 Micromechanical properties of reaction products in ITZ and paste matrix of AAFS concrete at different curing ages: cluster allocation of elastic modulus and hardness (left); volume fraction of different reaction products (right)

Figure 5-18 shows the change in volume fractions of different reaction products in ITZ and paste matrix. This information would be helpful for understanding the effects of reaction products on the development of elastic modulus of ITZ and paste matrix. Regarding the ITZ (Figure 5-18a), it can be observed that the volume fraction of N-A-S-H gels is generally higher than that of N-C-A-S-H gels and C-A-S-H gels, regardless of curing age. Nevertheless, the volume fraction of each reaction product varies with the increase of curing age. For N-A-S-H gels, the volume fraction decreases significantly from 67.44% to 38.1% at early 12 h, but increases steadily between 12 h and 1 d, reaching 60% at 1 d. Afterwards, it decreases to 43.75% at 3d, but increases again at later curing age and finally reaches 68.52% at 28 d. In contrast, the volume fraction of N-C-A-S-H gels increases significantly from 25.58% to 38.1% between 3 h and 12 h and then decreases steadily to 24% at 1 d. Subsequently, it increases to 40.62% at 3 d, followed by a decrease between 3 d and 28 d, reaching 27.78% at 28 d. The developing trend in volume fraction of C-A-S-H gels is similar to that of N-C-A-S-H gels, which is increased from 6.98% to 23.8% at early 12 h, followed by a steady decrease from 23.8% to 16% as the

curing age increases from 12 h to 3 d. Afterwards, it increases to 48.27% at 7 d, but then decreases dramatically to 3.7% at 28 d.

Regarding the paste matrix (Figure 5-18b), it can also be observed that the N-A-S-H gels dominate the volume fraction of reaction products, regardless of curing ages. However, the evolution process of reaction products in this region is less complicated compared to that in ITZ. At early curing ages (3 ~ 12 h), the volume fractions of all reaction products are stable. The volume fraction of N-A-S-H gels is stable at around 90%, while the volume fractions of N-C-A-S-H gels and C-A-S-H gels are stable at around 6% and 4%, respectively. At 1 d, the volume fraction of N-A-S-H gels is decreased dramatically to 36.36%, while the volume fractions of N-C-A-S-H gels and C-A-S-H gels are increased significantly to 45.45% and 18.19%, respectively. Afterwards, the volume fractions of all reaction products become relatively stable at later curing ages (3 ~ 28 d). At 28 d, the volume fractions of N-A-S-H gels, N-C-A-S-H gels and C-A-S-H gels reach 55%, 35% and 10%, respectively.

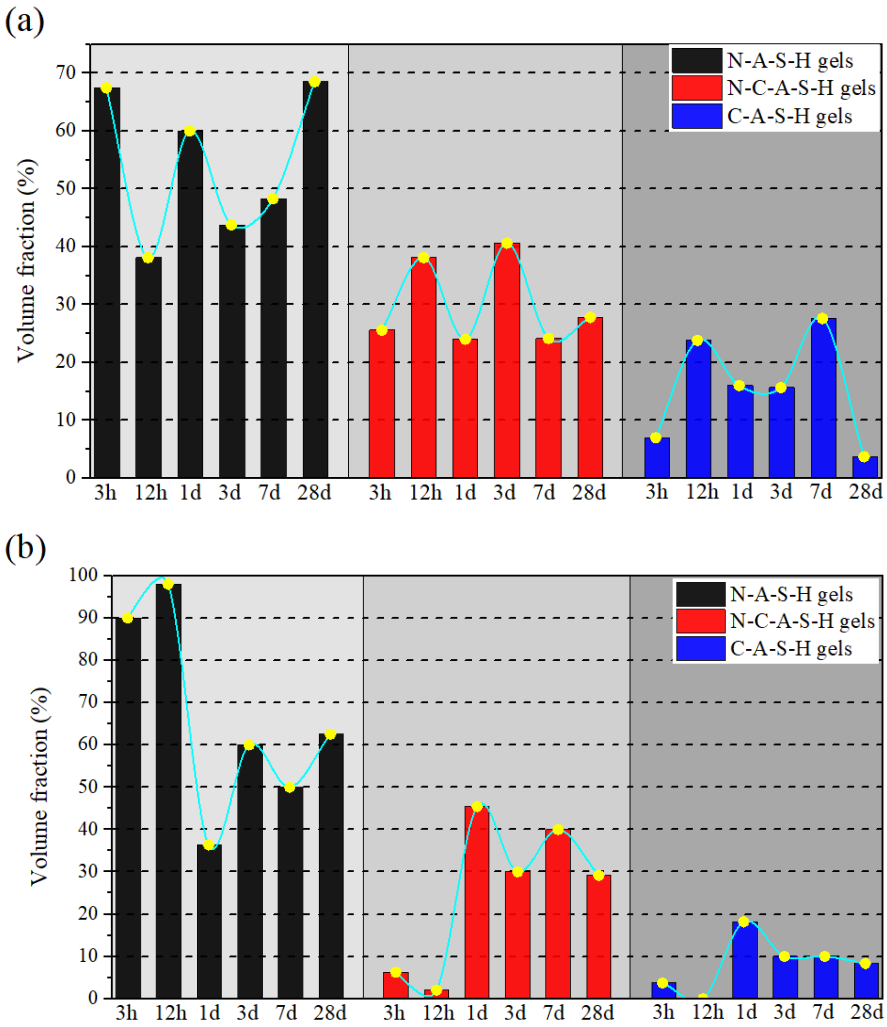

Figure 5-18 Volume fraction of reaction products in ITZ (a) and paste matrix (b) of AAFS concrete at different curing ages

5.4.3.4 Effects of reaction products on the mechanical properties of ITZ

Previous studies have reported that different reaction products have different micromechanical properties (Němeček et al., 2011; Thomas et al., 2018). The elastic modulus of reactions products in AAFS follows an order of N-A-S-H gels < N-C-A-S-H gels < C-A-S-H gels, which might attribute to their different level of structure disorder and gel porosity. This implies that the types and contents of reaction products in ITZ would determine its micromechanical properties.

Figure 5-19 shows the evolution of elastic modulus and volume fraction of reaction products in ITZ. During the early curing ages (3 ~ 12 h), the elastic modulus of ITZ is increased significantly from 13.58 GPa to 21.21 GPa. This can be ascribed to the increase in volume fractions of N-C-A-S-H gels and C-A-S-H gels from 25.58% to 38.1% and from 6.98% to 23.8%, respectively, which have relatively high elastic moduli. The increase in volume fractions of N-C-A-S-H gels and C-A-S-H gels is a result of the quick dissolution of Ca from slag due to its high reactivity.

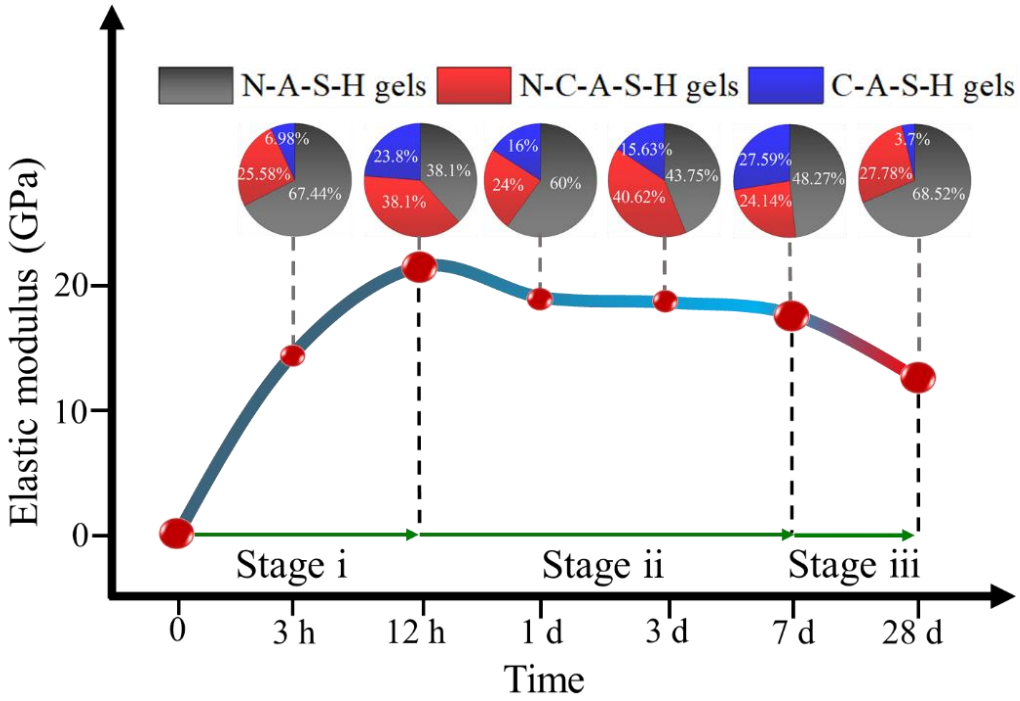

Figure 5-19 Evolution of elastic modulus and volume fraction of reaction products in ITZ of AAFS concrete

At 1 d, the elastic modulus of ITZ is decreased from 21.21 GPa to 18.37 GPa, which is related to the decrease in volume fractions of N-C-A-S-H gels and C-A-S-H gels from 38.1% to 24% and from 23.8% to 16%, respectively due to the reduction of free Ca releasing from slag, implying that slag in ITZ has been almost completely dissolved. This can be ascribed to the low content of slag that occupies 25% of the total precursors for AAFS concrete. In comparison, more Al and Si can be supplied from the continuous

dissolution of fly ash due to its high content (75% of the total precursors), contributing to the increase in volume fraction of N-A-S-H gels from 38.1% to 60%.

Between 1 d and 3 d, the elastic modulus of ITZ becomes stable at around 18.5 GPa, which is associated with the stable chemical reaction at this stage. During this period, the volume fraction of N-A-S-H gels is decreased from 60% to 43.75%, while the volume fraction of N-C-A-S-H gels is increased significantly from 24% to 40.62% and that of C-A-S-H gels remains stable at around 16%. This suggests that part of N-A-S-H gels have been transformed into N-C-A-S-H via interchanging between Ca and Na. Since Ca has a higher polarising power than Na, the Na within N-A-S-H gels would be replaced by Ca (García-Lodeiro et al., 2013). Given that slag in ITZ has been almost completely dissolved at 1 d, the mobile Ca in ITZ might be released from the paste matrix due to the concentration gradient between these two regions.

With the increase of curing age from 3 d to 7 d, the elastic modulus is declined slightly from 18.5 GPa to 17.68 GPa, attributing to the transformation between different reaction products. During this period, the volume fraction of N-A-S-H gels is increased slightly from 43.75% to 48.27%, which indicates that the effects of Ca on N-A-S-H gels become less sensitive to the decrease of mobile Ca. The volume fraction of N-C-A-S-H gels is declined from 40.62% to 24.14%, while that of C-A-S-H gels is increased from 15.63% to 27.59%, implying the transformation between N-C-A-S-H gels and C-A-S-H gels, where Na in N-C-A-S-H gels is continually replaced by Ca and eventually leading to the formation of C-A-S-H gels (García-Lodeiro et al., 2013).

At 28 d, a sharp decrease of elastic modulus from 17.68 GPa to 13.2 GPa can be observed, which can be explained by the significant increase in volume fraction of N-A-S-H gels with relatively low elastic modulus and the obvious decrease in volume fraction of C-A-S-H gels. In detail: the volume fraction of N-A-S-H gels is increased significantly from 48.27% to 68.52%, while the volume fraction of C-A-S-H gels is decreased dramatically from 27.59% to 3.7%. This can be ascribed to the reduction of free Ca releasing from slag, indicating that slag in both ITZ and paste matrix has been almost fully dissolved.

According to the discussion above, the evolution of micromechanical properties of ITZ can be divided into three stages: (i) accelerated growth stage (< 12 h), (ii) stationary stage (12 h ~ 7 d), and (iii) decrement stage (7 ~ 28 d). This finding is consistent with the microstructure evolution of ITZ, as discussed in Section 4.7.5.

5.4.3.5 Effects of microstructure characteristics on the mechanical properties of ITZ

It is known that the pores and microcracks are two key microstructural features, which would directly affect the micromechanical properties of ITZ (Akçaoğlu et al., 2005; Gao et al., 2013). As Figure 4-56 shown in Section 4.7.5, the total porosity of ITZ is decreased dramatically at early ages (< 12 h) due to the rapid chemical reactions occurred in this region, which would promote the formation of reaction products and refine the pore structure. As a result, the microstructure of ITZ becomes compact, leading to an obvious improvement in its micromechanical properties, from 13.58 GPa to 21.21 GPa (see Figure 5-19). Between 1 d and 7 d, the porosity of ITZ is stable at a relatively low level, which is corresponding to its stable elastic modulus with around 18 GPa during this period. With the increase of curing age from 7 d to 28 d, the microstructure of ITZ becomes less dense, accompanied by occurrence of microcracking, see Figure 4-48 in Section 4.7.5. The appearance of microcracks in ITZ would strongly reduce the bonding between solid phases and lead to the occurrence of micro gaps within the testing area itself. This would decrease the confinement of the surrounding matrix in the indented region and consequently result in a relatively low elastic modulus of ITZ (Figure 5-19). These findings indicate that the formation of reaction products would help reduce the pore size, refine the microstructure and consequently enhance the micromechanical properties of ITZ, especially at early ages (< 12 h). However, the microcracking induced by shrinkage may inversely affect the microstructure of ITZ and reduce its micromechanical properties at later curing ages (> 7 d).

5.4.3.6 Comparison of the micromechanical properties between ITZ and paste matrix

The relative micromechanical properties between ITZ and paste matrix play a significant role in the overall stress-strain relationship and failure patterns of concrete (Xiao et al., 2013a). Therefore, it is vital to make a direct comparison between the micromechanical properties of ITZ and paste matrix in order to further understand the effects of ITZ on the overall performance of AAFS concrete.

Figure 5-20 shows a comparison between the elastic moduli of ITZ and paste matrix of AAFS concrete at different curing ages. Within the first 12 h, the elastic modulus of ITZ (13.58 ~ 21.21 GPa) is obviously higher than that of paste matrix (4.32 ~ 7.45 GPa), which can be attributed to the accelerated chemical reactions occurred in ITZ due to the relatively high AL/P ratio in ITZ. The accelerated chemical reactions in ITZ would promote the formation of reaction products, resulting in a compact microstructure and a high elastic modulus in this region. In addition, the accelerated chemical reactions

facilitate the formation of N-C-A-S-H gels and C-A-S-H gels in ITZ. As seen in Figure 5-17a and b, the volume fractions of N-C-A-S-H gels and C-A-S-H gels in ITZ are higher than that in paste matrix, resulting in a high elastic modulus of ITZ.

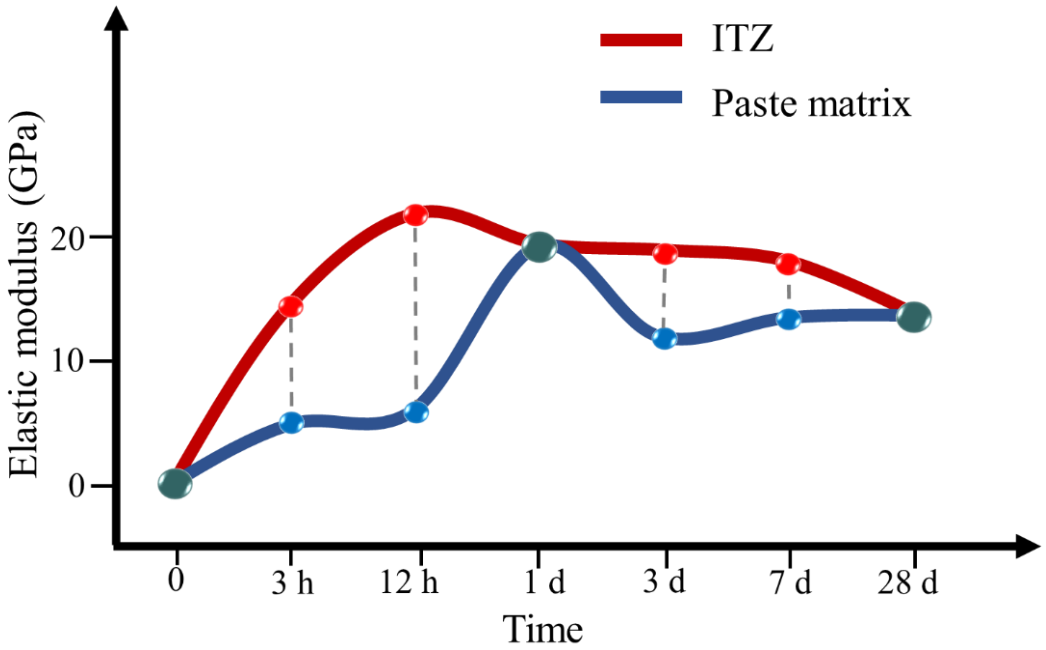

Figure 5-20 Comparison between elastic moduli of ITZ and paste matrix of AAFS concrete

At 1 d, the elastic modulus of ITZ (18.37 GPa) is close to that of paste matrix (19.59 GPa), which can be ascribed to the formation of more reaction products with high elastic modulus in paste matrix. The volume fractions of N-C-A-S-H gels and C-A-S-H gels in paste matrix become higher than those in ITZ (Figure 5-17c) as the chemical reactions proceed in paste matrix, which is consistent with the findings from EDS analysis that the contents of Si, Al and Ca in paste matrix become close to those in ITZ (see Figure 4-54 in Section 4.7.5). However, a sharp decrease in elastic modulus of paste matrix can be observed at 3 d, which can be attributed to the significant decrease in volume fractions of N-C-A-S-H gels and C-A-S-H gels in paste matrix (Figure 5-18b). This is due to the transport of Ca from paste matrix to ITZ, leading to the deficiency of Ca in paste matrix for generating N-C-A-S-H gels and C-A-S-H gels, as discussed in Section 4.7.5.

With the increase of curing age from 3 d to 28 d, the difference in elastic modulus between ITZ and paste matrix becomes less. The elastic modulus of ITZ is decreased from 18.5 GPa to 13.2 GPa, while the elastic modulus of paste matrix is increased steadily from 11.33 GPa to 13 GPa because of its stable chemical properties. As seen in Figure 5-18b, the volume fractions of N-A-S-H, N-C-A-S-H and C-A-S-H gels in paste matrix remain stable between 3 d and 28 d.

5.5 Concluding remarks

In this Chapter, the micromechanical properties of AAFS concrete at multiple length scales from Level I to Level III were investigated by experimental test and continuum micromechanics modelling. The micromechanical properties of individual solid phases in paste were characterised by nanoindentation test, while the effective mechanical properties of paste matrix were estimated by self-consistent continuum micromechanics model. The micromechanical properties of ITZ were evaluated through the statistical analysis of nanoindentation results. The main conclusions can be drawn as follows:

(i) Micromechanical properties of individual solid phases in paste

- The elastic modulus of individual solid phases follows and order of N-A-S-H gels < N-C-A-S-H gels < C-A-S-H gels < unreacted slag < unreacted fly ash. The C-A-S-H gels have the highest elastic modulus of around 30 GPa among the reaction products, followed by the N-C-A-S-H gels (~ 20 GPa) and N-A-S-H gels (~ 10 GPa). The C-A-S-H gels have a similar elastic modulus to the high-density C-S-H gels generated from PC concrete, while the elastic modulus of N-A-S-H gels close to that of low-density C-S-H gels. The unreacted fly ash and slag have the relatively high elastic modulus of around 75 GPa and 50 GPa, respectively. The elastic modulus of unreacted fly ash and slag is lower than that of anhydrous clinker (~ 100 GPa).
- The evolutions of elastic modulus of reaction products are different with each other. The elastic modulus of N-A-S-H gels is stable at 11 ~ 12 GPa regardless of curing age, whereas that of N-C-A-S-H gels and C-A-S-H gels is increased from 19 GPa to 23 GPa and from 28 GPa to 35 GPa, respectively, with the increase of curing age from 1 d to 28 d.

(ii) Micromechanical properties of paste matrix

- The effective elastic modulus and bulk modulus of paste matrix are fluctuant in the range of 14.69 ~ 16.80 GPa and 8.16 ~ 9.33 GPa, respectively, while effective shear modulus is stable between 6.12 GPa and 7 GPa during the curing ages of 1 ~ 28 d. The elastic modulus of AAFS paste is slightly lower than that of PC paste (~ 20 GPa).

(iii) Micromechanical properties of ITZ in concrete

- The micromechanical properties of ITZ depend on the chemical composition of reaction products and the microstructural characteristics. The ITZ with high proportion of N-C-A-S-H gels and C-A-S-H gels tends to have a high elastic modulus because of their superior micromechanical properties. Moreover, the formation of reaction products would refine the microstructure of ITZ and consequently improve its elastic modulus.

- The changes in chemical composition of reaction products and microstructure of ITZ would directly affect the development of micromechanical properties in this region. In detail: (1) The elastic modulus of ITZ is increased significantly from 13.58 GPa to 21.21 GPa at early curing ages (3 h ~ 12 h), which can be ascribed to the relatively high AL/P ratio in this region that facilitates the chemical reactions, promotes the formation of reaction products and refine the microstructure. Meanwhile, the volume fractions of N-C-A-S-H gels and C-A-S-H gels are increased dramatically due to the quick dissolution of Ca from slag, leading to a high elastic modulus of ITZ. (2) Between 12 h to 7 d, the elastic modulus of ITZ fluctuates between 17.68 GPa and 21.21 GPa, which can be attributed to the stable transformation among N-A-S-H, N-C-A-S-H and C-A-S-H gels. (3) The elastic modulus of ITZ is decreased from 17.68 GPa to 13.20 GPa between 7 d and 28 d due to the release of free Ca from slag due to its relatively low content, which would promote the formation of Ca-free reaction products, i.e. N-A-S-H gels, leading to the low elastic modulus of ITZ. Meanwhile, the microcracking occurred in ITZ would weaken the binding of reaction products and consequently decrease its elastic modulus.
- ITZ is not the weakest region in AAFS concrete owing to its desire micromechanical properties compared to paste matrix. At early ages (< 12 h), the elastic modulus of ITZ is found to be 13.58 ~ 21.21 GPa which is much higher than that of paste matrix, i.e., 4.32 ~ 7.45 GPa. At later ages (1 ~ 28 d), the elastic modulus of ITZ becomes close to that of paste matrix, reaching a similar elastic modulus of 13 GPa at 28 d. The relationship of elastic modulus between ITZ and paste matrix in AAFS concrete is different as compared to the relationship existing in PC concrete, in which the elastic modulus of ITZ is 70% ~ 85% of the elastic modulus of paste matrix.
- The evolution of micromechanical properties of ITZ can be divided into three stages: (i) accelerated growth stage via fast chemical reactions (< 12 h); (ii) stationary stage via stable chemical reactions (12 h ~ 7 d); (iii) decrement stage via microcrack propagation (7 ~ 28 d).

Chapter 6 Microstructure-mechanical properties relationship in AAFS concrete

6.1 Introduction

The multiscale microstructure and mechanical properties of AAFS concrete from nano- to macro-scale were characterised and presented in Chapters 3 ~ 5. The heterogeneous microstructures of AAFS concrete can be divided into different levels with multiscale (Level 0 to Level III) and multiphase (pores, reaction products, unreacted particles and aggregates), which are strongly associated with the micro-scale and macro-scale mechanical properties. According to the experimental results obtained above, this chapter attempts to establish the multiscale microstructure-mechanical properties relationship from Level 0 to Level III in AAFS concrete, which would enable us to better understand the development of overall mechanical properties of this new type of concrete.

6.2 Level I: Solid gel particle + gel pore → gel matrix

The combination of nanoindentation, NMR, XRD and FTIR test results provides a strong evidence that the microscopic performance of gel matrix at Level I is determined by two factors: (1) the physical chemistry within solid gel particles at Level 0, and (2) the gel porosity within gel matrix at Level I. These two characteristics determine the elastic modulus of different phases in gel matrix. As seen in Figure 5-11, the distinction of elastic modulus between different phases is clear and follows an order of N-A-S-H gels < N-C-A-S-H gels < C-A-S-H gels < unreacted slag < unreacted fly ash.

Regarding the first factor, previous studies have noted that the nanostructure and chemical composition of solid gel are strongly associated with its elastic modulus (Lolli et al., 2018). Generally, the elastic modulus of solid gel with crystalline structure (order structure) is obviously higher than that of the solid gel with amorphous structure (disorder structure) (Lolli et al., 2018), which implies that the level of structural disorder would determine the elastic modulus of solid gel. Thus, the unreacted particles with the highest elastic modulus might be attributed to their compact nonactivated crystal solid. The unreacted fly ash has the highest elastic modulus (above 70 GPa), followed by unreacted slag, the elastic modulus of which is around 50 GPa. Regarding the reaction products, the occurrence of crystalline phase can be observed in C-A-S-H gels of AAS (Haha et al., 2011), while the crystalline phase in N-A-S-H gels of AAF is extremely rare (Oh et al., 2010). This suggests that the C-A-S-H gels with a high elastic modulus of around 30 GPa can be ascribed to their comparatively low level of structural disorder, while the N-A-S-

H gels with a low elastic modulus of around 10 GPa are highly related to their high level of structural disorder. The N-C-A-S-H gels with a middle elastic modulus of around 20 GPa between N-A-S-H gels and C-A-S-H gels are associated with their middle level of structural disorder. The Ca-substituted N-A-S-H gels (N-C-A-S-H gels) may have a mineral feature between N-A-S-H gels and C-A-S-H gels, which retain the original 3D aluminosilicate framework structure but tend to have a similar composition with C-A-S-H gels (Garcia-Lodeiro et al., 2011). In a word, the micromechanical properties of gel matrix at Level I are determined by the structural disorder level of solid gel particles at Level 0, in which the gel matrix with a lower disorder level has a higher micromechanical property. For example, the C-A-S-H gels have the highest elastic modulus among the reaction products due to their relatively low level of structural disorder.

Regarding the second factor, previous research has shown that the gel porosity would directly affect the micromechanical properties of gel matrix at Level I (Tatar et al., 2019). Depending on the distinction of porosity, the C-S-H gels in PC paste can be divided into two types: low density and high density (Chen et al., 2010). It was reported that the low-density C-S-H gels have a relatively low elastic modulus due to their high porosity (Jennings et al., 2007). The high-density C-S-H gels have a comparatively high elastic modulus because of their densely packed structure and low porosity (Jennings et al., 2007). This indicates that gel porosity would determine the elastic modulus of gel matrix. Therefore, the difference of elastic modulus between C-A-S-H gels, N-A-S-H gels and N-C-A-S-H gels might be also ascribed to their different gel porosity. It was found that the C-A-S-H gels in AAFS paste have a similar structure with high-density C-S-H gels in PC paste (Puertas et al., 2011), which indicates that the C-A-S-H gels also have a less porous structure, leading to a high elastic modulus. Regarding the N-A-S-H gels, it was reported that they have similar mechanical properties to the low-density C-S-H gels in PC paste (Němecek et al., 2010). This suggests that the N-A-S-H gels with low elastic modulus might also be related to the relatively high porosity, which is probably a result of their syneresis process (Šmilauer et al., 2011). The syneresis of N-A-S-H gels would cause the expulsion of entrained water and produce gel shrinkage, which would consequently lead to a high porosity (Němecek et al., 2010). The N-C-A-S-H gels with middle elastic modulus among the reaction products are possibly associated with their middle level of porosity. The gel porosity within gel matrix would also affect the micromechanical properties of gel matrix, where the gel matrix with lower gel porosity tends to achieve better micromechanical properties.

In addition, the change in chemical composition and internal structure of solid gel particles at Level 0 would affect the evolution of elastic modulus of individual phases at Level I. As can be seen in Figure 5-11 that the elastic modulus of N-A-S-H gels is stable at 11 – 12 GPa during the curing ages between 1 d and 28 d, while the elastic moduli of N-C-A-S-H gels and C-A-S-H gels are increased steadily from 19 GPa to 23 GPa and from 28 GPa to 35 GPa, respectively. Meanwhile, the elastic moduli of unreacted slag and fly ash are decreased steadily. According to the NMR analysis presented in Table 4-4, the chemical composition of N-A-S-H gels is stable during the curing process, in which the Al/Si ratio is steady at around 0.5. Such stable composition might be associated with their constant elastic modulus. Besides, it can be seen from the FTIR results in Figure 4-16 that the position of the main band for reaction products in AAFS paste (i.e. 980 cm^{-1}) is at lower wavenumber than that in AAF paste based solely on fly ash (i.e. 1020 cm^{-1}), indicating that the presence of Ca released from slag would affect the formation of N-A-S-H gels (Ismail et al., 2014). The presence of Ca tends to hinder the crystallization of N-A-S-H gels and leads to a high level of structural disorder, resulting in a relatively low elastic modulus of N-A-S-H gels (Ye and Radlińska, 2016). In comparison, the change in chemical composition of C-A-S-H gels is obvious, where the Al/Si ratio is increased significantly from 0.29 to 0.40. This suggests that the silicate tetrahedron of C-A-S-H solid gel particles would be substituted by the aluminate species during the reaction process, which is consistent with the FTIR observations. As shown in Figure 4-16, the band of Al-O-Si bonds within C-A-S-H gels becomes sharper with the increase of curing ages, implying the higher Al content within the silica network of C-A-S-H gels (Walkley et al., 2016b). In addition, the internal structure of C-A-S-H gels is also changed apparently during the curing process. As seen in Figure 4-14, the amount of Q^1 sites is decreased dramatically from 18.15% to 7.09% as the curing age increases from 1 d to 28 d, while the content of Q^2(1Al) sites is increased from 25.41% to 28.06%. These structural changes would increase the Q sites connectivity, the cross-linking degree and the crystalline order (Yang et al., 2018). Furthermore, the packing density of C-A-S-H gels might be also changed with the increase of curing age. It is known that the C-A-S-H particles are linked together by condensation (Fernández-Jiménez et al., 2003; Lecomte et al., 2006) and the packing efficiency at the surface of particles would be improved with the progress of reaction, giving a high value of density and filling the pore space. These multiple effects known as the chemical composition and internal structure in C-A-S-H gels would consequently improve their elastic modulus. Furthermore, the internal structure of N-C-A-S-H gels is also altered during the reaction process. The silicate

tetrahedron of N-C-A-S-H solid gel particles would be also substituted by the aluminate species during reaction process, corresponding to the increase of Al/Si ratio of N-C-A-S-H gels from 0.20 to 0.29. These structural changes are related to the improvement of elastic modulus in N-C-A-S-H gels. The slight decline of elastic moduli of unreacted slag and fly ash can be explained by the decrease of particle size due to the artificial influence in sample preparation. The slag and fly ash particles with a lower size would substantially have a higher surface-to-volume ratio, which may promote the precipitation of reaction products on the surface of these particles. The relatively soft matrix (i.e. reaction products) attached on the surface of particles would change the load-displacement behaviour of particles during indentation loading, and consequently affect the elastic moduli of unreacted slag and fly ash.

Moreover, there are transformations between different reaction products during the reaction process, which would affect the evolution of their elastic moduli. As seen in Figure 5-12, the volume fraction of N-A-S-H gels is decreased from 65.01% to 54.76% at early 7 d, while the volume fraction of N-C-A-S-H gels is increased from 15.24% to 37.72%. This suggests that part of N-A-S-H gels have been transformed to N-C-A-S-H gels via interchanging between Ca and Na, due to the strong polarising power of the aqueous Ca ion relative to the Na ion (Garcia-Lodeiro et al., 2011). The substitution of Ca would drive the precipitation of N-C-A-S-H solid gel and contribute to the development of a comparable structure to C-A-S-H solid gel, leading to a higher elastic modulus (Garcia-Lodeiro et al., 2011; Ismail et al., 2014). At later curing ages (7 ~ 28 d), the volume fraction of N-A-S-H gels increases significantly from 54.76% to 77.98%, which implies that the effects of mobile Ca ion on the formation of N-A-S-H gels become less. This is mainly because of the reduction of free Ca releasing from slag due to the low content of slag (25% of the total precursors). At the same time, the volume fraction of N-C-A-S-H gels is decreased from 37.72% to 9.43%, while that of C-A-S-H gels is increased from 3.28% to 12.59%. This indicates the transformation between N-C-A-S-H gels and C-A-S-H gels, where the Na in N-C-A-S-H gels is continually replaced by Ca and eventually leads to the formation of C-A-S-H gels (García-Lodeiro et al., 2013). However, it is worth noting that the transformation from N-C-A-S-H gels to N-A-S-H gels is difficult to happen due to the strong binding of Ca within N-C-A-S-H gels. During the formation of N-C-A-S-H gels, the polarising effect of Ca ion would distort the Si-O-Al bonds and subsequently form the stable Si-O-Ca bonds (García-Lodeiro et al., 2010). These stable Si-O-Ca bonds are difficult to be distorted by the presence of Na ion, because the polarising power of Na ion is weaker than that of Ca ion.

6.3 Level II: Gel matrix + unreacted particle + capillary pore → paste

According to the experimental results obtained from nanoindentation, MIP and SEM tests as well as the theoretical results based on the self-consistent continuum micromechanics model, the effective mechanical properties of paste matrix at Level II is mainly dominated by two factors that exist at different scales: (1) the microscopic properties of gel matrix at Level I, and (2) the characteristics of pore structure at Level II (Constantinides and Ulm, 2004).

Regarding the gel matrix (i.e. reaction products), the micromechanical properties of reaction products are expected to determine the macroscopic performance of paste matrix as the reaction products dominate the volumetric proportion of paste matrix. As shown in Figure 6-1a, the overall elastic modulus of reaction products is fluctuant between 16.62 GPa and 17.62 GPa as the curing age increases from 1 d to 28 d. This phenomenon is similar to the development of elastic modulus in N-A-S-H gels but is different compared with the development in N-C-A-S-H gels and C-A-S-H gels. The elastic modulus of N-A-S-H gels is fluctuant between 11 GPa and 12 GPa. Nevertheless, the elastic moduli of N-C-A-S-H gels and C-A-S-H gels are increased from 19 GPa to 23 GPa and from 28 GPa to 35 GPa, respectively. This suggests that the overall elasticity of reaction products is primarily represented by the elastic moduli of N-A-S-H gels. It is mainly because of the existence of high-volume N-A-S-H gels, in which their volume occupies 54.76 ~ 77.98% of AAFS paste (see Figure 5-12). Furthermore, it can be seen from the data in Table 5-6 that the overall homogenised elastic modulus of AAFS paste is also fluctuant during the curing process. The effective elastic modulus and bulk modulus of AAFS paste fluctuate in the range of 14.69 ~ 16.80 GPa and 8.16 ~ 9.33 GPa, respectively, while the effective shear modulus is stable at 6.12 ~ 7.00 GPa. This indicates that the macroscopic elasticity of AAFS paste has a strong relation with the elasticity of reaction products. Besides, since the N-A-S-H gels dominate the volumetric proportions of reaction products, their contribution to the macroscopic elastic performance is therefore significant. It implies that the volume fraction of different reaction products would also affect the macroscopic elasticity of AAFS paste. However, the connection between the hardness of reaction products and macroscopic strength of AAFS paste is not strong. As seen in Figure 6-1b, the overall hardness of reaction products is increased slightly from 1.02 GPa to 1.45 GPa with the increase of curing age from 1 d to 28 d, which is different compared with the rigorous increase of compressive strength in AAFS paste. The compressive strength is increased dramatically from 18.5 MPa to 53.7 MPa with increasing curing age from 1

d to 28 d (Tu et al., 2019). In summary, the macroscopic mechanical properties of AAFS paste at Level II is highly dependent on the micromechanical properties of reaction products at Level I. The elastic modulus of reaction products and their relative volumetric proportions mainly determine the macroscopic elasticity of AAFS paste.

Regarding the pore structure, the change in pore size and porosity would directly affect the development of macroscopic mechanical properties of AAFS paste (Keulen et al., 2018). As seen in Figure 4-41, the total porosity of AAFS paste is decreased dramatically from about 28% to 10% at early curing ages (< 7 d). Meantime, the pore size is refined continuously during these early ages. Afterwards, the pore structure is changed slightly during the later curing ages between 7 d and 28 d. The developing trend of pore structure is similar to that of compressive strength in AAFS paste. According to the previous research (Tu et al., 2019), the compressive strength increases significantly from 18.5 MPa to 39.8 MPa between 1 d and 7 d, while it increases less significantly from 39.8 MPa to 53.7 MPa between 7 d and 28 d. This implies that the refinement of pore structure might be associated with the improvement of compressive strength, which is consistent with other research (Tatar et al., 2019). Nevertheless, the effects of pore structure on the macroscopic elasticity of paste matrix are less significance. The effective elastic modulus, bulk modulus and shear modulus of AAFS paste are fluctuant during the curing process (see Table 5-6), which are different compared with the continued refinement of pore structure (see Figure 4-41). The characteristic of pore structure at Level II would affect the mechanical properties of AAFS paste, in which the porosity and pore size distribution play a dominant role in affecting the compressive strength of AAFS paste.

The discussion presented above demonstrates that the macroscopic performance of AAFS paste is highly dependent on the microscopic properties of reaction products and the features of pore structure. The macroscopic elasticity is primarily influenced by the elasticity of reaction products and their relative volumetric proportions, while the macroscopic strength is mainly determined by the porosity and pore size distribution.

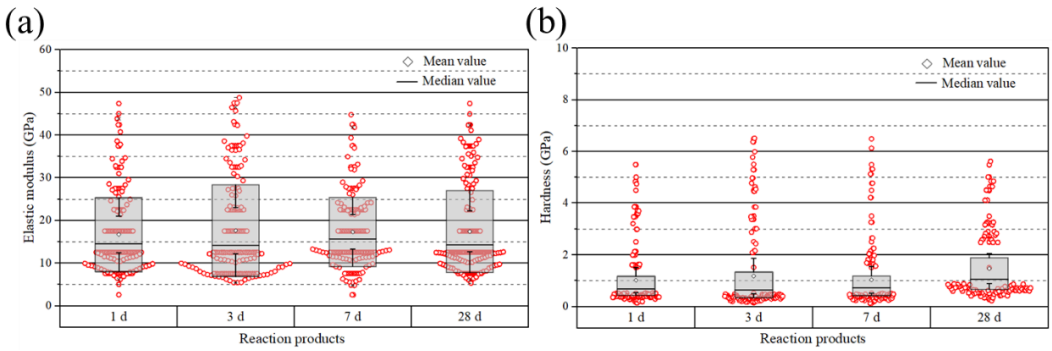

Figure 6-1 Elastic modulus and hardness of reaction products in AAFS paste at different curing ages

6.4 Level III: Paste + ITZ + aggregate → concrete

Concrete at Level III is generally considered as a three-phase composite consisting of paste matrix from Level II, aggregate and ITZ between aggregate and paste matrix. Therefore, the macroscopic mechanical properties of AAFS concrete are dependent on the microscopic properties of these three phases. Since the aggregates with stable chemical, physical and mechanical properties are kept constantly for each sample and expected to have a similar effect on the mechanical properties of PC concrete and AAFS concrete, this chapter will mainly discuss the effects of ITZ and paste matrix on the mechanical properties of AAFS concrete at different curing ages.

It is generally agreed that the microstructural and micromechanical properties of ITZ and paste matrix and their relative relationships would strongly affect the macroscopic properties of concrete such as strength, stiffness and fracture properties (Nili and Ehsani, 2015). This is mainly because of their relative weak nature with low strength in comparison with aggregate. In PC concrete, ITZ is considered as the weakest region in concrete and has a significant effect of the strength and fracture behaviour of concrete, due to its relatively low strength and high porosity compared to the surrounding paste (Ollivier et al., 1995; Scrivener et al., 2004; Mondal et al., 2009). The ITZ with low strength and stiffness is prone to cracking as a result of shrinkage or mechanical loading, which would consequently reduce the overall mechanical properties of concrete (Akçaoğlu et al., 2005; Zhang et al., 2018).

Nevertheless, the ITZ in AAFS concrete seems to play an entirely different role in governing the macroscopic properties of AAFS concrete. As shown in Figures 4-56 and 5-16, the porosity and mechanical properties (i.e. elastic modulus and hardness) of ITZ are comparable to those of paste matrix at different curing ages, indicating that ITZ is not the weakest region in AAFS concrete. This can be attributed to the formation of N-A-S-H gels and C-A-S-H gels instead of the CH crystals formed in PC concrete, which would enhance the bonding between aggregate and paste. The existence of compact and strong ITZ is expected to influence the failure mode of concrete under loading, due to the change of fracturing process, where the initiation and propagation of microcracks might not gather at ITZ. According to the numerical studies by previous research (Yu et al., 2018; Zhang et al., 2018), when the strength of ITZ approaches that of paste matrix, concrete can be considered as a two-phase medium made up of aggregate and paste. In this case, the microcracks will occur simultaneously at the ITZ and paste matrix and expand into a coalesced crack. Accordingly, the absence of weak region in AAFS concrete would help to improve its macroscopic mechanical strength, especially for the fracture properties. As

shown in Figure 3-19, the fracture energy of AAFS concrete is significantly higher than that predicted using the CEB-FIP model and the Bazant and Becq-Giraduon model used for the PC concrete, given the same compressive strength. This can be attributed to the presence of denser and stronger ITZ in AAFS concrete compared to the ITZ in PC concrete. It indicates that the macroscopic mechanical properties of AAFS concrete at Level III are affected by the microscopic properties of ITZ and paste matrix, especially the ITZ which acts a bridge transferring forces between aggregate and paste matrix. The ITZ with comparable microstructural and micromechanical properties to the paste matrix would help to improve the mechanical properties of AAFS concrete.

However, it should be noted that the quantification of the relationship between microstructure and mechanical properties is still a big challenge because that the microstructure and micromechanical properties of ITZ might vary from one location to another depending on the size and shape of aggregates. In this case, the quantification of microstructure-mechanical properties relationship of AAFS concrete needs a lot of tests in order to build a more reliable REV for the prediction of the macroscopic mechanical properties.

6.5 Concluding remarks

In this chapter, the microstructure-mechanical properties relationship in AAFS concrete at different multiple length scales was discussed. Based on the experimental results, the main conclusions can be drawn as follows:

- The microscopic properties of gel matrix at Level I are dependent on the structural disorder level of solid gel particles at Level 0 and the porosity of gel matrix at Level I. The solid phase with low level of structural disorder and gel porosity tends to have a high microscopic mechanical property. Here, the elastic modulus of individual solid phases follows an order of N-A-S-H gels < N-C-A-S-H gels < C-A-S-H gels < unreacted slag < unreacted fly ash. The unreacted fly ash and slag with highly dense nonactivated crystal solid have a higher elastic modulus than the reaction products. Due to their relatively low level of structural disorder and gel porosity, the C-A-S-H gels have the highest elastic modulus among the reaction products, followed by N-C-A-S-H gels and N-A-S-H gels.
- The change in chemical composition and internal structure of solid gel particles at Level 0 would affect the evolution of elastic modulus of solid phase at Level I. In detail: (1) The elastic modulus of N-A-S-H gels is stable at 11 ~ 12 GPa regardless of

curing age. It is associated with the stable chemical composition of N-A-S-H solid gel particles, in which the Al/Si ratio is steady at 0.5. Meanwhile, the presence of Ca released from slag would hinder the crystallization of N-A-S-H gels, which would lead to a high structural disorder level and a low elastic modulus. (2) The elastic modulus of C-A-S-H gels is increased from 28 GPa to 35 GPa as the curing age increases from 1 d to 28 d, which can be attributed to the increase of packing density, crystalline structure and cross-linking degree. These changes in structure are ascribed to the substitute of aluminate species, in which the Al/Si ratio is increased from 0.29 to 0.40. (3) The increase of elastic modulus of N-C-A-S-H gels from 19 GPa to 23 GPa is associated with their structure arrangement. During the reaction process, part of Na within N-C-A-S-H solid gel are replaced by Ca, which would drive the precipitation of N-C-A-S-H solid gel and contribute to the development of a structure comparable to C-A-S-H solid gel.

- The macroscopic performance of AAFS paste at Level II is highly dependent on the microscopic properties of reaction products at Level I and the characteristics of pore structure at Level II. The elasticity of reaction products and their relative volumetric proportions mainly determine the macroscopic elasticity, while the porosity and pore size distribution play a dominant role in affecting the macroscopic strength.
- The macroscopic mechanical properties of AAFS concrete at Level III are affected by the microscopic properties of ITZ and paste matrix, especially the ITZ which acts a bridge transferring forces between aggregate and paste matrix. The ITZ with comparable microstructural and micromechanical properties to the paste matrix would help to improve the mechanical properties of AAFS concrete.

Chapter 7 Conclusions and perspectives

7.1 Conclusions

In this thesis, the microstructure and mechanical properties of AAFS concrete at multiple length scales from level 0 (solid gel particle) to level III (concrete) were systematically investigated based on a series of experimental tests and statistical analysis. This research provides an in-depth understanding of reaction-microstructure-properties of AAFS concrete. The main research contributions and conclusions are given below.

7.1.1 Research contributions

The following contributions have been made to complement the existing knowledge of the microstructure and mechanical properties of AAFS concrete:

- The engineering properties of AAFS concrete are comprehensively investigated in this study considering the effects of main factors including fly ash/slag ratio, AL/P ratio, molarity of SH and SS/SH ratio, providing a thorough understanding of workability, setting time and mechanical properties of AAFS concrete cured at ambient curing conditions.
- The first-ever in-situ monitoring of the microstructure evolution of fly ash and slag particles in AAFS paste from the early age (1 d) to the later age (28 d) is given in this study, providing 3D morphological information of the surface and interior development of particles, which offers new insights into the reaction mechanism of these particles in AAFS paste.
- The microstructure evolution of ITZ in AAFS concrete from the very early age (3 h) to the later age (28 d) is systematically characterised in this study, indicating the morphology changes of unreacted particles, reaction products and pores in ITZ, which provides needed insights into the mechanism of ITZ evolution.
- The micromechanical analysis of AAFS concrete at multiple length scales from Level I (gel matrix) to Level III (concrete) is performed in this study, which offers the first-hand information of micromechanical properties of individual phases in AAFS concrete and their contributions to the macroscopic mechanical properties of AAFS concrete.
- The multiscale relationships between chemistry, microstructure, and mechanical properties in AAFS concrete are discussed in depth in this study, which provides a better understanding of the effect of individual phase on the overall performance of AAFS concrete.

7.1.2 Concluding remarks

According to the experimental results, the main conclusions can be drawn as follows:

(i) Macroscopic mechanical properties of AAFS concrete

- The workability, setting time and mechanical properties (e.g. compressive strength, elastic modulus and fracture properties) of AAFS concrete are dominantly affected by the slag replacement level for fly ash and the content of AL. Generally, the AAFS concrete with a high content of slag and low content of AL has high mechanical strength, but its workability and setting time would be relatively low.
- The mixtures of AAFS concrete with slag replacement level ranging from 10% to 25%, AL/P ratio in the range of 0.45 ~ 0.50, 8 ~ 10 M of SH, SS with a modulus of 2.0 and SS/SH ratio of 2.0 are suggested as the optimal mixtures to achieve the desired performance in terms of acceptable workability, suitable setting time and high compressive strength.

(ii) Multiscale microstructure of AAFS concrete

- The polymerisation degree and cross-linking of solid gels are improved over curing age, potentially through the initial formation of C-A-S-H gels followed by the gradual development of N-A-S-H and N-C-A-S-H gels with a higher cross-linking degree. During the curing process, the chemical composition of N-A-S-H gels is stable with a Al/Si ratio of around 0.5, whereas that of C-A-S-H gels and N-C-A-S-H gels are changed from 0.29 to 0.40 and from 0.20 to 0.29, respectively, along with the substitute of aluminate species.
- The dissolutions of fly ash and slag particles are not uniform due to their inherently heterogeneous characteristics, which would consequently lead to the formation of non-uniform reaction products, mostly accumulating within the boundary of the original particles (i.e. inner products). The inner reaction products would naturally build a physical barrier between the unreacted particles and the outside solution, which would inhibit the further reactions of fly ash and slag particles. In addition, the interactions between fly ash and slag particles exist in AAFS during chemical reactions, where the presence of slag would accelerate the microstructure evolution of fly ash at later curing ages (7 ~ 28 d).
- The ITZ in AAFS concrete originates from the so-called ‘wall effect’, which would lead to the deficit of large grains adjacent to aggregate and subsequently result in a higher effective activator to precursor ratio in ITZ than that in paste matrix. The alkaline reaction process is correspondingly accelerated in ITZ, which promotes the

formation of reaction products and reduces the porosity in this region. Afterwards, more reaction products are generated due to the dissolution of fly ash and slag particles, resulting in the continuous refinement of pores. Consequently, a compact and dense microstructure is formed in the ITZ at 28 d, which would be beneficial to the long-term performance of AAFS concrete.

(iii) Multiscale micromechanical properties of AAFS concrete

- The elastic modulus of individual solid phases follows an order of N-A-S-H gels < N-C-A-S-H gels < C-A-S-H gels < unreacted slag < unreacted fly ash. The elastic modulus of N-A-S-H gels is stable at 11 ~ 12 GPa regardless of curing age, whereas that of N-C-A-S-H gels and C-A-S-H gels is increased from 19 GPa to 23 GPa and from 28 GPa to 35 GPa, respectively, as the increase of curing age from 1 d to 28 d.
- The effective elastic modulus and bulk modulus of AAFS paste are fluctuant in the range of 14.69 ~ 16.80 GPa and 8.16 ~ 9.33 GPa, respectively, while the effective shear modulus is stable between 6.12 GPa and 7 GPa in the curing ages of 1 ~ 28 d.
- The micromechanical properties of ITZ depend on the chemical composition of reaction products, where ITZ with a high proportion of N-C-A-S-H gels and C-A-S-H gels tends to have a high elastic modulus because of the superior micromechanical properties of these reaction products. The evolution of micromechanical properties of ITZ can be divided into three stages: (i) accelerated growth stage via fast chemical reactions (< 12 h); (ii) stationary stage via stable chemical reactions (12 h ~ 7 d); (iii) decrement stage via microcrack propagation (7 ~ 28 d).

(iv) Microstructure-mechanical properties relationship in AAFS concrete

- The gel matrix with a low level of structural disorder and gel porosity tends to have a high microscopic mechanical property. The N-A-S-H gels have a relatively low elastic modulus due to their high level of structural disorder and gel porosity, while the C-A-S-H gels and N-C-A-S-H gels with a low level of structural disorder and gel porosity have a relatively high elastic modulus.
- The elasticity of reaction products and their relative volumetric proportions mainly determine the macroscopic elasticity of AAFS paste, while the porosity and pore size distribution primarily condition its macroscopic strength.
- The ITZ with a comparable microstructure and mechanical properties to the paste matrix in AAFS concrete would help to improve its macroscopic mechanical strength, especially for the fracture properties. The fracture energy of AAFS concrete is obviously higher than that of PC concrete, given similar compressive strength.

7.2 Perspectives

Although the multiscale characterisation of microstructure and mechanical properties of AAFS concrete has been presented in this thesis, some important aspects about the assessment of environmental impacts, the effects of raw materials, and the characterisation of long-term performance as well as the feasibility research of engineering application should be further explored in the future. The limitations and the associated future work aligned with the research developed in this thesis are highlighted below.

- The AAFS concrete has been regarded as a great alternative to PC concrete due to its potential low environmental impacts. Up to now, many studies have been conducted to quantify the environmental implications of AAFS concrete. However, there is still lack of systematic life cycle assessment (LCA) on the application of AAFS concrete with different mixtures, from raw materials acquisition to final disposition. The LCA can provide a thorough understanding of the potential environmental impacts of this new type of concrete and help to optimise the mix design and mitigate the environmental impacts. Thus, the LCA of AAFS concrete should be conducted in the future research.
- In this study, the commercial fly ash and slag are selected as raw materials to produce AAFS concrete with desired workability, setting time and mechanical properties. However, it should be noted that the natural characteristics of raw materials (i.e., fly ash and slag) vary from one place to another depending on the manufacturing process of industry. The physical properties (e.g., particle size distribution), the mineralogical characteristics (e.g., content of amorphous phases) and the chemical compositions (e.g., $[SiO_2]/[Al_2O_3]$ ratio of fly ash) of fly ash and slag will condition the reaction process and the formation of reaction products and consequently affect the overall performance of AAFS concrete. The change of raw materials might alter the results presented in this research. Therefore, it is important to investigate the effects of different types of fly ash and slag on the properties of AAFS concrete in the future.
- The commonly used alkaline activators (i.e. sodium hydroxide solution and sodium silicate solution) are applied as raw materials in this study to produce the AAFS concrete with desired workability, setting time and mechanical properties. However, the AAFS concrete activated by these activators has some potential issues. For instance, the problem of efflorescence can be found in the AAFS concrete activated

by the highly concentrated sodium hydroxide solution due to reaction between the excess alkali and the atmospheric CO_2. Therefore, it is important to investigate the application of other types of activator with relative low alkali such as sodium carbonate solution and sodium sulphate solution in the AAFS concrete.

- In this study, an optimal mixture based on the performance of workability, setting time and compressive strength is used to evaluate the multiscale microstructure and mechanical properties of AAFS concrete, which can provide some valuable information about the development of microstructure and micromechanical properties. Nevertheless, it is worth noting that the change of mix proportions would affect the chemical reaction process and the evolution of microstructure of AAFS concrete, which would consequently influence the development of micromechanical properties. Hence, the impacts of different mix proportions on the microstructure and micromechanical properties of AAFS concrete should be considered in the future work.
- It is known that the properties of aggregate (i.e. size, shape, surface texture and mineralogy) would strongly affect the formation of ITZ between aggregate and paste matrix, which would influence the microstructural and micromechanical properties of ITZ and consequently affect the macroscopic performance of AAFS concrete. Thus, it is vital to investigate the effects of aggregate properties on the development of microstructure and mechanical properties of AAFS concrete, which are not considered in this research.
- The relationship between microstructure and mechanical properties of AAFS concrete at early ages up to 28 d was investigated in this study. However, it should be noted that the microstructure can be changed over curing age due to the on-going chemical reaction, which may affect the development of mechanical properties of AAFS concrete at long-term age, such as 1 year or longer. Thus, a deep understanding of the multiscale microstructure-mechanical properties relationship in AAFS concrete at long-term period is extremely needed. In addition, durability of AAFS concrete under different environmental conditions is another key aspect that needs to be further investigated to enable the long-term use of these new material. The changes in the phase compositions and microstructure within AAFS concrete under the effect of aggressive environments should be investigated in the future for a better understanding of their long-term performance.
- In this study, the optimal mixtures of AAFS concrete have been identified to fulfil the requirement of engineering application of non-structural concrete (e.g., road),

regarding the workability, setting time and compressive strength. However, it is unknown whether this new type of concrete is suitable for the structural application (e.g., reinforced concrete structure) due to uncertain corrosion resistance of steel in this concrete. Thus, it is vital to investigate the corrosion behaviour of reinforced AAFS concrete in the future.

Appendixes

Appendix A. Phase segmentation for different fly ash particles

Additional information about the phase identification for different fly ash particles is presented in Table A and Figure A.

Table A Threshold values for phases identification in different fly ash particles

Particle No.	Unreacted fly ash	Inner products	Outer products	Paste matrix
Particle 1 (d_{Eq} = 56.59 μm)	255	255 ~ 175	175 ~ 100	100
Particle 2 (d_{Eq} = 41.30 μm)	153	153 ~ 146	146 ~ 99	99
Particle 3 (d_{Eq} = 28.14 μm)	150	150 ~ 140	140 ~ 100	100
Particle 4 (d_{Eq} = 16.63 μm)	163	163 ~ 152	152 ~ 94	94
Particle 5 (d_{Eq} = 12.93 μm)	233	233 ~ 222	222 ~ 104	104

Note: d_{Eq} is the spherical equivalent diameter.

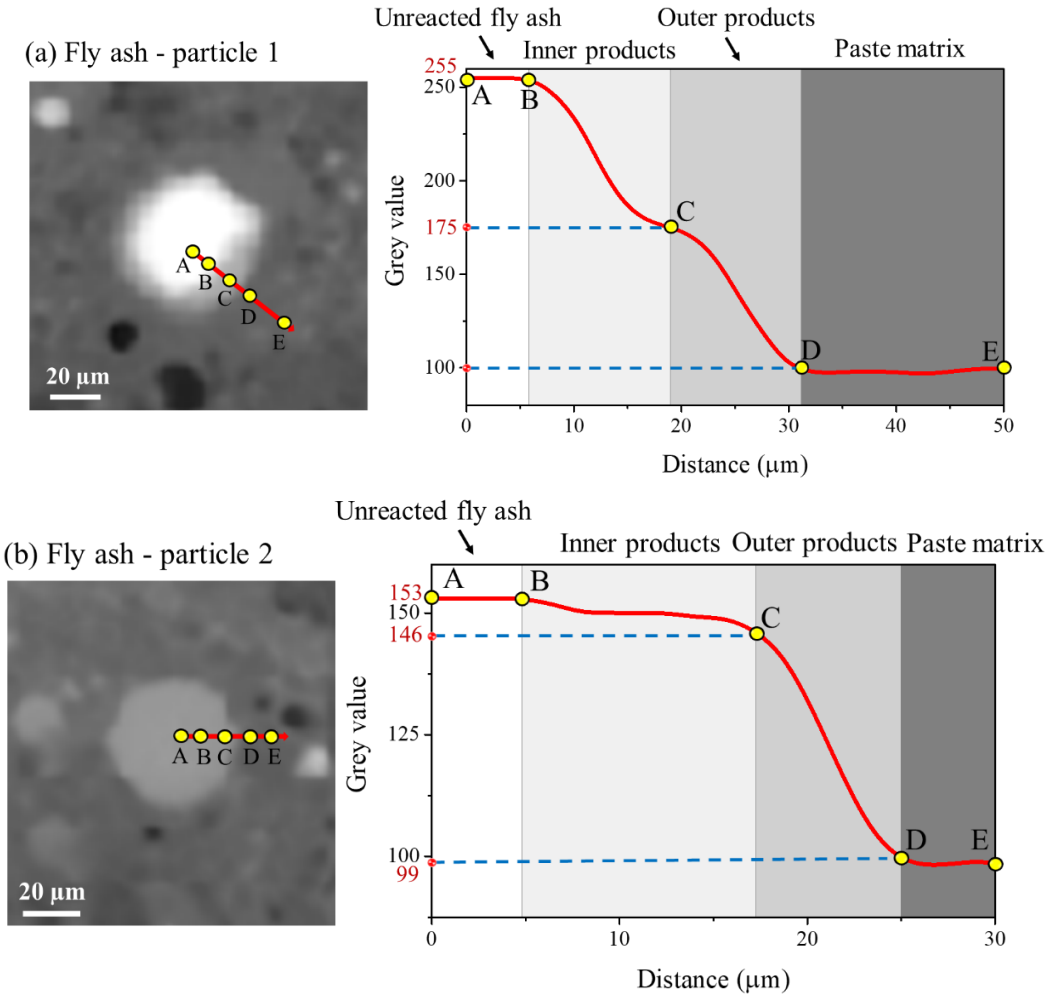

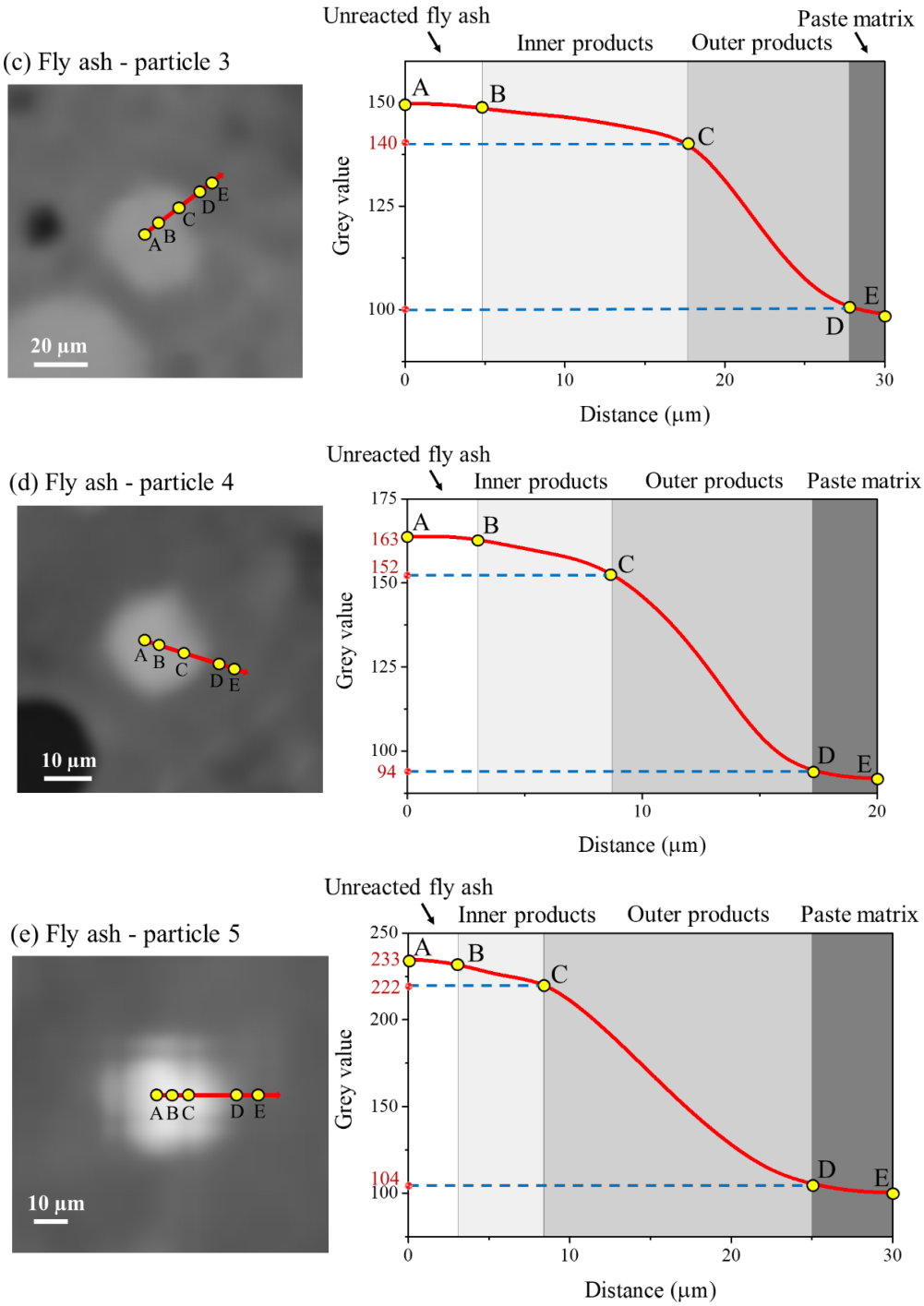

Figure A Phase identification of different fly ash particles (t = 7 d)

Appendix B. Phase segmentation for different slag particles

Additional information about the phase identification for different slag particles is presented in Table B and Figure B.

Table B Threshold values for phases identification in different slag particles

Particle No.	Unreacted slag	Inner products	Outer products	Paste matrix
Particle 1 (d_{Max}= 74.76 μm)	160	160 ~ 132	132 ~ 94	94
Particle 2 (d_{Max}= 64.22 μm)	203	203 ~ 175	175 ~ 97	97
Particle 3 (d_{Max}= 36.04 μm)	177	177 ~ 165	165 ~ 110	110
Particle 4 (d_{Max}= 21.42 μm)	165	165 ~ 156	156 ~ 110	110
Particle 5 (d_{Max}= 9.48 μm)	150	150 ~ 142	142 ~ 105	105

Note: d_{Maz} is the maximum distance between two points in the original boundary of the central slice.

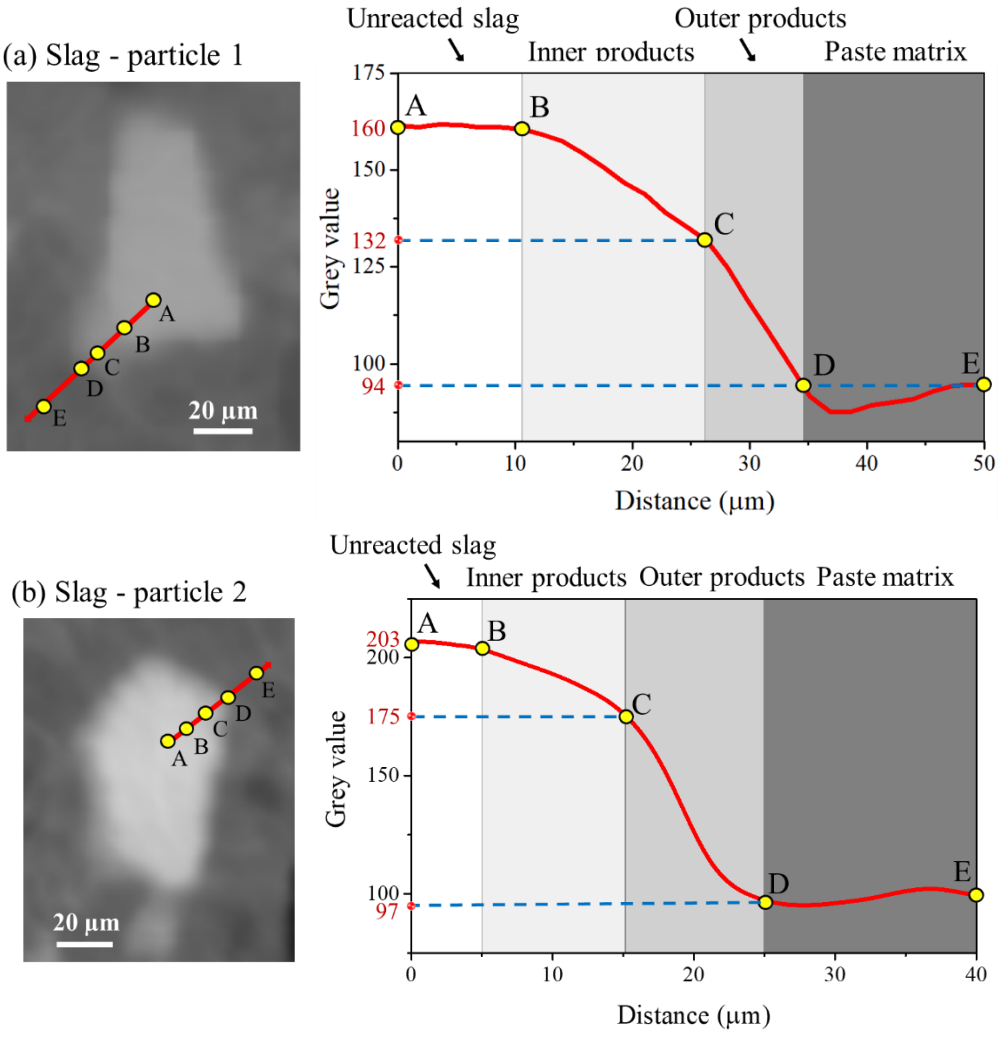

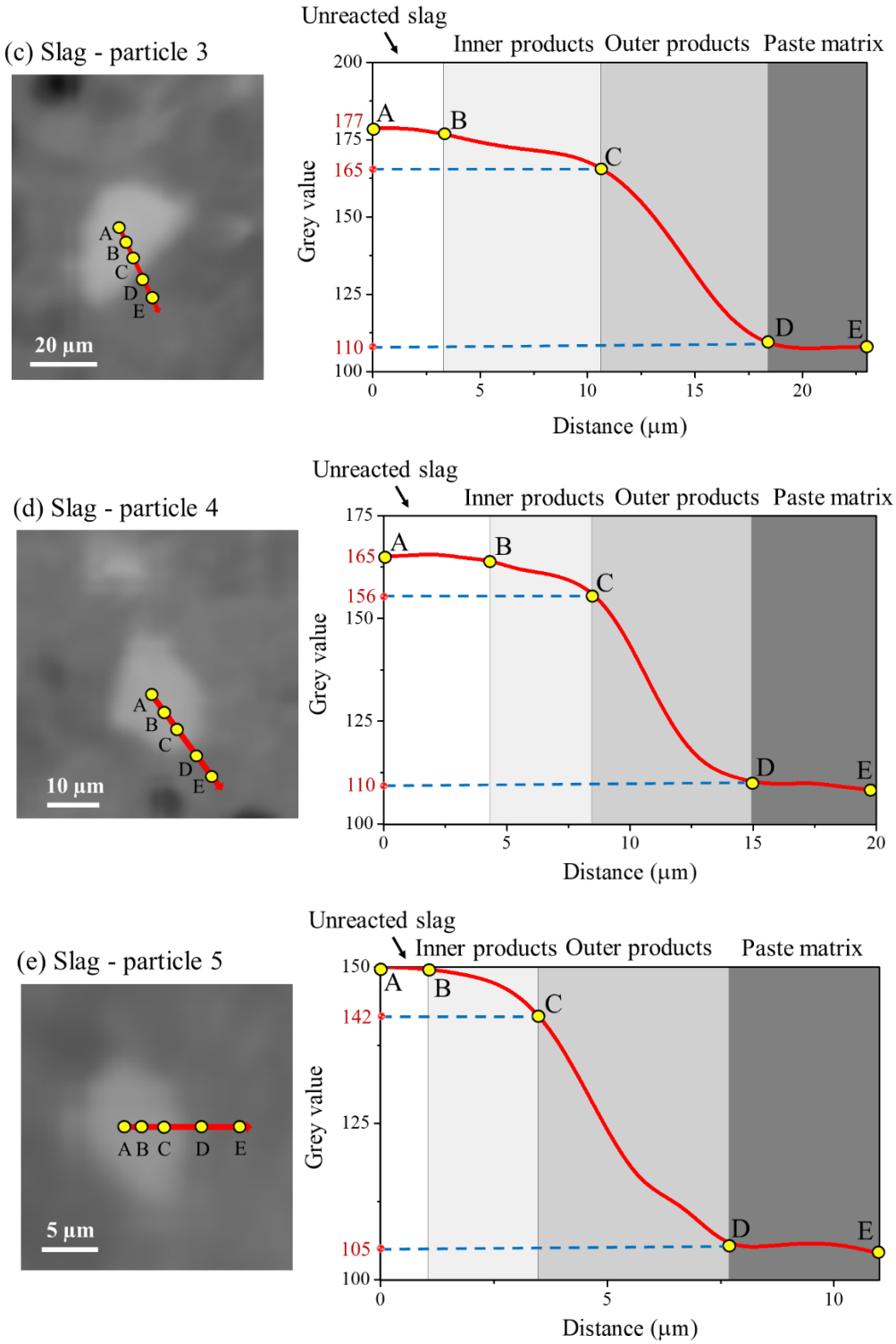

Figure B Phase identification of different slag particles (t = 1 d)

Appendix C. Phase segmentation for different AAFS samples

Additional information about the phase identification for AAFS samples at different curing ages is shown in Figure C.

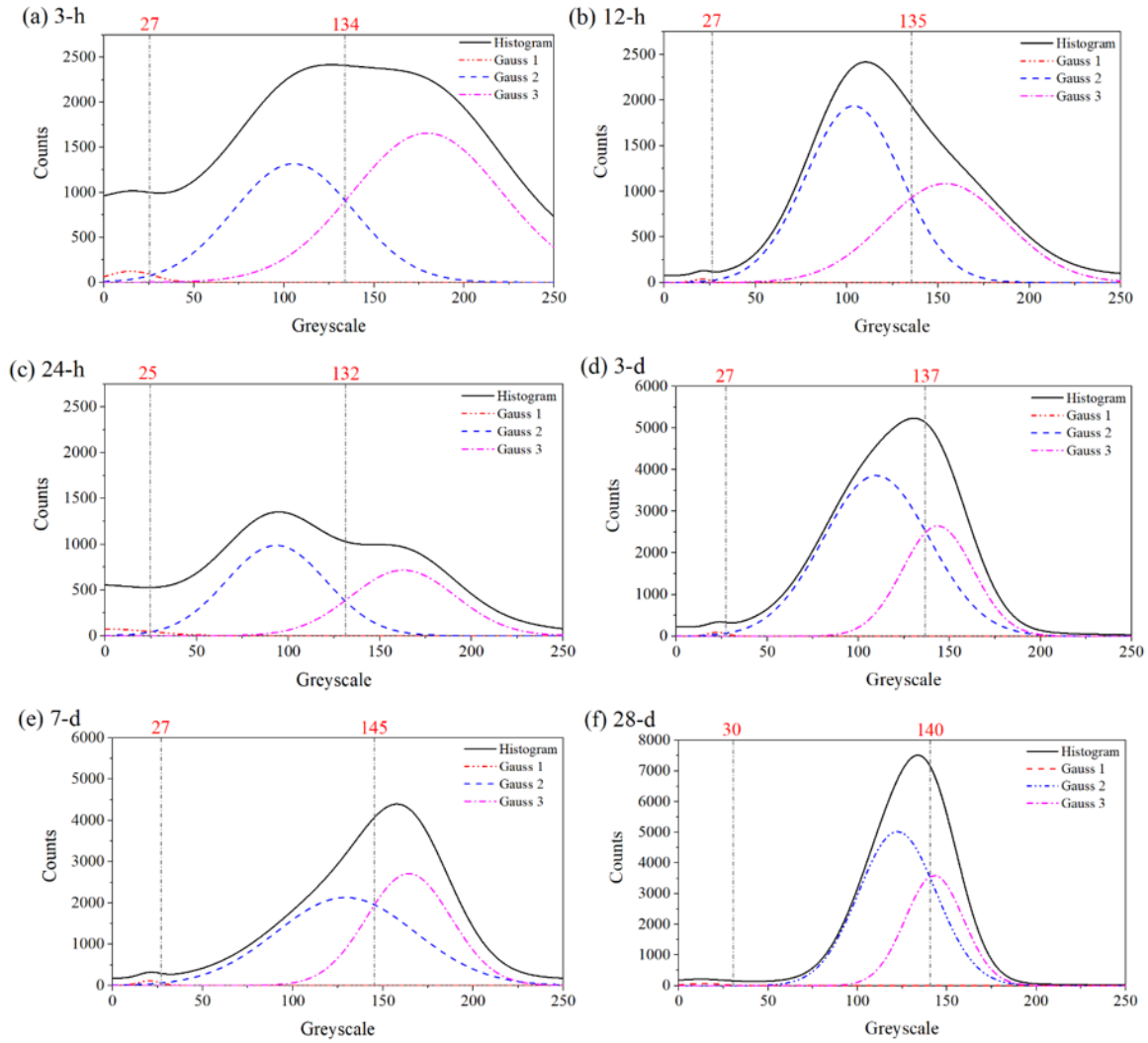

Figure C Determination of threshold values for AAFS samples at different curing ages

List of publications

Peer-Reviewed Journal Papers:

1. **Fang G.** and Zhang M. (2020) Multiscale micromechanical analysis of alkali-activated fly ash-slag paste, *Cement and Concrete Research*, 135, pp 106141.

2. **Fang G.** and Zhang M. (2020) The evolution of interfacial transition zone in alkali-activated fly ash-slag concrete, *Cement and Concrete Research*, 129, pp 105963.

3. **Fang G.** and Zhang M. (2020) In-situ X-ray tomographic image of microstructure evolution of fly ash and slag particles in alkali-activated fly ash-slag paste, *Cement and Concrete Research*, under review.

4. **Fang G.**, Wang Q. and Zhang M. (2020) Micromechanical analysis of interfacial transition zone in alkali-activated fly ash-slag concrete, *Cement and Concrete Composite*, minor correction.

5. **Fang G.,** Ho W.K., Tu W. and Zhang M. (2018) Workability and mechanical properties of alkali-activated fly ash-slag concrete cured at ambient temperature, *Construction and Building Materials*, 172, pp 476-487.

6. **Fang G.,** Bahrami H. and Zhang M. (2018) Mechanisms of autogenous shrinkage of alkali-activated fly ash-slag pastes cured at ambient temperature within 24 h, *Construction and Building Materials*, 171, pp 377-387.

7. Tu W., Zhu Y., **Fang G.,** Wang X. and Zhang M. (2019) Internal curing of alkali-activated fly ash-slag pastes using superabsorbent polymer, *Cement and Concrete Research*, 116, pp 179-190.

Conference Papers:

1. **Fang G.,** Tu W., Zhu Y. and Zhang M. (2018) Shrinkage characteristics of alkali-activated fly ash-slag pastes with impact of internal curing, *RILEMWEEK 2018*, 26-29 August 2018, TU Delft, Delft, The Netherlands.

2. **Fang G.** and Zhang M. (2017) Autogenous shrinkage of alkali-activated fly ash/slag paste, *37th Cement and Concrete Science Conference*, 11-12 September 2017, University College London, London, UK.

Bibliography

Abdalqader, A. F., Jin, F. & Al-Tabbaa, A. 2016. Development of greener alkali-activated cement: utilisation of sodium carbonate for activating slag and fly ash mixtures. *Journal of Cleaner Production,* 113(Supplement C)**,** pp 66-75.

Aboudi, J., Arnold, S. M. & Bednarcyk, B. A. 2013. Chapter 3 - Fundamentals of the Mechanics of Multiphase Materials. *In:* Aboudi, J., Arnold, S. M. & Bednarcyk, B. A. (eds.) *Micromechanics of Composite Materials.* Oxford: Butterworth-Heinemann.

ACI M318-08. 2008. Building Code Requirements for Structural Concrete and Commentary, American Concrete Institude.

Adrien, J., Meille, S., Tadier, S., Maire, E. & Sasaki, L. 2016. In-situ X-ray tomographic monitoring of gypsum plaster setting. *Cement and Concrete Research,* 82, pp 107-116.

Aïtcin, P.-C. 2000. Cements of yesterday and today: Concrete of tomorrow. *Cement and Concrete Research,* 30(9)**,** pp 1349-1359.

Akçaoğlu, T., Tokyay, M. & Çelik, T. 2004. Effect of coarse aggregate size and matrix quality on ITZ and failure behavior of concrete under uniaxial compression. *Cement and Concrete Composites,* 26(6)**,** pp 633-638.

Akçaoğlu, T., Tokyay, M. & Çelik, T. 2005. Assessing the ITZ microcracking via scanning electron microscope and its effect on the failure behavior of concrete. *Cement and Concrete Research,* 35(2)**,** pp 358-363.

Al-majidi, M., Lampropoulos, A. & Cundy, A. B. 2016. Effect of alkaline activator, water, superplasticiser and slag contents on the compressive strength and workability of slag-fly ash based geopolymer mortar cured under ambient temperature. *World Journal of Engineering and Technology,* 10(3)**,** pp 5.

Alanazi, H., Hu, J. & Kim, Y. R. 2019. Effect of slag, silica fume, and metakaolin on properties and performance of alkali-activated fly ash cured at ambient temperature. *Construction and Building Materials,* 197, pp 747-756.

Aligizaki, K. K. 2005. *Pore Structure of Cement-Based Materials: Testing, Interpretation and Requirements*: CRS Press.

Antoni, A., Halim, J. G., Kusuma, O. C. & Hardjito, D. 2017. Optimizing Polycarboxylate Based Superplasticizer Dosage with Different Cement Type. *Procedia Engineering,* 171, pp 752-759.

Antonić, T., Čižmek, A., Kosanović, C. & Subotić, B. 1993. Dissolution of amorphous aluminosilicate zeolite precursors in alkaline solutions. Part 1. - Kinetics of the dissolution. *Journal of the Chemical Society, Faraday Transactions,* 89(11)**,** pp 1817-1822.

Arbi, K., Nedeljkovic, M., Zuo, Y., Grünewald, S., Keulen, A. & Ye, G. 2015. Experimental study on workability of alkali activated fly ash and slag-based geopolymer concretes. *Geopolymers Route to Elimin. Waste Emiss. Ceram. Cem. Manuf.,* pp 75-78.

ASTM C143-15a. 2015. Standard Test Method for Slump of Hydraulic-Cement Concrete, ASTM International. West Conshohocken, PA.

ASTM C191-08. 2008. Standard Test Methods for Time of Setting of Hydraulic Cement by Vicat Needle, American Society for Testing and Materials, ASTM International. West Conshohocken, PA.

ASTM C230-14. 2014. Standard specification for flow table for use in tests of hydraulic cement, ASTM International. West Conshohocken, PA.

Bae, S., Meral, C., Oh, J.-e., Moon, J., Kunz, M. & Monteiro, P. J. M. 2014. Characterization of morphology and hydration products of high-volume fly ash paste by monochromatic scanning x-ray micro-diffraction (μ-SXRD). *Cement and Concrete Research,* 59, pp 155-164.

Barnes, B. D., Diamond, S. & Dolch, W. L. 1979. Micromorphology of the interfacial zone around aggregates in portland cement mortar. *Journal of the American Ceramic Society,* 62(1 - 2)**,** pp 21-24.

Bažant, Z. P. & Becq-Giraudon, E. 2002. Statistical prediction of fracture parameters of concrete and implications for choice of testing standard. *Cement and Concrete Research,* 32(4)**,** pp 529-556.

Bentur, A., Alexander, M. G. & Comm, R. T. 2000. A review of the work of the RILEM TC 159-ETC: Engineering of the interfacial transition zone in cementitious composites. *Materials and Structures,* 33(226)**,** pp 82-87.

Bentz, D. P. 2009. Influence of internal curing using lightweight aggregates on interfacial transition zone percolation and chloride ingress in mortars. *Cement and Concrete Composites,* 31(5)**,** pp 285-289.

Beppu, M., Miwa, K., Itoh, M., Katayama, M. & Ohno, T. 2008. Damage evaluation of concrete plates by high-velocity impact. *International Journal of Impact Engineering,* 35(12)**,** pp 1419-1426.

Beran, A., Voll, D. & Schneider, H. 2001. Dehydration and structural development of mullite precursors: an FTIR spectroscopic study. *Journal of the European Ceramic Society,* 21(14)**,** pp 2479-2485.

Bernal, S. A., Mejía de Gutiérrez, R., Pedraza, A. L., Provis, J. L., Rodriguez, E. D. & Delvasto, S. 2011a. Effect of binder content on the performance of alkali-activated slag concretes. *Cement and Concrete Research,* 41(1)**,** pp 1-8.

Bernal, S. A., Provis, J. L., Rose, V. & Mejía de Gutierrez, R. 2011b. Evolution of binder structure in sodium silicate-activated slag-metakaolin blends. *Cement and Concrete Composites,* 33(1)**,** pp 46-54.

Bernal, S. A., Provis, J. L., Walkley, B., San Nicolas, R., Gehman, J. D., Brice, D. G., Kilcullen, A. R., Duxson, P. & van Deventer, J. S. J. 2013. Gel nanostructure in alkali-activated binders based on slag and fly ash, and effects of accelerated carbonation. *Cement and Concrete Research,* 53, pp 127-144.

Bernard, O., Ulm, F.-J. & Lemarchand, E. 2003. A multiscale micromechanics-hydration model for the early-age elastic properties of cement-based materials. *Cement and Concrete Research,* 33(9)**,** pp 1293-1309.

Bewick, V., Cheek, L. & Ball, J. 2004. Statistics review 9: One-way analysis of variance. *Critical Care,* 8(2)**,** pp 130.

Borges, P. H. R., Banthia, N., Alcamand, H. A., Vasconcelos, W. L. & Nunes, E. H. M. 2016. Performance of blended metakaolin/blastfurnace slag alkali-activated mortars. *Cement and Concrete Composites,* 71, pp 42-52.

Bossa, N., Chaurand, P., Vicente, J., Borschneck, D., Levard, C., Aguerre-Chariol, O. & Rose, J. 2015. Micro- and nano-X-ray computed-tomography: A step forward in the characterization of the pore network of a leached cement paste. *Cement and Concrete Research,* 67, pp 138-147.

Brisard, S., Serdar, M. & Monteiro, P. J. M. 2020. Multiscale X-ray tomography of cementitious materials: A review. *Cement and Concrete Research,* 128, pp 105824.

Brough, A. R. & Atkinson, A. 2000. Automated identification of the aggregate-paste interfacial transition zone in mortars of silica sand with Portland or alkali-activated slag cement paste. *Cement and Concrete Research,* 30(6)**,** pp 849-854.

Brough, A. R. & Atkinson, A. 2002. Sodium silicate-based, alkali-activated slag mortars: Part I. Strength, hydration and microstructure. *Cement and Concrete Research,* 32(6)**,** pp 865-879.

Brown, L., Allison, P. G. & Sanchez, F. 2018. Use of nanoindentation phase characterization and homogenization to estimate the elastic modulus of heterogeneously decalcified cement pastes. *Materials & Design,* 142, pp 308-318.

BS EN 196-1:2016. 2016. Method of testing cement Part 1: Determination of strength, BSI Standards Publication.

BS EN 197-1:2011. 2011. Cement part 1: Composition, specifications and conformity criteria for common cements, BSI Standards Publication.

BS EN 206:2013+A1:2016. 2016. Concrete — Specification, performance, production and conformity, BSI Standards Publication.

BS EN 12390-3:2009. 2009. Testing hardened concrete Part 3: Compressive strength of test specimens, BSI Standards Publication.

BS EN 12390-6:2009. 2009. Testing hardened concrete-Part 6: Tensile splitting strength of test specimens, BSI Standards Publication.

BS EN 12390-13:2013. 2013. Testing hardened concrete-Part 13: Determination of secant modulus of elasticity in compression, BSI Standards Publication.

Buades, A., Coll, B. & Morel, J. M. 2005. A Review of Image Denoising Algorithms, with a New One. *Multiscale Modeling & Simulation,* 4(2)**,** pp 490-530.

Buckle, H. 1973. Applications to other material properties. *In:* Westbrook, J. H. & Conrad, H. (eds.) *The science of hardness testing and its applications.* Ohio.

CEB-FIP Model Code. 1995. Comite Euro-International Du Beton.

Chancey, R. T., Stutzman, P., Juenger, M. C. G. & Fowler, D. W. 2010. Comprehensive phase characterization of crystalline and amorphous phases of a Class F fly ash. *Cement and Concrete Research,* 40(1)**,** pp 146-156.

Chen, J. J., Sorelli, L., Vandamme, M., Ulm, F.-J. & Chanvillard, G. 2010. A Coupled Nanoindentation/SEM-EDS Study on Low Water/Cement Ratio Portland Cement

Paste: Evidence for C–S–H/Ca(OH)2 Nanocomposites. *Journal of the American Ceramic Society,* 93(5)**,** pp 1484-1493.

Chen, M., Chen, W., Zhong, H., Chi, D., Wang, Y. & Zhang, M. 2019. Experimental study on dynamic compressive behaviour of recycled tyre polymer fibre reinforced concrete. *Cement and Concrete Composites,* 98, pp 95-112.

Chen, X., Wu, S. & Zhou, J. 2013. Experimental and modeling study of dynamic mechanical properties of cement paste, mortar and concrete. *Construction and Building Materials,* 47, pp 419-430.

Chen, X., Zhu, G., Zhou, M., Wang, J. & Chen, Q. 2018. Effect of Organic Polymers on the Properties of Slag-based Geopolymers. *Construction and Building Materials,* 167, pp 216-224.

Chindaprasirt, P., Jaturapitakkul, C. & Sinsiri, T. 2005. Effect of fly ash fineness on compressive strength and pore size of blended cement paste. *Cement and Concrete Composites,* 27(4)**,** pp 425-428.

Constantinides, G. 2006. *Invariant Mechanical Properties of Calcium-Silicate-Hydrates (C-S-H) in Cement-Based Materials: Instrumented Nanoindentation and Microporomechanical Modeling (PhD thesis).* Doctor of Philosophy, Massachusetts Institute of Technology.

Constantinides, G., Ravi Chandran, K. S., Ulm, F. J. & Van Vliet, K. J. 2006. Grid indentation analysis of composite microstructure and mechanics: Principles and validation. *Materials Science and Engineering: A,* 430(1)**,** pp 189-202.

Constantinides, G. & Ulm, F.-J. 2004. The effect of two types of C-S-H on the elasticity of cement-based materials: Results from nanoindentation and micromechanical modeling. *Cement and Concrete Research,* 34(1)**,** pp 67-80.

Constantinides, G. & Ulm, F.-J. 2007. The nanogranular nature of C–S–H. *Journal of the Mechanics and Physics of Solids,* 55(1)**,** pp 64-90.

Constantinides, G., Ulm, F.-J. & Van Vliet, K. 2003. On the use of nanoindentation for cementitious materials. *Materials and Structures,* 36(3)**,** pp 191-196.

Criado, M., Fernández-Jiménez, A. & Palomo, A. 2007. Alkali activation of fly ash: Effect of the SiO2/Na2O ratio: Part I: FTIR study. *Microporous and Mesoporous Materials,* 106(1–3)**,** pp 180-191.

Criado, M., Fernández-Jiménez, A. & Palomo, A. 2010. Alkali activation of fly ash. Part III: Effect of curing conditions on reaction and its graphical description. *Fuel,* 89(11)**,** pp 3185-3192.

CSI Progress Report. 2009. Recycling Concrete, https://docs.wbcsd.org/2009/07/CSI-RecyclingConcrete-FullReport.pdf,

Cwirzen, A. & Penttala, V. 2005. Aggregate–cement paste transition zone properties affecting the salt–frost damage of high-performance concretes. *Cement and Concrete Research,* 35(4)**,** pp 671-679.

da Silva, W. R. L., Němeček, J. & Štemberk, P. 2013. Application of multiscale elastic homogenization based on nanoindentation for high performance concrete. *Advances in Engineering Software,* 62-63, pp 109-118.

Das, S., Yang, P., Singh, S. S., Mertens, J. C. E., Xiao, X., Chawla, N. & Neithalath, N. 2015. Effective properties of a fly ash geopolymer: Synergistic application of X-ray synchrotron tomography, nanoindentation, and homogenization models. *Cement and Concrete Research,* 78, pp 252-262.

Davydov, D., Jirásek, M. & Kopecký, L. 2011. Critical aspects of nano-indentation technique in application to hardened cement paste. *Cement and Concrete Research,* 41(1)**,** pp 20-29.

Deb, P. S., Nath, P. & Sarker, P. K. 2014. The effects of ground granulated blast-furnace slag blending with fly ash and activator content on the workability and strength properties of geopolymer concrete cured at ambient temperature. *Materials and Design,* 62, pp 32-39.

Deb, P. S., Nath, P. & Sarker, P. K. 2015. Drying shrinkage of slag blended fly ash geopolymer concrete cured at room temperature. *Procedia Engineering,* 125, pp 594-600.

Diamond, S. 2001. Considerations in image analysis as applied to investigations of the ITZ in concrete. *Cement and Concrete Composites,* 23(2)**,** pp 171-178.

Diamond, S. & Leeman, M. E. 2011. Pore Size Distributions in Hardened Cement Paste by Sem Image Analysis. *MRS Proceedings,* 370, pp 217.

Ding, Y., Dai, J.-G. & Shi, C.-J. 2018a. Fracture properties of alkali-activated slag and ordinary Portland cement concrete and mortar. *Construction and Building Materials,* 165, pp 310-320.

Ding, Y., Dai, J. & Shi, C. 2016. Mechanical properties of alkali-activated concrete: A state-of-the-art review. *Construction and Building Materials*, 127, pp 68-79.

Ding, Y., Shi, C.-J. & Li, N. 2018b. Fracture properties of slag/fly ash-based geopolymer concrete cured in ambient temperature. *Construction and Building Materials,* 190, pp 787-795.

Dong, B., Fang, G., Liu, Y., Dong, P., Zhang, J., Xing, F. & Hong, S. 2017. Monitoring reinforcement corrosion and corrosion-induced cracking by X-ray microcomputed tomography method. *Cement and Concrete Research,* 100, pp 311-321.

Durdziński, P. T., Dunant, C. F., Haha, M. B. & Scrivener, K. L. 2015. A new quantification method based on SEM-EDS to assess fly ash composition and study the reaction of its individual components in hydrating cement paste. *Cement and Concrete Research,* 73, pp 111-122.

Duxson, P., Provis, J. L., Lukey, G. C., Mallicoat, S. W., Kriven, W. M. & van Deventer, J. S. J. 2005. Understanding the relationship between geopolymer composition, microstructure and mechanical properties. *Colloids and Surfaces A: Physicochemical and Engineering Aspects,* 269(1)**,** pp 47-58.

Elices, M., Guinea, G. V. & Planas, J. 1992. Measurement of the fracture energy usign three-point bend tests: Part 3-Influence of cutting the P-σ tail. *Materials and Structures*, 25, pp 327-334.

Elsharief, A., Cohen, M. D. & Olek, J. 2003. Influence of aggregate size, water cement ratio and age on the microstructure of the interfacial transition zone. *Cement and Concrete Research,* 33(11)**,** pp 1837-1849.

Engelhardt, G. n. & Michel, D. 1987. *High-resolution solid-state NMR of silicates and zeolites*, Chichester: Wiley.

Escalante-García, J. I., Campos-Venegas, K., Gorokhovsky, A. & Fernández, A. 2006. Cementitious composites of pulverised fuel ash and blast furnace slag activated by sodium silicate: effect of Na2O concentration and modulus. *Advances in Applied Ceramics,* 105(4)**,** pp 201-208.

Escalante-García, J. I., Gorokhovsky, A. V., Mendoza, G. & Fuentes, A. F. 2003. Effect of geothermal waste on strength and microstructure of alkali-activated slag cement mortars. *Cement and Concrete Research,* 33(10)**,** pp 1567-1574.

Escalante García, J. I., K, C.-V., A, G. & A, F. 2006. Cementitious composites of pulverised fuel ashand blast furnace slag activated by sodium silicate:effect of

Na2O concentration and modulus. *Advances in Applied Ceramics,* 105(4)**,** pp 201-208.

Eshelby, J. D. The determination of the elastic field of an ellipsoidal inclusion, and related problems. Proceedings of the royal society London A, 1957, pp 376-396.

Eurocode 2 2004. Design of concrete structures-Part 1-2: General rules-Structural fire design. *European Standards, London*.

Fan, Y., Yin, S., Wen, Z. & Zhong, J. 1999. Activation of fly ash and its effects on cement properties. *Cement and Concrete Research,* 29(4)**,** pp 467-472.

Fang, G., Ding, W., Liu, Y., Zhang, J., Xing, F. & Dong, B. 2019. Identification of corrosion products and 3D distribution in reinforced concrete using X-ray micro computed tomography. *Construction and Building Materials,* 207, pp 304-315.

Fang, G., Liu, Y., Qin, S., Ding, W., Zhang, J., Hong, S., Xing, F. & Dong, B. 2018. Visualized tracing of crack self-healing features in cement/microcapsule system with X-ray microcomputed tomography. *Construction and Building Materials,* 179, pp 336-347.

Ferdous, W., Manalo, A., Khennane, A. & Kayali, O. 2015. Geopolymer concrete-filled pultruded composite beams – Concrete mix design and application. *Cement and Concrete Composites,* 58, pp 1-13.

Fernández-Jiménez, A. & Palomo, A. 2003. Characterisation of fly ashes. Potential reactivity as alkaline cements☆. *Fuel,* 82(18)**,** pp 2259-2265.

Fernández-Jiménez, A., Palomo, A. & Criado, M. 2005. Microstructure development of alkali-activated fly ash cement: a descriptive model. *Cement and Concrete Research,* 35(6)**,** pp 1204-1209.

Fernández-Jiménez, A., Palomo, A., Sobrados, I. & Sanz, J. 2006. The role played by the reactive alumina content in the alkaline activation of fly ashes. *Microporous and Mesoporous Materials,* 91(1)**,** pp 111-119.

Fernández-Jiménez, A., Puertas, F., Sobrados, I. & Sanz, J. 2003. Structure of Calcium Silicate Hydrates Formed in Alkaline-Activated Slag: Influence of the Type of Alkaline Activator. *Journal of the American Ceramic Society,* 86(8)**,** pp 1389-1394.

Fischer-Cripps, A. C. 2004. *Nanoindentation*, New York: Springer-Verlag.

Flatabø, R., Coste, A. & Greve, M. M. 2017. A systematic investigation of the charging effect in scanning electron microscopy for metal nanostructures on insulating substrates. *Journal of Microscopy,* 265(3)**,** pp 287-297.

Gallucci, E., Scrivener, K., Groso, A., Stampanoni, M. & Margaritondo, G. 2007. 3D experimental investigation of the microstructure of cement pastes using synchrotron X-ray microtomography (μCT). *Cement and Concrete Research,* 37(3)**,** pp 360-368.

Gao, X., Wei, Y. & Huang, W. 2017a. Effect of individual phases on multiscale modeling mechanical properties of hardened cement paste. *Construction and Building Materials,* 153, pp 25-35.

Gao, X., Yu, Q. & Brouwers, H. J. H. 2015. Reaction kinetics, gel character and strength of ambient temperature cured alkali activated slag–fly ash blends. *Construction and Building Materials,* 80(Supplement C)**,** pp 105-115.

Gao, X., Yu, Q. & Brouwers, H. J. H. 2017b. Apply ^{29}Si, ^{27}Al MAS NMR and selective dissolution in identifying the reaction degree of alkali activated slag-fly ash composites. *Ceramics International,* 43(15)**,** pp 12408-12419.

Gao, Y., De Schutter, G., Ye, G., Huang, H., Tan, Z. & Wu, K. 2013. Porosity characterization of ITZ in cementitious composites: Concentric expansion and overflow criterion. *Construction and Building Materials,* 38, pp 1051-1057.

García-Lodeiro, I., Fernández-Jiménez, A. & Palomo, A. 2013. Variation in hybrid cements over time. Alkaline activation of fly ash-portland cement blends. *Cement and Concrete Research,* 52, pp 112-122.

García-Lodeiro, I., Fernández-Jiménez, A., Palomo, A. & Macphee, D. E. 2010. Effect of Calcium Additions on N–A–S–H Cementitious Gels. *Journal of the American Ceramic Society,* 93(7)**,** pp 1934-1940.

Garcia-Lodeiro, I., Palomo, A. & Fernández-Jiménez, A. 2015. 3 - Crucial insights on the mix design of alkali-activated cement-based binders. *Handbook of Alkali-Activated Cements, Mortars and Concretes.* Oxford: Woodhead Publishing.

Garcia-Lodeiro, I., Palomo, A., Fernández-Jiménez, A. & Macphee, D. E. 2011. Compatibility studies between N-A-S-H and C-A-S-H gels. Study in the ternary diagram Na2O–CaO–Al2O3–SiO2–H2O. *Cement and Concrete Research,* 41(9)**,** pp 923-931.

Gastaldi, D., Canonico, F., Capelli, L., Boccaleri, E., Milanesio, M., Palin, L., Croce, G., Marone, F., Mader, K. & Stampanoni, M. 2012. In situ tomographic investigation on the early hydration behaviors of cementing systems. *Construction and Building Materials,* 29, pp 284-290.

Gebregziabiher, B. S., Thomas, R. & Peethamparan, S. 2015. Very early-age reaction kinetics and microstructural development in alkali-activated slag. *Cement and Concrete Composites,* 55, pp 91-102.

Ghosh, K. & Ghosh, P. 2012. Effect of synthesizing papameters on compressive strength of fly ash based geopolymer paste. *International Journal of Structural and Civil Engineering,* 1(8)**,** pp 1-11.

Girão, A. V., Richardson, I. G., Porteneuve, C. B. & Brydson, R. M. D. 2007. Composition, morphology and nanostructure of C–S–H in white Portland cement pastes hydrated at 55 °C. *Cement and Concrete Research,* 37(12)**,** pp 1571-1582.

Gołaszewski, J. & Szwabowski, J. 2004. Influence of superplasticizers on rheological behaviour of fresh cement mortars. *Cement and Concrete Research,* 34(2)**,** pp 235-248.

Goldstein, J. I., Newbury, D. E., Michael, J. R., Ritchie, N. W. M., Scott, J. H. J. & Joy, D. C. 2018. *Scanning Electron Microscopy and X-ray Microanalysis*: Springer US.

Gomaa, E., Sargon, S., Kashosi, C. & ElGawady, M. Fresh Properties and Early Compressive Strength of Alkali-Activated High Calcium Fly Ash Paste. 2018 Singapore. Springer Singapore, 497-507.

Griffiths, P. R. & Haseth, J. A. d. 2007. Introduction to Vibrational Spectroscopy. *Fourier Transform Infrared Spectrometry.*

Gu, Y., Martin, R.-P., Omikrine Metalssi, O., Fen-Chong, T. & Dangla, P. 2019. Pore size analyses of cement paste exposed to external sulfate attack and delayed ettringite formation. *Cement and Concrete Research,* 123, pp 105766.

Guinea, G. V., Planas, J. & Elices, M. 1992. Measurement of the fracture energy using three-point bend tests: Part 1-Inflence of experimental procedures. *Materials and Structures,* 25, pp 212-218.

Haha, M. B., Lothenbach, B., Le Saout, G. & Winnefeld, F. 2011. Influence of slag chemistry on the hydration of alkali-activated blast-furnace slag — Part I: Effect of MgO. *Cement and Concrete Research,* 41(9)**,** pp 955-963.

Hajimohammadi, A., Provis, J. L. & van Deventer, J. S. J. 2010. Effect of Alumina Release Rate on the Mechanism of Geopolymer Gel Formation. *Chemistry of Materials,* 22(18)**,** pp 5199-5208.

Hajimohammadi, A. & van Deventer, J. S. J. 2016. Dissolution behaviour of source materials for synthesis of geopolymer binders: A kinetic approach. *International Journal of Mineral Processing,* 153, pp 80-86.

Hill, R. J. & Howard, C. J. 1987. Quantitative phase analysis from neutron powder diffraction data using the Rietveld method. *Journal of Applied Crystallography,* 20(6)**,** pp 467-474.

Hou, D., Zhang, Y., Yang, T., Zhang, J., Pei, H., Zhang, J., Jiang, J. & Li, T. 2018. Molecular structure, dynamics, and mechanical behavior of sodium aluminosilicate hydrate (NASH) gel at elevated temperature: a molecular dynamics study. *Physical Chemistry Chemical Physics,* 20(31)**,** pp 20695-20711.

Hu, C. 2014. Microstructure and mechanical properties of fly ash blended cement pastes. *Construction and Building Materials,* 73, pp 618-625.

Hu, C. & Li, Z. 2015a. Property investigation of individual phases in cementitious composites containing silica fume and fly ash. *Cement and Concrete Composites,* 57, pp 17-26.

Hu, C. & Li, Z. 2015b. A review on the mechanical properties of cement-based materials measured by nanoindentation. *Construction and Building Materials,* 90, pp 80-90.

Hu, Q., Aboustait, M., Kim, T., Ley, M. T., Bullard, J. W., Scherer, G., Hanan, J. C., Rose, V., Winarski, R. & Gelb, J. 2016. Direct measurements of 3d structure, chemistry and mass density during the induction period of C3s hydration. *Cement and Concrete Research,* 89, pp 14-26.

Hughes, J. J. & Trtik, P. 2004. Micro-mechanical properties of cement paste measured by depth-sensing nanoindentation: a preliminary correlation of physical properties with phase type. *Materials Characterization,* 53(2)**,** pp 223-231.

Ishwarya, G., Singh, B., Deshwal, S. & Bhattacharyya, S. K. 2019. Effect of sodium carbonate/sodium silicate activator on the rheology, geopolymerization and strength of fly ash/slag geopolymer pastes. *Cement & Concrete Composites,* 97, pp 226-238.

Ismail, I., Bernal, S. A., Provis, J. L., San Nicolas, R., Hamdan, S. & van Deventer, J. S. J. 2014. Modification of phase evolution in alkali-activated blast furnace slag by the incorporation of fly ash. *Cement and Concrete Composites,* 45, pp 125-135.

Jang, J. G., Lee, N. K. & Lee, H. K. 2014. Fresh and hardened properties of alkali-activated fly ash/slag pastes with superplasticizers. *Construction and Building Materials,* 50, pp 169-176.

Jennings, H. M. 2000. A model for the microstructure of calcium silicate hydrate in cement paste. *Cement and Concrete Research,* 30(1)**,** pp 101-116.

Jennings, H. M., Thomas, J. J., Gevrenov, J. S., Constantinides, G. & Ulm, F.-J. 2007. A multi-technique investigation of the nanoporosity of cement paste. *Cement and Concrete Research,* 37(3)**,** pp 329-336.

Ji, T., Gao, Q. L., Zheng, W. Y., Lin, X. J. & Wu, H. C. 2017. Interfacial transition zone of alkali-activated slag concrete. *ACI Materials Journal,* 114(3)**,** pp 347-354.

Justnes, H., Skocek, J., Østnor, T. A., Engelsen, C. J. & Skjølsvold, O. 2020. Microstructural changes of hydrated cement blended with fly ash upon carbonation. *Cement and Concrete Research,* 137, pp 106192.

Kapeluszna, E., Kotwica, Ł., Różycka, A. & Gołek, Ł. 2017. Incorporation of Al in C-A-S-H gels with various Ca/Si and Al/Si ratio: Microstructural and structural characteristics with DTA/TG, XRD, FTIR and TEM analysis. *Construction and Building Materials,* 155, pp 643-653.

Kaufmann, J., Loser, R. & Leemann, A. 2009. Analysis of cement-bonded materials by multi-cycle mercury intrusion and nitrogen sorption. *Journal of Colloid and Interface Science,* 336(2)**,** pp 730-737.

Keulen, A., Yu, Q. L., Zhang, S. & Grünewald, S. 2018. Effect of admixture on the pore structure refinement and enhanced performance of alkali-activated fly ash-slag concrete. *Construction and Building Materials,* 162, pp 27-36.

Khedmati, M., Kim, Y.-R., Turner, J. A., Alanazi, H. & Nguyen, C. 2018. An integrated microstructural-nanomechanical-chemical approach to examine material-specific characteristics of cementitious interphase regions. *Materials Characterization,* 138, pp 154-164.

Kim, S.-M. & Abu Al-Rub, R. K. 2011. Meso-scale computational modeling of the plastic-damage response of cementitious composites. *Cement and Concrete Research,* 41(3)**,** pp 339-358.

Kjellsen, K. O., Monsøy, A., Isachsen, K. & Detwiler, R. J. 2003. Preparation of flat-polished specimens for SEM-backscattered electron imaging and X-ray

microanalysis—importance of epoxy impregnation. *Cement and Concrete Research,* 33(4)**,** pp 611-616.

Knapen, E., Cizer, O., Van Balen, K. & Van Gemert, D. 2009. Effect of free water removal from early-age hydrated cement pastes on thermal analysis. *Construction and Building Materials,* 23(11)**,** pp 3431-3438.

Komljenović, M., Baščarević, Z. & Bradić, V. 2010. Mechanical and microstructural properties of alkali-activated fly ash geopolymers. *Journal of Hazardous Materials,* 181(1–3)**,** pp 35-42.

Korpa, A. & Trettin, R. 2006. The influence of different drying methods on cement paste microstructures as reflected by gas adsorption: Comparison between freeze-drying (F-drying), D-drying, P-drying and oven-drying methods. *Cement and Concrete Research,* 36(4)**,** pp 634-649.

Kosmatka, S. H., Kerkhoff, B. & Panarese, W. C. 2002. *Design and Control of Concrete Mixtures,* Skokie, Illinois: Portland Cement Association.

Kumar, S., Kumar, R., Alex, T. C., Bandopadhyay, A. & Mehotra, S. P. 2007. Influence of reactivity of fly ash on geopolymerisation. *Advances in Applied Ceramics,* 106, pp 120-127.

Kumar, S., Kumar, R. & Mehrotra, S. P. 2010. Influence of granulated blast furnace slag on the reaction, structure and properties of fly ash based geopolymer. *Journal of Materials Science,* 45(3)**,** pp 607-615.

Kumarappa, D. B. & Peethamparan, S. 2020. Stress-strain characteristics and brittleness index of alkali-activated slag/class C fly ash mortars. *Journal of Building Engineering,* pp 101595.

L'Hôpital, E., Lothenbach, B., Le Saout, G., Kulik, D. & Scrivener, K. 2015. Incorporation of aluminium in calcium-silicate-hydrates. *Cement and Concrete Research,* 75, pp 91-103.

Landis, E. N. & Keane, D. T. 2010. X-ray microtomography. *Materials Characterization,* 61(12)**,** pp 1305-1316.

Larbi, J. A. & Bijen, J. M. J. M. 1990. Effects of water-cement ratio, quantity and fineness of sand on the evolution of lime in set portland cement systems. *Cement and Concrete Research,* 20(5)**,** pp 783-794.

Lecomte, I., Henrist, C., Liégeois, M., Maseri, F., Rulmont, A. & Cloots, R. 2006. (Micro)-structural comparison between geopolymers, alkali-activated slag cement and Portland cement. *Journal of the European Ceramic Society,* 26(16)**,** pp 3789-3797.

Lee, H., Vimonsatit, V. & Chindaprasirt, P. 2016. Mechanical and micromechanical properties of alkali activated fly-ash cement based on nano-indentation. *Construction and Building Materials,* 107, pp 95-102.

Lee, N. K. & Lee, H. K. 2013. Setting and mechanical properties of alkali-activated fly ash/slag concrete manufactured at room temperature. *Construction and Building Materials,* 47, pp 1201-1209.

Lee, N. K. & Lee, H. K. 2015. Reactivity and reaction products of alkali-activated, fly ash/slag paste. *Construction and Building Materials,* 81, pp 303-312.

Lee, W. K. W. & van Deventer, J. S. J. 2004. The interface between natural siliceous aggregates and geopolymers. *Cement and Concrete Research,* 34(2)**,** pp 195-206.

Leemann, A., Loser, R. & Münch, B. 2010. Influence of cement type on ITZ porosity and chloride resistance of self-compacting concrete. *Cement and Concrete Composites,* 32(2)**,** pp 116-120.

Leemann, A., Münch, B., Gasser, P. & Holzer, L. 2006. Influence of compaction on the interfacial transition zone and the permeability of concrete. *Cement and Concrete Research,* 36(8)**,** pp 1425-1433.

Li, C., Sun, H. & Li, L. 2010. A review: The comparison between alkali-activated slag (Si+Ca) and metakaolin (Si+Al) cements. *Cement and Concrete Research,* 40(9)**,** pp 1341-1349.

Li, D., Xu, Z., Luo, Z., Pan, Z. & Cheng, L. 2002. The activation and hydration of glassy cementitious materials. *Cement and Concrete Research,* 32(7)**,** pp 1145-1152.

Li, Z. & Huang, Y. 1998. Effect of Strain Rate on the Compressive Strength Surface Cracking and Failure Mode of Mortar. *ACI Materials Journal,* 95(5)**.**

Lippmaa, E., Maegi, M., Samoson, A., Engelhardt, G. & Grimmer, A. R. 1980. Structural studies of silicates by solid-state high-resolution silicon-29 NMR. *Journal of the American Chemical Society,* 102(15)**,** pp 4889-4893.

Lloyd, R. R., Provis, J. L., Smeaton, K. J. & van Deventer, J. S. J. 2009a. Spatial distribution of pores in fly ash-based inorganic polymer gels visualised by Wood's metal intrusion. *Microporous and Mesoporous Materials,* 126(1)**,** pp 32-39.

Lloyd, R. R., Provis, J. L. & van Deventer, J. S. J. 2009b. Microscopy and microanalysis of inorganic polymer cements. 1: remnant fly ash particles. *Journal of Materials Science,* 44(2)**,** pp 608-619.

Lloyd, R. R., Provis, J. L. & van Deventer, J. S. J. 2009c. Microscopy and microanalysis of inorganic polymer cements. 2: the gel binder. *Journal of Materials Science,* 44(2)**,** pp 620-631.

Lolli, F., Manzano, H., Provis, J. L., Bignozzi, M. C. & Masoero, E. 2018. Atomistic Simulations of Geopolymer Models: The Impact of Disorder on Structure and Mechanics. *ACS Applied Materials & Interfaces,* 10(26)**,** pp 22809-22820.

Luo, X., Xu, J.-y., Bai, E.-l. & Li, W. 2013. Research on the dynamic compressive test of highly fluidized geopolymer concrete. *Construction and Building Materials,* 48, pp 166-172.

Luo, X., Xu, J.-y., Li, W. & Bai, E. 2014. Effect of alkali-activator types on the dynamic compressive deformation behavior of geopolymer concrete. *Materials Letters,* 124, pp 310-312.

Luo, Z., Li, W., Gan, Y., Mendu, K. & Shah, S. P. 2020. Maximum likelihood estimation for nanoindentation on sodium aluminosilicate hydrate gel of geopolymer under different silica modulus and curing conditions. *Composites Part B: Engineering,* 198, pp 108185.

Ma, H. 2014. Mercury intrusion porosimetry in concrete technology: tips in measurement, pore structure parameter acquisition and application. *Journal of Porous Materials,* 21(2)**,** pp 207-215.

Ma, Y., Wang, G., Ye, G. & Hu, J. 2018. A comparative study on the pore structure of alkali-activated fly ash evaluated by mercury intrusion porosimetry, N2 adsorption and image analysis. *Journal of Materials Science,* 53(8)**,** pp 5958-5972.

Ma, Y. & Ye, G. 2015. The shrinkage of alkali activated fly ash. *Cement and Concrete Research,* 68, pp 75-82.

Ma, Y., Ye, G. & Hu, J. 2017. Micro-mechanical properties of alkali-activated fly ash evaluated by nanoindentation. *Construction and Building Materials,* 147, pp 407-416.

Madsen Ian, C., Scarlett Nicola, V. Y. & Kern, A. 2011. Description and survey of methodologies for the determination of amorphous content via X-ray powder diffraction. *Zeitschrift für Kristallographie Crystalline Materials.*

Marcin, M., Sisol, M. & Brezani, I. 2016. Effect of Slag Addition on Mechanical Properties of Fly ash Based Geopolymers. *Procedia Engineering,* 151, pp 191-197.

Marjanović, N., Komljenović, M., Baščarević, Z., Nikolić, V. & Petrović, R. 2015. Physical–mechanical and microstructural properties of alkali-activated fly ash–blast furnace slag blends. *Ceramics International,* 41(1, Part B)**,** pp 1421-1435.

McCullough, E. C. 1975. Photon attenuation in computed tomography. *Medical Physics,* 2(6)**,** pp 307-320.

Mehta, P. K. & Monterio, P. J. M. 2013. *Concrete: Microstructure, Properties, and Materials*: McGraw-Hill Education.

Memon, F. A., Nuruddin, M. F., Khan, S., Shafiq, N. & Ayub, T. 2013. Effect of Sodium Hydroxide Concentration on Fresh Properties and Compressive Strength of Self-compacting Geopolymer Concrete. *Journal of Engineering Science and Technology,* 8(1)**,** pp 44-56.

Mondal, P., Shah, S. P. & Marks, L. D. Nanomechanical Properties of Interfacial Transition Zone in Concrete. 2009 Berlin, Heidelberg. Springer Berlin Heidelberg, pp 315-320.

Mori, T. & Tanaka, K. 1973. Average stress in matrix and average elastic energy of materials with misfitting inclusions. *Acta Metallurgica,* 21(5)**,** pp 571-574.

Mostafa, N. Y., El-Hemaly, S. A. S., Al-Wakeel, E. I., El-Korashy, S. A. & Brown, P. W. 2001. Characterization and evaluation of the hydraulic activity of water-cooled slag and air-cooled slag. *Cement and Concrete Research,* 31(6)**,** pp 899-904.

Myers, R. J., Bernal, S. A. & Provis, J. L. 2014. A thermodynamic model for C-(N-)A-S-H gel: CNASH_ss. Derivation and validation. *Cement and Concrete Research,* 66, pp 27-47.

Myers, R. J., Bernal, S. A., San Nicolas, R. & Provis, J. L. 2013. Generalized Structural Description of Calcium–Sodium Aluminosilicate Hydrate Gels: The Cross-Linked Substituted Tobermorite Model. *Langmuir,* 29(17)**,** pp 5294-5306.

Nath, P. & Sarker, P. K. 2014. Effect of GGBFS on setting, workability and early strength properties of fly ash geopolymer concrete cured in ambient condition. *Construction and Building Materials,* 66, pp 163-171.

Nath, P. & Sarker, P. K. 2016. Fracture properties of GGBFS-blended fly ash geopolymer concrete cured in ambient temperature. *Materials and Structures,* 50(1)**,** pp 32.

Nath, S. K. & Kumar, S. 2017. Reaction kinetics, microstructure and strength behavior of alkali activated silico-manganese (SiMn) slag – Fly ash blends. *Construction and Building Materials,* 147, pp 371-379.

Nedeljković, M., Šavija, B., Zuo, Y., Luković, M. & Ye, G. 2018. Effect of natural carbonation on the pore structure and elastic modulus of the alkali-activated fly ash and slag pastes. *Construction and Building Materials,* 161, pp 687-704.

Němeček, J., Šmilauer, V. & Kopecký, L. 2011. Nanoindentation characteristics of alkali-activated aluminosilicate materials. *Cement and Concrete Composites,* 33(2)**,** pp 163-170.

Němecek, J., Smilauer, V., Kopecky, L. & Německová, J. 2010. Nanoindentation of Alkali-Activated Fly Ash. *Transportation Research Record,* 2141(1)**,** pp 36-40.

Nguyen, T. H. Y., Tsuchiya, K. & Atarashi, D. 2018. Microstructure and composition of fly ash and ground granulated blast furnace slag cement pastes in 42-month cured samples. *Construction and Building Materials,* 191, pp 114-124.

Nicolas, R. S. & Provis, J. L. 2015. The interfacial transition zone in alkali-activated slag mortars. *Frontiers in Materials,* 2

Nikolov, A., Rostovsky, I. & Nugteren, H. 2017. Geopolymer materials based on natural zeolite. *Case Studies in Construction Materials,* 6, pp 198-205.

Nili, M. & Ehsani, A. 2015. Investigating the effect of the cement paste and transition zone on strength development of concrete containing nanosilica and silica fume. *Materials & Design,* 75, pp 174-183.

Oh, J. E., Jun, Y. & Jeong, Y. 2014. Characterization of geopolymers from compositionally and physically different Class F fly ashes. *Cement and Concrete Composites,* 50, pp 16-26.

Oh, J. E., Monteiro, P. J. M., Jun, S. S., Choi, S. & Clark, S. M. 2010. The evolution of strength and crystalline phases for alkali-activated ground blast furnace slag and fly ash-based geopolymers. *Cement and Concrete Research,* 40(2)**,** pp 189-196.

Oliver, W. C. & Pharr, G. M. 2011. An improved technique for determining hardness and elastic modulus using load and displacement sensing indentation experiments. *Journal of Materials Research,* 7(6)**,** pp 1564-1583.

Ollivier, J. P., Maso, J. C. & Bourdette, B. 1995. Interfacial transition zone in concrete. *Advanced Cement Based Materials,* 2(1)**,** pp 30-38.

Pacheco-Torgal, F., Labrincha, J. A., Leonelli, C., Palomo, A. & Chindaprasirt, P. 2014. *Handbook of alkali-activated cements, mortars and concretes*: Woodhead Publishing.

Palacios, M., Banfill, P. F. G. & Puertas, F. 2008. Rheology and setting of alkali-cctivated slag pastes and mortars: effect of organic admixture. *ACI Materials Journal,* 105(2)**,** pp 140-148.

Palomo, Á., Alonso, S., Fernandez-Jiménez, A., Sobrados, I. & Sanz, J. 2004. Alkaline Activation of Fly Ashes: NMR Study of the Reaction Products. *Journal of the American Ceramic Society,* 87(6)**,** pp 1141-1145.

Palomo, A., Grutzeck, M. W. & Blanco, M. T. 1999. Alkali-activated fly ashes: A cement for the future. *Cement and Concrete Research,* 29(8)**,** pp 1323-1329.

Park, S. M., Khalid, H. R., Seo, J. H., Yoon, H. N., Son, H. M., Kim, S. H., Lee, N. K., Lee, H. K. & Jang, J. G. 2018. Pressure-Induced Geopolymerization in Alkali-Activated Fly Ash. *Sustainability,* 10(10)**,** pp 3538.

Part, W. K., Ramli, M. & Cheah, C. B. 2015. An overview on the influence of various factors on the properties of geopolymer concrete derived from industrial by-products. *Construction and Building Materials,* 77, pp 370-395.

Parthiban, K., Saravanarajamohan, K., Shobana, S. & Bhaskar, A. A. 2013. Effect of replacement of slag on the mechanical properties of fly ash based geopolymer concrete. *International Journal of Engineering and Technology,* 5(3)**,** pp 2555-2559.

Pereira, A. P. d. S., Silva, M. H. P. d., Lima Júnior, É. P., Paula, A. d. S. & Tommasini, F. J. 2017. Processing and characterization of PET composites reinforced with geopolymer concrete waste. *Materials Research,* 20, pp 411-420.

Peterson, P. E. 1980. Fracture energy of concrete: Method of determination. *Cement and Concrete Research,* 10(1)**,** pp 79-89.

Pichler, B. & Hellmich, C. 2011. Upscaling quasi-brittle strength of cement paste and mortar: A multi-scale engineering mechanics model. *Cement and Concrete Research,* 41(5)**,** pp 467-476.

Pichler, B., Hellmich, C. & Eberhardsteiner, J. 2008. Spherical and acicular representation of hydrates in a micromechanical model for cement paste: prediction of early-age elasticity and strength. *Acta Mechanica,* 203(3)**,** pp 137.

Planas, J., Elices, M. & Guinea, G. V. 1992. Measurement of the fracture energy using three-point bend tests: Part 2-Influence of bulk energy dissipation. *Materials and Structures,* 25, pp 305-312.

Pope, A. W. & Jennings, H. M. 1992. The influence of mixing on the microstructure of the cement paste/aggregate interfacial zone and on the strength of mortar. *Journal of Materials Science,* 27(23)**,** pp 6452-6462.

Promentilla, M. A. B., Sugiyama, T., Hitomi, T. & Takeda, N. 2009. Quantification of tortuosity in hardened cement pastes using synchrotron-based X-ray computed microtomography. *Cement and Concrete Research,* 39(6)**,** pp 548-557.

Provis, J. L. 2014. Geopolymers and other alkali activated materials: why, how, and what? *Materials and Structures,* 47(1)**,** pp 11-25.

Provis, J. L. 2018. Alkali-activated materials. *Cement and Concrete Research,* 114, pp 40-48.

Provis, J. L. & Bernal, S. A. 2014. Geopolymers and Related Alkali-Activated Materials. *Annual Review of Materials Research,* 44(1)**,** pp 299-327.

Provis, J. L., Myers, R. J., White, C. E., Rose, V. & van Deventer, J. S. J. 2012. X-ray microtomography shows pore structure and tortuosity in alkali-activated binders. *Cement and Concrete Research,* 42(6)**,** pp 855-864.

Provis, J. L., Rose, V., Winarski, R. P. & van Deventer, J. S. J. 2011. Hard X-ray nanotomography of amorphous aluminosilicate cements. *Scripta Materialia,* 65(4)**,** pp 316-319.

Provis, J. L. & van Deventer, J. S. J. 2014. *Alkali activated materials: State-of-the-art report, RILEM TC 224-AAM,* Netherlands: Springe.

Puertas, F., Martínez-Ramírez, S., Alonso, S. & Vázquez, T. 2000. Alkali-activated fly ash/slag cements: Strength behaviour and hydration products. *Cement and Concrete Research,* 30(10)**,** pp 1625-1632.

Puertas, F., Palacios, M., Manzano, H., Dolado, J. S., Rico, A. & Rodríguez, J. 2011. A model for the C-A-S-H gel formed in alkali-activated slag cements. *Journal of the European Ceramic Society,* 31(12)**,** pp 2043-2056.

Puligilla, S. & Mondal, P. 2013. Role of slag in microstructural development and hardening of fly ash-slag geopolymer. *Cement and Concrete Research,* 43, pp 70-80.

Qian, S., Yao, Y., Wang, Z., Cui, S., Liu, X., Jiang, H., Guo, Z., Lai, G., Xu, Q. & Guan, J. 2018. Synthesis, characterization and working mechanism of a novel polycarboxylate superplasticizer for concrete possessing reduced viscosity. *Construction and Building Materials,* 169, pp 452-461.

Rafeet, A., Vinai, R., Soutsos, M. & Sha, W. 2017. Guidelines for mix proportioning of fly ash/GGBS based alkali activated concretes. *Construction and Building Materials,* 147, pp 130-142.

Randall, N. X., Vandamme, M. & Ulm, F.-J. 2011. Nanoindentation analysis as a two-dimensional tool for mapping the mechanical properties of complex surfaces. *Journal of Materials Research,* 24(3)**,** pp 679-690.

Rattanasak, U., Pankhet, K. & Chindaprasirt, P. 2011. Effect of chemical admixtures on properties of high-calcium fly ash geopolymer. *International Journal of Minerals, Metallurgy, and Materials,* 18(3)**,** pp 364.

Reddy, M. S., Dinakar, P. & Rao, B. H. 2018. Mix design development of fly ash and ground granulated blast furnace slag based geopolymer concrete. *Journal of Building Engineering,* 20, pp 712-722.

Richardson, I. G. 2008. The calcium silicate hydrates. *Cement and Concrete Research,* 38(2)**,** pp 137-158.

RILEM TC 50-FMC 1985. Determination of the fracture energy of mortar and concrete by means of three-point bend tests on notched beams. *Materials and Structures,* 18(4)**,** pp 287-290.

Rivera, O. G., Long, W. R., Weiss Jr, C. A., Moser, R. D., Williams, B. A., Torres-Cancel, K., Gore, E. R. & Allison, P. G. 2016. Effect of elevated temperature on alkali-activated geopolymeric binders compared to portland cement-based binders. *Cement and Concrete Research,* 90, pp 43-51.

Ryu, G. S., Lee, Y. B., Koh, K. T. & Chung, Y. S. 2013. The mechanical properties of fly ash-based geopolymer concrete with alkaline activators. *Construction and Building Materials,* 47, pp 409-418.

Saha, S. & Rajasekaran, C. 2017. Enhancement of the properties of fly ash based geopolymer paste by incorporating ground granulated blast furnace slag. *Construction and Building Materials,* 146, pp 615-620.

Salkind, N. J. 2007. *Encyclopedia of Measurement and Statistics,* Thousand Oaks, California: SAGE Publications.

San Nicolas, R., Bernal, S. A., Mejía de Gutiérrez, R., van Deventer, J. S. J. & Provis, J. L. 2014. Distinctive microstructural features of aged sodium silicate-activated slag concretes. *Cement and Concrete Research,* 65, pp 41-51.

Sarker, P. K., Haque, R. & Ramgolam, K. V. 2013. Fracture behaviour of heat cured fly ash based geopolymer concrete. *Materials and Design,* 44, pp 580-586.

Sauvola, J. & Pietikäinen, M. 2000. Adaptive document image binarization. *Pattern Recognition,* 33(2)**,** pp 225-236.

Scarlett, N. V. Y., Madsen, I. C., Cranswick, L. M. D., Lwin, T., Groleau, E., Stephenson, G., Aylmore, M. & Agron-Olshina, N. 2002. Outcomes of the International Union of Crystallography Commission on Powder Diffraction Round Robin on Quantitative Phase Analysis: samples 2, 3, 4, synthetic bauxite, natural granodiorite and pharmaceuticals. *Journal of Applied Crystallography,* 35(4)**,** pp 383-400.

Scherer, G. W. 1999. Structure and properties of gels. *Cement and Concrete Research,* 29(8)**,** pp 1149-1157.

Schindelin, J., Arganda-Carreras, I., Frise, E., Kaynig, V., Longair, M., Pietzsch, T., Preibisch, S., Rueden, C., Saalfeld, S., Schmid, B., Tinevez, J.-Y., White, D. J., Hartenstein, V., Eliceiri, K., Tomancak, P. & Cardona, A. 2012. Fiji: an open-source platform for biological-image analysis. *Nature Methods,* 9(7)**,** pp 676-682.

Scrivener, K., Snellings, R. & Lothenbach, B. 2016. *A practical guide to microstructural analysis of cementitious materials,* Boca Raton, Florida, United States: Taylor & Francis.

Scrivener, K. L., Crumbie, A. K. & Laugesen, P. 2004. The interfacial transition zone (ITZ) between cement paste and aggregate in concrete. *Interface Science,* 12(4)**,** pp 411-421.

Scrivener, K. L., Crumbie, A. K. & Pratt, P. L. 1988. A Stludy of the Interfacial Region Between Cement Paste and Aggregate in Concrete. *MRS Proceedings,* 114, pp 87.

Scrivener, K. L. & Kirkpatrick, R. J. 2008. Innovation in use and research on cementitious material. *Cement and Concrete Research,* 38(2)**,** pp 128-136.

Scrivener, K. L. & Nemati, K. M. 1996. The percolation of pore space in the cement paste/aggregate interfacial zone of concrete. *Cement and Concrete Research,* 26(1)**,** pp 35-40.

Shang, J., Dai, J., Zhao, T., Guo, S., Zhang, P. & Mu, B. 2018. Alternation of traditional cement mortars using fly ash-based geopolymer mortars modified by slag. *Journal of Cleaner Production,* 203, pp 746-756.

Shi, C., Jiménez, A. F. & Palomo, A. 2011. New cements for the 21st century: The pursuit of an alternative to Portland cement. *Cement and Concrete Research,* 41(7)**,** pp 750-763.

Shi, C., Krivenko, P. V. & Roy, D. 2006. *Alkali-Activated Cements and Concretes*, London: Taylor & Francis.

Shi, C., Shi, Z., Hu, X., Zhao, R. & Chong, L. 2015. A review on alkali-aggregate reactions in alkali-activated mortars/concretes made with alkali-reactive aggregates. *Materials and Structures,* 48(3)**,** pp 621-628.

Shi, C. & Xie, P. 1998. Interface between cement paste and quartz sand in alkali-activated slag mortars. *Cement and Concrete Research,* 28(6)**,** pp 887-896.

Simeonov, P. & Ahmad, S. 1995. Effect of transition zone on the elastic behavior of cement-based composites. *Cement and Concrete Research,* 25(1)**,** pp 165-176.

Singh, B., Rahman, M. R., Paswan, R. & Bhattacharyya, S. K. 2016. Effect of activator concentration on the strength, ITZ and drying shrinkage of fly ash/slag geopolymer concrete. *Construction and Building Materials,* 118, pp 171-179.

Singh, P. S., Bastow, T. & Trigg, M. 2005. Structural studies of geopolymers by ^{29}Si and ^{27}Al MAS-NMR. *Journal of Materials Science,* 40(15)**,** pp 3951-3961.

Siyal, A. A., Azizli, K. A., Man, Z. & Ullah, H. 2016. Effects of Parameters on the Setting Time of Fly Ash Based Geopolymers Using Taguchi Method. *Procedia Engineering,* 148, pp 302-307.

Šmilauer, V., Hlaváček, P., Škvára, F., Šulc, R., Kopecký, L. & Němeček, J. 2011. Micromechanical multiscale model for alkali activation of fly ash and metakaolin. *Journal of Materials Science,* 46(20)**,** pp 6545-6555.

Sofi, M., van Deventer, J. S. J., Mendis, P. A. & Lukey, G. C. 2007. Engineering properties of inorganic polymer concretes (IPCs). *Cement and Concrete Research,* 37(2)**,** pp 251-257.

Somna, K., Jaturapitakkul, C., Kajitvichyanukul, P. & Chindaprasirt, P. 2011. NaOH-activated ground fly ash geopolymer cured at ambient temperature. *Fuel,* 90(6)**,** pp 2118-2124.

Sua-iam, G., Sokrai, P. & Makul, N. 2016. Novel ternary blends of Type 1 Portland cement, residual rice husk ash, and limestone powder to improve the properties of self-compacting concrete. *Construction and Building Materials*, 125, pp 1028-1034.

Sun, Z. & Vollpracht, A. 2018. Isothermal calorimetry and in-situ XRD study of the NaOH activated fly ash, metakaolin and slag. *Cement and Concrete Research,* 103, pp 110-122.

Swamy, R. N. & Ammar, B. 1990. Some Engineering Properties of Slag Concrete as Influenced by Mix Proportioning and Curing. *Materials Journal,* 87(3)**,** pp 210-220.

Szechyńska-Hebda, M., Marczyk, J., Ziejewska, C., Hordyńska, N., Mikuła, J. & Hebda, M. 2019. Neutral geopolymer foams reinforced with cellulose studied with the FT-Raman spectroscopy. *IOP Conference Series: Materials Science and Engineering,* 706, pp 012017.

Taiwo, O. O., Finegan, D. P., Gelb, J., Holzner, C., Brett, D. J. L. & Shearing, P. R. 2016. The use of contrast enhancement techniques in X-ray imaging of lithium–ion battery electrodes. *Chemical Engineering Science,* 154, pp 27-33.

Talha Junaid, M., Kayali, O., Khennane, A. & Black, J. 2015. A mix design procedure for low calcium alkali activated fly ash-based concretes. *Construction and Building Materials*, 79, pp 301-310.

Talling, B. & Brandstetr, J. 1989. Present State and Future of Alkali-Activated Slag Concretes. *Special Publication,* 114, pp 1519-1546.

Tang, Z., Li, W., Tam, V. W. Y. & Luo, Z. 2020. Investigation on dynamic mechanical properties of fly ash/slag-based geopolymeric recycled aggregate concrete. *Composites Part B: Engineering,* 185, pp 107776.

Tatar, J., Taylor, C. R. & Hamilton, H. R. 2019. A multiscale micromechanical model of adhesive interphase between cement paste and epoxy supported by nanomechanical evidence. *Composites Part B: Engineering,* 172, pp 679-689.

Temuujin, J., van Riessen, A. & Williams, R. 2009a. Influence of calcium compounds on the mechanical properties of fly ash geopolymer pastes. *Journal of Hazardous Materials,* 167(1)**,** pp 82-88.

Temuujin, J., Williams, R. P. & Riessen, A. V. 2009b. Effect of mechanical activation of fly ash on the properties of geopolymer cured at ambient temperature. *J. Mater. Process. Technol.,* 209, pp 5276-5280.

Thakur, R. N. & Ghosh, S. 2009. Effect of mix composition on compressive strength and microstructure of fly ash based gepolymer composites. *ARPN Journal of Engineering and Applied Sciences,* 4(4)**,** pp 68-74.

Thomas, J. J. & Jennings, H. M. 2006. A colloidal interpretation of chemical aging of the C-S-H gel and its effects on the properties of cement paste. *Cement and Concrete Research,* 36(1)**,** pp 30-38.

Thomas, M. D. A. & Folliard, K. J. 2007. 7 - Concrete aggregates and the durability of concrete. *In:* Page, C. L. & Page, M. M. (eds.) *Durability of Concrete and Cement Composites.* Woodhead Publishing.

Thomas, R. J., Gebregziabiher, B. S., Giffin, A. & Peethamparan, S. 2018. Micromechanical properties of alkali-activated slag cement binders. *Cement and Concrete Composites,* 90, pp 241-256.

Thomas, R. J. & Peethamparan, S. 2015. Alkali-activated concrete: Engineering properties and stress–strain behavior. *Construction and Building Materials,* 93, pp 49-56.

Timakul, P., Thanaphatwetphisit, K. & Aungkavattana, P. 2015. Effect of Silica to Alumina Ratio on the Compressive Strength of Class C Fly Ash-Based Geopolymers. *Key Engineering Materials,* 659, pp 80-84.

Trtik, P. & Bartos, P. J. M. 2000. Micromechanical properties of cementitious composites. *Materials and Structures,* 33(2)**,** pp 144-144.

Tu, W., Zhu, Y., Fang, G., Wang, X. & Zhang, M. 2019. Internal curing of alkali-activated fly ash-slag pastes using superabsorbent polymer. *Cement and Concrete Research,* 116, pp 179-190.

Ulm, F.-J., Delafargue, A. & Constantinides, G. 2005. Experimental Microporomechanics. *In:* Dormieux, L. & Ulm, F.-J. (eds.) *Applied Micromechanics of Porous Materials.* Vienna: Springer Vienna.

Ulm, F.-J., Vandamme, M., Jennings, H. M., Vanzo, J., Bentivegna, M., Krakowiak, K. J., Constantinides, G., Bobko, C. P. & Van Vliet, K. J. 2010. Does microstructure matter for statistical nanoindentation techniques? *Cement and Concrete Composites,* 32(1)**,** pp 92-99.

Ulm, F. J., Constantinides, G. & Heukamp, F. H. 2004. Is concrete a poromechanics materials?—A multiscale investigation of poroelastic properties. *Materials and Structures,* 37(1)**,** pp 43-58.

Ulrik Nilsen, A. & Monteiro, P. J. M. 1993. Concrete: A three phase material. *Cement and Concrete Research,* 23(1)**,** pp 147-151.

van Deventer, J. S. J., San Nicolas, R., Ismail, I., Bernal, S. A., Brice, D. G. & Provis, J. L. 2015. Microstructure and durability of alkali-activated materials as key parameters for standardization. *Journal of Sustainable Cement-Based Materials,* 4(2)**,** pp 116-128.

Vandamme, M. & Ulm, F.-J. 2009. Nanogranular origin of concrete creep. *Proceedings of the National Academy of Sciences,* 106(26)**,** pp 10552-10557.

Vandamme, M. & Ulm, F. J. 2013. Nanoindentation investigation of creep properties of calcium silicate hydrates. *Cement and Concrete Research,* 52, pp 38-52.

Walkley, B., San Nicolas, R., Sani, M.-A., Gehman, J. D., van Deventer, J. S. J. & Provis, J. L. 2016a. Synthesis of stoichiometrically controlled reactive aluminosilicate and calcium-aluminosilicate powders. *Powder Technology,* 297, pp 17-33.

Walkley, B., San Nicolas, R., Sani, M.-A., Rees, G. J., Hanna, J. V., van Deventer, J. S. J. & Provis, J. L. 2016b. Phase evolution of C-(N)-A-S-H/N-A-S-H gel blends investigated via alkali-activation of synthetic calcium aluminosilicate precursors. *Cement and Concrete Research,* 89, pp 120-135.

Wang, L., Yang, B., Abraham, A., Qi, L., Zhao, X. & Chen, Z. 2014. Construction of dynamic three-dimensional microstructure for the hydration of cement using 3D image registration. *Pattern Analysis and Applications,* 17(3)**,** pp 655-665.

Wang, P. Z., Trettin, R. & Rudert, V. 2005. Effect of fineness and particle size distribution of granulated blast-furnace slag on the hydraulic reactivity in cement systems. *Advances in Cement Research,* 17(4)**,** pp 161-167.

Wang, S.-D. & Scrivener, K. L. 1995. Hydration products of alkali activated slag cement. *Cement and Concrete Research,* 25(3)**,** pp 561-571.

Wang, S. & Scrivener, K. L. 2003. ^{29}Si and ^{27}Al NMR study of alkali-activated slag. *Cement and Concrete Research,* 33(5)**,** pp 769-774.

Wang, W.-C., Wang, H.-Y. & Lo, M.-H. 2015. The fresh and engineering properties of alkali activated slag as a function of fly ash replacement and alkali concentration. *Construction and Building Materials,* 84, pp 224-229.

Wilson, W., Sorelli, L. & Tagnit-Hamou, A. 2018. Automated coupling of Nanolndentation and Quantitative Energy-Dispersive Spectroscopy (NI-QEDS): A comprehensive method to disclose the micro-chemo-mechanical properties of cement pastes. *Cement and Concrete Research,* 103, pp 49-65.

Winnefeld, F., Ben Haha, M., Le Saout, G., Costoya, M., Ko, S.-C. & Lothenbach, B. 2015. Influence of slag composition on the hydration of alkali-activated slags. *Journal of Sustainable Cement-Based Materials,* 4(2)**,** pp 85-100.

Winslow, D. N., Cohen, M. D., Bentz, D. P., Snyder, K. A. & Garboczi, E. J. 1994. Percolation and pore structure in mortars and concrete. *Cement and Concrete Research,* 24(1)**,** pp 25-37.

Wong, H. S. & Buenfeld, N. R. 2006. Patch microstructure in cement-based materials: Fact or artefact? *Cement and Concrete Research,* 36(5)**,** pp 990-997.

Wong, H. S., Head, M. K. & Buenfeld, N. R. 2006. Pore segmentation of cement-based materials from backscattered electron images. *Cement and Concrete Research,* 36(6)**,** pp 1083-1090.

Wong, H. S., Zobel, M., Buenfeld, N. R. & Zimmerman, R. W. 2009. Influence of the interfacial transition zone and microcracking on the diffusivity, permeability and sorptivity of cement-based materials after drying. *Magazine of Concrete Research,* 61(8)**,** pp 571-589.

Wu, K.-R., Chen, B., Yao, W. & Zhang, D. 2001. Effect of coarse aggregate type on mechanical properties of high-performance concrete. *Cement and Concrete Research,* 31(10)**,** pp 1421-1425.

Wu, K., Shi, H., Xu, L., Ye, G. & De Schutter, G. 2016. Microstructural characterization of ITZ in blended cement concretes and its relation to transport properties. *Cement and Concrete Research,* 79, pp 243-256.

Wu, Z., Shi, C., He, W. & Wang, D. 2017. Static and dynamic compressive properties of ultra-high performance concrete (UHPC) with hybrid steel fiber reinforcements. *Cement and Concrete Composites,* 79(148-157.

Xiao, J., Li, W., Corr, D. J. & Shah, S. P. 2013a. Effects of interfacial transition zones on the stress–strain behavior of modeled recycled aggregate concrete. *Cement and Concrete Research,* 52, pp 82-99.

Xiao, J., Li, W., Sun, Z., Lange, D. A. & Shah, S. P. 2013b. Properties of interfacial transition zones in recycled aggregate concrete tested by nanoindentation. *Cement and Concrete Composites,* 37, pp 276-292.

Xie, J. & Kayali, O. 2014. Effect of initial water content and curing moisture conditions on the development of fly ash-based geopolymers in heat and ambient temperature. *Construction and Building Materials,* 67, Part A, pp 20-28.

Xie, P., Beaudoin, J. J. & Brousseau, R. 1991. Effect of aggregate size on transition zone properties at the portland cement paste interface. *Cement and Concrete Research,* 21(6)**,** pp 999-1005.

Xu, H., Gong, W., Syltebo, L., Izzo, K., Lutze, W. & Pegg, I. L. 2014. Effect of blast furnace slag grades on fly ash based geopolymer waste forms. *Fuel,* 133, pp 332-340.

Yang, J., Hou, D. & Ding, Q. 2018. Structure, Dynamics, and Mechanical Properties of Cross-Linked Calcium Aluminosilicate Hydrate: A Molecular Dynamics Study. *ACS Sustainable Chemistry & Engineering,* 6(7)**,** pp 9403-9417.

Yang, K.-H., Song, J.-K. & Song, K.-I. 2013. Assessment of CO2 reduction of alkali-activated concrete. *Journal of Cleaner Production,* 39, pp 265-272.

Yang, T., Yao, X., Zhang, Z. & Wang, H. 2012. Mechanical property and structure of alkali-activated fly ash and slag blends. *Journal of Sustainable Cement-Based Materials,* 1(4)**,** pp 167-178.

Ye, H. & Radlińska, A. 2016. Fly ash-slag interaction during alkaline activation: Influence of activators on phase assemblage and microstructure formation. *Construction and Building Materials,* 122, pp 594-606.

Yin, B., Kang, T., Kang, J. & Chen, Y. 2018. Analysis of Active Ion-Leaching Behavior and the Reaction Mechanism During Alkali Activation of Low-Calcium Fly Ash. *International Journal of Concrete Structures and Materials,* 12(1)**,** pp 50.

Yio, M. H. N., Wong, H. S. & Buenfeld, N. R. 2019. 3D pore structure and mass transport properties of blended cementitious materials. *Cement and Concrete Research,* 117, pp 23-37.

Yip, C. K., Lukey, G. C., Provis, J. L. & van Deventer, J. S. J. 2008. Effect of calcium silicate sources on geopolymerisation. *Cement and Concrete Research,* 38(4)**,** pp 554-564.

Yon, J.-H., Hawkins, N. M. & Kobayashi, A. S. 1992. Strain-rate sensitivity of concrete mechanical properties. *ACI Materials Journal,* 89(2)**,** pp 146-153.

Young, R. A., Mackie, P. E. & von Dreele, R. B. 1977. Application of the pattern-fitting structure-refinement method of X-ray powder diffractometer patterns. *Journal of Applied Crystallography,* 10(4)**,** pp 262-269.

Yu, Q., Liu, H., Yang, T. & Liu, H. 2018. 3D numerical study on fracture process of concrete with different ITZ properties using X-ray computerized tomography. *International Journal of Solids and Structures,* 147, pp 204-222.

Zaoui, A. 2002. Continuum micromechanics: Survey. *Journal of Engineering Mechanics,* 128(8)**,** pp 808-816.

Zhang, J. & Scherer, G. W. 2011. Comparison of methods for arresting hydration of cement. *Cement and Concrete Research,* 41(10)**,** pp 1024-1036.

Zhang, M. 2017. Pore-scale modelling of relative permeability of cementitious materials using X-ray computed microtomography images. *Cement and Concrete Research,* 95, pp 18-29.

Zhang, M. & Gjørv, O. E. 1990. Microstructure of the interfacial zone between lightweight aggregate and cement paste. *Cement and Concrete Research,* 20(4)**,** pp 610-618.

Zhang, M., He, Y., Ye, G., Lange, D. A. & Breugel, K. v. 2012a. Computational investigation on mass diffusivity in Portland cement paste based on X-ray computed microtomography (μCT) image. *Construction and Building Materials,* 27(1)**,** pp 472-481.

Zhang, S., Zhang, C., Liao, L. & Wang, C. 2018. Numerical study of the effect of ITZ on the failure behaviour of concrete by using particle element modelling. *Construction and Building Materials,* 170, pp 776-789.

Zhang, Z., Wang, H. & Provis, J. L. 2012b. Quantitative study of the reactivity of fly ash in geopolymerization by FTIR. *Journal of Sustainable Cement-Based Materials,* 1(4)**,** pp 154-166.

Zhang, Z., Yao, X., Zhu, H. & Chen, Y. 2009. Role of water in the synthesis of calcined kaolin-based geopolymer. *Applied Clay Science,* 43(2)**,** pp 218-223.

Zheng, J., Wong, H. S. & Buenfeld, N. R. 2009. Assessing the influence of ITZ on the steady-state chloride diffusivity of concrete using a numerical model. *Cement and Concrete Research,* 39(9)**,** pp 805-813.

Zhou, J., Ye, G. & van Breugel, K. 2010. Characterization of pore structure in cement-based materials using pressurization–depressurization cycling mercury intrusion porosimetry (PDC-MIP). *Cement and Concrete Research,* 40(7)**,** pp 1120-1128.

Zhu, W., Hughes, J. J., Bicanic, N. & Pearce, C. J. 2007. Nanoindentation mapping of mechanical properties of cement paste and natural rocks. *Materials Characterization,* 58(11)**,** pp 1189-1198.

Zhu, X., Yuan, Y., Li, L., Du, Y. & Li, F. 2017. Identification of interfacial transition zone in asphalt concrete based on nano-scale metrology techniques. *Materials and Design,* 129, pp 91-102.

Zhu, X., Zhang, Z., Yang, K., Magee, B., Wang, Y., Yu, L., Nanukuttan, S., Li, Q., Mu, S., Yang, C. & Basheer, M. 2018. Characterisation of pore structure development of alkali-activated slag cement during early hydration using electrical responses. *Cement and Concrete Composites,* 89, pp 139-149.

Zhuang, X., Chen, L., Komarneni, S., Zhou, C., Tong, D., Yang, H., Yu, W. & Wang, H. 2016. Fly ash-based geopolymer: clean production, properties and applications. *Journal of Cleaner Production,* 125, pp 253-267.